Modelling Frequency-based Neural Responses to Deep Brain Stimulation in Parkinson's Disease

James J. Sermon

Wolfson College
University of Oxford

A thesis submitted for the degree of
Doctor of Philosophy

Hilary 2024

Abstract

Deep Brain Stimulation (DBS) is an established therapy for Parkinson's disease (PD) when pharmacological measures have been exhausted or following medication-associated motor control side effects. DBS has been implanted in over 100,000 patients with PD, and is also used in other neurological disorders, such as epilepsy and psychiatric conditions. Despite this success and widespread adoption, the underlying methods of DBS therapy have not changed in over a decade and can introduce side effects, for example on coordination and cognition. Improvements in therapeutic outcome as well as side effects can likely be addressed through real time adaptation to both patient and pathology. This could be achieved using closed-loop DBS in sense-stimulation devices. However, there is a lack of understanding of how stimulation artefacts infiltrate the neural signals as well as how DBS affects neural activity, which even limits the application of current open-loop DBS techniques. To investigate observed signal changes from DBS, we analyse and develop computational models of signals whose frequency signature changes in response to neuromodulation. In Chapter 2, we review hypothesised causes of sub-harmonic artefacts and analyse whether these represent feasible sources of the activity seen in data. In addition, we provide methods to confirm physiological origin as well as tools to improve the design of future sense-stimulation protocols. In Chapter 3, we predict regions of medically-induced prokinetic motor cortical rhythm entrainment (frequency locking) to variable stimulation parameters using a computational model and validate the predictions against data. We demonstrate that DBS can produce nonlinear neuronal responses to inform future clinical paradigms. In Chapter 4, we create a network model that can reproduce long-term dynamic frequency responses to DBS. We suggest that single neuronal populations may be able to replicate these observations and that vesicle depletion may be a fundamental neural response to DBS. Together, this thesis advances our understanding of DBS-associated changes in neural recordings and suggests potential neural or electrical underlying mechanisms. Using computational models of these responses to DBS, we look to advance our understanding of the mechanisms of existing open-loop DBS with direct applications to techniques for future closed-loop approaches.

Modelling Frequency-based Neural Responses to Deep Brain Stimulation in Parkinson's Disease



James J. Sermon

Wolfson College

University of Oxford

A thesis submitted for the degree of

Doctor of Philosophy

Hilary 2024

Supervised by Prof. Timothy Denison, Prof. Huiling Tan and Dr. Benoît Duchet

Acknowledgements

I would like to express my deepest gratitude and appreciation for my supervisors, Prof. Tim Denison, Prof. Huiling Tan, and Dr. Benoît Duchet, for their guidance, expertise and support.

Tim, it has been an honour to be part of the Bioelectronics lab and your return to academia. I will always be grateful that you stepped in as the 3YP mentor in your first year, which upon reflection was a pivotal career moment for myself. The opportunities and connections that you have provided me with is far more than I could have hoped for at the outset of this DPhil, and your mentorship has allowed me to grow and develop my passion. To the past and present members of the Bioelectronics lab, I would like to express my appreciation for you all both as people and researchers.

Huiling, I am sincerely thankful for the advice you have given me over the last three years. The opportunities to work with and present to your lab, with particular thanks to Dr. Christoph Wiest, have advanced me as a researcher and given me the confidence that I can academically debate with anyone.

Benoît, it has been a privilege to be your first DPhil student. You gave me both the room to pursue the questions I thought were interesting and the honesty to make both our work and myself better. I think we made a great team, and I will sincerely miss our Tuesday afternoon meetings. Having experienced your mentorship firsthand, I have no doubt of the success of both yourself and your future lab. I cannot wait to see what you achieve next.

I would not have been able to complete this thesis without the help of Dr. Phil Starr and the Starr lab at UCSF who had both a problem that need solving as well as data. I would also like to thank the other members of the MRC BNDU, especially Prof. Rafal Bogacz, for your insights and academic debates.

Funding from the Medical Research Council and the use of the University of Oxford Advanced Research Computing facility were fundamental in conducting this work.

Thank you to my family and friends for your unwavering love and support. I will never tire of the continual messages or conversations of “have you seen this latest neuroscience/neurotechnology article?”. To my parents, your support has allowed me to pursue this incredible opportunity. Thank you for continuously believing in

me, and providing me with opportunities and the strong base that you have. Sonia, you continue to inspire me every day. I will forever be grateful for the collection of small probabilities that allowed us to meet that first day of our degrees at Oxford. Thank you for always believing in me during the toughest moments as well as never letting my head get too big when things seem too good to be true.

Abstract

Deep Brain Stimulation (DBS) is an established therapy for Parkinson's disease (PD) when pharmacological measures have been exhausted or following medication-associated motor control side effects. DBS has been implanted in over 100,000 patients with PD, and is also used in other neurological disorders, such as epilepsy and psychiatric conditions. Despite this success and widespread adoption, the underlying methods of DBS therapy have not changed in over a decade and can introduce side effects, for example on coordination and cognition. Improvements in therapeutic outcome as well as side effects can likely be addressed through real time adaptation to both patient and pathology. This could be achieved using closed-loop DBS in sense-stimulation devices. However, there is a lack of understanding of how stimulation artefacts infiltrate the neural signals as well as how DBS affects neural activity, which even limits the application of current open-loop DBS techniques. To investigate observed signal changes from DBS, we analyse and develop computational models of signals whose frequency signature changes in response to neuromodulation. In Chapter 2, we review hypothesised causes of sub-harmonic artefacts and analyse whether these represent feasible sources of the activity seen in data. In addition, we provide methods to confirm physiological origin as well as tools to improve the design of future sense-stimulation protocols. In Chapter 3, we predict regions of medically-induced prokinetic motor cortical rhythm entrainment (frequency locking) to variable stimulation parameters using a computational model and validate the predictions against data. We demonstrate that DBS can produce nonlinear neuronal responses to inform future clinical paradigms. In Chapter 4, we create a network model that can reproduce long-term dynamic frequency responses to DBS. We suggest that single neuronal populations may be able to replicate these observations and that vesicle depletion may be a fundamental neural response to DBS. Together, this thesis advances our understanding of DBS-associated changes in neural recordings and suggests potential neural or electrical underlying mechanisms. Using computational models of these responses to DBS, we look to advance our understanding of the mechanisms of existing open-loop DBS with direct applications to techniques for future closed-loop approaches.

Contents

List of Figures **x**

List of Abbreviations **xii**

1 Introduction **1**

1.1 Thesis Overview 1
1.2 Background 5
1.2.1 Parkinson's Disease 5
1.2.1.1 Symptoms 5
1.2.1.2 Therapy Options 6
1.2.1.3 Pathophysiology 6
1.2.1.4 Neural Mechanisms of Parkinson's Disease 7
1.2.2 Neural Rhythms 8
1.2.2.1 General Rhythms of the Brain 8
1.2.2.2 Broadband Gamma 8
1.2.2.3 Finely-Tuned Gamma(FTG) 8
1.2.3 DBS 9
1.2.3.1 Therapeutic Development 9
1.2.3.2 Current Applications 10
1.2.3.3 Future Applications, aDBS and Current Blocks . . 10
1.2.3.4 Hypothesised Neural Mechanisms of DBS 12
1.2.3.5 Characteristics of DBS Sites 14
1.2.3.6 DBS Artefacts 15
1.2.4 Entrainment 16
1.2.4.1 Arnold Tongues and Rotation Number 16
1.2.4.2 Neuromodulatory Entrainment Examples 17
1.2.4.3 Case-Study in an Epileptic Canine 20
1.2.4.4 Clinical Significance 22
1.2.4.5 Other Examples of Entrainment in Biology 22
1.2.5 Evoked Resonant Neural Activity (ERNA) 23
1.2.5.1 Characteristics of ERNA 23
1.2.5.2 Confirmation of Physiological Origin 25

1.2.5.3 Clinical Significance 26
1.2.6 Modelling Approaches 26
1.2.6.1 Sine Circle Map 27
1.2.6.2 Wilson-Cowan Model 28
1.2.6.3 Kuramoto Model 29
1.2.6.4 Next Generation Neural Mass Model 30
1.2.6.5 Suitability of Models for Each Application 31
1.3 Thesis Outline 31

2 Artefact Checking **37**
2.1 Abstract 38
2.2 Introduction 38
2.3 Model Predictions and Theory (Is Entrainment Expected?) 42
2.4 Physiological Confirmation Steps 43
2.4.1 Medication and Arousal State Dependent Response 43
2.4.2 Nonlinear Response to Stimulation 44
2.4.3 Location Specific 45
2.4.4 Clinical Observations 46
2.5 Electrical Signal Chain Checklist 46
2.5.1 Tissue Electrode Interface 47
2.5.2 Stimulator Circuits 48
2.5.3 Aliasing and Analogue to Digital Converters (ADCs) 51
2.6 Discussion 54
2.6.1 Limitations 55
2.6.2 Implications 56
2.7 Conclusion 57

3 Stationary Responses - Entrainment **58**
3.1 Abstract 59
3.2 Introduction 60
3.3 Materials and methods 61
3.3.1 Wilson-Cowan Model 61
3.3.2 Data Collection 63
3.3.3 Fitting Process 66
3.3.4 Providing Stimulation and Entrainment Analysis in the Model 69
3.3.5 Entrainment Analysis of the ECoG Recordings 70
3.3.6 Correspondence Between Stimulation Amplitude in the Model and in the Data 71
3.4 Results 71

3.4.1 Prediction of 1:2 Entrainment of FTG Using a Fitted Wilson-Cowan Model . . . 72
3.4.2 Validation of Model Predictions in Human Patient During Chronic Therapeutic Stimulation . . . 73
3.5 Discussion . . . 76
3.5.1 Entrainment and adaptive DBS . . . 77
3.5.2 Entrainment in the Wilson-Cowan Model . . . 77
3.5.3 Limitations . . . 82
3.5.4 Implications . . . 84
3.6 Conclusion . . . 84

4 Dynamic Responses - ERNA **86**
4.1 Abstract . . . 87
4.2 Introduction . . . 87
4.3 Results . . . 89
4.3.1 Results of Fitting Process . . . 89
4.3.2 Long-Term Spectrogram . . . 92
4.3.3 Variable Stimulation Frequency . . . 93
4.3.4 Variable Stimulation Amplitude . . . 94
4.3.5 Variable Medication State . . . 95
4.3.6 Post Stimulation Bursting . . . 98
4.3.7 Individual Oscillator Perturbation . . . 98
4.3.8 Replication of In Vitro Slice Experiments . . . 100
4.4 Methods . . . 101
4.4.1 The Kuramoto Model . . . 102
4.4.1.1 Modelling the Effect of Vesicle Depletion and Replenishment on Coupling Strength . . . 103
4.4.1.2 Coupling Function and PRC . . . 107
4.4.1.3 Distributions of Oscillators' Natural Frequency . . . 108
4.4.2 Fitting Process . . . 108
4.4.3 Simulation of Various Stimulation Paradigms . . . 110
4.4.3.1 Long-Term Spectrogram . . . 110
4.4.3.2 Simulations for Validation with Variable Neuromodulation . . . 110
4.4.3.3 Simulation for Validation with Biophysical Evidence 112
4.4.4 Evaluation of ERNA Frequency and Amplitude Over Time . 112
4.4.5 Statistics for ERNA Amplitude On and Off Medication . . . 113
4.5 Discussion . . . 113
4.5.1 Hypothesised Mechanisms and Models of ERNA . . . 114

4.5.2 Proposed Computational Model 116
4.5.3 Model Predictions for Further Validation 118
4.5.4 Limitations 119
4.6 Conclusion 122

5 General discussion **123**
5.1 Contributions 124
5.2 Implications 126
5.3 Common Threads 128
5.4 Limitations 129
5.5 Future Work 130
5.6 Concluding Remarks 133

Appendices

A Appendix to Entrainment Modelling Chapter **135**
A.1 Optimisation Details 136
A.1.1 Correlation and Redundancy Between Features 136
A.1.2 Evaluation of Cost 137
A.1.3 Robustness to Noise 137
A.1.4 Top-Ranked Wilson-Cowan Model Parameter Set 138
A.2 Clinical Symptoms of all Patients 138
A.3 Off-Stimulation Data and Model Features in RCS18 and RCS02 . . 138
A.4 Sine Circle Map 141
A.5 Fitting Robustness 142
A.5.1 Consistency Across Best Parameter Fits 142
A.5.2 Alternate Stimulation Pulse Shapes with Recharge All Predict Left Leaning 1:2 Tongues 142
A.5.3 Alternate Stimulation Waveforms Predict Different 1:2 Tongues 143
A.5.4 Tongue Lean and the Wilson-Cowan Vector Field 144
A.5.5 Stimulating the Excitatory Population Instead of the Inhibitory Population 148
A.6 Entrained Signals Exhibit Phase-Locking 148

B Appendix to ERNA Modelling Chapter **151**
B.1 Fitted Model Parameter Set 151
B.2 Explaining Model Dynamics 154
B.2.1 Amplitude Response 154
B.2.2 Frequency Response 154
B.3 Current Model Shortcomings 156

B.3.1 Fast Dynamics 156
B.3.2 Subtherapeutic Stimulation 156
B.4 Fitting Robustness 158
B.4.1 Sensitivity of Coupling Function 158
B.4.2 Sensitivity of Phase Response Curve 160
B.5 Alternative Parameter Set with Lower Natural Frequency 162
B.6 Dynamic Oscillations 164

References **167**

List of Figures

1.1 Human recordings of 1:2 entrainment with an interpretation to the expected brain rhythm and stimulation phase-locked pattern 18
1.2 Epileptic canine resting and seizure associated frequencies and corresponding Arnold tongues 21
1.3 Human recordings of the fast and slow dynamics of ERNA 24
1.4 Generic two-population Wilson-Cowan model 29
1.5 Relevance of each chapter in the general space of neural responses to DBS. 34

2.1 A flow diagram of the framework used to investigate half harmonic activity. 41
2.2 The sine circle map and Wilson-Cowan model predictions of sub-harmonic entrainment 43
2.3 Modulation of 1:2 entrainment with medication state 44
2.4 Modulation of 1:2 entrainment with variable stimulation parameters 45
2.5 1:2 entrainment is only present in the cortex and not seen in the pallidum during pallidal-DBS 46
2.6 Computational simulations of stimulation across tissue-electrode interfaces do not produce sub-harmonic artefacts 49
2.7 Saline tank tests of sense-stimulation devices do not show any sub-harmonic artefacts 51
2.8 Sub-harmonic artefacts can be introduced through aliasing from poor stimulation/sampling frequency combinations. 54

3.1 The two-population Wilson-Cowan model. 63
3.2 Contact localisation for the three patients. 67
3.3 Off-stimulation FTG features and parameter fitting process. 69
3.4 Comparison of fitting features between the data and the model. . . 72
3.5 Half-harmonic entrainment comparison between model predictions and data. 78
3.6 1:2 entrained power correlates with stimulation parameters. 79
3.7 Correlation between model predictions for 1:2 entrained peak power and data. 80

4.1 Results and features of fitted Kuramoto model. 90
4.2 Long-term spectrogram of successive on/off DBS windows comparison to data. 93
4.3 Comparison of ERNA frequency and amplitude over variable stimulation frequency between model and data. 95
4.4 Comparison of ERNA frequency and amplitude over variable stimulation amplitude between model and data. 96
4.5 Comparison of ERNA frequency and amplitude over variable medication state between model and data. 97
4.6 Comparison of ERNA frequency and amplitude over bursting stimulation between model and data. 99
4.7 Oscillator responses to individual oscillator perturbation. 100
4.8 Oscillator response to high-frequency stimulation in a smaller network. 102
4.9 The model network and vesicle depletion. 105

A.1 Comparison of only fitting to one data feature. 136
A.2 Off-stimulation cortical data features for other two patients. 139
A.3 Comparison of model off-stimulation performance of other two patients. 140
A.4 Top six ranked parameter fits for RCS10 show clear similarities. . . 142
A.5 Comparison of pulse recharge lengths to entrainment field. 144
A.6 Comparison of entrainment field for four different pulse shapes. . . 145
A.7 Phase space explanation of left leaning 1:2 tongue. 147
A.8 Entrainment field for stimulating the excitatory population. 149
A.9 Gamma phase locking at 4 different stimulation amplitudes. 150

B.1 ERNA amplitude explanation through analysis of model oscillator phase relationships. 155
B.2 ERNA fast dynamics. 157
B.3 Subtherapeutic stimulation frequency model ERNA predictions with and without vesicle depletion. 159
B.4 Model ERNA predictions for three different coupling functions. . . . 160
B.5 Model ERNA predictions for varying coupling function Fourier coefficients. 161
B.6 Model ERNA predictions for three different phase response curves. . 162
B.7 Model ERNA dynamics for lowered oscillator natural frequency. . . 164
B.8 Model ERNA dynamics for lowered oscillator natural frequency and modulated vesicle depletion to match settled ERNA frequency. . . . 165
B.9 Small parameter adjustments can predict on-stimulation dynamic oscillation data. 166

List of Abbreviations

AD . . . . . Alzheimer's disease.

aDBS . . . . . adaptive deep brain stimulation.

ADC . . . . . analogue-to-digital converter.

ChAT . . . . . choline acetyltransferase.

CT . . . . . computed tomography.

DBS . . . . . deep brain stimulation.

ECG . . . . . electrocardiogram.

ECoG . . . . . electrocorticogram.

EEG . . . . . electroencephalography.

ERNA . . . . . evoked resonant neural activity.

FTG . . . . . finely-tuned gamma.

GABA . . . . . gamma aminobutyric acid.

GP . . . . . glubus pallidus.

GPe . . . . . globus pallidus externus.

GPi . . . . . globus pallidus internus.

HF . . . . . high-frequency.

HFO . . . . . high-frequency oscillation.

HH . . . . . Hodgkin-Huxley.

LFP . . . . . local field potential.

MER . . . . . microelectrode recording.

MRI . . . . . magnetic resonance imaging.

N1 . . . . . non-rapid eye movement sleep stage 1.

PD . . . . . Parkinson's disease.

PDF . . . . . probability density function.

PRC . . . . . phase response curve.

PSD . . . . . power spectral density.

REM . . . . . rapid eye movement.

RP . . . . . recycling pool.

RRP . . . . . readily-releasable pool.

RtP . . . . . resting pool.

SN . . . . . substantia nigra.

STDP . . . . . spike-timing-dependent plasticity.

sTMS . . . . . synchronised transcranial magnetic stimulation

STN . . . . . subthalamic nucleus.

tACS . . . . . transcranial alternating current stimulation.

TEI . . . . . tissue-electrode interface.

V1 . . . . . primary visual cortex.

1 Introduction

Contents

1.1 Thesis Overview 1
1.2 Background 5
1.2.1 Parkinson's Disease 5
1.2.2 Neural Rhythms 8
1.2.3 DBS 9
1.2.4 Entrainment 16
1.2.5 Evoked Resonant Neural Activity (ERNA) 23
1.2.6 Modelling Approaches 26
1.3 Thesis Outline 31

1.1 Thesis Overview

Deep Brain Stimulation (DBS) is an established therapy for pathological motor activity in Parkinson's disease (PD), as well as other movement disorders such as essential tremor and dystonia. There have been over 100,000 DBS systems implanted for PD therapy (Pycroft et al. 2018). The wide adoption of this therapy has further demonstrated the ability of DBS to reduce the frequency and severity of both hypo- and hyperkinetic episodes. The option of DBS is only advocated after alternative pharmacological options have been exhausted (Sironi 2011; Oliveria 2018). Despite the wide adoption of DBS, the vast numbers of patients that have been implanted

and the hardware continuing to advance, clinical therapeutic techniques have not changed greatly in over two decades. The approach continues to focus on open-loop DBS, supplying stimulation at a fixed frequency and amplitude combination continuously. Both pharmacological options and DBS provide significant benefit to motor control in their current therapeutic configurations. However, whether DBS slows the progression of PD is a matter of debate and neither option provides a cure (Herrington et al. 2016). Furthermore, the potential side effects on other neural functions such as cognition and mental health are not well understood (Rodriguez-Oroz et al. 2005; Benabid et al. 2009) and may provide an opportunity to further improve current therapeutic paradigms. It has been acknowledged that the likely next advancement in therapeutic approaches of DBS is through closed-loop adaptive deep brain stimulation (aDBS) (Pycroft et al. 2018; Frey et al. 2022; Schulder et al. 2023), which would provide patient specific therapy and respond to the pathology in real time. However, there are key obstacles to the clinical implementation of aDBS. These primarily include the contamination of signals with artefacts making the use of biomarkers unreliable (Ramírez et al. 2011; Noury et al. 2016; Abbasi et al. 2016; Qian et al. 2017; Thenaisie et al. 2021; Chen et al. 2021) and a lack of understanding regarding the effects of DBS on neural circuits.

When artefacts are avoided, spectral analysis of neuronal rhythms can offer key insights into the underlying physiological response to DBS. In the case of frequency responses that do not change with time on stimulation, recent studies have suggested that medication-induced gamma frequency peaks can be modulated by independent physiological perturbations (Swann et al. 2016; Gilron et al. 2021; Smyth et al. 2023; Oehrn et al. 2023). This indicates that these observations are likely not artefactual, but instead are of potential clinical relevance. Furthermore, studies have been performed to characterise stimulation artefacts as well as the appearance of these spectral features in certain sense-stimulation devices (Stanslaski et al. 2018; Thenaisie et al. 2021; Chen et al. 2021). These results indicate it is possible to devise paradigms that keep spectral ranges free of artefacts and available for biomarker exploitation.

Several studies have reported entrainment of neural rhythms at harmonics of stimulation frequency (Swann et al. 2016; Swann et al. 2018a; Gilron et al. 2021; Chan et al. 2021; Thenaisie et al. 2021; Smyth et al. 2023; Oehrn et al. 2023). Entrainment (the synchronisation of an oscillation to a harmonic of an external, perturbing frequency) is a basic property of perturbed oscillatory systems, at least for entrainment at stimulation frequency. However, many clinicians remain cautious about using these results for clinical purposes as the underlying mechanisms are poorly understood. A recent study demonstrated the clinical relevance of 1:2 finely-tuned gamma (FTG) entrainment by reducing severity of bothersome motor symptoms when the entrained rhythm was used as the biomarker for an aDBS algorithm in PD patients (Oehrn et al. 2023). This motivates the further study of this phenomenon in PD.

In addition to these stationary frequency responses to stimulation, recent results have demonstrated a physiological response to DBS that decays in frequency over time (Wiest et al. 2020; Wiest et al. 2023). This neural response, termed evoked resonant neural activity (ERNA), appears immediately following stimulation onset and at much higher frequencies than stimulation frequency. Additionally, ERNA has been demonstrated to provide the strongest biomarker of contact selection for DBS in PD patients (Xu et al. 2022). However, despite the clinical significance of ERNA, its underlying mechanisms remain uncertain.

Overall, stimulation artefacts together with stationary and dynamic frequency responses represent a broad overview of the potential observations from sense-stimulation devices. Characterising and investigating the underlying mechanisms of each of these phenomena will provide greater opportunities for aDBS algorithms to both observe neural signals as well as modulate them with greater confidence. In this thesis we use a combination of mathematical models, computational simulations, bench top testing and prior literature to understand the conditions for each of these phenomena to appear and postulate the underlying mechanisms.

In Chapter 2, we analyse the appearance of stimulation artefacts in the specific case of sub-harmonic entrainment. We provide a method to confirm physiological

origin through several independent physiological perturbation tests. Furthermore, we provide a step-by-step walk through of the signal chain to identify where artefacts can arise at sub-harmonics.

Confident that sub-harmonic activity is a neural response in the data analysed, we proceed to develop a patient specific model to predict half harmonic entrainment in Chapter 3. We use a computational neural population model of the cortex fitted to off-stimulation data in three patients with PD to predict the response on-stimulation. We follow this by validating the model's predictions against data collected at variable stimulation parameters.

In Chapter 4, we investigate the underlying mechanisms of the dynamic frequency response of ERNA through a model of interacting oscillators subject to high-frequency periodic perturbation. We fit this model to long-term spectral features of ERNA, something which has not been done before. We look to validate this model by comparing its response across different neuromodulation paradigms.

This thesis advances our understanding of both physiological and unphysiological responses to DBS for the potential improvement of clinical therapeutic approaches. In our artefact investigation, we demonstrate that sub-harmonic artefacts can be avoided. In addition, we provide researchers with a clear framework to rule out the presence of artefacts when the characterisation of their signal chain may not be complete. We also provide a list of the most common sources of artefacts from the signal chain as well as tools that can be used to avoid artefacts in the design of stimulation protocols. Our entrainment chapter reveals that DBS can produce nonlinear patterns of entrainment in neural circuits. As the clinical implications of entrainment continue to become clearer, this framework may inform clinicians and increase the efficiency of obtaining therapeutic effects. The results from our ERNA model reveal that we are able to capture the slow dynamics of ERNA with a single neuronal population. This was not considered previously within other modelling efforts. We identify fundamental properties that are key to producing ERNA in the model, such as vesicle depletion, and further hypotheses that can be used to validate

our findings. Collectively, we provide a comprehensive insight into the underlying mechanisms of a wide variety of neural and non-neural responses to DBS (see Fig 1.5).

1.2 Background

In this thesis I will present analysis and models of the observed responses to DBS in PD. To provide the most efficient documentation of this contribution, I will summarise the prior work and understanding of PD as well as DBS. I will also clarify the field's prior understanding and observations of the neural responses discussed in this thesis, entrainment and ERNA, before discussing modelling approaches and the most appropriate methods to approach these phenomena.

1.2.1 Parkinson's Disease

In 2016 over 6 million patients were reported to have PD worldwide, this figure is expected to increase to around 10 million by the year 2030 (Ou et al. 2021). While PD does not directly cause death, the progressive neurodegeneration lowers a sufferer's quality of life and can reduce life expectancy (Ou et al. 2021).

In this section I will present the general observations of PD, current therapeutic measures as well as the underlying changes in physiology that contribute to the PD-associated neurodegeneration.

1.2.1.1 Symptoms

There have been several studies that attempt to categorise PD into subtypes based on symptoms, age and rate of progression (Marras et al. 2020). However, the field has not reached a collective conclusion to exclusively categorise these subtypes. Hence, in this thesis we will consider this neuropathology homogeneously with the caution that there exists greater heterogeneity between patients.

PD is a slow neurodegenerative disorder where symptoms progress over decades. Pre-diagnosis symptoms can be tracked up to 20 years before diagnosis in some cases, with these early symptoms including autonomic and gastrointestinal dysfunction (Kalia and Lang 2015; Castilla-Cortázar et al. 2020). In the immediate

years before diagnosis, a patient is likely to still only be suffering from non-motor symptoms. In these years, symptoms such as depression, sleep disorders, cognitive impairment and sensory abnormalities are likely to appear (Kalia and Lang 2015; Castilla-Cortázar et al. 2020), leading to consultations with a neurologist and diagnosis as these symptoms worsen. In the early stages (around 5 years) after diagnosis is usually made, motor symptoms begin to evolve in the form of tremor, rigidity and bradykinesia (slow movement) (Kalia and Lang 2015; Castilla-Cortázar et al. 2020). These accompany worsening non-motor symptoms of fatigue and pain. Into the later stages of the disease, complications from chronic pharmacological intervention can arise introducing fluctuating dyskinesia (involuntary, erratic movements) (Kalia and Lang 2015; Castilla-Cortázar et al. 2020). These complications can also include psychosis. During these later stages, other symptoms progress including dysphagia (difficulty swallowing), freezing, dystonia (muscle spasms) and dementia (Kalia and Lang 2015; Castilla-Cortázar et al. 2020).

1.2.1.2 Therapy Options

The common therapeutic approach to PD is through a pharmacological option to address dopamine depletion and dopaminergic neuronal cell death (Marras et al. 2020; Church 2021). This is commonly done through Levodopa, which replaces dwindling dopamine supplies as the dopamine precursor (Church 2021). However, complications can arise after a few years of Levodopa therapy in the form of dyskinesia (Kalia and Lang 2015; Castilla-Cortázar et al. 2020; Church 2021). These complications have become commonly treated through DBS of the basal ganglia and have proven to be effective in the modulation of these Levodopa-associated kinetic side effects (Church 2021).

1.2.1.3 Pathophysiology

The most commonly accepted pathophysiological change observed in PD patients across subtypes is the death of neuronal cells associated with dopamine production (Church 2021). Post-mortem studies of PD sufferers have revealed some crossover with commonly accepted Alzheimer's disease (AD) biomarkers of amyloid

plaques and tau protein tangles (Brandão et al. 2020). However, the exact role of these biomarkers in PD is uncertain. More commonly across PD patients, atrophy of grey matter regions in the frontal cortex as well as temporal, occipital and some subcortical areas has been observed through magnetic resonance imaging (Burton et al. 2004). However, this can vary largely between patients and classification of these observations based on PD subtype and stage have not been made yet. (Brandão et al. 2020) discusses the neurotransmitter changes during PD, which we summarise here. There have been clear correlations seen between dysfunction of dopamine, acetycholine and noradrenaline transmission to the early cognitive impairment symptoms of PD. In particular, the treatment of dopamine dysfunction has proven to be therapeutic, although this operates on an inverted U-shaped curve where dosage is required to be monitored around key levels for maximum benefit. Additionally, serotonin regulation is thought to be important later in the PD progression given this system's propensity to produce hallucinations and psychosis, which can develop in the later stages of PD.

Synchronisation of different neural rhythms has also been observed as a pathological feature of PD. See Section 1.2.2 for a general summary of neural rhythms. In particular, excessive synchronisation in the beta band is a common characteristic of PD (Oswal et al. 2013) and beta suppression has been linked to the improvement of motor symptoms in PD (Little et al. 2013; Little et al. 2016). Furthermore, the presence of prokinetic narrowband gamma rhythms (see Section 1.2.2.3) has been seen to be enhanced following Levodopa therapy administration (Oswal et al. 2013). In addition, the modulation of this narrowband gamma signal with the aim of further enhancing or maintaining the activity has been observed to improve PD-associated motor symptoms (Oehrn et al. 2023).

1.2.1.4 Neural Mechanisms of Parkinson's Disease

The elucidation of the effects of PD in the basal ganglia is the subject of debate (see Neumann et al. 2023 for a detailed summary). There are three main propositions of the network effect of dopamine depletion caused by PD. (1) Modulation of firing

rate where changes to tonic basal ganglia inputs see an increase in firing rate in the STN, (2) firing pattern/synchronisation promotion through increased connectivity in the STN-GPe (globus pallidus externus) loop and (3) reduced dynamic clarity in the basal ganglia of motor related firing (Chiken and Nambu 2016).

1.2.2 Neural Rhythms

Neural rhythms are commonly grouped according to their frequency bands. In this section, we summarise these groups and provide more detail on gamma band activity, which is important for the context of Chapter 3.

1.2.2.1 General Rhythms of the Brain

The general rhythms of the brain are characterised into delta (<4Hz), theta (4-8Hz), alpha (8-12Hz), beta (12-30Hz), gamma (30-100Hz) and high gamma (>100Hz) frequency bands. Each rhythm is associated with different neural functions and responses. For instance, lower frequency rhythms like delta are more associated with relaxation and sleep, while higher frequencies like gamma are linked to motor control.

1.2.2.2 Broadband Gamma

Activity in the gamma band (approximately 30 to 100Hz) has become a target for neuromodulation as it is associated with various cognitive performance features (Bosman et al. 2014) as well as motor control (Nowak et al. 2018). This is a broadband feature that reflects neuronal spiking over a broad frequency range.

1.2.2.3 Finely-Tuned Gamma(FTG)

It is necessary to distinguish between broadband gamma and FTG. FTG represents narrowband oscillatory activity with a peak frequency between 60-90Hz (Swann et al. 2016; Wiest et al. 2022). FTG oscillations were first revealed through invasive recordings of the basal ganglia in PD patients on antiparkinsonian medications (Cassidy et al. 2002; Williams et al. 2002). These have been thought to represent a "prokinetic" brain rhythm, in contrast to "antikinetic" beta rhythms (12-30Hz). Recently, prominent FTG oscillations have been found during invasive recordings

from motor cortical areas in PD (Swann et al. 2016; Gilron et al. 2021), and may be associated with dyskinesias. Additionally, similar cortical oscillations have been observed in rat models of dyskinesia (Halje et al. 2012; Güttler et al. 2021).

1.2.3 DBS

DBS is a commonly used therapeutic intervention for PD. However, despite being common practice for over two decades, there remain several opportunities to refine and improve its therapeutic approach.

1.2.3.1 Therapeutic Development

Records of electrical stimulation of the brain date back over 2000 years, yet only since the 1800s has electrical neuromodulation been recorded with any systematic approach (Sironi 2011). It wasn't until the early 1900s and the development of stereotactic frames that the safer implantation of electrodes to deeper targets in the brain became possible (Pycroft et al. 2018). This provided a greater accuracy of mapping brain function with localised targets that was only improved with the invention of brain imaging (Pycroft et al. 2018). Despite the increased safety and accuracy of neuromodulation, surgical efforts to treat neuropathologies remained primarily focused on neural structure ablation of pathological targets (Frey et al. 2022). Following the development of intraoperative stimulation in the mid-1950s, low-frequency stimulation (5-10Hz) was observed to exacerbate tremor and high-frequency stimulation (>50Hz) to suppress tremor, which gave hope of a cure for PD (Schulder et al. 2023; Frey et al. 2022). However, in the late 1960s the approval of Levodopa almost stopped the use of neuromodulation for PD altogether due to the early efficacy of the pharmacological approach and not requiring invasive surgery (Oliveria 2018; Sironi 2011; Gardner 2013). Overtime, Levodopa was proven not to provide the cure that had previously been hoped. By this point, most of the invasive electrical options that remained in clinical use were regarding lesioning brain structures through radiofrequency ablation (Frey et al. 2022; Gardner 2013). It was not until the development of implantable pulse generators in the 1970s and

80s that chronic high frequency brain stimulation became a realistic option (Sironi 2011; Schulder et al. 2023). This coincided with Alim Benabid's work (Benabid et al. 1987), delivering high frequency electrical stimulation to the basal ganglia. This was shown to strongly decrease tremor and has since been developed into the modern therapeutic DBS approach for PD (Oliveria 2018; Sironi 2011).

1.2.3.2 Current Applications

DBS is now a well-established therapy for PD to alleviate motor symptoms (bradykinesia, rigidity and tremor (Koller et al. 1997; Koeglsperger et al. 2019)) when medications provide inadequate benefit. Medtronic delivered the first commercially available implantable device in the mid-1970s, coining the term DBS (Pycroft et al. 2018). Since then, and with the development of competing companies there have been over 100,000 PD patients implanted with a DBS device (Pycroft et al. 2018). These devices are primarily implanted in the STN or GPi (globus pallidus internus). More recently, DBS has been used in different neural structures to treat other pathologies outside of movement disorders. These include investigations into therapeutic effects in obsessive compulsive disorder, chronic pain, Tourette's, epilepsy and depression (Oliveria 2018; Sironi 2011; Pycroft et al. 2018). While these applications of DBS have shown promising results, most have not obtained regulatory approval beyond investigational purposes at this stage. Other conditions, such as addiction and AD are also being investigated, but these neuropathologies require further investigation (Oliveria 2018; Pycroft et al. 2018).

1.2.3.3 Future Applications, aDBS and Current Blocks

Currently established DBS protocols are largely open-loop, taking in little consideration for both patient variability and the time-scale over which a neuropathological state can change. Additionally, the clinical approach has not changed significantly over the last few decades. Therapeutic paradigms are dictated mainly by trial-and-error and clinical experience, not from an understanding of the system being stimulated. Many current research investigations explore the use of DBS in new brain regions and for the treatment of previously untested neuropathologies. However,

DBS can yet provide further benefit through both a patient specific and pathology-state dependent approach in the pathologies in which DBS is currently established. Hence, the future of DBS likely lies in closed-loop adaptive DBS (aDBS) (Pycroft et al. 2018; Schulder et al. 2023; Frey et al. 2022).

The technology used in DBS devices is continuously improving, but the potential advancements all coincide with the same problems. Firstly, despite having a plethora of sense-stimulation devices on the market at the moment, there is a lack of confidence in the physiological validity of signals recorded by these systems because of potential stimulation artefacts. This prevents the algorithms from adapting in real time to a signal that may not accurately reflect neural behaviour. Hence, more research is required to understand and eliminate stimulation artefacts from frequency bands of biophysical interest. Secondly, there is not a clear understanding of the mechanisms of action of DBS. For many conditions, the field does not understand how changing stimulation will affect the neural response. It is therefore difficult to assemble an aDBS protocol that provides clinical benefit as there is little understanding of the underlying function of the algorithm. This is regardless of how many different waveforms the implantable pulse generators can produce. Hence, it is fundamental to understand the mechanisms of action of DBS and how DBS affects pathologies over a wide range of stimulation parameters.

aDBS algorithms have been previously used to improve motor symptoms in PD (Little et al. 2013) as well as to reduce the continuous DBS-associated speech side effects (Little et al. 2016). In both of these cases beta amplitude was used as a trigger for the aDBS algorithm, which looked to suppress the beta activity (DBS turned on when beta was above a certain amplitude and off when it dropped below). aDBS in PD has also used FTG as a biomarker (Oehrn et al. 2023). Unlike the studies that focused on beta, the studies that used FTG looked to increase the amplitude of the neural activity. As with the beta studies, it was also shown to improve motor score. Phase-locked close-loop DBS has also been explored in essential tremor, where providing stimulation synchronised with the tremor rhythm was shown to reduce tremor severity (Cagnan et al. 2017). In each case, quality of life of the patients

was seen to improve. However, each study used an aDBS algorithm that operated with a different trigger. This demonstrates the importance of understanding the effect of stimulation on the neural target for optimising clinical benefit.

1.2.3.4 Hypothesised Neural Mechanisms of DBS

There is no unifying and complete explanation of the mechanisms through which DBS acts. The reality is that DBS likely acts through a combination of many different mechanisms. The mechanisms of DBS are also likely heavily dependent on the target being stimulated, the pathology DBS is attempting to treat and other potential factors including time of day, medication intake, pathological state and even the stimulation parameters themselves. The latency of clinical responses after stimulation is turned on and how long clinical effects remain after stimulation is terminated can provide a key indication into the likely mechanisms of DBS (Herrington et al. 2016; Johnson et al. 2008; McIntyre and Anderson 2016). Here we present an overview of the most commonly hypothesised mechanisms, which will be crucial for consideration of modelling neural phenomena.

Inhibition The initial observations of high frequency DBS showed that it provided similar results in PD patients to lesioning the same structures. However, when DBS was turned off the symptoms were seen to return. Hence, it was assumed to act as a reversible lesion and inhibit neuronal firing at the structure responsible for the pathological activity (Chiken and Nambu 2016). This was later supported by recordings from the basal ganglia that showed reduced firing rate at the site of the electrode (Welter et al. 2004; Meissner et al. 2005; Degos et al. 2005).

Excitation More recording electrodes were introduced to improve the understanding of the network response to stimulation. This demonstrated that although neurons were locally suppressed, there was an excitation of efferent axons projecting from the site of stimulation. The excitation occurred in an oscillatory pattern that was time-locked to the pulses of stimulation (Chiken and Nambu 2016; Johnson et al. 2008).

Neurotransmitter release The overall network effect of DBS depends on the excitatory/inhibitory properties of the neurotransmitters at the synapses that are excited (Chiken and Nambu 2016; Herrington et al. 2016; Udupa and Chen 2015). For example, STN-DBS was seen to increase firing rate of GPi neurons, while GPi-DBS resulted in reduced firing rate of the STN. This aligns with STN-GPi connections having glutamergic properties, while GPi-STN projections are GABAergic (Udupa and Chen 2015).

Antidromic Activation DBS triggers time-locked excitation of efferent neurons, but also causes antidromic activation of afferent neurons as well (Chiken and Nambu 2016). Antidromic activation is observed at the stimulation site as short latency evoked responses. However, there is some debate regarding the generalisability of this mechanism, the unstable nature of antidromic activation and how it is present for STN-DBS, but not GPi-DBS (as summarised by (Neumann et al. 2023)).

Information Blockade An alternative hypothesis that potentially aligns with antidromic activation is the disruption hypothesis (Chiken and Nambu 2016). Antidromic action potentials can collide with intrinsic orthodromic projections, blocking information from passing the stimulation site (Jakobs et al. 2019). This therefore supports the information blockade effect of DBS through antidromic action potentials colliding with action potentials from pathological activity. This could act to suppress the spread of pathological behaviour, instead replacing it with efferent excitation that is time-locked to the stimulation.

Plasticity There also exists longer term latency (called chronic latency) neural responses. One of the more prominent of these being spike-timing-dependent plasticity (STDP) which is only observed from between multiple seconds to as long as weeks after stimulation onset. The long-term plastic changes are due to DBS causing persistent activation or suppression of synaptic activity, triggering similar mechanisms to learning (Herrington et al. 2016).

Neurogenesis and Neuroprotection In PD, another consideration may be the slowing of the rate of degeneration of dopaminergic neurons. However, this hypothesis is primarily based on animal models and is yet to be supported by

human recordings, where DBS has not been shown to stop, reverse or even slow the overall progression of PD yet (Herrington et al. 2016).

1.2.3.5 Characteristics of DBS Sites

STN Given the widespread adoption of STN-DBS as a treatment of PD, substantial amounts of data are available regarding the characteristics of the STN in both on- and off-stimulation conditions.

In-vivo recordings of the human STN show activity in the off-stimulation state around the high beta or low gamma range at approximately 40Hz (Wiest et al. 2020). Ex-vivo recordings from rat STN slices show neuronal firing rate does not differ too much in the off-stimulation state, at approximately 20Hz (Hallworth et al. 2003; Wilson et al. 2004). In the presence of constant current stimulation (<0.5nA), the firing rate of neurons in these slices increases up to frequencies greater than 200Hz. Furthermore, recordings of both in-vivo and in-vitro rat STN neurons showed neuronal firing rates able to reach 500Hz in response to constant current stimulation of around 1nA (Kitai and Kita 1987).

The STN is a glutamatergic structure of neurons, which primarily use glutamate as their neurotransmitter (Bolam et al. 2009; Worbe et al. 2010). This indicates that STN neurons will tend to synchronise and increase the firing rate of the neurons and networks connected to their neuronal outputs. (Steiner et al. 2019) showed that by triggering four action potentials through microelectrode stimulation in one neuron, the surrounding neurons would not respond by firing themselves. Given the glutamergic connectivity of the STN, this was interpreted as STN neurons having an absence of intrinsic connectivity and acting like independent processing elements.

The STN receives two key network inputs: a glutamergic input from the cortex (the hyperdirect pathway), and a GABAergic input from the GPe (the indirect pathway) (Bolam et al. 2000). The GPe input is known to have a prominent inhibitory effect on the STN. The STN also has an excitatory effect on the GPe through observations of increasing GPe firing rate with STN-DBS (Reese et al. 2011; Schmidt et al. 2020) and given the glutamatergic nature of the STN.

Pallidum The globus pallidus (GP) is a structure within the basal ganglia which plays an important role in motor control, particularly regarding coordination (Javed and Cascella 2020). The GP is comprised of two segments. The external segment (GPe) is interconnected with the STN and the striatum within the basal ganglia. The internal segment (GPi) directs information from the basal ganglia to the thalamus as well as throughout the body through the brain stem and spinal cord (Jaeger and Kita 2011; Bolam et al. 2000; Worbe et al. 2010).

In vivo recordings of the GP showed off-stimulation baseline firing rate at similar frequencies in both internal and external segments, between 10-50Hz in the GPe and 5-30Hz in the GPi (Hashimoto et al. 2003; Reese et al. 2011). Both segments also exhibited the ability to fire at much higher rates in the presence of high-frequency stimulation. Firing rate was observed over 100Hz in some cases with 136Hz stimulation (Reese et al. 2011) and even higher than 200Hz immediately after 180Hz high frequency stimulation onset (Hashimoto et al. 2003).

The GP is predominately a GABAergic structure of neurons (Hegeman et al. 2016; Dong et al. 2021). The GPe is estimated to have over 95% GABAergic neurons (Hegeman et al. 2016; Dong et al. 2021) and exhibits inhibitory activity on the STN (Bolam et al. 2000; Worbe et al. 2010). This prevents basal ganglia activity from increasing exponentially due to feedback from the glutamergic nature of the STN. The GPi is also considered GABAergic due to periods of high GPi activity strongly inhibiting thalamic neurons (Alavi et al. 2022).

1.2.3.6 DBS Artefacts

A current obstacle to advancing the use of aDBS is the poor understanding of how artefacts can contaminate neural signals. Artefacts come in many forms, the most common artefact in sense-stimulation devices is at stimulation frequency which is difficult to avoid (Hammer et al. 2022; Alarie et al. 2022). Measures have been taken to blank recordings around stimulation pulses to avoid this, but this has limitations and can miss key neural responses (Nie et al. 2021; Chen et al. 2022). In addition, large stimulation artefacts are observed with turning stimulation on and

off, as well as during stimulation ramping (Hammer et al. 2022). These artefacts have not been fully characterised, but their occurrence has been connected with stimulation transients causing the discharge of residual potential difference over the electrode coupling capacitor (Hammer et al. 2022). However, these artefacts are easily avoided by only observing neural responses outside of these conditions as they last for short periods. In sense-stimulation devices another common artefact is ECG artefact, caused by the leakage of cardiac activity into the recorded neural signal for chest mounted DBS systems (Hammer et al. 2022; Sorkhabi et al. 2020; Thenaisie et al. 2021). These artefacts can be present throughout a frequency range of 0.05-150Hz (Hammer et al. 2022; Sorkhabi et al. 2020) and can be significantly larger than the local field potential (LFP) signals (Sorkhabi et al. 2020). However, finite element analysis has shown that by moving DBS devices away from the commonly chest mounted set up, these artefacts can be limited (Sorkhabi et al. 2020). As with any signal analysis, aliasing must be considered. Aliasing artefacts are difficult to avoid, but they can be systematically controlled to limit their size and keep key frequencies of the signal free of artefacts.

1.2.4 Entrainment

Entrainment of neural signals, specifically in the case of half harmonic entrainment of FTG, was long thought to be artefactual. However, entrainment (at least to perturbations of a similar frequency to the natural frequency of the system being stimulated) is a basic property of oscillators, whether linear or nonlinear. Only nonlinear systems have the ability to entrain at sub-harmonics of stimulation frequency. The brain is a nonlinear system, and it therefore stands to reason that it may be able to entrain at sub-harmonics. We introduce the concept of entrainment for Chapter 3 in this section.

1.2.4.1 Arnold Tongues and Rotation Number

The frequency locking (entrainment) behaviour of a neural rhythm to external stimulation across stimulation frequency and amplitude can be described by Arnold

tongues (Arnol'd 1983; Pikovsky et al. 2002). Arnold tongues are the regions in the stimulation frequency and amplitude space where frequency-locking occurs (see examples in Figs 1.2B and 2.2). Frequency locking is observed when a rotation number (also called the winding number in mathematical literature) of the form p:q, where p and q are coprime integers (i.e. no integer other than 1 divides both p and q), is maintained for several stimulation periods. In general, the rotation number may not be a ratio of integers (it is a ratio of integers only when there is frequency locking) and corresponds to the average number of oscillatory cycles achieved by the rhythm between two periodic pulses of the driving stimulation. This is calculated for periodic signals as

$$\frac{\theta_N - \theta_0}{2\pi N}, \tag{1.1}$$

where θ_N is the phase after N stimulation pulses and θ_0 is the initial phase. Previously, Arnold tongues have been used to describe 1:1 entrainment in response to noninvasive neuromodulation (Fröhlich 2015; Notbohm et al. 2016; Ali et al. 2013; Hanslmayr et al. 2019). Depending on the system considered and the stimulation waveform, Arnold tongues can theoretically exist for various rotation numbers, including p:q with large p and/or q. However, in real systems, often only the tongues corresponding to the most stable rotation numbers, with low p and q values, will be observed. Arnold tongues often have different shapes for different dynamical systems. Generally, an Arnold tongue expands in width across larger frequency ranges as stimulation amplitude increases. This continues up until an amplitude where the tongue may border a region with another frequency-locking ratio or lose entrainment altogether.

1.2.4.2 Neuromodulatory Entrainment Examples

Several studies have noted the presence of a shifted gamma peak in response to stimulation (Swann et al. 2016; Swann et al. 2018a). These papers demonstrate the consistent pulling of a FTG peak, off-stimulation at between 75-80Hz, and locking to the half harmonic of stimulation, see Fig 1.1. This introduces the possibility

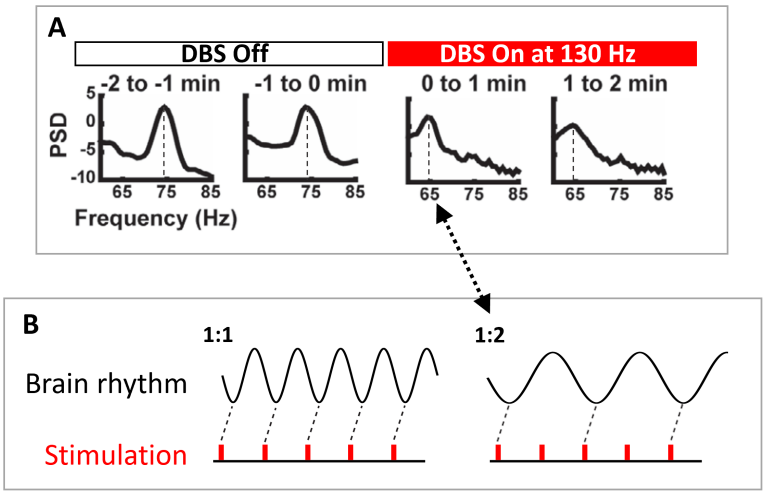


Figure 1.1: Prior human recordings demonstrate 1:2 entrainment of cortical FTG rhythms from subcortical stimulation. (A) Power spectral density (PSD) of FTG activity recorded from the motor cortex before and during DBS to the STN at 130Hz. In the DBS Off state, a natural ∼75Hz rhythm can be observed. This is entrained at 65Hz during the following two minutes of DBS On at 130Hz. (B) 1:1 entrainment corresponds to one stimulation pulse per brain rhythm cycle and a rotation number of 1, 1:2 entrainment corresponds to two stimulation pulses per brain rhythm cycle and a rotation number of 0.5. Hence, during 1:2 entrainment, the brain rhythm locks to a frequency of half that from the external stimulation. This corresponds to the DBS On state of panel A. Panel A is adapted from (Swann et al. 2016).

that responses to stimulation can go beyond inducing rhythms at the frequency being applied, or suppressing them like an information blockade.

Gamma rhythms have been seen to interact with stimulation from other studies as well. The ability to instantaneously modulate gamma frequencies has been shown by varying visual stimulation in the Macaque primary visual cortex (V1) (Lowet et al. 2017). Here gamma was locked to stimulation frequency, at the 1:1 tongue, where entrainment could be observed as visual stimulation does not produce stimulation artefacts. Additionally, 1:1 entrainment was also hypothesised in response to DBS as a mechanism behind observations of FTG immediately locking to stimulation frequency (Muthuraman et al. 2020). These results indicate that gamma can reliably be entrained at stimulation frequency, but robust predictions remain unsolved.

Further evidence of the ability to shift gamma activity is provided from behavioural and physiological changes in the presence of stimulation. Stimulating at gamma frequencies was observed to have a similar effect on improving PD

symptoms to high frequency stimulation (Tsang et al. 2012). This would suggest the potential to entrain the same oscillations through similar mechanisms when stimulating at both gamma frequency (1:1 entrainment) and at twice gamma frequency (1:2 entrainment). This was compared to no difference or improvement in the effects when stimulating at theta and beta frequencies, with similar results to no stimulation. Additionally, similar results were observed with transcranial alternating current stimulation (tACS), where gamma stimulation was observed to reduce the severity of bradykinesia, whilst beta-tACS saw it increase (Guerra et al. 2021). It was further hypothesised that entrainment of beta oscillations at stimulation frequency would explain this observation. Whilst these studies do not document observed changes to brain rhythms, the observed behavioural differences are also an indication of the ability of stimulation to modulate neuronal oscillations to a frequency component of the input.

Entrainment to periodic stimulation is not exclusive to the gamma frequency band, with studies observing this in other bands as well. For example, it has been observed in the alpha band through synchronised transcranial magnetic stimulation (sTMS) when treating depression (Fröhlich 2015), with rhythmic visual stimulation (Notbohm et al. 2016), and with tACS (Huang et al. 2021). Furthermore, entrainment of individual neurons has been seen in rodent and non-human primates to transcranial stimulation over large stimulation frequency ranges (0.8-40Hz) (Ozen et al. 2010; Krause et al. 2019; Johnson et al. 2020). These results show that simple stimulation mechanisms can achieve similar and notable effects across neural frequency bands.

The effect of stimulation across neural frequencies can also be observed in behavioural changes. In subjects with epilepsy, the impact of stimulation on the number of seizures was shown to depend on stimulation frequency (Deng and Luan 2017). For both high (>70Hz) and low (<12Hz) frequency stimulation, the number of seizures was reduced, whilst stimulation in the mid band frequency range (≈50Hz) increased the number of seizures. This may indicate the possibility of entraining seizure associated rhythms at this mid band, whilst stimulation sufficiently far

away may entrain other rhythms. This was further explored in (Zamora et al. 2021) where entrainment theory was used to select stimulation parameters (see Section 1.2.4.3). Rhythms associated with a healthy state were targeted, noting to avoid frequencies that arose immediately before or during seizures. The number of seizures was shown to decrease significantly. These results further demonstrate the potential of targeted stimulation entrainment as a method that might provide therapeutic benefit across neurological conditions.

1.2.4.3 Case-Study in an Epileptic Canine

We were approached regarding a genetically epileptic canine that had been implanted with a Picostim DyNeuMo system due to it having cluster seizure events that would result in status epilepticus (Zamora et al. 2021). Status epilepticus is recurrent seizure activity without time between consecutive seizures and in this case it could only be broken with pharmacological intervention. Initially post-implantation, the dog was treated with high frequency stimulation (130Hz) as this was the commonly accepted therapeutic approach for epilepsy. However, this approach was unable to interrupt the seizures during the dog's first cluster seizure event post-implantation. We were approached to theorise an alternative method that may be able to interrupt this activity.

Recordings after implantation revealed a key change in the frequency activity between the healthy and epileptic states. During resting conditions there was an observed frequency peak around 12-13Hz, while during the seizure a prominent peak around 2Hz was revealed (see Fig 1.2A). The decision was made to target this resting rhythm continuously through a method of low frequency entrainment to promote this healthy resting state and avoid the transition to seizures. Through modelling techniques of the sine circle map (see Section 1.2.6.1), it was decided to use 13Hz stimulation to target the resting rhythm at the 1:1. The corresponding effect on the 2Hz rhythm was likely to be minimal, being sufficiently far away from the 13Hz stimulation frequency (see Fig 1.2B).

The introduction of this low frequency entrainment method provided significant reductions in both the number of seizures and time spent in a seizure. Pharmacological measures had to be withdrawn around three months into the low frequency entrainment application due to severe medication-associated side effects. This showed that the low frequency entrainment protocol alone was able to produce almost complete cluster seizure cessation for the remainder of the trial until unrelated complications arose. Even when cluster seizures arose, they were seen to be short and few in number during the low frequency entrainment period.

This case study provides initial evidence that it may be possible to entrain neural rhythms to provide clinical benefit. However, it is difficult to say the exact effect on this 13Hz "healthy" rhythm during low frequency entrainment given that any physiological signal will likely be masked by the stimulation artefact. Hence, 1:1 entrainment may not be practical for adaptive neuromodulatory approaches. Sub-harmonic entrainment offers a promising alternative. Sub-harmonic entrainment was not considered in this case study given the time critical nature of its approach and that there are a larger range of stimulation parameters that produce 1:1 entrainment compared to sub-harmonic entrainment in most cases.

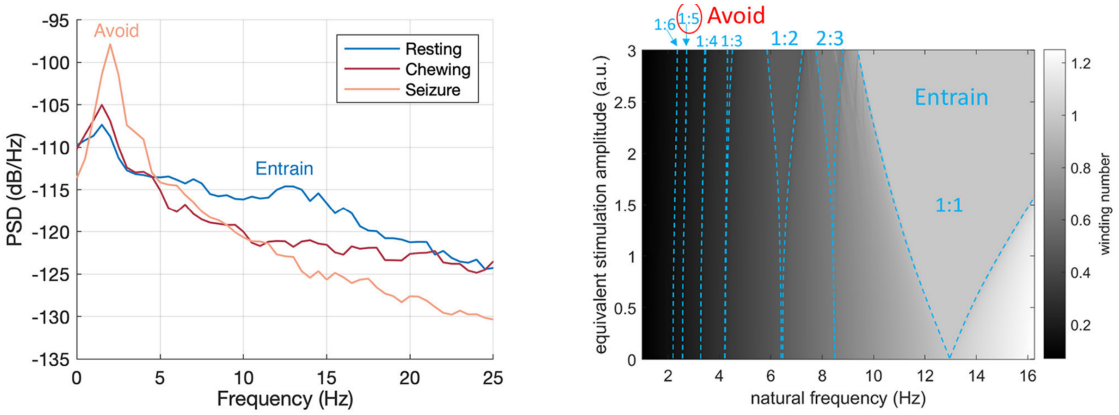


Figure 1.2: Epileptic canine frequencies of interest and entrainment-based approach. (A) Low-frequency PSD of resting, chewing and seizure states, with associated target frequencies to entrain (13Hz) and avoid (2Hz). (B) Arnold tongues for sine circle map of variable oscillator natural frequency and stimulation amplitude for a set stimulation frequency of 13Hz. Figures taken from (Zamora et al. 2021).

1.2.4.4 Clinical Significance

1:2 entrainment of FTG has been shown to correspond with periods of dyskinesia in a cohort of PD patients (Swann et al. 2016; Swann et al. 2018a). In addition, a recent study has demonstrated that the half harmonic entrained FTG signal is the optimal biomarker for aDBS protocols to reduce motor symptom severity in PD (Oehrn et al. 2023). The aDBS protocol with 1:2 entrained FTG as the biomarker provided significant improvements to quality of life and reduced the severity of the most bothersome motor symptoms compared to continuous DBS protocols. As stated previously, neural signals at sub-harmonics of stimulation frequency were previously ruled out as artefactual up until recently. Therefore, there are not examples where entrained rhythms have been used as a clinical biomarker. However, the early study (Oehrn et al. 2023) that builds directly on the work discussed in Chapter 3 demonstrates the potential clinical significance of this phenomenon. While the artefact at stimulation frequency makes it difficult to quantify the 1:1 entrainment, the results described in Sections 1.2.4.2 and 1.2.4.3 that target 1:1 entrainment demonstrate the ability to provide clinically significant changes.

1.2.4.5 Other Examples of Entrainment in Biology

Entrainment can be observed in a wider range of biological examples, not just in the brain in response to unphysiological electrical stimulation. A common example of entrainment that humans experience every day is that of the circadian rhythm. It is thought that every organ, if not every cell, has a clock that is coupled to central clock in the brain (Koronowski and Sassone-Corsi 2021). The natural frequencies of these clocks are around 24 hours and hence, the light cycle entrains them at the 1:1 Arnold tongue through the central clock. However, the circadian rhythm can adapt, with each clock becoming phase-locked to a new circadian cycle at different rates. This is why different bodily functions are able to adapt at different rates in response to changing time zones.

Entrainment in the human body exists in ratios outside of the 1:1 too. Complex interaction ratios have been seen between heart rate and respiratory rate for periods

of over 20 minutes during rest (Schäfer et al. 1998). These interactions demonstrate the ability to lock between two weakly coupled systems in the absence of external perturbation or control, such as the conscious decision to breath. These phase-locked regions often exist in frequency ratios around 1:3 (also seen at 2:5) if the heart rate was seen to be the driving frequency (Schäfer et al. 1998).

1.2.5 Evoked Resonant Neural Activity (ERNA)

Despite STN-DBS being a common therapeutic option for PD for several decades, ERNA was only discovered comparatively recently. This was due to the recent deployment of techniques with high enough sampling rates in human patients that allow ERNA to be observed. ERNA has since been demonstrated to be of physiological origin (Sinclair et al. 2019) (see Section 1.2.5.2), however, the underlying mechanisms behind this phenomenon remain elusive. In this section we summarise the basic features and history of ERNA observations that the work documented in Chapter 4 looks to build on.

1.2.5.1 Characteristics of ERNA

The initial observations of ERNA were fast dynamics of high amplitude oscillations in response to high frequency DBS (HF-DBS), that increased in amplitude for every DBS pulse over the first 100ms of stimulation (Sinclair et al. 2018) (Fig 1.3A). It was later demonstrated that this was a physiological signal and not artefact (Sinclair et al. 2019) (see Section 1.2.5.2 for more details). Following the termination of HF-DBS, it was also shown that ERNA would have several oscillations that decreased in amplitude back to baseline, over a period of approximately 10-20ms. There is little to no high frequency or high amplitude activity in the STN preceding stimulation or after this 20ms period after stimulation termination.

More recently, observations of slow dynamics of ERNA demonstrate that it is also a phenomenon that changes over a time period greater than 100 seconds of HF-DBS (Fig 1.3B). (Wiest et al. 2020) showed that over longer periods of HF-DBS it is possible to observe high frequency activity (>350Hz) immediately after stimulation

onset which decays to around 250Hz, where it stabilises, over around 200 seconds with 130Hz stimulation. It was also observed that not only did the ERNA frequency decay, but also its amplitude. The amplitude peaked very soon after stimulation onset before decaying continuously for over 100 seconds of continuous HF-DBS.

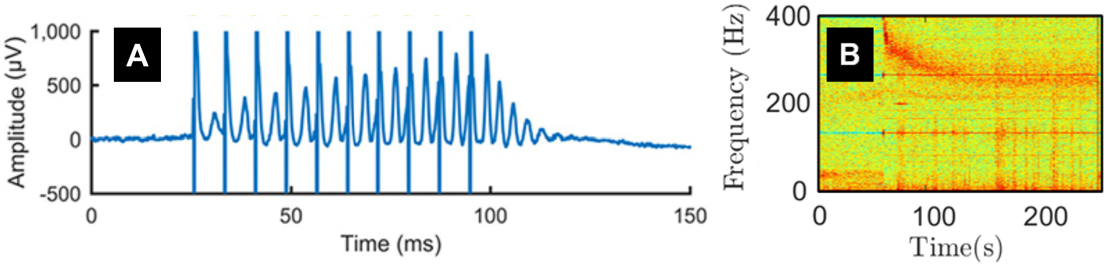


Figure 1.3: Human recordings of the STN demonstrate the fast and slow dynamics of ERNA. (A) The fast dynamics of ERNA over ≈70ms of stimulation and evoked ringing after stimulation termination, from (Thevathasan et al. 2020). (B) The slow dynamics of ERNA over 200 seconds of stimulation, from (Wiest et al. 2020).

Following the discovery of the slow dynamics of ERNA, further studies demonstrated that it was possible to modulate both the amplitude and frequency characteristics of ERNA by changing the stimulation and/or medication state of the patient (Wiest et al. 2023).

Variable Stimulation Frequency It was seen that greater stimulation frequencies corresponded to an ERNA frequency response that decayed faster and to lower frequencies. This was accompanied by higher amplitudes following stimulation onset for higher stimulation frequencies before dropping down to similar ranges regardless of stimulation frequency later in the DBS window. Both high frequency and high amplitude activity was seen for the entire range of stimulation frequencies (70-180Hz) tried in (Wiest et al. 2023). However, when stimulating with subtherapeutic STN-DBS of less than 20Hz, only high amplitude activity was seen with a complete absence of activity above 150Hz (Ozturk et al. 2021; Zapata Amaya et al. 2023).

Variable Stimulation Amplitude For larger stimulation amplitudes there was also a faster decay in the ERNA frequency (Wiest et al. 2023). The amplitude of

ERNA was also larger following stimulation onset for larger stimulation amplitudes, again before dropping to similar ranges regardless of stimulation amplitude.

Variable Medication State ERNA was present regardless of medication state (Wiest et al. 2023). The frequency of ERNA did not differ greatly between states for the first 40 seconds, before separating and the off-medication state decaying to a lower frequency later in the stimulation window. The amplitude of ERNA was higher following stimulation onset in the off-medication state before both states maintained similar amplitudes later in the window.

Post Stimulation Bursting Following long-term stimulation termination, the frequency and amplitude of ERNA was also observed with bursts of 10 pulses of stimulation every second for 20 seconds (Wiest et al. 2023). Over this 20 second period, both the frequency and amplitude of ERNA were observed to increase back up to and stabilise at the frequency and amplitude that ERNA was present at around the start of the long period of HF-DBS.

In Chapter 4, we focus on ERNA recorded from the STN, however, it is important to note that it is not a property that is exclusive to the STN. Within the basal ganglia, ERNA has been shown to be present or at least display signals that resemble ERNA from local recordings and stimulation in the GPe (Hashimoto et al. 2003) and the GPi (Johnson et al. 2023). ERNA-type responses in the GP have also been displayed in response to STN-DBS (Reese et al. 2011; Schmidt et al. 2020). Although this was only shown to increase firing rates of pallidal neurons to around 60Hz (Reese et al. 2011), short of the 350Hz frequency of ERNA (Wiest et al. 2020; Wiest et al. 2022; Wiest et al. 2023).

1.2.5.2 Confirmation of Physiological Origin

Evidence that ERNA is a physiological signal was provided by intraoperative recordings taken simultaneously with 130Hz DBS at different sites through the subthalamic region (Sinclair et al. 2019). It was demonstrated that ERNA had the largest amplitude in the dorsal regions of the STN. Furthermore, there was no

appearance of any high frequency evoked potentials in neighbouring brain regions (a graphical interpretation of these results can be seen in Fig 1.5C). In a system where the stimulation and signal processing are identical for all recordings, to have a signal that is only present in certain locations must reflect a change in the system being stimulated. We use a similar technique as part of our half harmonic artefact study in Section 2.4.3. Furthermore, (Sinclair et al. 2019) demonstrated that the polarity of ERNA was not inverted when the polarity of the stimulus was reversed. This provided additional evidence that ERNA is a physiological response to stimulation.

1.2.5.3 Clinical Significance

Recent investigations have shown that ERNA represents the strongest predictor for contact selection for STN-DBS implantation for PD (Xu et al. 2022). Previously, contact selection relied on trial and error after implantation and clinical experience of the neurosurgeons and neurologists. However, given the large heterogeneity that is exhibited throughout the STN, having a reliable biomarker may improve efficiency and the standard of care for this disease.

ERNA remains present during general anaesthesia at comparatively higher levels than other LFPs (Sinclair et al. 2022). Furthermore, the observation of ERNA as the strongest predictor of therapeutic target was maintained despite the administration of the general anaesthetic (Sinclair et al. 2022). This may provide further opportunities for using ERNA as a biomarker for contact selection over other LFP signals.

1.2.6 Modelling Approaches

Computational models are useful tools to investigate underlying mechanisms of neural responses to stimulation. Even when clinical experiments may be available, there is a wide range of computational approaches that can quickly provide insights at no risk to patients (Holt and Netoff 2013). This means that computational models represent valuable tools when refining investigations and experiments. Furthermore, when a model is demonstrated to capture certain important physiological responses,

it can be shared far more readily than an experimental set up (Holt and Netoff 2013). This allows for a wider range of experts to analyse and improve this tool. Computational models also allow us to perturb individual model parameters to understand what components are fundamental in reproducing the dynamics of interest. This is difficult to do in a biophysical context and therefore computational models represent valuable tools for developing hypotheses and understanding neural behaviour.

It is important to consider the computational complexity of the model as well as their scale relative to the physiological system they are representing when selecting a model. While detailed neuron-level models can represent valuable tools when investigating neural circuit behaviour, they are computationally expensive when scaling up to a network due to many physiological processes having to be accounted for. When fitting models to data, this introduces more model parameters that not only make model fitting computationally prohibitive, but also the likelihood of over-fitting the model. Instead, mesoscale models can be chosen to represent the activity of larger collections of neurons (e.g. LFPs) while not requiring a large number of parameters.

In this thesis, we focus on mesoscale models that are able to represent networks while also being able to be constrained to data. In this section, we introduce the sine circle map which captures the response of a single oscillator to stimulation. We also introduce the Wilson-Cowan model that represents interacting neural populations and is the primary modelling tool for Chapter 3. Lastly, we discuss the Kuramoto model, a mesoscale network of coupled oscillators that represents a population of interacting neurons. We use the Kuramoto model as a tool to investigate ERNA in Chapter 4. While we do not discuss neuron-level models in this thesis, several studies summarise these approaches (Holt and Netoff 2013; Ashwin et al. 2016).

1.2.6.1 Sine Circle Map

The sine circle map is the simplest model that describes the influence of periodic stimulation on an oscillator. The model stroboscopically observes the phase, θ, of

a single oscillator of natural frequency f_0, periodically stimulated at frequency f_s and stimulation intensity A_s. The map between the oscillator phase right after stimulation pulse i and its phase right after stimulation pulse $i+1$ is given by

$$\theta_{i+1} = \theta_i + 2\pi(f_0/f_s) + A_s \mathrm{PRC}(\theta_i), \tag{1.2}$$

where PRC denotes the oscillator phase response curve and describes the change in the oscillator phase as a function of the stimulation phase. For the sine circle map, the PRC is given by $\mathrm{PRC}(\theta) = \sin(\theta)$. Experimentally evaluated PRCs have been calculated for cortical pyramidal neurons (Stiefel et al. 2008; Netoff et al. 2012). From studies like these, type II PRCs (PRCs with some phases that have a positive phase advancement and some that are negative) can be approximated by $-\sin(\theta)$. The sine circle map is identical for $-\sin(\theta)$ and $\sin(\theta)$. A theoretical study exploring PRCs in different mathematical models can be found in (Brown et al. 2004).

1.2.6.2 Wilson-Cowan Model

The Wilson-Cowan model is a mean field model and represents two interacting neuronal populations, one excitatory and one inhibitory (Wilson and Cowan 1972; Cowan et al. 2016). The Wilson-Cowan model has been used in the analysis of oscillatory neuronal responses to periodic and varying stimulation (Lea-Carnall et al. 2016; Velarde et al. 2017; Cutsuridis 2019; Yousif et al. 2017; Duchet et al. 2020) and in theoretical studies of entrainment (Pérez-Cervera et al. 2019; Papasavvas et al. 2020). Additionally, the model has been used in the analysis of resonances (Veltz and Sejnowski 2015), as well as in the communication of information (Hoppensteadt and Izhikevich 1998).

The Wilson-Cowan model outputs the activity of the excitatory and inhibitory populations, denoted by E and I, respectively. A graphical summary of the population interactions can be seen in Fig 1.4. The population activities are proportional to the firing rate of that population's neurons. Stochastic differential equations describe the evolution of E and I as

$$dE = \frac{1}{\tau_E}(-E + f(\eta_E + \omega_{EE}E - \omega_{IE}I))dt + \zeta dW_E,$$
$$dI = \frac{1}{\tau_I}(-I + f(\eta_I + \omega_{EI}E - \omega_{II}I))dt + \zeta dW_I, \tag{1.3}$$
$$f(x) = \frac{1}{1 + e^{-b(x-1)}}.$$

These interactions are weighted by coupling strengths denoted ω_{PQ} (going from population P to population Q), and occur through a sigmoid function, f, of steepness coefficient b. τ_E and τ_I represent the time constants of the excitatory and inhibitory populations, respectively. η_E and η_I are the constant inputs to the respective populations. Stochasticity is introduced to the model through Wiener processes, W_E and W_I, with noise standard deviation denoted by ζ.

The Wilson-Cowan model has a limited number of model parameters which makes it feasible to constrain the model with a low risk of over-fitting the data. Despite the relatively small number of parameters, it is able to capture a wide variety of dynamics (Borisyuk and Kirillov 1992; Onslow et al. 2014; Pérez-Cervera et al. 2019).

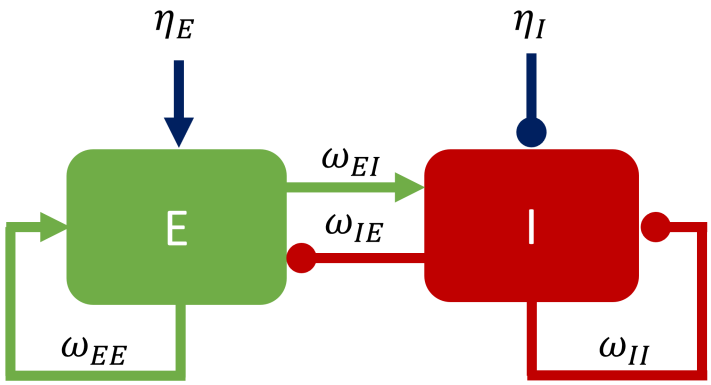


Figure 1.4: The Generic two-population Wilson-Cowan model. The interconnections between the excitatory population, E, and inhibitory population, I. All terms are consistent with Eq. (1.3).

1.2.6.3 Kuramoto Model

Unlike the Wilson-Cowan model, the Kuramoto model observes the rates of phase progression of individual phase oscillators. The Kuramoto model is capable of representing oscillatory neural activity and is one of the simplest models that can

describe populations of interconnected neurons. The Kuramoto model has been frequently used to represent oscillatory neural activity as well as the effect of DBS (Tass and Majtanik 2006; Asllani et al. 2018; Weerasinghe et al. 2019; Bick et al. 2020; Weerasinghe et al. 2021; Duchet et al. 2023).

The Kuramoto model was the foundation of a model that observed short-term ERNA with multiple interacting populations of Kuramoto oscillators (Realmuto et al. 2023). The Kuramoto model is therefore a suitable choice for modelling evoked responses (in Chapter 4) that both capture (greatly simplified) individual neuron responses as well as a mesoscale neural structure response.

The basic Kuramoto model describes the phase evolution of a series of interconnected oscillators (Kuramoto 1983). The Kuramoto model describes oscillator phase progression by the differential equation

$$d\theta_i = \left(\omega_i + \frac{k}{N}\sum_{j=1}^{N}\sin\left(\theta_j - \theta_i\right)\right)dt \quad \text{for } i = 1, ..., N, \tag{1.4}$$

where θ_i and ω_i represent the phase and natural frequency of the i^{th} oscillator, respectively. k is the homogeneous coupling strength between oscillators, where sin is used as the coupling function. N represents the number of Kuramoto oscillators in the model. To measure synchrony in the network, we use the order parameter given by

$$Z = \frac{1}{N}\sum_{j=1}^{N} e^{i\theta_j}. \tag{1.5}$$

In Chapter 4 we make a series of modifications from the standard Kuramoto model that allow the model to reproduce the dynamics of ERNA.

1.2.6.4 Next Generation Neural Mass Model

A further model that may be of interest is the next generation neural mass model, which provides an exact mean field description of a population of theta neurons (formally equivalent to quadratic-integrate-and-fire neurons) (Coombes and Byrne 2019; Byrne et al. 2020). The model can also accommodate synapses between the theta neurons (Coombes and Byrne 2019) as well as gap junctions (Pietras et al. 2019). While this mesoscale model may prove suitable to represent local field

potentials in this thesis, it is more complex than any of the previously discussed models. Hence, we do not consider it here as the Wilson-Cowan model and Kuramoto model proved sufficient in capturing the phenomena with which they were tasked.

1.2.6.5 Suitability of Models for Each Application

Prior to assessing whether a model is capable of capturing a given phenomenon, it is important to select the right model. When looking to fit the model parameters to data, it is necessary for the model outputs to be comparable to the data features of interest. In the cases of entrainment and ERNA, both sets of fitting features importantly contain an amplitude scale. This eliminates the sine circle map from consideration in these applications. Furthermore, fitting a model to data requires the model to have as few variable parameters as possible (the search space grows exponentially with the number of parameters) and a brief forward simulation time (the fitting process involves simulating the model a very large number of times). In addition, the model selected must be representative of the size of the neural structure being modelled and detailed enough to capture the neural phenomenon of interest (for example, a model cannot be linear to predict sub-harmonic entrainment). Taken together, we assess the suitability of each model for the task in accordance with the quote (usually attributed to Einstein), "Everything should be made as simple as possible, but no simpler". Further justification of each model choice can be found in Sections 3.3.1 and 4.4.1.

1.3 Thesis Outline

As revealed from our background review (Section 1.2), insights from sense-stimulation devices have revealed two previously unknown phenomena, half-harmonic entrainment and ERNA, in response to high-frequency DBS of the PD brain. In the early years after these were first discovered, these phenomena were thought by the majority of the field to be artefactual. More recently, improved characterisation of stimulating devices, along with initial indications of potential clinical relevance for both of these phenomena, has heightened interest in understanding their underlying mechanisms.

Often in neuromodulatory clinical research, trial and error plays a major role in the early stages. This is despite an ever-increasing range of technologically improving options in the neuromodulatory space. The trial-and-error approach is employed due to there being a lack of understanding as to how techniques like DBS modulate neural circuits. Phenomena such as half harmonic entrainment and ERNA provide valuable opportunities to get insights into the response of neural circuits to DBS. Through identifying the underlying mechanisms, we may be able to inform clinicians on how neural circuits are being modulated as well as how clinical improvements can be reached (see the thesis breakdown into modelling potential underlying mechanisms in Fig 1.5). Therefore, by developing computational models we may be able to improve the efficiency to which clinical benefit can be reached. Hence, the overall aim of this thesis is

to improve the understanding of the underlying mechanisms and dynamics that are responsible for DBS-induced phenomena through computational modelling with the view to inform the future design of DBS devices and stimulation protocols.

However, this would be essentially meaningless without first proving that these phenomena are not artefacts. I look to address this in Chapter 2 by asking the question

"How to investigate whether frequency peaks at sub-harmonics of the stimulation frequency are of artefactual origin?"

Once we have obtained confidence that these observed responses are non-artefactual, it is possible to investigate these responses more closely. In Chapter 3, I focus on the stationary responses (responses that do not change frequency with extended periods on stimulation) of motocortical FTG to DBS in PD patients and ask the question

"Can we predict half harmonic entrainment as a function of the applied stimulation parameters using patient data from an off-stimulation PD cohort?"

While Chapter 3 captures stationary responses to DBS, Chapter 4 focuses on modelling dynamic responses (those that change frequency over time on stimulation).

In particular, I focus on modelling the long-term dynamics of ERNA that have eluded the field so far. In Chapter 4 I ask the question

"Can we reproduce the long-term characteristics of ERNA using a computational model of a single population of neurons and identify potential underlying mechanisms of this phenomenon?"

I conclude this thesis with a general discussion, in Chapter 5, which summarises the work accomplished within this thesis. In addition, I provide a summary of the implications of this work as well as some of the key limitations and next steps that naturally follow on from the work performed here.

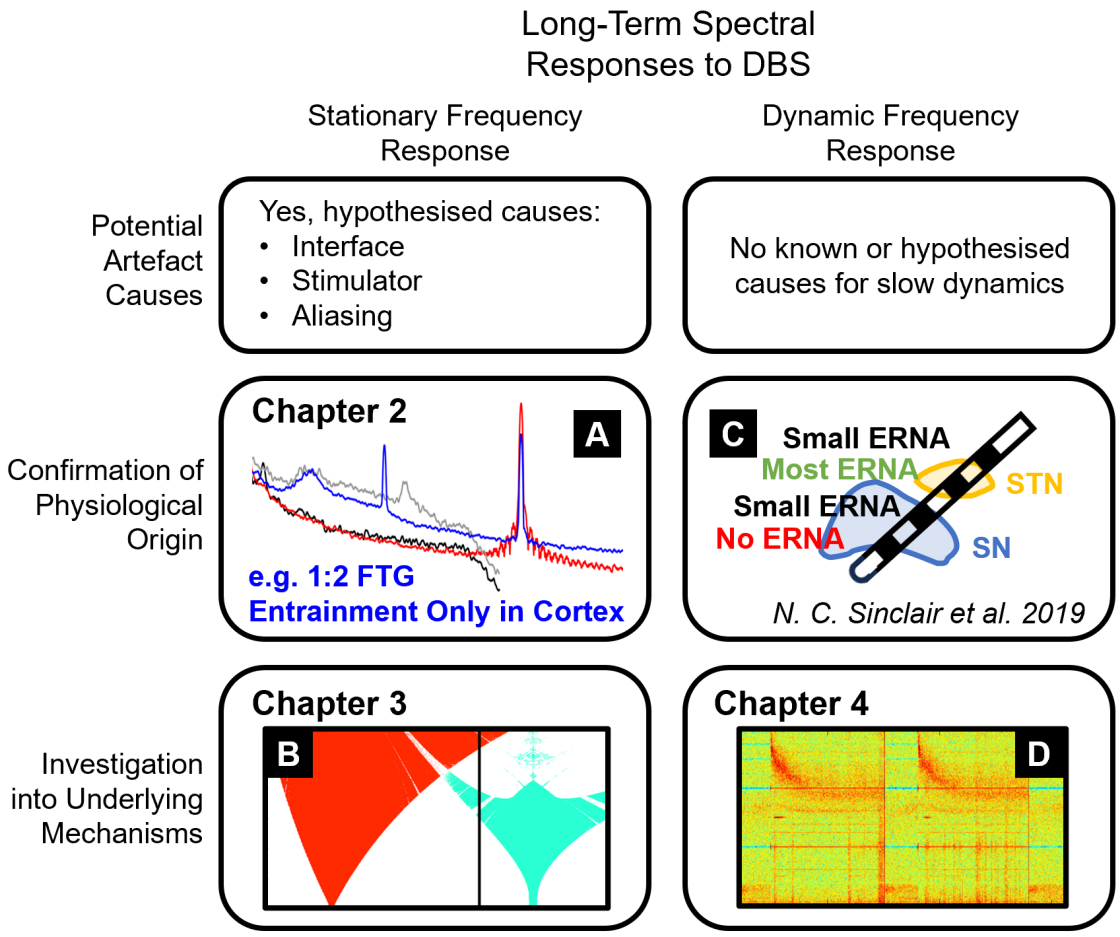


Figure 1.5: Relevance of each chapter in the general space of neural responses to DBS. Stationary Frequency Responses: We list the primary hypothesised sources of sub-harmonic artefacts as covered in Chapter 2. In Chapter 2 we use data from prior studies to confirm physiological origin of sub-harmonic FTG entrainment. (A) One of the confirmation examples is the location specific nature of 1:2 FTG entrainment as we demonstrate in this preview of Fig 2.5. We investigate the underlying mechanisms of sub-harmonic FTG entrainment in Chapter 3. (B) Entrainment field showing two different Arnold tongues of the sine circle map, which is shown again in Fig 2.2A in more detail. **Dynamic Frequency Response:** There are no known hypotheses for artefacts that have dynamic frequencies at this stage. However, confirming physiological origin of ERNA is demonstrated (as discussed in Section 1.2.5.2) through only being present in specific parts of the subthalamic region (C, a graphical interpretation of the subthalamic nucleus (STN), substantia nigra (SN) and the results from (Sinclair et al. 2019)). We investigate potential underlying mechanisms of the long-term characteristics of ERNA (D, adapted from (Wiest et al. 2020) and shown in more detail in Fig 4.2) in Chapter 4.

Publications A summary of the published or under review work achieved over the course of this thesis and how it pertains to specific chapters.

Chapter 2 is adapted from

James J. Sermon et al. (2024a). "1:2 entrainment is not a device-induced artefact, except when it is". In: *Brain Stimulation* 17.2, pp. 149–151. DOI: 10.1016/j.brs.2024.01.010

Chapter 3 is adapted from

James J. Sermon et al. (2023). "Sub-harmonic entrainment of cortical gamma oscillations to deep brain stimulation in Parkinson's disease: Model based predictions and validation in three human subjects". In: *Brain Stimulation*. DOI: 10.1016/j.brs.2023.08.026

Chapter 4 is adapted from

James J. Sermon et al. (2024b). "Evoked Resonant Neural Activity Long-Term Dynamics can be Reproduced by a Computational Model with Vesicle Depletion". In: *bioRxiv*. DOI: 10.1101/2024.02.25.582012

which is under review at Neurobiology of Disease

My contributions to (Zamora et al. 2021) (as summarised in Section 1.2.4.3), providing a revision to the stimulation protocol, were part of the early work to demonstrate the motives behind further work into entrainment. Contributions to (Duchet et al. 2023), which builds on the work in Chapter 3, are not discussed in this thesis. Neither are the contributions to (Arruda et al. 2021), modelling the phase-locked properties of stimulation on tremor.

Mayela Zamora et al. (Sept. 2021). "Case Report: Embedding "Digital Chronotherapy" Into Medical Devices—A Canine Validation for Controlling Status Epilepticus Through Multi-Scale Rhythmic Brain Stimulation". In: *Frontiers in Neuroscience* 15, p. 1196. DOI: 10.3389/fnins.2021.734265

Benoit Duchet et al. (Apr. 2023). "How to entrain a selected neuronal rhythm but not others: open-loop dithered brain stimulation for selective entrainment". In: *Journal of Neural Engineering* 20.2, p. 026003. DOI: 10.1088/1741-2552/acbc4a

Beatriz S. Arruda et al. (2021). "Identifying and modulating distinct tremor states through peripheral nerve stimulation in Parkinsonian rest tremor". In: *Journal of NeuroEngineering and Rehabilitation* 18 (1). DOI: 10.1186/s12984-021-00973-6

2

Artefact Checking - 1:2 Entrainment Is Not A Device-Induced Artefact, Except When It Is

Contents

2.1 Abstract 38
2.2 Introduction 38
2.3 Model Predictions and Theory (Is Entrainment Expected?) 42
2.4 Physiological Confirmation Steps 43
2.4.1 Medication and Arousal State Dependent Response . . . 43
2.4.2 Nonlinear Response to Stimulation 44
2.4.3 Location Specific 45
2.4.4 Clinical Observations 46
2.5 Electrical Signal Chain Checklist 46
2.5.1 Tissue Electrode Interface 47
2.5.2 Stimulator Circuits 48
2.5.3 Aliasing and Analogue to Digital Converters (ADCs) . . 51
2.6 Discussion 54
2.6.1 Limitations 55
2.6.2 Implications 56
2.7 Conclusion 57

2.1 Abstract

Several sense-stimulation device studies have observed signals at the half harmonic of stimulation frequency. However, the field remains cautious about using biomarkers around sub-harmonics of stimulation frequency over concerns regarding contamination from artefacts. In this chapter, we aim to devise a framework to assess whether a signal at a sub-harmonic of stimulation frequency is likely to be of physiological or artefactual origin. Initially, we investigate the theoretical requirements for sub-harmonic entrainment. We then focus on the case of motocortical FTG at the half-harmonic of DBS in PD and show how examples of modulation of the signal through independent physiological perturbations (from our own work and the literature) provide strong evidence of physiological origin. Furthermore, we perform computational simulations and bench top testing to characterise artefacts from the most commonly hypothesised artefact sources in the electrical signal chain. The results of this investigation show that it is possible to provide strong evidence supporting the physiological origin of a signal, even when it is not possible to be certain that every potential artefact source has been accounted for. Additionally, while artefacts can arise from components of the electrical signal chain, they are often predictable and can be characterised by testing the stimulation device as well as the signal processing pathway. It is our hope that the framework introduced in this chapter will allow researchers to perform their own investigations to confirm the origin of subharmonic signals. This may provide new opportunities for aDBS algorithms and improve clinical approaches.

2.2 Introduction

DBS is a widely used invasive therapy for PD as well as many other conditions. The development of sense-stimulation devices has demonstrated the ability to elicit a wide range of neural responses to DBS. However, the physiological validity of recorded signals during DBS is often a matter of debate (as discussed in Section 1.2.3.3) and can be contaminated by artefacts (see Section 1.2.3.6). In particular, the field tends

to avoid using biomarkers around harmonics of stimulation frequency as they have previously been assumed to be artefact. As discussed in Section 1.2.3.3, the future of sense-stimulation therapies and aDBS is reliant on the further development of understanding which frequency bands remain artefact free, which would provide clarity on where biomarkers can be consistently monitored. This is an area that so far has not been addressed in a manner that can be adapted to specific brain rhythms, devices or protocols that can be used for researchers and clinicians.

Artefacts are a known issue for sense-stimulation devices. There are many potential causes of artefacts in the closed-loop pathway of sense-stimulation devices (as highlighted in Section 1.2.3.6), which include artefacts of physiological (but not neural) (Thenaisie et al. 2021; Noury et al. 2016), device (Chen et al. 2021) or signal processing (Qian et al. 2017; Abbasi et al. 2016; Ramírez et al. 2011) origin, all with varying spectral characteristics. These artefacts are generally not structured enough to be present at exactly the half harmonic of stimulation frequency in a robust manner. This is demonstrated in the data, where often sub-harmonics (in particular around the half harmonic) are not seen in neural recordings from studies aiming to identify artefacts (Lim et al. 2018; Nie et al. 2021; Noury et al. 2016; Scheller et al. 2019). However, sometimes sub-harmonic activity that is hypothesised to be artefactual can be observed, but the appearance is consistent across recordings from patients or bench top tests (Chen et al. 2021) or is very patient dependent (Thenaisie et al. 2021; Wiest et al. 2021). In these patient dependent cases, the signal being of physiological origin cannot be ruled out. In some cases, activity around the half harmonic is strongly believed to be of physiological origin and is actively preserved through artefact removal algorithms (Caldwell et al. 2020). Additionally, most artefact removal algorithms do not even consider artefacts below stimulation frequency (Lim et al. 2019; Nie et al. 2021; Chen et al. 2022; Qian et al. 2017; Hammer et al. 2022).

Sub-harmonic entrainment is becoming of greater clinical interest, which emphasises the importance of characterising and avoiding sub-harmonic artefacts. As outlined in Section 1.2.4.4, 1:2 entrained FTG has been demonstrated to

be an effective biomarker for an adaptive DBS protocol for the prediction and reduction of hypo- and hyper-kinetic episode severity and fluctuation in a PD patient group (Oehrn et al. 2023). The application of sub-harmonic entrainment to closed-loop DBS therapies also extends beyond motor symptoms within PD, where entrainment has already been shown as a viable method to reduce seizure count and severity in epilepsy (Zamora et al. 2021).

In this chapter, we aim to develop a framework to assess whether signals at subharmonics of stimulation frequency are artefacts or of physiological origin. In order to characterise sub-harmonic artefacts, we apply this framework through the specific context of 1:2 FTG entrainment in PD and demonstrate that it is a viable potential biomarker for closed-loop DBS. We develop this framework through a combination of computational simulations, bench testing and literature review. We investigate the theoretical underpinnings of sub-harmonic entrainment and describe how it is not a surprising observation (Fig 2.1: Theory). It is important to consider sub-harmonic activity cautiously and as artefactual until evidence indicates otherwise. Consequently, we look to confirm physiological origin through a review of studies that show the modulation of 1:2 entrained FTG with a variety of different independent physiological perturbations (Fig 2.1: Physiological Confirmation). These perturbations include medication, stimulation, location, time as well as clinical response. When physiological evidence, it is beneficial to confirm that artefacts are not being induced from potential sources in the electrical signal chain (Fig 2.1: Signal Chain Artefact Check). We demonstrate through theoretical analysis and computational simulations that tissue-electrode-interfaces (TEIs) are unlikely to produce sub-harmonic artefacts. Additionally, we characterise sub-harmonic artefacts from devices and signal processing through benchwork and computational simulations, respectively. Finally, we discuss our framework, its clinical implications and the importance of being able to take advantage of sub-harmonic entrainment when physiological origin can be demonstrated.

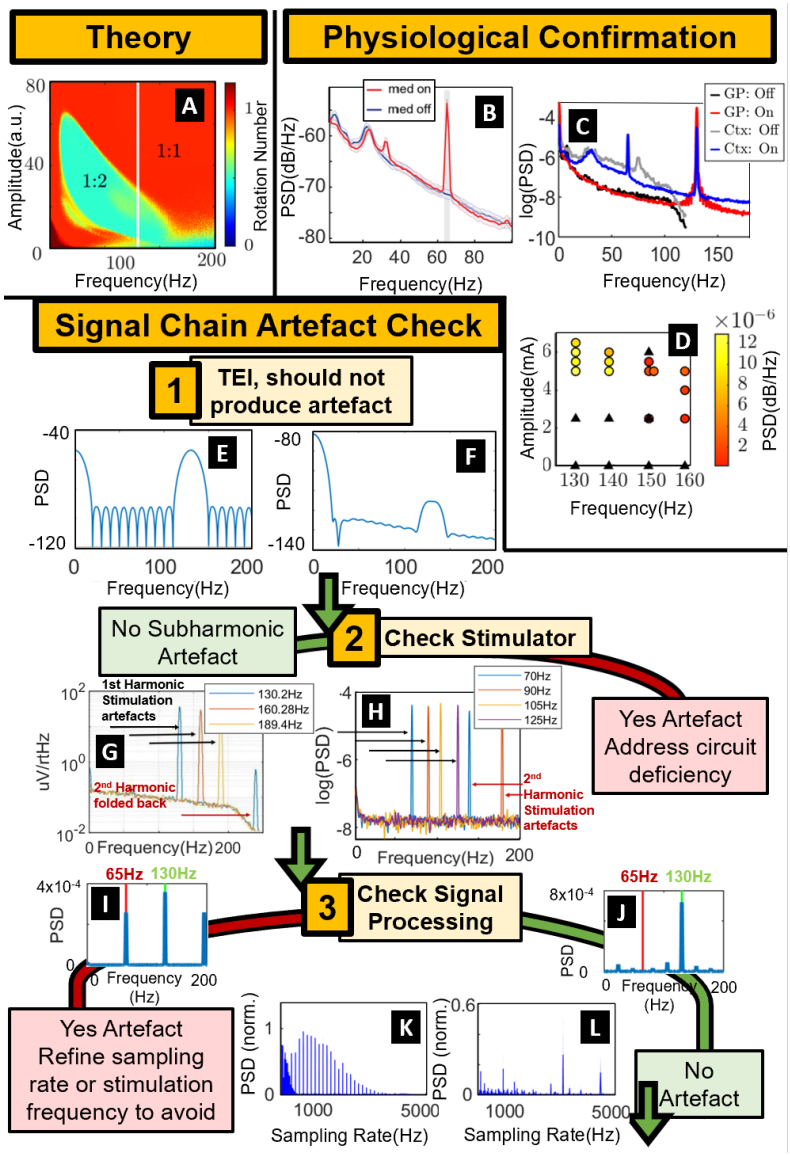


Figure 2.1: A flow diagram for addressing entrainment vs artefact with previews of each key section. Theory: (A) Prediction of entrainment regions from a two-population Wilson-Cowan model fitted to off-stimulation data of the motor cortex, Fig 2.2B. Physiological Confirmation: (B) The modulation of 1:2 entrainment in different medication states, Fig 2.3A adapted from (Oehrn et al. 2023). (C) The modulation of 1:2 entrainment with recording location (globus pallidus (GP) and cortex (Ctx)), Fig 2.5. (D) The modulation of 1:2 entrainment with stimulation parameters, Fig 2.4A. Signal Chain Artefact Check: (E and F) The spectrum of the voltage outputs of two TEIs, Fig 2.6. (G and H) The outputs of a summit RC+S device (Stanslaski et al. 2018) (G) and a DyNeuMo-2 (H), Fig 2.7. (I, J, K and L) The normalised PSD at the half harmonic (65Hz) downsampled through a conventional analogue-to-digital (ADC) (K) and delta-sigma ADC (L), with individual investigations into the delta-sigma ADC at sampling rates of 3185Hz (I, half harmonic artefact) and 3100Hz (J, no half harmonic artefact), Fig 2.8.

2.3 Model Predictions and Theory (Is Entrainment Expected?)

It should be noted that theoretically we expect to see sub-harmonic entrainment to periodic perturbations in certain nonlinear systems (Mitarai et al. 2013). 1:1 entrainment is a fundamental property of all resonant systems, regardless of their complexity or linearity. All resonant systems, from a single oscillator to a large network, have a natural frequency. Hence, it is possible to drive them at this frequency. Additionally, it is possible to drive them at supra-harmonics where the perturbation only provides an input every other cycle (2:1 entrainment), every three cycles (3:1 entrainment), etc. However, only certain systems have the capacity to be entrained at sub-harmonics. While additive forcing to simple (linear) systems will only result in 1:1 and supra harmonic entrainment (Mitarai et al. 2013), the introduction of some form of nonlinearity can result in sub-harmonic entrainment (Komarov and Pikovsky 2014). Depending on the system, sub-harmonic entrainment could appear at any integer combination of frequency locking ratios (Arnol'd 1983) (see Section 1.2.4 for more details). Hence, in a system that is as nonlinear and diverse as the brain it should not come as a surprise that sub-harmonic entrainment has been observed in some instances in response to high amplitude periodic inputs.

As we will see in Chapter 3, Sub-harmonic entrainment (specifically 1:2 entrainment) can be predicted from a model of off-stimulation cortical FTG. The predictions of the model were compared to follow-up data recordings and shown to be significantly accurate in two out of three patients. Hence, indicating this is likely a physiological response.

While these theoretical predictions are valuable and represent good indications of the origin of these observations, this alone does not provide evidence of physiological origin. Theory can account for entrainment as a neurophysiological phenomenon, but further checks are required to rule out the presence of artefacts. It is therefore

necessary to undertake further investigations and provide further evidence to support a physiological or artefactual origin.

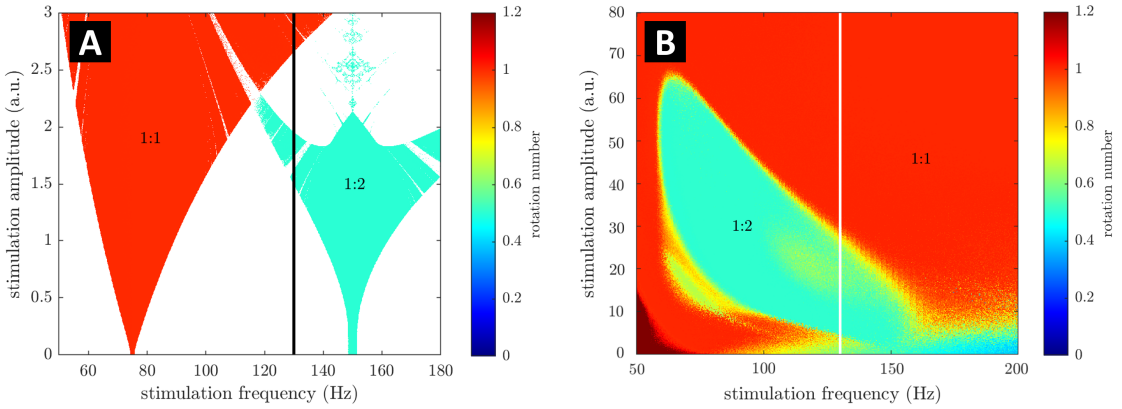


Figure 2.2: Sub-harmonic entrainment is predicted by computational models. Predictions of sub-harmonic entrainment regions from (A) the sine circle map of a 75Hz oscillator and (B) the two-population Wilson-Cowan model fitted to off-stimulation data of the motor cortex, adapted from (Wiest et al. 2021). The 1:2 entrainment region (1:2 Arnold tongue) is indicated by the green region with a rotation number of 0.5 and the 1:1 entrainment region in red.

2.4 Physiological Confirmation Steps

Initially, it is important to treat sub-harmonic activity cautiously and as an artefact. However, when evidence demonstrates physiological origin, we must be open to exploit the potential clinical implications. We can demonstrate physiological origin by considering how sub-harmonic entrainment evolves around independent perturbations to physiology.

2.4.1 Medication and Arousal State Dependent Response

A clear indication of physiological origin is the modulation of sub-harmonic entrainment with variable neural states. 1:2 entrainment has been observed to be modulated by medication state, only being present after Levodopa intake in many patients (Swann et al. 2016; Swann et al. 2018a; Oehrn et al. 2023) (see Fig 2.3B). Given the correlation between medication and 1:2 entrainment, 1:2 entrainment has also been considered to be associated with dyskinesia state (Swann et al. 2016). In addition, neural activity may selectively entrain at subharmonics of stimulation

frequency according to sleep-wake state (Smyth et al. 2023). This may reflect changes in neural properties modulated with vigilance and activity across sleep states.

For both the cases of modulation by medication or sleep-wake state, the stimulation and signal processing remain unchanged. For 1:2 entrainment (or other sub-harmonics) to appear or disappear solely reflects a change in the underlying neural circuitry. Therefore, this elucidates the origin of the sub-harmonic entrainment observations as physiological.

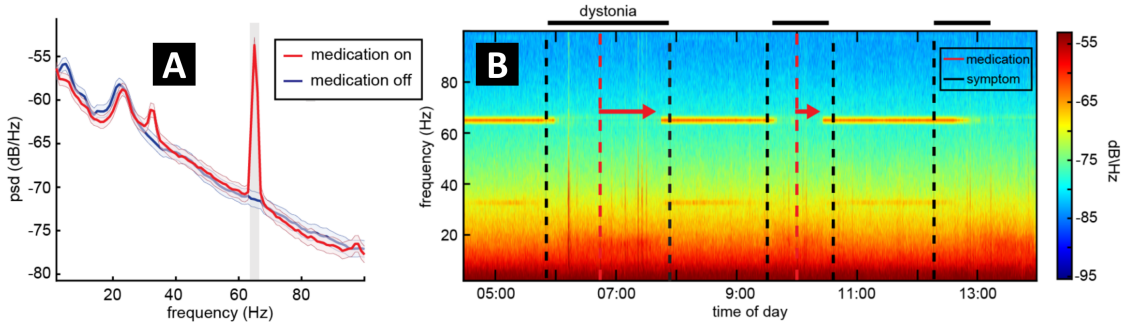


Figure 2.3: The modulation of 1:2 entrainment in different medication states with 130Hz stimulation. (A) PSD of medication on and off states with stimulation constant at 130Hz. 1:2 entrainment at 65Hz is only seen in the medication on state (red). (B) Spectrogram showing modulation of 1:2 entrainment over several medication on/off states. Medication taken with red dashed lines and dystonia symptoms only present between black dashed lines. Both panels adapted from (Oehrn et al. 2023).

2.4.2 Nonlinear Response to Stimulation

To provide additional physiological confirmation of the origins of this phenomenon, we can observe the modulation of 1:2 entrainment with variable stimulation parameters. This modulation is observed with variation of both stimulation amplitude and frequency (see Chapter 3). This can be more easily seen in (Oehrn et al. 2023) where 1:2 entrainment cannot be seen below a certain stimulation amplitude, but is maintained for all stimulation amplitudes above that threshold. The loss of 1:2 entrainment as stimulation amplitude is increased for constant stimulation frequency is seen in Chapter 3. This indicates that we are not simply observing an aliased signal; amplifier saturation might have some effect, but this can be monitored. Furthermore, PSD within the 1:2 tongue is seen to be greatest

for the lowest stimulation frequencies (and maybe stimulation amplitudes as well) that result in 1:2 entrainment.

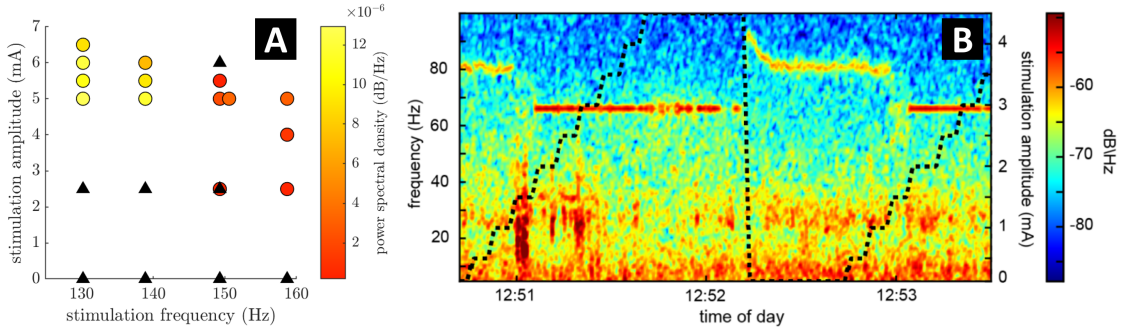


Figure 2.4: The modulation of 1:2 entrainment with variable stimulation parameters. (A) Charting the 1:2 tongue of FTG in the cortex from variable STN-DBS. Circles indicate 1:2 entrainment observed with power spectral density (PSD) corresponding to the colour. Black triangles indicate no 1:2 entrainment. (B) Modulation of FTG with variable stimulation amplitude, adapted from (Oehrn et al. 2023).

2.4.3 Location Specific

1:2 entrainment is also only seen in specific neural structures. During 130Hz GP stimulation, 1:2 entrainment was only observed in the motor cortex (Gilron et al. 2021). Theoretically, we believe this is primarily due to the motor cortex having an on-medication neural rhythm (approx. 75Hz) close to the half harmonic of stimulation frequency, while the GP does not appear to. From the concept of Arnold tongues, this is intuitive as more energy is required to entrain oscillators with natural frequencies further from the harmonic of the perturbing frequency. It is therefore logical that only the motor cortex, which does have natural high frequency oscillations is capable of entraining to the half harmonic of 130Hz stimulation.

The observation of 1:2 entrainment in response to pallidal stimulation is limited to cortical contacts in the data analysed in Fig 2.5. These contacts are not close to the stimulating electrode. This indicates that volume conduction of a stimulation artefact from the stimulating electrode is not the source of cortical half harmonic activity. Additionally, the signal processing is the same for all recording contacts regardless of location in the brain. Hence, by only observing 1:2 entrainment in the cortex, we provide further evidence that this phenomenon is not an artefact.

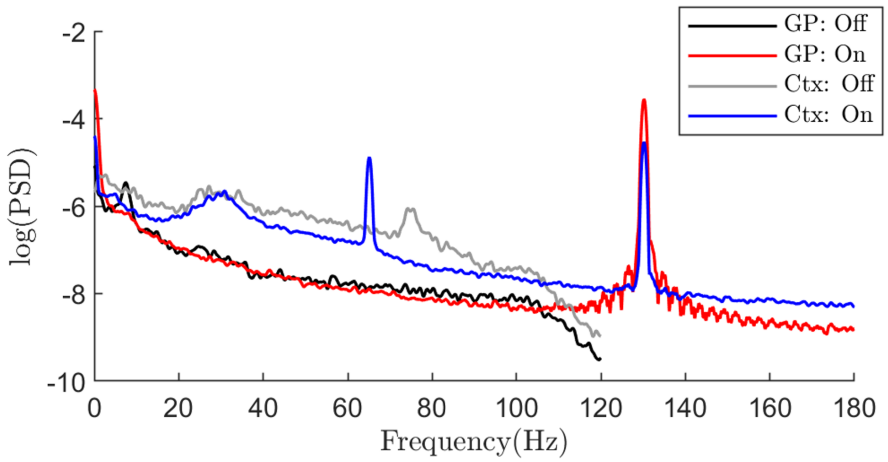


Figure 2.5: The modulation of 1:2 entrainment with recording location. (globus pallidus (GP) and cortex (Ctx)) for both on pallidal stimulation at 130Hz and off-stimulation conditions.

2.4.4 Clinical Observations

A clinical response provides one of the most important physiological confirmation steps. Entrainment for clinical benefit has now been used in two studies that have been supported by the author and supervisors of this thesis. As outlined in Section 1.2.4.4, FTG power entrained at half stimulation frequency was shown to predict prokinetic states in PD patients and was identified as the optimal control signal for aDBS for reducing residual motor fluctuation (Oehrn et al. 2023). As summarised in Section 1.2.4.3, targeting 1:1 low-frequency entrainment was seen to significantly reduce seizure frequency and duration in an epileptic canine (Zamora et al. 2021). Regardless of artefacts masking neural signals, an artefact is not able to provide clinical benefit. Furthermore, this demonstrates the clinical importance of entrainment for some neural ensembles.

2.5 Electrical Signal Chain Checklist

When there is physiological evidence, we can proceed to eliminate the most commonly hypothesised sources of artefacts through bench top testing and simulations. We begin our checklist with the most difficult to change potential sources, through to the easiest to modulate.

2.5.1 Tissue Electrode Interface

Tissue-Electrode Interfaces (TEIs) have been hypothesised as a potential source of sub-harmonic artefacts (Chen et al. 2021). However, circuit theory and linear time-invariant components demonstrate that this hypothesis is unlikely. A PINS device was shown to exhibit artefacts at a variety of sub-harmonics with varying stimulation amplitude when placed across a resistor network (Chen et al. 2021) (resistor network shown in Fig 2.6Bi). However, this artefact cannot be a response of this circuit as it only includes linear time invariant components and must instead be a property of the stimulator. Alternatively, the typical TEI is considered to be a circuit constituting of a resistor and a capacitor in series or parallel. Here, we consider the two components in parallel, however, this does not affect the outcome as all components are linear-time invariant.

In Fig 2.6, we present the PSD (Fig 2.6Aii and Bii) from the output signal of each of the TEI circuits (Fig 2.6Ai and Bi) considered in (Chen et al. 2021) and the majority of TEI literature (Das et al. 2020; Zhang et al. 2020). Both circuits are stimulated with a 130Hz 90μs pulse width monophasic pulse train for one second. Whether the pulses were monophasic or biphasic was not seen to change the key observations of the resulting spectra or introduce any sub-harmonic artefacts. For the results presented in Fig 2.6A, C_A was chosen to be 100μF and both $R_{A,1}$ and $R_{A,2}$ were selected as 2$k\Omega$. In Fig 2.6B, resistor values were chosen in line with (Chen et al. 2021) where $R_{B,1}$ was 100Ω, $R_{B,2}$ as $k1\Omega$, $R_{B,3}$ as 1$k\Omega$ and $R_{B,4}$ as 1.9$k\Omega$. It was said in (Chen et al. 2021) that the selection of $R_{B,3}$ and $R_{B,4}$ influenced the magnitude of stimulation artefacts when recorded with the PINS device. In our simulations, while varying all values in both TEI models, we never saw any appearance of sub-harmonic artefacts.

Neither of these TEI circuits produce any sub-harmonic artefacts. The only artefacts observed occur at 0Hz, stimulation frequency and all supra-harmonics of stimulation frequency. This matches the theoretical expectation of these network. This is because these components (resistors, capacitors and/or even adding an inductor) are linear time-invariant and can therefore not produce sub-harmonics. In

order to produce sub-harmonic artefacts, nonlinear components would be required. In a biophysical system, this nonlinear component could be a contribution from the ion channel dynamics as well as other potential nonlinearities of the brain, but these have not been well characterised and are not commonly used in models of the TEI. This could, however, be the subject of future research.

When considering the ion channel dynamics at the TEI as a potential artefact source, we can look to the modulation of 1:2 entrainment with variable stimulation parameters to confirm physiological origin. It is not possible to remove these concerns with the results of modulation with medications state, sleep-wake state or location. Each of these cases relies on different neural ensemble behaviour across either different states or different neural structures. It therefore stands to reason that different ion channel dynamics could represent this varying neural behaviour. Hence, we look elsewhere to the entrainment response with variable stimulation parameters where we can consider the underlying ion channel dynamics to remain unchanged over different stimulation parameters. We can make this assumption as we only observe the sub-harmonic entrainment response in single location and over a short enough time frame that we would not expect significant changes to the ion channel dynamics due to medication wearing off or from changes in alertness.

2.5.2 Stimulator Circuits

Unlike TEIs, stimulators do have the ability to produce sub-harmonic artefacts (Chen et al. 2021). This is not surprising due to the presence of many nonlinear components within a neuromodulation device. It is possible to avoid these artefacts as demonstrated through characterisation of commonly used DBS devices, the Percept PC (Thenaisie et al. 2021) and the Summit RC+S (Stanslaski et al. 2018). Neither device produces sub-harmonic artefacts for any stimulation parameters tried in saline tank tests. This demonstrates the necessity to purposefully design stimulators when considering the application to sub-harmonic biomarkers as well as to characterise the device in saline tank tests after construction. The source of sub-harmonic artefacts that stimulators can introduce in the sense-stimulation pathway is in the

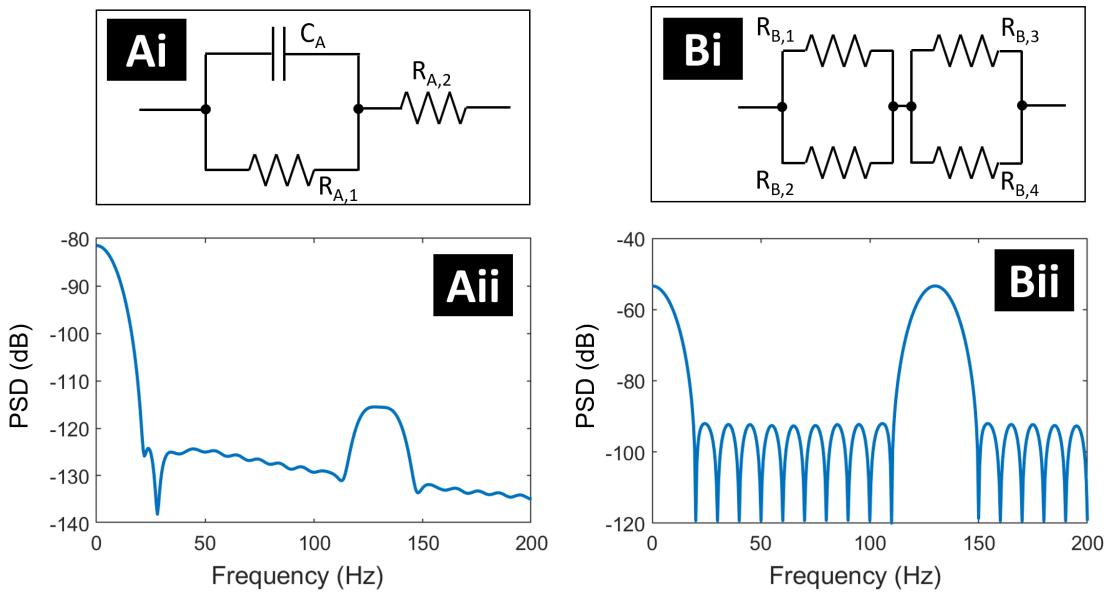


Figure 2.6: The spectrum of the voltage outputs of resistor capacitor circuit models. (Ai) The more common resistor-capacitor tissue-electrode interface (TEI) and (Bi) a resistor network TEI (Chen et al. 2021) stimulated at 130Hz with monophasic stimulation pulses. (ii) The associated voltage outputs from each TEI.

stimulation signal itself. While stimulators are complex assemblies of engineering, if they produce a linear stationary signal (as is the intention), this will not produce sub-harmonic artefacts (Qian et al. 2017). Where a linear stationary signal is defined as having a spectrum with harmonic components at only integer multiples of the fundamental frequency and a signal that does not evolve outside of the time period defined by its fundamental frequency. This can be seen as the Fourier transform of a linear stationary square wave does not include any sub-harmonic terms.

Stimulators can produce sub-harmonic artefacts and investigations of the PINS device demonstrated that it produced a series of noise ripples in its pulse train. However, in order to provide "noise" ripples that are structured enough to produce exact half, third or quarter harmonics requires very consistent and reproducible ripples. Hence, there is likely some form of structured amplifier reset which is dictated by the stimulation amplitude that is responsible for this. This would potentially explain why we see artefacts that drop in the order of the harmonics as stimulation amplitude is decreased in this device (see Figures 5a,c and d in Chen et al. 2021). As previously stated, a nonlinear system is required to generate a

signal with sub-harmonics. If the PINS device has an amplifier that resets on alternating pulses, then this would provide that nonlinearity.

We provide supporting evidence that DBS devices do not necessarily produce sub-harmonic artefacts with saline tank tests of the Picostim DyNeuMo-2 (Fig 2.7). We submerge the DyNeuMo-2 in a saline tank of 0.9% saline solution, a test bench similar to that used in (Stanslaski et al. 2018; Thenaisie et al. 2021; Fleming et al. 2023). The device is placed in the saline tank with the measurement electrodes either side. This set-up approximates a similar charge distribution to that of biological tissue. The DyNeuMo then produces pulsatile stimulation, while recording through the measurement electrodes in the absence of any other external signals being injected. We cycle through a range of stimulation frequencies and amplitudes, recalibrating the device between each parameter selection. Fig 2.7 shows the signals produced for variable stimulation frequency with 4mA amplitude. The spectra are produced using the pwelch Matlab function after high-pass filtering all signals with a 2Hz cutoff frequency. No sub-harmonic artefacts were seen for any of the stimulation parameter combinations used in these tests.

Bilateral stimulation may also be concerning as a possible source of artefacts from the stimulators. A secondary stimulation pulse being recorded from across hemispheres would potentially add secondary activation to the time series recording while incorporating some form of neural circuit filtering and network delays. This signal should still reach the cross-hemisphere recording electrode with a consistent time difference that has not changed from the stimulation site. Hence, this would not introduce sub-harmonic artefacts, as long as both stimulation frequencies were matched. Further evidence is demonstrated for this from observations of FTG 1:2 entrainment in a three PD patient cohort, where two received bilateral stimulation (RCS02 and RCS10 from Chapter 3) and the other received mono lateral (RCS18 from Chapter 3). The key features of the 1:2 entrainment region were consistent across these two stimulation paradigms.

Impedance mismatch across the measuring and reference electrodes has also been suggested as a source of stimulation artefact (Tiruvadi et al. 2023). However,

this is unlikely to introduce sub-harmonic artefacts in sense-stimulation devices that are properly managed. In physiological environments their behaviour is usually stationary in time and follows small signal theory and is therefore linear. Simulations have shown that in the presence of unphysiological levels of impedance the resulting compression gain from the mismatch can produce stimulation artefacts around the sub-harmonics of stimulation frequency (Tiruvadi et al. 2023). As modern sense-stimulation systems can measure impedance, these conditions can be avoided.

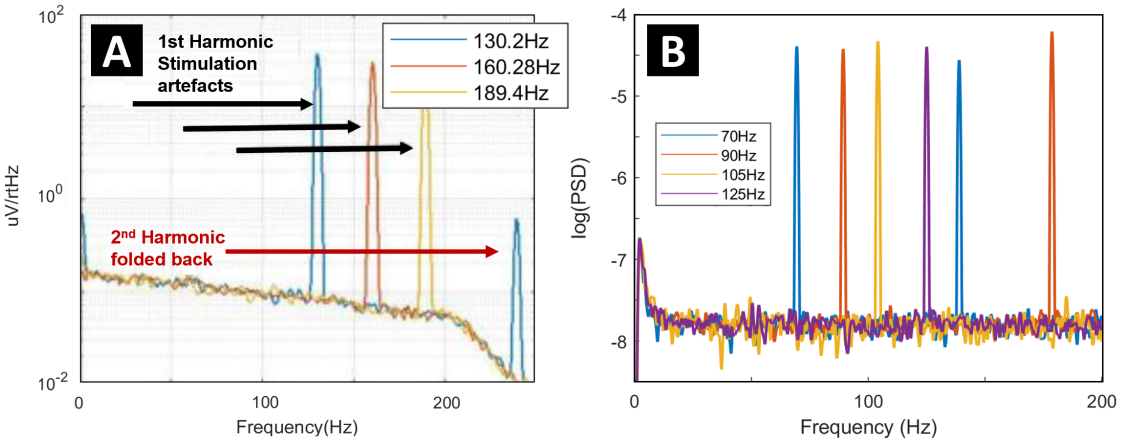


Figure 2.7: The outputs of two sense-stimulation devices from saline tank testing. (A) Summit RC+S device (Stanslaski et al. 2018) and a DyNeuMo-2 (B) in saline tank recordings for a range of stimulation frequencies.

2.5.3 Aliasing and Analogue to Digital Converters (ADCs)

Aliasing artefacts are a known issue in sense-stimulation interactions, introduced from nonlinearities in the signal processing pathway. "Sense friendly" stimulation settings have been introduced, which aim to manage where artefacts from these interactions can appear (Herron et al. 2018). In addition, the general spectral features that can be introduced from aliasing artefacts has been explored in (Debarros et al. 2020).

The primary property of a signal processing pathway that determines the presence of sub-harmonic artefacts is the sampling frequency. It is necessary to understand the effect of the Nyquist frequency on any potential sub-harmonic biomarker. The Nyquist frequency dictates that the sampling rate must be at

least twice the frequency of any signal of interest in order to obtain an accurate replication of the signal. Any dominant spectral features greater than the Nyquist frequency (sampling rate/2) will be reflected back into PSD. This contaminates PSD below the Nyquist frequency and is why low-pass filters are often used around the Nyquist frequency to prevent this.

For most signal processing pathways, the sampling rate is much higher than the main frequency of the stimulation. However, as the signal is a series of pulses and not perfectly sinusoidal there are other frequency components in the stimulation signal. Notably there exists higher frequency components due to the much shorter period of stimulation pulse width (Lio et al. 2018). For example, if this pulse width is around 60µs this cannot be fully captured by a commonly used 4kHz sampling rate, having a frequency component closer to 16.67kHz therefore requiring a sampling frequency closer to 34kHz (Qian et al. 2017; Abbasi et al. 2016; Ramírez et al. 2011). The lower sampling rate is often a constraint of DBS devices that would introduce additional complications if increased.

A lower sampling rate does not guarantee the appearance of dominant sub-harmonic artefacts. Furthermore, the appearance of stimulation artefacts from aliasing can be predicted for different analogue to digital converters (ADCs) by considering the sampling rate and stimulation parameters (Qian et al. 2017). Hence, we investigate this by simulating the spectral output of different ADCs across varying sampling rates (Fig 2.8). We simulate the output from a 130Hz 90μs pulsewidth monophasic pulse train passing through a delta-sigma ADC (Fig 2.8A) and a standard downsampling ADC (Fig 2.8B) over a one-second period. In each case, Fig 2.8 shows the PSD at the half harmonic (65Hz) of stimulation frequency normalised against the PSD at stimulation frequency (130Hz). For each simulation, an arbitrary unit amplitude of 10 is used for stimulation amplitude. For the delta-sigma ADC, a threshold of 900 is used for Fig 2.8A and sampling rate refers to the inverse of the predetermined observation period. For each ADC and at each sampling rate, the resultant PSD is calculated over 100 trials with randomised starting points. This is because it is possible to get different artefacts at the

relative time that samples are taken, especially when sampling rate is a multiple of stimulation frequency. The resultant plot shows both the mean of the half harmonic artefact (solid line) and the standard deviation (shaded area).

For both of the ADCs shown here, many stimulation-sampling frequency combinations produce half harmonic artefacts. For the standard ADC, these artefacts can be quite prominent compared to the artefact at stimulation frequency. However, these artefacts occur at regular, precise and predictable sampling frequencies (we provide the code for the two ADCs mentioned here: Github ADC Artefact Calculator). Half harmonic artefacts are generally much smaller comparatively in the delta-sigma ADC. Additionally, they are less easily predicted. Figs 2.8Ai and Aii show the PSD for two specific sampling rate cases that although close in frequency produce different responses at the half harmonic. While Bii shows a clear half harmonic artefact, Bi does not. However, Bi does produce artefacts at other sub-harmonics (fifth harmonics) although they are small. This demonstrates the necessity to know which sub-harmonic is being targeted in sense-stimulation protocol so that the corresponding sampling rate can be chosen accordingly.

Modulation with variable physiological states (Section 2.4.1) can provide confirmation that the ADC is not producing sub-harmonic artefacts, but only when stimulation frequency (and sampling frequency) remains constant. Furthermore, as 1:2 entrainment is observed over a wide and bounded range of stimulation parameters (Section 2.4.2), this provides further evidence that the ADC is not a source of artefacts at these frequencies. As the ADC can only produce sub-harmonic artefacts at specific combinations of stimulation and sampling frequency, it makes it highly unlikely to consistently choose combinations that result in half harmonic aliasing artefacts. Additionally, the structured PSD nature of the entrainment regions directly disagrees with the expected aliasing response, which would be predicted to increase in PSD with increasing stimulation amplitude. The loss of 1:2 entrainment at increasing stimulation amplitude further supports this argument as there would not be a maximum amplitude for which an aliasing artefact could be observed.

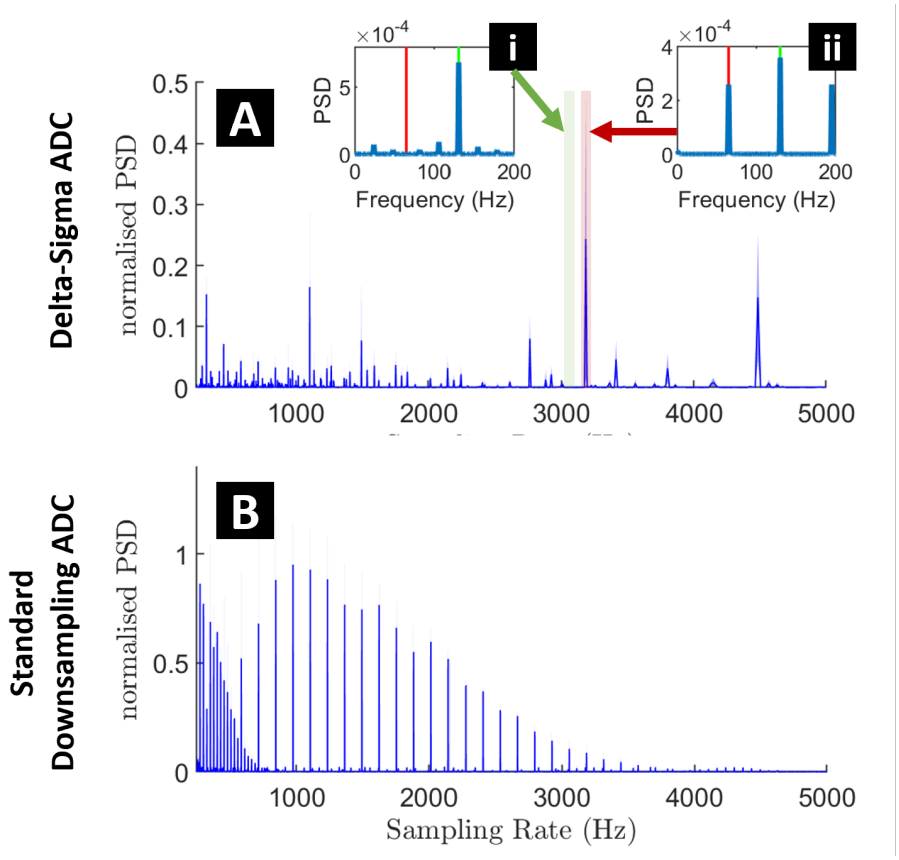


Figure 2.8: The potential sub-harmonic artefacts that can originate from aliasing through analogue-to-digital converters. (A and B) The PSD at the half harmonic (65Hz) normalised by the PSD at stimulation frequency (130Hz) after downsampling through a delta-sigma ADC (A) and a conventional ADC (B). Panel inserts showing the PSD from a 130Hz monophasic pulse train downsampled through a delta-sigma analogue-to-digital converter (ADC) with sampling rate 3100Hz (Ai, no half harmonic artefact) and 3185Hz (Aii, half harmonic artefact).

2.6 Discussion

In this chapter we demonstrate the collection of evidence for the physiological origin of 1:2 entrainment for motocortical FTG in patients with PD. Sub-harmonic entrainment can be observed in nonlinear systems and it should not be surprising that some neural ensembles are capable of demonstrating this. However, demonstrating that sub-harmonics can happen and confirming our observations are of physiological origin are very different. We provide physiological perturbation examples that confirm the physiological origin of sub-harmonic entrainment through modulation by medication state, sleep-wake state, stimulation, recording site, and through

clinical studies. In addition, we identify the hypothesised potential causes of artefacts in the electrical signal chain and provide a checklist to address these concerns. The three hypothesised sources we consider are the TEI, stimulator and ADC. For each of these components we conduct bench testing and computational simulations to investigate the appearance of sub-harmonic artefacts. While we eliminate many potential causes of artefacts, we demonstrate that artefacts can still be caused and provide methods to avoid this. Furthermore, this chapter provides a framework to establish whether signals at sub-harmonic frequencies of stimulation are likely to be of physiological or artefactual origin.

2.6.1 Limitations

In the absence of individual neuron recordings (micro-electrode recordings) that show neurons firing at a harmonic of stimulation it will always be difficult to completely rule out this phenomenon as being an artefact. There always exists the possibility, despite being unlikely, that we could be observing a far more complicated artefactual response that captures all these observations through mechanisms we have not considered. However, the work presented here provides us with enough confidence that we have characterised artefacts from the most commonly hypothesised potential sources and that the phenomena studied later in this thesis are physiological. In this limitations section, we will discuss some of the limitations of this chapter and future work that could be performed to address these gaps.

There may remain a concern that electro-chemical ion channel dynamics could introduce a nonlinearity at the TEI. Despite being confident that this is not responsible for the sub-harmonic activity seen here (see Section 2.5.1), the field could still benefit from characterising this response to DBS. While this has not been studied in great detail, this could be the subject of future studies. Namely in vitro models of the TEI could be used to observe the interaction of high amplitude and high frequency stimulation with different neural tissue setups across a variety of ion channel dynamics. An important measurement to capture would be the ion channel dynamics following Levodopa administration, given this often precedes observations

of 1:2 entrainment. Furthermore, techniques using genetically encoded calcium indicators or voltage-sensitive fluorescent proteins (where neurons flash with action potentials) would allow for precise recording of neuronal firing. This could provide confirmation of sub-harmonic entrainment of neurons to stimulation as we would not observe any co-ordinated response for a TEI-based artefactual response.

Recordings of a variety of stimulators in saline showed no sub-harmonic artefactual response from their outputs (RC+S, PC and DyNeuMo). However, the PINS device results did demonstrate that stimulators do have the ability to produce sub-harmonic artefacts if not properly characterised or designed with this goal in mind. In this study of the PINS device, the exact cause of the artefacts was not discovered. We instead demonstrated that the most commonly used sense-stimulation devices do not produce sub-harmonic artefacts. To avoid designing stimulators with these artefacts from residual noise, it would be valuable to identify the component responsible. By breaking down the design of a PINS device it would be possible to identify the responsible component. Alternatively, circuit simulations or adapting other stimulators on the market with the goal of reproducing the pulse train from the PINS device could also shed light on the responsible component.

2.6.2 Implications

This chapter demonstrates that sub-harmonic frequencies should remain artefact free, providing the electrical signal chain has been correctly designed. This is important both for interpretation of previously published results as well as future sense-stimulation paradigms. For the observation thought to demonstrate 1:2 entrainment of FTG in PD (Swann et al. 2016; Swann et al. 2018a; Gilron et al. 2021; Oehrn et al. 2023), we provide additional and more comprehensive evidence that this is a neural response. This should allow researchers to pursue future studies using sub-harmonic entrainment with more confidence. For the purposes of Chapter 3, it is necessary to confirm the physiological origin sub-harmonic FTG entrainment. This is crucial for ensuring that modelling these neural responses is both relevant and feasible.

To maximise the efficiency of future therapies, a transition to aDBS is envisioned to provide maximal benefit across large patient cohorts. A requirement for this is to identify spectral regions that remain consistently artefact free to provide robust biomarkers to the aDBS algorithm. The work presented here, in combination with early evidence showing the clinical impact of half harmonic entrained FTG (Oehrn et al. 2023), indicates that sub-harmonic entrainment may provide a useful mechanism for aDBS to exploit.

2.7 Conclusion

In this chapter we address a variety of hypothesised sources of sub-harmonic artefact, demonstrating that each of these sources are unlikely to be responsible for the observations from data. We provide confirmation of physiological origin through conceptual investigations of independent physiological perturbations. Each of these cases individually offers a compelling indication of a physiological response. However, when considered together, they collectively present a detailed picture that renders the possibility of the observed sub-harmonic activity being an artefact highly improbable. Hence, we can proceed with caution, but also confidently that these complex responses that have been observed in response to DBS are indeed physiological and worthy of further analysis and modelling.

3

Stationary Responses - Sub-harmonic Entrainment of Cortical Gamma Oscillations to Deep Brain Stimulation in Parkinson's Disease

Contents

3.1 Abstract 59
3.2 Introduction 60
3.3 Materials and methods 61
3.3.1 Wilson-Cowan Model 61
3.3.2 Data Collection 63
3.3.3 Fitting Process 66
3.3.4 Providing Stimulation and Entrainment Analysis in the Model 69
3.3.5 Entrainment Analysis of the ECoG Recordings 70
3.3.6 Correspondence Between Stimulation Amplitude in the Model and in the Data 71
3.4 Results 71
3.4.1 Prediction of 1:2 Entrainment of FTG Using a Fitted Wilson-Cowan Model 72
3.4.2 Validation of Model Predictions in Human Patient During Chronic Therapeutic Stimulation 73
3.5 Discussion 76
3.5.1 Entrainment and adaptive DBS 77
3.5.2 Entrainment in the Wilson-Cowan Model 77
3.5.3 Limitations 82
3.5.4 Implications 84

3.6 Conclusion 84

3.1 Abstract

The exact mechanisms of DBS are still an active area of investigation, in spite of its clinical successes. This is due in part to the lack of understanding of the effects of stimulation on neuronal rhythms. Entrainment of brain oscillations has been hypothesised as a potential mechanism of neuromodulation. A better understanding of entrainment might further inform existing methods of continuous DBS and help refine algorithms for adaptive methods. The purpose of this chapter is to develop and test a theoretical framework to predict entrainment of cortical rhythms to DBS across a wide range of stimulation parameters. We fit a model of interacting neural populations to selected features characterising PD patients' off-stimulation finely-tuned gamma rhythm recorded through electrocorticography. Using the fitted models, we predict basal ganglia DBS parameters that would result in 1:2 entrainment, a special case of sub-harmonic entrainment observed in patients and predicted by theory. We show that the neural circuit models fitted to patient data exhibit 1:2 entrainment when stimulation is provided across a range of stimulation parameters. Furthermore, we verify key features of the region of 1:2 entrainment in the stimulation frequency/amplitude space with follow-up recordings from the same patients, such as the loss of 1:2 entrainment above certain stimulation amplitudes. Our results reveal that continuous, constant frequency DBS in patients may lead to nonlinear patterns of neuronal entrainment across stimulation parameters, and that these responses can be predicted by modelling. Should entrainment prove to be an important mechanism of therapeutic stimulation, our modelling framework may reduce the parameter space that clinicians must consider when programming devices for optimal benefit.

3.2 Introduction

Building on the established physiological origin of 1:2 FTG entrainment from Chapter 2, in this chapter we predict the response of entrained motocortical FTG at variable DBS parameters. As is demonstrated by the need to confirm the physiological origin of 1:2 entrained FTG and as mentioned in Chapter 2, the field has been rightly cautious to interpret sub-harmonic activity in response to DBS. As a result of this, there were previously no studies that explored sub-harmonic entrainment or the underlying mechanisms of this activity. In this chapter, we aim to address this in the specific context of 1:2 entrained motocortical FTG in PD to DBS. We introduce FTG oscillations in Section 1.2.2.3 as well as the important differentiating factors to broadband gamma.

As discussed in Section 1.2.4.2, entrainment of broadband gamma and FTG rhythms has been observed or is believed to have been a primary mechanism behind clinically significant neuromodulation investigations. Examples include transcranial alternating current stimulation (tACS) at gamma frequency, which was observed to increase motor velocity in PD. It was hypothesised that entrainment (specifically 1:1 entrainment at stimulation frequency, as depicted in Fig 1.1B) of gamma oscillations would explain this observation by enhancing the prokinetic rhythm. Additionally, a shifted FTG peak frequency has been noted in the motor cortex in response to high-frequency DBS of the STN (Swann et al. 2016; Swann et al. 2018a; Gilron et al. 2021). The gamma peak, off-stimulation between 65 and 80Hz, locks to the half harmonic of stimulation (see Fig 1.1), corresponding to 1:2 entrainment. We are confident that 1:2 FTG entrainment represents a physiological response to stimulation from the work in Chapter 2. More recently, the modulation of 1:2 entrained FTG was demonstrated to be the strongest predictor of prokinetic state in an aDBS algorithm for PD (Oehrn et al. 2023). Together, these studies suggest that the entrainment of FTG by DBS could play a role in ameliorating PD-associated motor symptoms. Moreover, the half harmonic lock indicates that the response to stimulation is complex and goes beyond entraining rhythms solely at the frequency of stimulation or suppressing them. However, there is currently no theoretical understanding of 1:2

gamma entrainment in PD and generally no framework to predict the occurrence of specific entrainment regimes in response to brain stimulation.

In this chapter, we use a model-based approach that utilises chronic invasive cortical recordings in PD patients to predict the properties of entrainment of cortical activity by basal ganglia DBS. We postulate that by constraining the parameters of a neuronal population model, it will be possible to predict stimulation parameters that lead to 1:2 gamma entrainment for patients with off-stimulation (medication induced) FTG. We provide a theoretical introduction to 1:2 gamma entrainment through the concepts of Arnold tongues (regions of entrainment in the stimulation frequency and amplitude space) and rotation number (the ratio of the average number of oscillation cycles to stimulation pulses). We proceed to develop a patient-specific approach by fitting a model representing interacting neural populations, the Wilson-Cowan model, to features of invasive chronic electrocorticography (ECoG) data recorded off stimulation from patients with PD. Using the fitted-models, we predict the regions of 1:2 entrainment in the stimulation parameter (frequency and amplitude) space. We proceed to verify key features of the 1:2 entrainment regions with follow-up recordings from the same patients. Lastly, these results are discussed and the implications are highlighted for future stimulation therapies.

3.3 Materials and methods

3.3.1 Wilson-Cowan Model

As introduced in Section 1.2.6.2, the Wilson-Cowan model is a mean-field model describing interacting neuronal populations (Wilson and Cowan 1972; Cowan et al. 2016) and, hence, is a natural choice to represent off-stimulation ECoG recordings and predict 1:2 gamma entrainment. While the sine circle map (see Section 1.2.6.1), a simpler model, can provide a first level description of 1:2 gamma entrainment (see Appendix A.4), it only represents a single neural oscillator and cannot fit population-level brain recordings.

We use the two-population Wilson-Cowan model to represent excitatory and inhibitory cortical populations with reciprocal connections (see Fig 3.1). We do

not include subcortical populations in this model and assume that subcortical stimulation is transmitted unperturbed to the cortex. We use the Wilson-Cowan model to predict the interactions of two groups of cortical neurons, excitatory (E) and inhibitory population (I). The stochastic differential equations (adapted from Eq (1.3) in section 1.2.6.2 to include stimulation) describe the evolution of the cortical population activities as

$$\begin{aligned} dE &= \frac{1}{\tau_E}(-E + f(\eta_E + \omega_{EE}E - \omega_{IE}I))dt + \zeta dW_E, \\ dI &= \frac{1}{\tau_I}(-I + f(\eta_I + \omega_{EI}E) + A_{stim}(t))dt + \zeta dW_I, \\ f(x) &= \frac{1}{1 + e^{-b(x-1)}}. \end{aligned} \tag{3.1}$$

As defined in Section 1.2.6.2, the coupling strength weights are denoted ω_{PQ} (going from population P to population Q). The interactions between populations are processed through a sigmoid function, f, of steepness coefficient b. τ_E and τ_I represent the time constants of the corresponding populations, and η_E and η_I are the constant inputs to their respective populations. Wiener processes, W_E and W_I, introduce stochasticity to the model with a noise standard deviation denoted by ζ. Noise is required to reproduce the off-stimulation data, which is characterised by bursts of activity rather than perfectly periodic dynamics (see Fig 3.4D).

It is unclear whether the effect of subcortical stimulation on the motor cortex is excitatory or inhibitory (more details Section 3.5). In this chapter of the cortical response, we model the effect as inhibitory by applying periodic high-frequency stimulation, $A_{stim}(t)$, to the inhibitory population, while the ECoG local field potential (LFP) is modelled as the activity of the excitatory population. However, we also verify in Appendix A.5.5 that our results hold for stimulation applied to the excitatory population and ECoG LFP obtained as the activity of the inhibitory population. Additionally, stimulation is applied directly to the inhibitory population, not through the sigmoid function, as this provides a greater wealth of dynamics by avoiding saturation effects (Duchet et al. 2020).

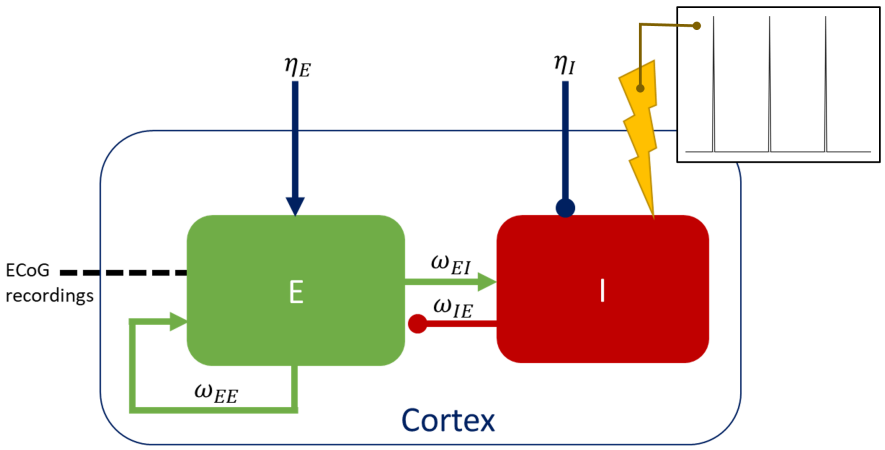


Figure 3.1: The two-population Wilson-Cowan model. Stimulation is applied to the inhibitory population (I) and data recorded from the excitatory population (E). The weights of the three connections present in this model are ω_{EI} (excitatory connection from E to I), ω_{IE} (inhibitory connection from I to E), and ω_{EE} (self-excitatory connection from E to E). Additionally, there are external inputs, η_E and η_I, to each population. The insert displays the single time step stimulation pulse with no recharge used throughout this chapter (pulses with different active recharge durations, and with passive recharge are considered in Appendix A.5.2).

3.3.2 Data Collection

Human neural data were collected from three patients with PD (Table 3.1). Cortical data off-stimulation were collected to fit the Wilson-Cowan model. On-stimulation data (subcortical stimulation) at variable stimulation frequencies and amplitudes were then used to validate predictions from the fitted model. Patient clinical symptoms assessed 90 days pre-operation are summarised in Appendix Table A.2.

Patients were selected for participation in this study based on the presence of a peak in gamma band activity in the primary motor cortex off-stimulation (which is a necessary condition to fit a model to off-stimulation gamma activity). Patients were diagnosed with idiopathic PD by a movement disorders neurologist and underwent DBS surgery of either the subthalamic nucleus (STN) or globus pallidus (GP). Target choice was based on the patients' neuropsychological test results, which indicated pallidal implantation for patients with mild cognitive impairment or history of clinical depression (Okun et al. 2009; Follett et al. 2010). Patients were bilaterally implanted with the Medtronic Summit RC+S bidirectional

Table 3.1: Patient information summary. LEDD: Levodopa equivalent daily dose, UPDRS: Movement Disorders Society Unified Parkinson's Disease Rating Scale, UPDRS (off-on): percent change off vs on medication, STN: subthalamic nucleus. "Time of charting" refers to on-stimulation data collection to test model predictions. *RCS18s right lead was deactivated during testing since it was recently reimplanted and undergoing clinical optimisation.

Patient	RCS02	RCS10	RCS18
Age (years)	54	64	67
Disease Duration (years)	7	13	7
Gender	M	F	M
LEDD (mg/day)	1425	1083	2031
UPDRS-III off-med	49	89	49
UPDRS (off-on)	90%	53%	76%
DBS Target	STN	Pallidum	STN
Duration of chronic DBS prior to collection of entrainment data (months)	30	10	7
Clinical Stimulation Settings	R: 1-C+, 2.6 mA, 60 us, 130 Hz L: 2-C+, 2.4 mA, 60 us, 130 Hz	R: 1-2-C+, 5.0 mA, 90 us, 150 Hz L: 2-C+, 5.0 mA, 90 us, 150 Hz	R: 2-C+, 2.3 mA, 60 us, 130 Hz L: 2-C+, 2.4 mA, 60 us, 130 Hz
Titration Ranges	R/L: Freq.: 110-170 Hz, Amp.: 0.7-3.1 mA	R/L: Freq.: 130-150 Hz, Amp.: 0-6.5 mA	R: OFF* L: Freq.: 40-180 Hz, Amp.: 0.9-4.3 mA

neural interface (clinicaltrials.gov identifier NCT03582891, USA FDA investigational device exemption number 180097, IRB number 18-24454) quadripolar cylindrical leads into subcortical nuclei (Medtronic model 3389 or 3387 for STN and pallidum, respectively), and subdural paddle-type leads over the primary motor cortex in the subdural space (Medtronic model 0913025), see Figs 3.2A1-3 for RCS02, Figs 3.2B1-3 for RCS10 and Figs 3.2C1-2 for RCS18. Implantations of subcortical leads were performed using frame-based stereotaxy and confirmed by intraoperative cone beam

CT and microelectrode recording (MER) in the awake state using standard methods in RCS02 and RCS10 (Starr 2002), and by intraoperative cone-beam CT alone in RCS18 (Shahlaie et al. 2011). For RCS10, the active contact array was localised in the GP using MER mapping of single-unit cells to traverse the postero-lateral regions of the external globus pallidus (GPe) and globus pallidus internus (GPi), Fig 3.2B1. For RCS02, the motor territory of the STN was confirmed by eliciting movement-related single-cell discharge patterns during MER when the DBS lead was placed with the middle two contacts in dorsal STN. Surgical placement of subdural cortical paddles has been previously described in detail (Swann et al. 2018b). Similar to subcortical contacts, localisation of subdural paddles was confirmed by computationally fusing a postoperative CT scan to the preoperative planning MRI scan, Figs 3.2B1-3, A2-3 and C1-2.

Prior to the initiation of standard therapeutic DBS, we recorded four-channel LFPs of the cortical, and pallidal (n=1) or subthalamic (n=2) sites of each hemisphere between two- and four-weeks post implantation. The data were streamed from patients during normal activities of daily living and while on their schedule of antiparkinsonian medication. Only the cortical prestimulation data were used to fit the Wilson-Cowan model. The recording methods and data processing were similar to those described in (Gilron et al. 2021). Briefly, neural data were recorded from subcortical (STN or GP, as per patient's DBS target; Fig 3.2A1, B2, C1) and cortical (contact pairs 11-9 and 10-8 for RCS02, Fig 3.2A2-3; 11-10 and 9-8 for RCS10 and RCS18, Fig 3.2B3, C2) sensing electrodes via a patient-facing graphical user interface application. Neural data were collected at 250 Hz. The Summit RC+S has two onboard filters applied after digitisation that were set to a high pass of 0.85 Hz and a low pass of 450 Hz before amplification followed by 1700 Hz low pass filter after amplification.

After several months of continuous subthalamic (n=2) or pallidal (n=1) stimulation at clinically optimised parameters, we conducted a follow-up in-clinic recording session with each subject in their on-medication state to validate the initial model predictions. During recordings, we cycled through a range of stimulation frequencies

and amplitudes to further explore the DBS parameter space (Table 3.1). In each participant, we delivered stimulation at their clinical contact in the STN or GP, while recording from cortical sensing contacts 11-10 and 9-8. In each trial, we tested a single frequency-amplitude combination for 30 seconds while the patient was at rest. Sessions lasted two to three hours, and the number of data points collected was different in each patient due to patient fatigue. While it is not clear if fatigue plays into 1:2 entrainment, the testing order of stimulation parameters was not predetermined, making the point at which each tongue boundary was tested effectively random. In particular, the top tongue boundaries were not tested only later in the sessions when we would expect fatigue to be higher. It should also be acknowledged that non-stationary medication levels, associated with intermittent medication intake, could affect 1:2 entrainment at certain stimulation parameters. Filter settings for cortical contacts were the same as during off-stimulation recordings.

3.3.3 Fitting Process

To fit the parameters of our Wilson-Cowan model to prestimulation cortical FTG, we processed the off-stimulation cortical recordings (over three hours for each subject, collected between two- and four-weeks post implantation) to obtain data features for each patient. We separated the off-stimulation sessions into epochs with a minimum of 30 seconds of continuous and uninterrupted recordings. Longer uninterrupted recordings were not consistently available in some of the patients due to packet losses during streaming. However, 30-second epochs were sufficient to capture stable FTG properties. For the fitting process, we only used one epoch for each patient which was selected by identifying the epoch with the most prominent cortical gamma peak (to maximise signal-to-noise ratio) within the frequency range ±3Hz of the approximate average peak gamma frequency of the overall dataset, i.e. 75Hz for RCS02 and RCS10, 78Hz for RCS18 (the ±3Hz frequency range captured all variation in off-stimulation FTG frequencies in each dataset). From this epoch, the signal was band-passed between ±3Hz of the gamma peak (the

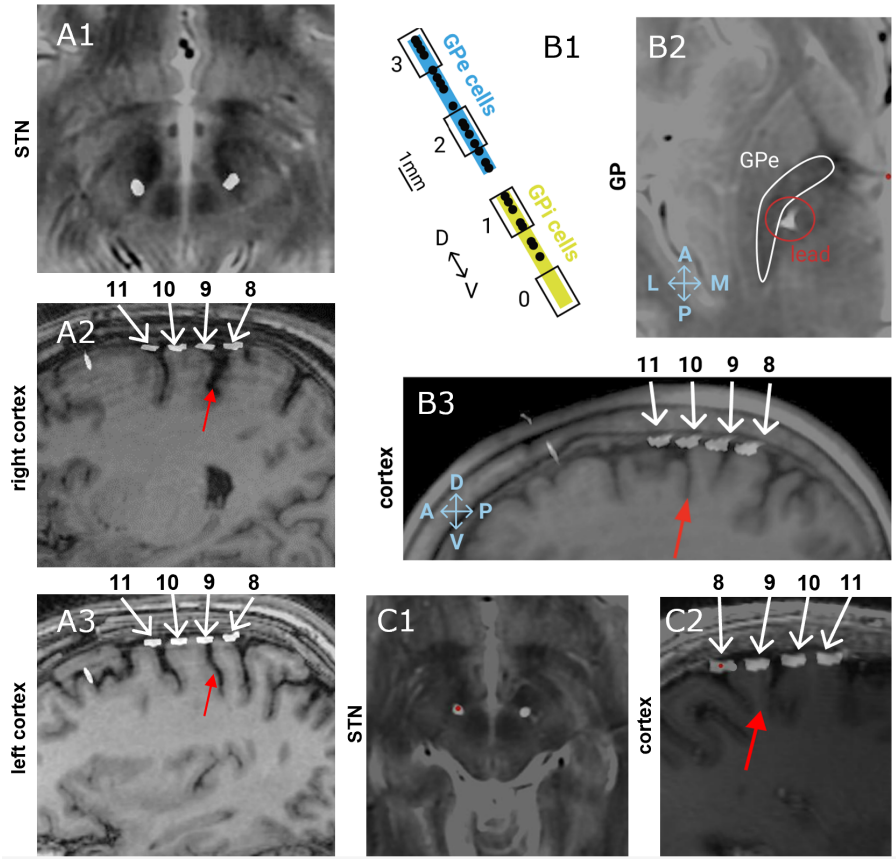


Figure 3.2: Contact localisation across the three subjects. The patients are presented as RCS02 (A1-3), RCS10 (B1-3) and RCS18 (C1 and 2). (A1-3, B2-3, C1-2) Localisation of contacts with a postoperative CT scan that is computationally fused with the preoperative planning MRI scan.(A1 and C1) subthalamic nucleus (STN) lead on a T2-weighted MRI scan. In C1, the red dot indicates the left STN lead. (A2-3, B3, C2) Quadripolar subdural paddle lead on sagittal T1-weighted MRI shows the relationship between the central sulcus (red arrow) and contacts (white numbered arrows). For RCS10 (A2-3) and RCS18 (C2), contacts 11 and 10 were both over the pre-central gyrus whereas contact 9 was on the post-central. RCS02 (B3) was implanted slightly more anteriorly and contacts 9 and 10 were on the pre-central gyrus and 11 on the superior frontal gyrus. (B1) globus pallidus (GP) contact localisation (black numbered rectangles) with respect to the boundaries of the internal globus pallidus (GPi) (yellow) and external globus pallidus (GPe) (blue) as defined by micro-electrode recording mapping of single-unit cells (black dots). (B2) GP lead on an axial T2-weighted MRI, which visualises the GP as regions of T2 hypointensity (GPe highlighted by a white contour).

band-pass width was chosen to capture the whole width of the FTG peak). Three features were selected for the purposes of fitting the model to each patient: the power spectral density (PSD) of the cortical FTG signal, its envelope PSD, and its envelope probability density function (PDF). These features are shown for RCS10 in Fig 3.3A1-3, and for RCS02 and RCS18 in Appendix Fig A.2. The envelope

is the modulus of the analytical signal of the band-passed recording and refers to a curve that traces the upper bound of the signal, providing a measure of the oscillation's amplitude. The envelope PDF represents the distribution of the values of the envelope over the duration of the signal. These features were selected to provide a representation of the signal and its envelope in the frequency domain, as well as a representation of the statistics of the envelope in the time domain. We demonstrate in Appendix A.1.1 that there is little correlation between the three features mentioned here, and that all three features are required to capture the full dynamics of the data. Fitting to off-stimulation features ensured that any presence of 1:2 entrainment is not predetermined, as could have been the case if fitting to on-stimulation data. The bipolar contact pairs used for fitting were 11-9 in RCS02, and 11-10 in RCS10 and RCS18. In all cases, at least one of the contacts was localised over the pre-central gyrus (see Fig 3.2A2, A3, B3, and C2). Contact pairs were selected for the fitting process of each patient by which pairs had the most consistent gamma power over time.

Model parameters were then optimised to best match the selected cortical FTG data features (Fig 3.3A1-3). This process follows a fitting methodology similar to Duchet et al. 2020; Duchet et al. 2021, repeated for each patient. It begins by generating random sets of parameters, and selecting parameter sets with a PSD broadly similar to that of the data (the first loop of Fig 3.3B), i.e. with a gamma peak between 70 to 80Hz. This improves the computational efficiency of the parameter fitting. Accepted parameters enter an optimisation loop (the second loop of Fig 3.3B) using the patternsearch function of Matlab2020b, which minimises the cost function capturing the distance between model and data features (see Appendix A.1.2). We run this optimisation to obtain approximately 2500 parameter sets fitted to the 30 seconds of off-stimulation cortical data, each corresponding to a different local minimum of the cost function. From the resulting fits, we select the 20 with the greatest R^2 values and perform further simulations to refine the ranking of the fits (the third loop of Fig 3.3B), more details can be found in Appendix A.1.3. The top-ranked fit is then selected based on these simulations. We do not expect

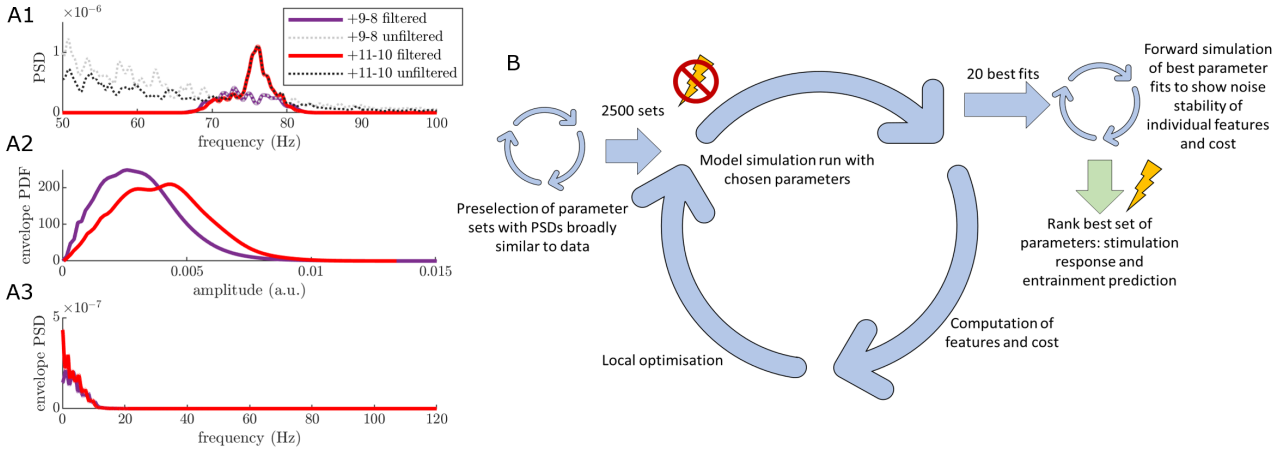


Figure 3.3: Use of prestimulation human cortical recordings to fit Wilson-Cowan model parameters. (A1-3) The three data features from RCS10 off-stimulation cortical recordings: power spectral density (PSD) (A1), envelope probability density function (PDF) (A2) and envelope PSD (A3), for the selected epoch, based on the gamma peak height in the cortical 9-8 and 11-10 contact pairs. The features shown are from the cortical contacts as labelled in 3.2B3. The solid red and purple lines display the band-pass filtered cortical signals between 72Hz and 78Hz, as the peak occurred at 75Hz for this patient. The black and grey dotted line in the PSD plot show the unfiltered signal which, for the 11-10 contact pair, still displays the FTG peak seen in the filtered data. The fitting is based off the filtered data from the 11-10 contact pair. (B) The optimisation pathway for fitting the model to off-stimulation data. This process is broken down into three main loops, as discussed in Section 3.3.3. Once a fitted set of model parameters is obtained, we are able to make predictions for the neuronal population responses in the on-stimulation state.

overfitting to be an issue given that we are fitting to off-stimulation data, where there is no entrainment in the signal. Predictions of the response to external stimuli are then made by introducing stimulation to the off-stimulation fitted model.

3.3.4 Providing Stimulation and Entrainment Analysis in the Model

We obtain entrainment predictions in the model (i.e. Arnold tongues, in particular the 1:2 Arnold tongue) by providing high-frequency DBS at variable stimulation amplitudes and frequencies. The stimulation pulse provided throughout the majority of the modelling work in this chapter, unless mentioned otherwise, is a single time step positive pulse with no recharge (see the insert in Fig 3.1). This stimulation pulse was chosen for simplicity. Different recharge lengths and stimulation waveforms

are explored in Appendices A.5.2 and A.5.3. Stimulation is introduced in the model as described in Section 3.3.1.

In the presence of stimulation, entrainment is assessed in the model by computing the rotation number using Eq (1.1) where θ_i is taken as the unwrapped Hilbert phase of the excitatory population activity after i stimulation pulses. This was calculated over 50 stimulation cycles and averaged over five repeats at each stimulation parameter. To compare with data, the PSD of the model output with stimulation applied was calculated using Welch's PSD estimate over the same number of stimulation cycles and repeats as the rotation number. The peak PSD was calculated as the maximum power in the 0 to 200Hz frequency range.

3.3.5 Entrainment Analysis of the ECoG Recordings

Entrainment of cortical FTG to DBS was assessed in the data using a spectral method since the rotation number cannot be reliably computed in the data. The PSD of the data (from the bipolar recordings based on cortical contacts 11-9 in RCS02 and cortical contacts 11-10 in RCS10 and RCS18) was calculated in a similar way to that of the model, using Welch's PSD estimate. Only frequencies recorded within the 40 to 120Hz range were considered when computing the peak power. To determine whether each set of stimulation parameters achieved entrainment we first determined the approximate PSD slope on stimulation by averaging the PSD in the ranges $[f_s/2 - 10, f_s/2 - 5]$ and $[f_s/2 + 5, f_s/2 + 10]$, where f_s denotes stimulation frequency. These ranges were chosen to avoid spectral changes around the half harmonic. The signal was then determined to be showing 1:2 entrainment if the height of the PSD at half the stimulation frequency was over three times greater than the approximated baseline expected from the measured slope. This placed the threshold over any variation due to noise. The threshold was chosen such that there was very little variation in the results when increasing it and it provided a conservative assessment of entrainment (less likely to lead to spurious entrainment than a lower threshold such as three standard deviations of the noise).

3.3.6 Correspondence Between Stimulation Amplitude in the Model and in the Data

While the stimulation frequency unit is the same in the model and the data (Hz), the stimulation amplitude unit is arbitrary in the model. To correlate peak PSD predictions in the model and the data, it is therefore a pre-requisite to establish a correspondence between stimulation amplitude in the model and in the data. This was done by selecting the scaling of the model stimulation amplitude axis that maximised the correlation of peak PSD of 1:2 entrained points (as assessed in the data) between the data and the model (grid search over a linear scale).

Optimising the scaling of the model stimulation amplitude introduces an additional free parameter which needs to be accounted for in statistical analyses. For each patient, significance of the correlation between peak PSD predictions in the model and the data is therefore assessed using an approximation of the distribution of correlation coefficients under the null hypothesis (no correlation) obtained from 10,000 permutations. For each patient, we randomly reassign PSDs from the data to the different stimulation parameters used. Each permutation is then compared against model PSD predictions and the scaling is optimised to maximise the correlation between the peak PSD at the half harmonic of stimulation frequency between the model and the data, as outlined above. Only permutations which resulted in at least five 1:2 entrained results from the model simulations were accepted. This was to avoid spurious correlations in the surrogate distribution that would result from a very low number of datapoints. Placing the threshold at five is also conservative as all patient datasets have more than five entrained points. P-values are then calculated using the resulting (approximately) normal distribution of correlation coefficients.

3.4 Results

We fitted the Wilson-Cowan model, a model of interacting neuronal populations, to prestimulation ECoG recordings in three patients with PD. Using the fitted models, we predicted for each patient the stimulation parameters leading to 1:2

entrainment of FTG. We then verified these predictions in follow-up on-stimulation recordings from the same patients.

3.4.1 Prediction of 1:2 Entrainment of FTG Using a Fitted Wilson-Cowan Model

For all patients, the Wilson-Cowan model fitted to the patient's prestimulation cortical FTG successfully reproduced all three FTG features. The top ranked model parameter sets (Appendix Table A.1) had average R^2 values (across 50 simulations) of 0.961, 0.944 and 0.868 for RCS02, RCS10 and RCS18 respectively, with good or satisfactory fits across all three features (Fig 3.4 for RCS10, and in Appendix Fig A.3 for RCS02 and RCS18). The fitted models oscillate at the patient's FTG natural frequency (between 75-80Hz in the absence of stimulation), as seen in Fig 3.4A for RCS10, and Appendix Fig A.3A1 and B1 for RCS02 and RCS18.

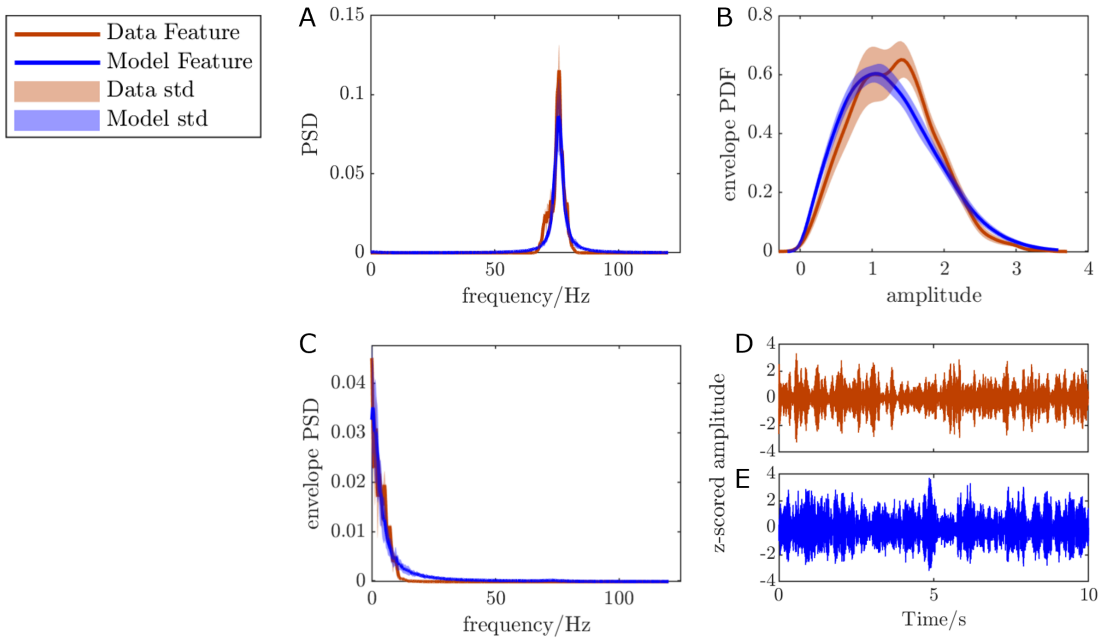


Figure 3.4: Comparison of the cortical FTG features from z-scored data and the features from z-scored model output of the best ranked model parameter set for RCS10. $R^2 = 0.944$ on average across 50 simulations lasting 100 seconds each. The model closely matches the data PSD (A), envelope PDF (B), and envelope PSD (C). (D-E) Comparison of the band-passed off-stimulation time series from patient data (D) and model output (E) show that the model is capable of replicating similar time-domain dynamics. In all panels, the data is in red, and the model in blue.

In the presence of low amplitude stimulation, all three models display a 1:2 Arnold tongue (i.e. entrainment region) around a stimulation frequency between 150-160Hz (the 1:2 tongue stems from twice the natural frequency of the model). This is shown by the green 1:2 Arnold tongue in Figs 3.5A, D and G, which correspond to a region of 1:2 entrainment (constant rotation number of 0.5). The 1:2 Arnold tongue is bordered by a larger zone of 1:1 entrainment, indicated by the red regions. When stimulation is provided at 130Hz (indicated by the black line), the excitatory population can be entrained at 65Hz for a range of stimulation amplitudes. In all three fitted models, the 1:2 tongue is left leaning (more of the tongue is to the left of the frequency it stems from, see Figs 3.5A, D and G), which suggests that stimulation frequencies lower than the stem of the tongue are more likely to lead to 1:2 entrainment. The range of stimulation frequencies that can give rise to 1:2 entrainment (given an appropriate stimulation amplitude) is the narrowest in RCS02 (110-160Hz), and the broadest in RCS18 (60-160Hz). In all cases, we note that increasing stimulation amplitude above a certain value will result in the loss of 1:2 entrainment.

The left lean of the 1:2 Arnold tongues does not depend on whether stimulation is applied to the inhibitory population or the excitatory population (see Appendix A.5.5). Additionally, the 1:2 entrainment region exhibits a left lean regardless of whether the stimulation being applied is in the form of a single time step pulse train, pulse trains with various recharge durations or more complicated waveforms (see Appendices A.5.2 and A.5.3).

Additionally, the fitted Wilson-Cowan models predict that the highest spectral peaks will occur at the lowest frequencies for which 1:2 entrainment arises, as seen in Figs 3.5B, E and H.

3.4.2 Validation of Model Predictions in Human Patient During Chronic Therapeutic Stimulation

The presence of 1:2 entrainment at variable stimulation parameters was investigated in follow-up recordings for the same patients as the Wilson-Cowan model was

fitted to (see recording details in Section 3.3.2). These data were only examined following the core predictions from the model.

Left lean of the 1:2 tongue, and loss of entrainment for large stimulation amplitudes. For all three patients, the data show regions of stimulation parameters for which 1:2 entrainment can be observed (Figs 3.5C, F and I), and these Arnold tongues appear to exhibit overall similar shapes to the Wilson-Cowan model predictions (shown in Figs 3.5A, D and G). For RCS10, while 1:2 entrainment was seen for amplitudes greater than 5.5mA for 140 and 130Hz, it was lost for 150Hz (Fig 3.5F). This is a robust observation as three repeats lead to the same outcome for this particular combination of stimulation parameters (150Hz, 5.5mA, labelled 2 in Fig 3.5F). Hence, the 1:2 tongue has a left lean in this set of data with 1:2 entrainment being maintained at higher amplitudes for lower frequencies of stimulation, which is also the case in the model (Fig 3.5D). RCS18 also exhibits a left-leaning 1:2 tongue. There is no 1:2 entrainment at 2mA for stimulation frequencies above 150Hz, however, in the range of 50-140Hz we can see 1:2 entrainment up to 4mA (Fig 3.5I). This forms part of the top boundary of the 1:2 Arnold tongue. Additionally, there is a boundary to the right of the 1:2 tongue where no entrainment is seen for any amplitude with stimulation frequencies greater than 155Hz. We are also able to see loss of entrainment on the lower left boundary from 50-150Hz to further demonstrate the left lean. The corresponding model also predicts 1:2 entrainment down to 60Hz in Fig 3.5G, which is not seen in all other model predictions and is further supported by the data (Fig 3.5I). Due to patient fatigue, we were unable to chart the right boundary of the 1:2 tongue in RCS02 (Fig 3.5C). Hence, we are unable to determine if this patient does exhibit a left lean from their data. However, the 1:2 tongue of the model prediction for RCS02 (Fig 3.5A) is smaller than the other model predictions, with a significantly lower top boundary (stimulation amplitude at which 1:2 entrainment is lost, around 3.5mA). This can also be seen in the corresponding data (Fig 3.5C).

Change in entrained gamma power with stimulation frequency and amplitude. Overall, the data validate the model's prediction of highest power for the lower frequencies within the 1:2 tongue. In RCS10, changing stimulation parameters from 130Hz, 6.5mA to 150Hz, 5mA results in a drop in entrained peak power, as indicated by the colourscale in Fig 3.5F. The increase in PSD with decreasing stimulation frequency ($p < 1\times10^{-4}$, Fig 3.6C) and increasing stimulation amplitude ($p < 0.05$, Fig 3.6D) are statistically significant. RCS18 also displays a statistically significant increase in entrained peak power as stimulation frequency is decreased ($p < 0.001$, Fig 3.6E) and stimulation amplitude is increased ($p < 1\times10^{-9}$, Fig 3.6F). Power changes with stimulation parameters do not show statistically significant trends within the 1:2 tongue in RCS02 (Figs 3.6A-B). The increase in entrained peak power with decreasing stimulation frequency in RCS10 and RCS18 is in agreement with model predictions. The increase in entrained peak power with increasing stimulation amplitude is also consistent in the data and the model across the 1:2 tongue, but the relationship reverses in the model when controlling for stimulation frequency (see Fig 3.5B, E, and H). This is likely to also be the case in the data, although there are not enough data points to run a statistical analysis for RCS10.

Comparing model predictions of entrained peak power to data provides further support for the models fitted to RCS10 and RCS18 (Fig 3.7). The correspondence between stimulation amplitude in the model (arbitrary units) and in the data (mA) was established as described in Section 3.3.6. In Fig 3.7, green points indicate stimulation parameters resulting in 1:2 entrainment in both model and data (where the tongues overlap). This choice is the most natural to study the relationship between entrained peak power in the model and the data. Black points indicate stimulation parameters that are inside the data 1:2 tongue, but outside the model 1:2 tongue, and thus have an entrained PSD power in the model of very close to zero. This analysis mixes power prediction with tongue shape prediction, but is more conservative which is why we are presenting both results. There is a significant correlation between data and model predictions for RCS10 ($p < 1\times10^{-3}$,

Fig 3.7B) regardless of whether the model predictions produce 1:2 entrainment or not. RCS18 had a significant correlation for model results that resulted in 1:2 entrainment ($p < 0.05$, Fig 3.7C), but not for all model predictions. This is due to some stimulation parameters causing 1:2 entrainment far from the natural FTG frequency falling outside of the model 1:2 tongue, where there is a lower PSD (collection of black points in Fig 3.7C where the model PSD prediction is close to zero). While there were no significant correlations between model and data entrained peak power in RCS02 (Figs 3.7A-B), the lack of correlation may be explained by a stronger impact on entrainment of fluctuations in the endogenous FTG in this patient (more details in the discussion).

3.5 Discussion

Here, we studied entrainment of cortical FTG by basal ganglia deep brain stimulation, using a computational model in conjunction with sensorimotor cortex ECoG sensed from chronically implanted bidirectional interfaces in three patients with PD. We show that through fitting a model of interacting neuronal populations to off-stimulation data, we are able to predict the region of stimulation parameters (frequency and amplitude) for which 1:2 entrainment is possible. In particular, our model predicts that 1:2 entrainment is lost when stimulation amplitude is increased above a certain value. Furthermore, the 1:2 Arnold tongue is generally left leaning, implying that 1:2 entrainment can be achieved for stimulation frequencies markedly lower than twice the frequency of the natural gamma rhythm, but not for frequencies markedly higher. Lastly, the model further predicts that there would be a greater entrained gamma power at lower stimulation frequencies that result in 1:2 entrainment. Data recorded during therapeutic neurostimulation, after the modelling results were obtained, showed 1:2 Arnold tongues that generally validate these predictions. Hence, the model can capture a range of sub-harmonic entrainment features without being constrained by entrainment data. The work indicates that effects of DBS at clinically relevant stimulation parameters can be understood using

the conceptual framework of a mathematical model representing interacting neural populations being externally perturbed by the periodic neurostimulation.

3.5.1 Entrainment and adaptive DBS

By solely analysing the presence of 1:2 entrainment, we avoid the prominent artefact at stimulation frequency. Hence, this analysis of the data provides a valuable insight into the neuronal responses to stimulation. Bounding the 1:2 tongue from above, as we lose 1:2 entrainment at increased stimulation amplitudes (all three patients at 150Hz), which provides further evidence that the gamma peak at half stimulation frequency is unlikely to be artefactual. This is aligned with the model prediction that 1:2 entrainment will be lost when amplitude is increased beyond a certain point. Additionally, the model predicts that parameter changes that result in the loss of 1:2 entrainment would see a transition to 1:1 entrainment. However, the presence of 1:1 entrainment is difficult to assess as the resulting power spectral peak can be masked by the stimulation artefact.

Given the results of Chapter 2 that demonstrate FTG 1:2 entrainment is not an artefact, it presents opportunities for aDBS. As mentioned in Section 1.2.3.3, aDBS relies on a closed-loop control policy where a biomarker is used to adjust DBS parameters. Cortical FTG activity was shown to be a promising candidate biomarker for aDBS (Swann et al. 2016; Gilron et al. 2021; Oehrn et al. 2023). Additionally, entrainment in the gamma frequency band has been linked with medications state and dyskinesia (as discussed in Section 2.4.1 and Swann et al. 2016). Moreover, 1:2 entrainment has an entirely predictable frequency, which simplifies implementation, particularly for chronic devices with limited spectral recording frequency bands (such as the Medtronic Percept).

3.5.2 Entrainment in the Wilson-Cowan Model

1:2 entrainment is not an intrinsic property of the Wilson-Cowan model (large regions of parameter space do not lead to 1:2 entrainment). Additionally, if the parameters of the Wilson-Cowan model do produce 1:2 entrainment, the 1:2 tongue

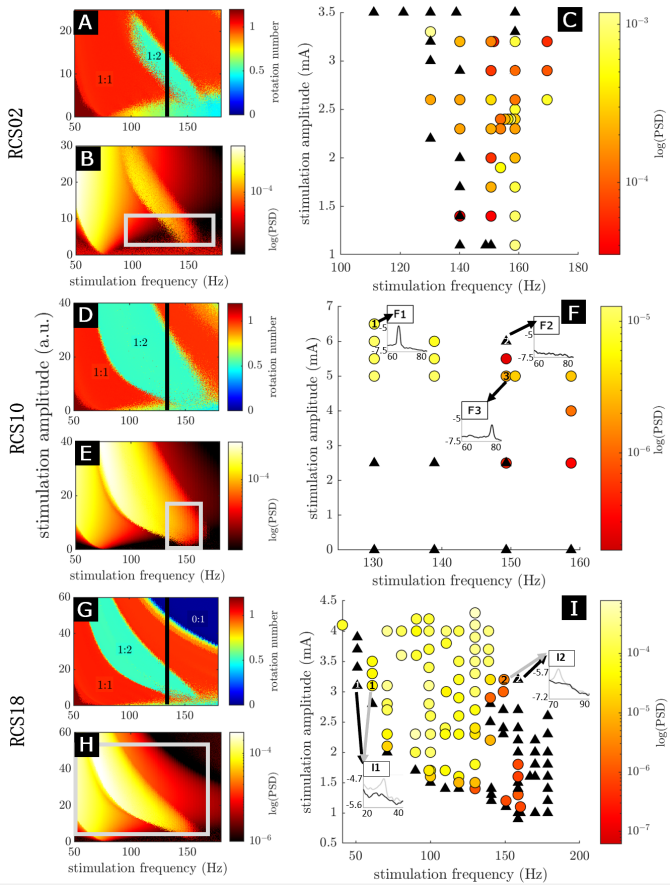


Figure 3.5: Testing model predictions of a cortical circuit's response to an external stimulus using human neural data during neurostimulation. Stimulation frequency is the horizontal axis for all panels, while stimulation amplitude is the vertical axis for all panels. Stimulation amplitude has arbitrary units (a.u.) for all model panels (A, B, D, E, G, and H) and is in mA for the data panels (C, F and I). Panels A-C are for RCS02, D-F for RCS10 and G-I for RCS18. Panels A, D and G have colour scales indicating the rotation number (as explained in Section 1.2.4.1) resulting from the stimulation parameters at that point, where 1:1 entrainment is in red and 1:2 entrainment is in green. For these panels, the black line indicates the 130Hz stimulation condition used in (Swann et al. 2016; Swann et al. 2018a). (A, D, G) The entrainment field of the Wilson-Cowan model with the top ranked parameters. The stimulation applied is a single time step pulse with no recharge. (B, E, H) The maximum height of the entrained peaks as predicted by the top-ranked Wilson-Cowan model fit, calculated as laid out in Section 3.3.4. The grey rectangles indicate comparable stimulation parameter ranges to those used in the variable stimulation response data, with stimulation amplitude scaling calculated as outlined in Section 3.3.6. (C, F, I) The height of entrained peaks obtained from patient recordings for a series of different stimulation parameters. Circles display peak height (represented by the colour scale) of parameters that displayed entrainment (as seen e.g. in inserts F1-2) , while black triangles are for parameters that did not display entrainment (as seen e.g. in insert F2). The occurrence of both a black triangle and a circle at the point (140Hz, 1.4mA) in panel C and point (150Hz, 2.5mA) in panel F indicate intermittent entrainment, hence, this will likely be on the boundary of the tongue. Inserts F1-3 and I1-2 show the logarithm of PSDs over frequencies around half the stimulation frequency. For inserts I1-2 the grey arrow and line indicate stimulation parameters where 1:2 entrainment was observed and black where it was not.

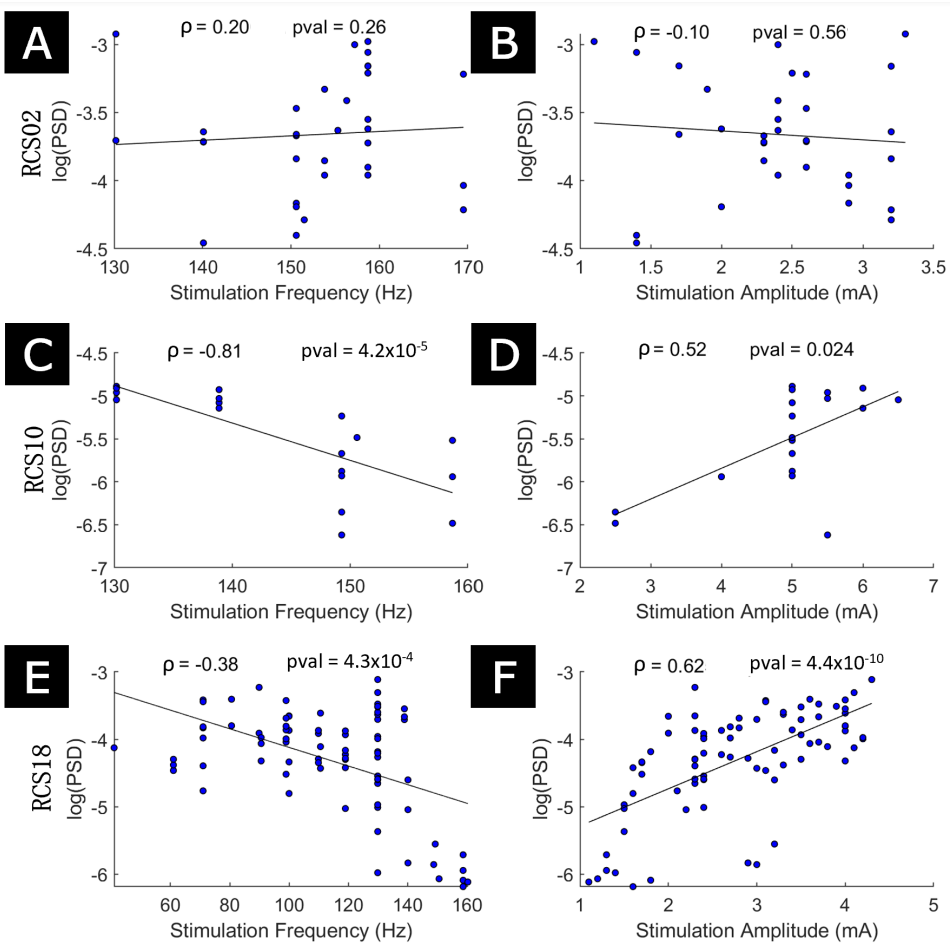


Figure 3.6: 1:2 entrained power correlates with stimulation parameters in two out of three patient datasets. The results for RCS02, RCS10, and RCS18 are presented in the first row, second row, and third row, respectively. The first column displays the comparison of the PSD of 1:2 entrained peak heights against stimulation frequency, with stimulation frequency acting as the sole predictor of the linear regression. The second column shows the comparison of the 1:2 entrained PSD against stimulation amplitude, where stimulation amplitude acts as the sole predictor of the linear regression. In all panels, datapoints considered are stimulation parameter combinations that resulted in 1:2 entrainment. The correlations are Spearman's.

can also be right leaning or symmetrical about the central frequency. Hence, the parameters of the Wilson-Cowan model need to be tuned to reproduce the data. Among the top-ranked Wilson-Cowan fits, there is some variability between the parameter sets and the corresponding entrainment predictions (see Appendix A.5.1). This demonstrates that the model parameters are non-identifiable. However, as the best fits converge on results that all include a left leaning 1:2 tongue and given the validation of some of the model predictions by follow-up recordings, we can

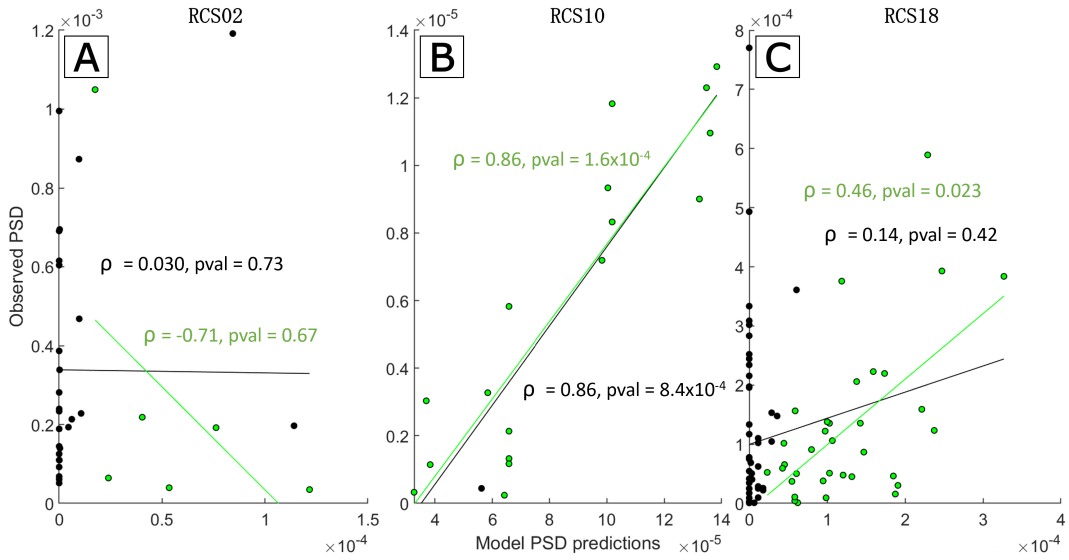


Figure 3.7: Correlation between model predictions for 1:2 entrained peak power and data. Panel A is for RCS02, B for RCS10 and C for RCS18. Across the three panel, all the data points presented are stimulation parameters that resulted in 1:2 entrainment in the data. The model PSD predictions are obtained using the same stimulation parameters as in the data. Points in green represent stimulation parameters that also achieved 1:2 entrainment in the model, whereas black points did not. The green linear regression fit, ρ value and p-value (pval) are calculated using only the points resulting in 1:2 entrainment in the fitted Wilson-Cowan model. The black equivalent are calculated using all points, regardless of whether the fitted model predicted 1:2 entrainment or not. The correlations reported are Spearman's and p-values are calculated using a permutation test as outlined in Section 3.3.6.

conclude that the fitted model remains a good candidate to make predictions for future investigations. It would be possible to fit Wilson-Cowan model parameters to on-stimulation entrainment data, which may or may not reproduce off-stimulation data. This is not something we are investigating as more value is provided by predicting the response from off-stimulation fits.

While only 1:2 entrainment is investigated here, entrainment will occur at other sub-harmonics of stimulation if there is a neuronal rhythm present to entrain and the corresponding tongue is large enough to encompass the neuronal rhythm. Similarly to 1:2 entrainment, sub-harmonic entrainment at every harmonic of stimulation is not an intrinsic property of Wilson-Cowan models. However, other sub-harmonic entrainment ratios can be observed for certain model parameter sets. By increasing stimulation frequency, for example to around 225Hz, it would

be possible to investigate other sub-harmonic entrainment ratios such as 1:3 entrainment of this rhythm.

The observation of the highest spectral peaks occurring at the lowest frequencies of stimulation in the model may be somewhat counter-intuitive, since one could expect more stimulation energy to provide more oscillatory power. However, due to the increased time between successive pulses of stimulation at lower frequencies, the trajectory of the population activity covers a larger distance in phase space (see Appendix A.5.4, specifically Fig A.7 for more details on population activity vector fields and trajectories). This means that the range of values that activity reaches for each population is greater, producing a higher power spectral peak for the given resultant frequency. Population activity having a larger range can also be interpreted as there being greater synchrony of neurons within the populations, as increased peak firing rates and decreased minima suggest more neurons are firing together.

Because the endogenous FTG is stronger for RCS02 and stimulation amplitude is lower, more variability in the on-stimulation entrained power is expected, which may explain the worse model performance for this patient (Fig 3.5 and 3.7). Specifically, the off-stimulation features of RCS02 (Appendix Fig A.2A) show a higher gamma peak in the PSD, a larger peak amplitude of the envelope PDF, and a shallower slope at lower amplitudes of the envelope PDF than RCS10 (Fig 3.3 and RCS18 (Appendix Fig A.2B). Therefore, it is expected to be more difficult to perturb the underlying oscillators away from the natural gamma frequency of the network, which leads to a 1:2 tongue with a much smaller width over the stimulation frequency axis. Given that the stimulation amplitude used for RCS02 is also smaller than for the other patients (see Fig 3.5), the strength of the endogenous FTG relative to stimulation amplitude is significantly greater, and natural fluctuations in the endogenous FTG have a larger impact on the power measured. This leads to more variability in Fig 3.5C and a worse correspondence with the fitted model. However, the fitted model still manages to predict a 1:2 tongue with a smaller area and a significantly lower top boundary compared to the other models, as observed in the

entrainment data. Hence, the model is able to predict features of the 1:2 tongue even with stronger endogenous rhythms.

Our modelling approach is based on ECoG recordings, but alternatives could be explored in future work. While non-invasive electroencephalography (EEG) has been used to study cortical gamma cross-frequency coupling with DBS (Muthuraman et al. 2020), ECoG recordings have a markedly better signal-to-noise ratio. Thus, whether FTG features obtained from EEG are sufficiently accurate to enable reliable FTG entrainment predictions through model fitting requires further investigation.

3.5.3 Limitations

As a pilot study, there was no systematic mapping of tongue boundaries, with large regions of untested parameters for some patients and a non-standardised approach to selecting stimulation parameters. Both of these shortcomings will be the focus of further investigations. However, extensive mapping of the 1:2 Arnold tongue boundary may be limited by patient fatigue and discomfort as some parameters tested are subtherapeutic and thus likely to lead to brief exacerbation of motor signs. In particular, there are relatively few data points to show the disappearance of 1:2 entrainment at high stimulation amplitudes (see Fig 3.5C, F, and I). At these higher amplitudes, patients often experienced adverse effects which could be mildly unpleasant. Hence, following the documentation of loss or reduction of entrainment, higher amplitudes were not explored further. Provided these adverse effects can be better mitigated, the disappearance of 1:2 entrainment at high stimulation amplitudes will be confirmed in future studies. Additionally, the clinical effects of gamma entrainment were not explored here and will be a focus for future work.

Given that ECoG data represents the activity of populations of neurons, the Wilson-Cowan model (a neural population model) is the appropriate level of description for this type of data. However, this does not allow us to observe or model the behaviour of individual neurons in response to stimulation and during 1:2 entrainment. Our approach is nonetheless adequate to predict stimulation parameters leading to 1:2 entrainment. Additionally, we have not included a

population to represent the basal ganglia in our model. This was because there was no consistent subcortical off-stimulation gamma peak to fit a Wilson-Cowan network to for these patients. Subcortical narrowband oscillations in the basal ganglia have been recorded in long term recordings in other patients (Gilron et al. 2021). It may also be possible to observe 1:2 entrainment in the subcortex and while this chapter only considers cortical populations, the methodology presented here can be translated to any network of interacting excitatory and inhibitory populations of neurons. Furthermore, we did not consider plasticity in our model. While short-term response to stimulation (such as during the follow-up on-stimulation recordings reported here) can be described by models without plasticity, the several months of chronic stimulation between the prestimulation and follow-up recordings are likely to have led to plasticity, which we did not account for here.

The orthodromic projections from STN or pallidum to cortex are all polysynaptic, and whether the effect of basal ganglia DBS on cortex is excitatory or inhibitory is not well understood. There exist strong connections from STN to GPe (Calabresi et al. 2014; Dong et al. 2021) and direct GABAergic projections from ChAT (choline acetyltransferase) and prototypic neurons from the GPe to the cortex (Dong et al. 2021). Hence, stimulation from these two sites may act primarily on the inhibitory population of the cortex. Furthermore, the cortico-basal ganglia network has been shown to exhibit complex coupling behaviour across frequencies (Oswal et al. 2016). However, there is not sufficient understanding of either the effects of DBS on the basal ganglia as well as the exact nature of the projections from the basal ganglia to the cortex. It is also unclear how antidromic activation of the stimulation targets would affect the motor cortex. To accommodate for this uncertainty, we consider DBS with both GABAergic and glutamergic tendencies (see Appendix A.5.5). Stimulation to our fitted models consistently produces 1:2 entrainment with a left leaning tongue regardless of the population being stimulated. Hence, this choice is inconsequential and the presence of 1:2 entrainment is more specific to the dynamics of the cortical populations than the excitatory bias of the stimulating pulse.

3.5.4 Implications

This work demonstrates that brain rhythms can have nonlinear responses to stimulation, such as entrainment at harmonics of stimulation frequency, and non-monotonic rhythmic responses to stimulation amplitude. We argue against the simple view that only brain rhythms close to the stimulation frequency can be entrained (through 1:1 entrainment).

These findings might have implications across frequencies. As mentioned in Section 1.2.4.2, 1:1 entrainment has been reported in other neural frequency bands to a variety of different methods of stimulation, including visual stimulation and tACS. If rhythms can lock to harmonics of stimulation frequency, as supported by the results of this chapter, it is possible that current stimulation protocols targeting any frequency band could induce unexpected responses at sub- or supra-harmonics of the stimulation frequency. Thus, when designing stimulation protocols, one should be aware of potential ramifications of stimulation on neuronal rhythms at multiple frequencies. For instance, stimulation targeting lower frequency oscillations, such as beta rhythms, may be able to entrain gamma at a 2:1 rotation number, or even alpha at a 1:2 rotation number. Similar considerations have been employed when designing stimulation protocols in a canine with epilepsy (Zamora et al. 2021). More recently, a principled approach to selectively promote rhythms close to the stimulation frequency while preventing entrainment at sub- and supra-harmonics was put forward in (Duchet et al. 2023).

3.6 Conclusion

We show that for certain network parameters, simple neural circuits can support 1:2 entrainment to DBS. Our fitted Wilson-Cowan model provides theoretical evidence for a neural circuit origin of 1:2 entrainment of cortical FTG oscillation to high-frequency DBS in PD patients. Furthermore, it predicts a larger region of stimulation parameters, at frequencies corresponding to less than twice the natural frequency of

the system, for which 1:2 entrainment would be observed. These results are validated by 1:2 Arnold tongue charting from the same patients to whom the model was fitted.

Understanding the variety of effects of stimulation on various brain rhythms would provide valuable insights into designing stimulation protocols to provide maximum therapeutic benefit with minimal side effects. This model provides a first step to predicting these responses. Computational models enable us to experiment with a variety of waveforms without the burdensome tests and validation that would be associated with in patient trials. Prediction of the neuronal responses to stimulation is a fundamental step in the design of future therapeutic protocols. Our model predicts that these responses are not a simple one-for-one mapping of stimulation frequency and amplitudes to brain network activity and that stimulation may have significant effects, even when the stimulation frequency is outside of the frequency band of interest.

4

Dynamic Responses - Evoked Resonant Neural Activity Long-Term Dynamics can be Reproduced by a Computational Model with Vesicle Depletion

Contents

4.1 Abstract 87
4.2 Introduction 87
4.3 Results 89
4.3.1 Results of Fitting Process 89
4.3.2 Long-Term Spectrogram 92
4.3.3 Variable Stimulation Frequency 93
4.3.4 Variable Stimulation Amplitude 94
4.3.5 Variable Medication State 95
4.3.6 Post Stimulation Bursting 98
4.3.7 Individual Oscillator Perturbation 98
4.3.8 Replication of In Vitro Slice Experiments 100
4.4 Methods 101
4.4.1 The Kuramoto Model 102
4.4.2 Fitting Process 108
4.4.3 Simulation of Various Stimulation Paradigms 110
4.4.4 Evaluation of ERNA Frequency and Amplitude Over Time 112
4.4.5 Statistics for ERNA Amplitude On and Off Medication 113
4.5 Discussion 113
4.5.1 Hypothesised Mechanisms and Models of ERNA 114
4.5.2 Proposed Computational Model 116
4.5.3 Model Predictions for Further Validation 118

4.5.4 Limitations 119
4.6 Conclusion 122

4.1 Abstract

Subthalamic DBS robustly generates high-frequency oscillations known as evoked resonant neural activity (ERNA) in patients with PD. Recently the importance of ERNA has been demonstrated through its ability to predict the optimal DBS contact selection in the subthalamic nucleus. However, the underlying mechanisms of ERNA are not well understood, and previous modelling efforts have not managed to reproduce the wealth of published data describing the dynamics of ERNA. Here, we therefore aim to present a minimal model capable of reproducing the characteristics of the slow ERNA dynamics published to date. We make biophysically-motivated modifications to the Kuramoto model and fit its parameters to the slow dynamics of ERNA as obtained from data. We further validate the model against experimental data from PD patients by simulating variable stimulation and medication states, as well as the response of individual neurons. Our results demonstrate that it is possible to reproduce the slow dynamics of ERNA with a single neuronal population, and, crucially, with vesicle depletion as one of the key mechanisms behind the ERNA frequency decay in our model. We provide a series of predictions from the model that could be the subject of future studies for further validation.

4.2 Introduction

In Chapter 3, we looked at DBS responses that have a stationary frequency profile, in this chapter we will investigate responses that can have dynamic frequency activity. A dynamic frequency response is observed during STN-DBS, termed evoked resonant neural activity (ERNA), in simultaneous recordings of the STN. However, the underlying mechanisms of this phenomenon are not well understood.

As introduced in Section 1.2.5, ERNA is a series of high-frequency oscillations (HFOs, >200Hz) of high-amplitude in response to 70-180Hz stimulation, despite

there being very little to no high frequency activity at the stimulation site pre-stimulation (Wiest et al. 2020) (also see 4 in Fig 4.2A). ERNA has been observed in different neural structures, but so far only in the pallidal (Schmidt et al. 2020; Johnson et al. 2023) and thalamic regions (Sinclair et al. 2018; Sinclair et al. 2019; Wiest et al. 2020; Wiest et al. 2023). Furthermore, ERNA has also been characterised as a robust response across different devices, patient groups and stimulation conditions (Sinclair et al. 2018; Sinclair et al. 2019; Wiest et al. 2020; Wiest et al. 2023). However, the reproducibility and unphysiological appearance of ERNA have led to questions of whether it is of physiological origin. The physiological origin of ERNA was later demonstrated in (Sinclair et al. 2019) as discussed in Section 1.2.5.2, but many questions regarding the mechanisms of ERNA still remain.

Since Sinclair et al. observed the presence of ERNA in the PD STN (Sinclair et al. 2018), several hypotheses and models attempting to explain the presence of ERNA have been proposed. These hypotheses range from inhibition and/or excitation of neural ensembles to recruitment of inter-component projections between the STN and GPe (Chiken and Nambu 2016; Milosevic et al. 2018; Steiner et al. 2019; Wiest et al. 2023). However, thus far none of these propositions have managed to explain all ERNA characteristics. Recently, the significance of comprehending the fundamental mechanisms of ERNA has become more apparent with evidence that ERNA may provide the strongest predictor of clinical performance for STN-DBS contact selection (Xu et al. 2022).

In this chapter, we propose a biophysically-motivated computational model that is capable of reproducing the key long-term ERNA characteristics currently described in the literature under a variety of stimulation paradigms, with a view to hypothesise the fundamental mechanisms responsible for ERNA. We assembled a single population of Kuramoto oscillators intended to represent the STN. Through the addition of synaptic vesicle depletion and a variable coupling function to the standard Kuramoto model, we were able to fit the parameters of the modified Kuramoto model to key features of ERNA. We simulate further stimulation paradigms to validate and gain insights into the key properties of the computational

model. In addition, we suggest predictions that can be used to further validate the computational model.

4.3 Results

We modified the Kuramoto model to include a second-order coupling function and the effect of vesicle depletion from high-frequency DBS (see Section 4.4). We fitted the modified model to salient long-term features of ERNA observed in patient data with DBS at 130Hz, 3mA. By comparing simulations of the fitted model to ERNA frequency responses recorded in patients under varying stimulation frequencies, and with minimal additional parametrisation under varying stimulation amplitudes as well as medication states, we characterize the model and test its predictive power. We provide validation for the model by comparing the model's ERNA amplitude response (which is not considered in the parameter tuning) to that of the data. Lastly, we perform analogous simulations of the model to in vitro and in vivo recordings of the STN to further test the model against biophysical data.

4.3.1 Results of Fitting Process

The best-ranked parameter set resulting from the fitting to the peak frequency ERNA decay while limiting off-stimulation high-frequency activity (see Section 4.4.2), provided a good approximation of the peak frequency ERNA decay estimated from data recorded in a PD patient with 130Hz, 3mA STN DBS (Fig 4.1C). The corresponding model parameters are given in Table B.1 in the Appendix. In the spectrogram, the fitted model shows a broad ERNA decay approximating patient data (compare Fig 4.1A and Fig 4.1B). Before stimulation onset, high-amplitude and high-frequency activity is absent in the model, with a lower amplitude peak at around 40Hz as in the data (compare Fig 4.1A and characteristic 3 in Fig 4.2A).

The first key modification of the Kuramoto model that was found to be sufficient for reproducing the slow ERNA dynamics in the frequency domain is the reduction of coupling strength through vesicle depletion during stimulation (Fig 4.1D). Over the timescale during which the slow ERNA dynamics develop,

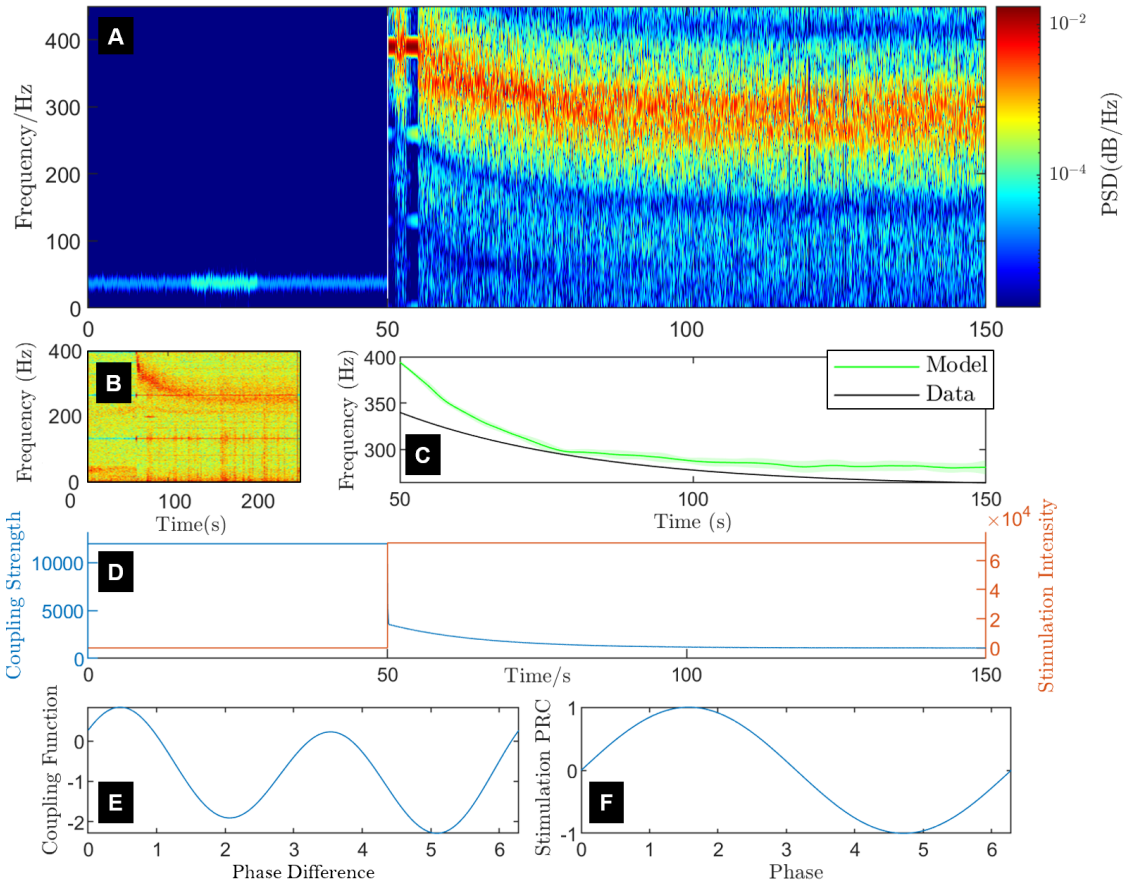


Figure 4.1: Fitted slow dynamics of the modified Kuramoto model on and off stimulation and model's key properties. (A) Spectrogram showing the fitted model's ERNA response to 130Hz stimulation (fitted stimulation amplitude). The transition from off to on stimulation happens at 50 seconds. The colour scale represents the power spectral density (PSD). (B) Example of the slow ERNA dynamics in the frequency domain for 130Hz and 3mA stimulation adapted from (Wiest et al. 2020). (C) Comparison of the peak ERNA frequency decay estimated from panel B and fed into the fitting process (black), and the model predicted ERNA frequency peak (green) averaged over 15 realisations of noise, natural frequencies and initial conditions for the 100 second period of stimulation following 50 seconds of the model settling off-stimulation. We also display the standard error of the mean for the averaged model output in the lighter green band. (D) Evolution of coupling strength in the model (blue) and stimulation intensity (orange) over the full stimulation window. Stimulation is a pulse train at 130Hz, but intensity is depicted as constant following stimulation onset in this figure for demonstrative purposes. (E) The fitted second-order Fourier series coupling function, and (F) the phase-response curve (PRC, here a sine wave) used in the model.

the readily-releasable vesicle pool (RRP) and the recycling pool (RP) are very quickly exhausted, and the resting pool (RtP) becomes the dominant vesicle pool for synaptic transmission (Fernández-Alfonso and Ryan 2004; Rizzoli and Betz

2005; Kaeser and Regehr 2017). Although larger, the RtP is the furthest away from the synaptic terminal and unable to provide vesicles to facilitate synaptic transmission as readily as other pools (Rizzoli and Betz 2005; Denker and Rizzoli 2010; Alabi and Tsien 2012), which we model as a reduction in coupling between neurons. Our vesicle depletion and replenishment model is expressed by Eqs (4.3) and (4.4) (parameters in Table B.1), and presented in detail in Section 4.4.1.1. Hence, Fig 4.1D exhibits a fast initial drop in coupling strength as the RRP and RP are quickly depleted, and the RtP becomes dominant.

The second key modification of the Kuramoto model that was found to be sufficient for reproducing the slow ERNA dynamics is the second-order Fourier series coupling function (Fig 4.1E, and see Section 4.4.1.2). The coupling function is denoted by f in the model (see Eq (4.1)) and captures how each neuron's phase is influenced by the phase of other neurons. The fitted coupling function has a strong second harmonic as well as a negative shift (Fig 4.1E). We show in Appendix B.4.1 that neither a coupling function derived from the Hodgkin-Huxley model, nor a sine coupling function are suitable to reproduce the slow ERNA dynamics. We also demonstrate in Appendix B.4.1 that the noughth and second harmonic of the coupling function have a larger impact on the ERNA frequency decay than the first harmonic. The importance of the second harmonic is related to the clustering behaviour exhibited by the model (see Appendix B.2). In the Kuramoto model, stimulation can advance or delay a neuron's spiking by advancing or delaying the phase of individual oscillators. This effect is captured by the phase response curve (PRC), which characterises the change in an individual oscillator's phase as a function of the phase at the time of stimulation and is denoted by g in Eq (4.1). For this parameter set, a sine wave PRC (Fig 4.1F) was sufficient to provide an accurate fit to the features, which further limited the number of parameters that needed to be optimised.

4.3.2 Long-Term Spectrogram

While Fig 4.1A captures the slow dynamics of ERNA over more than a minute on-stimulation, (Wiest et al. 2020) provide a series of on-DBS windows and pauses that demonstrate how reproducible ERNA is. Additionally, Fig 4.1A does not demonstrate the ability of the model to return to baseline following stimulation, a key observation of ERNA dynamics. We address this by simulating the same DBS on/off paradigm used in (Wiest et al. 2020) and depicted in Fig 4.2A. The spectrogram (with the addition of white noise) appears similar to that of the data (compare Fig 4.2A and Fig 4.2B), and consistently returns to baseline after stimulation is turned off.

Wiest et al. outline four key characteristics of the ERNA spectrogram, see annotations in Fig 4.2A: (1) Initial high frequency, high amplitude response; (2) Steady state reached at a peak of approximately 250Hz after around 100 seconds of stimulation; (3) Activity off-stimulation at the low gamma/high beta frequency range of approximately 40Hz, and; (4) low amplitude, high frequency activity at around 250Hz off-stimulation (Wiest et al. 2020). The long-term spectrogram from the model (Fig 4.2B) demonstrates most of these characteristics and is capable of explaining all of them through model dynamics. Characteristics 1,2 and 3 can each be seen in the spectrogram regardless of the length of the DBS window. Characteristic 3 cannot be seen in first off-stimulation period as the model is in a settled state. However, in each of the following periods between DBS windows the amplitude of the low frequency activity (characteristic 3) decreases with time after DBS termination in both the data and the model. While the signal appears to remain at a high amplitude immediately after stimulation termination, the stable dynamics off-stimulation are low amplitude and low frequency in the model. Characteristic 4 cannot be seen in the model's spectrogram; however, this is approximately the mean natural frequency of the oscillators in the model. Neurons occasionally being released to their natural frequency by a decrease in network coupling due to stronger fluctuating neural synchronisation or noise in the data could therefore account for characteristic 4.

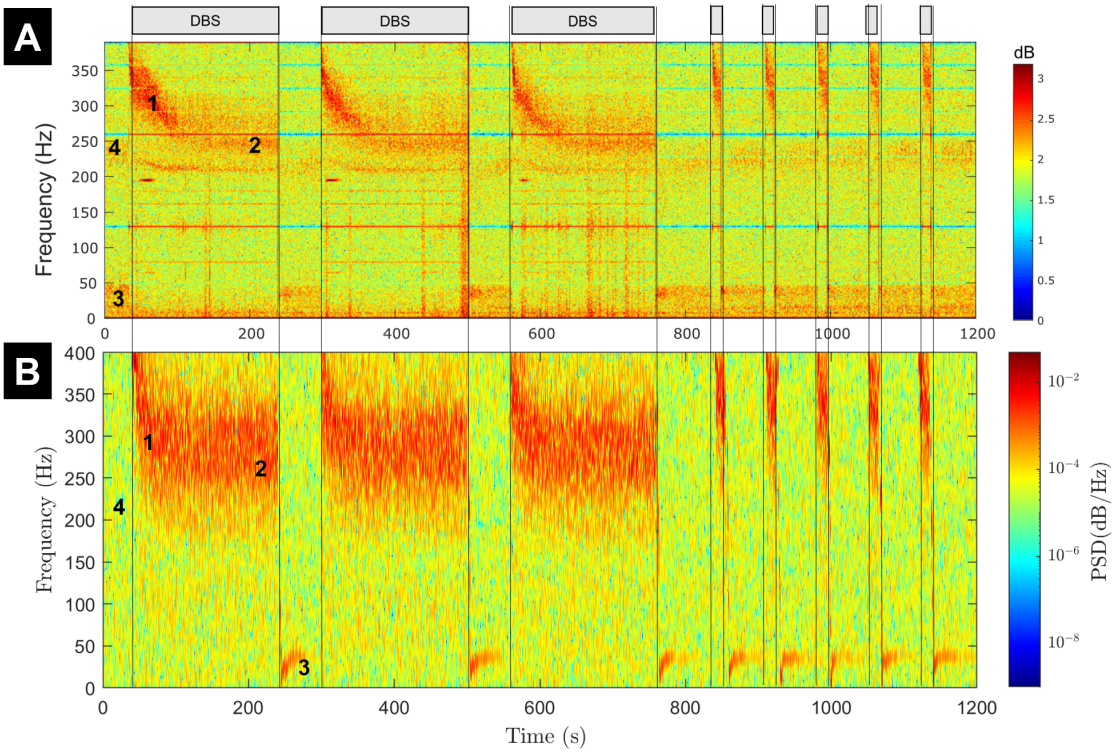


Figure 4.2: The modified Kuramoto model replicates ERNA characteristics observed in data during multiple on-DBS windows with pauses. (A) Data spectrogram, adapted from (Wiest et al. 2020). On-DBS periods (with 130Hz, 3mA STN DBS) are indicated by grey rectangles. (B) Spectrogram from the modified Kuramoto model with added white noise. Both panels use similar time points of DBS initiation and termination. Annotations are described in the main text.

4.3.3 Variable Stimulation Frequency

We simulate the fitted model for various stimulation frequencies as was done in (Wiest et al. 2023). The variation in stimulation frequency is captured by the delta term in Eq (4.3) and will have the effect of depleting all three vesicle pools further and more quickly with higher stimulation frequency. Without making any changes to the model besides the frequency of the pulse train we are able to replicate most features of the ERNA frequency decay over time at each stimulation frequency reported in (Wiest et al. 2023) (compare Fig 4.3A and B). All ERNA frequency decays initiate at similar high frequencies around 380Hz in both the model and the data. The decays also stabilise after around 60 seconds of stimulation in both model and data. The 180Hz stimulation frequency line finishes at around 270Hz and the 70Hz stimulation frequency line at around 310Hz, much higher than the

100Hz stimulation frequency line, in both model and data. The 180Hz line finishes higher than the 150Hz line in the data, however, in the model the 180Hz line finishes lowest. The 150Hz line finishes above the 130Hz line in the model though, showing that there is enough variability in the model to have some crossover amongst the various stimulation frequencies. The amplitude lines also demonstrate similarities in both cases (Fig 4.3C and D). The 180Hz stimulation frequency line is initially higher than the other stimulation frequencies, with the 130Hz line starting above the 150Hz line. The 100Hz and 70Hz stimulation frequency lines are lower at around one. Later in the stimulation window, the 180Hz stimulation frequency line decreases quickly towards the 130Hz stimulation and falls below both 150 and 130Hz lines after 40 seconds on-stimulation. Both frequency and amplitude lines have little variation regardless of the realisation of noise, natural frequency distribution and initial conditions (Fig 4.3B and D).

4.3.4 Variable Stimulation Amplitude

We also simulate the fitted model for various stimulation amplitudes as was done in (Wiest et al. 2023). Unlike stimulation frequency, the inclusion of variable stimulation amplitude needs to be made through a biophysically-motivated model parameter adjustment (see Section 4.4.3.2-*Variable Stimulation Amplitude*, Eq (4.10)). This adjustment provided enough flexibility to closely resemble the ERNA frequency decay at each stimulation amplitude (Fig 4.4A and B). All frequency decays initiate around 380Hz in both the model and the data. The greatest stimulation amplitude consistently produces the largest frequency decay, dropping to 300Hz after around 30 seconds before continuing below that. The lowest stimulation amplitude generally has the highest frequency, finishing around 320Hz after 30 seconds like the data and 300Hz at the end of the stimulation period. The amplitude lines of the model also demonstrate similarities to the data (Fig 4.4C and D). The highest stimulation amplitude initially has the highest amplitude response and is grouped with other higher stimulation amplitude lines. The lowest stimulation amplitude

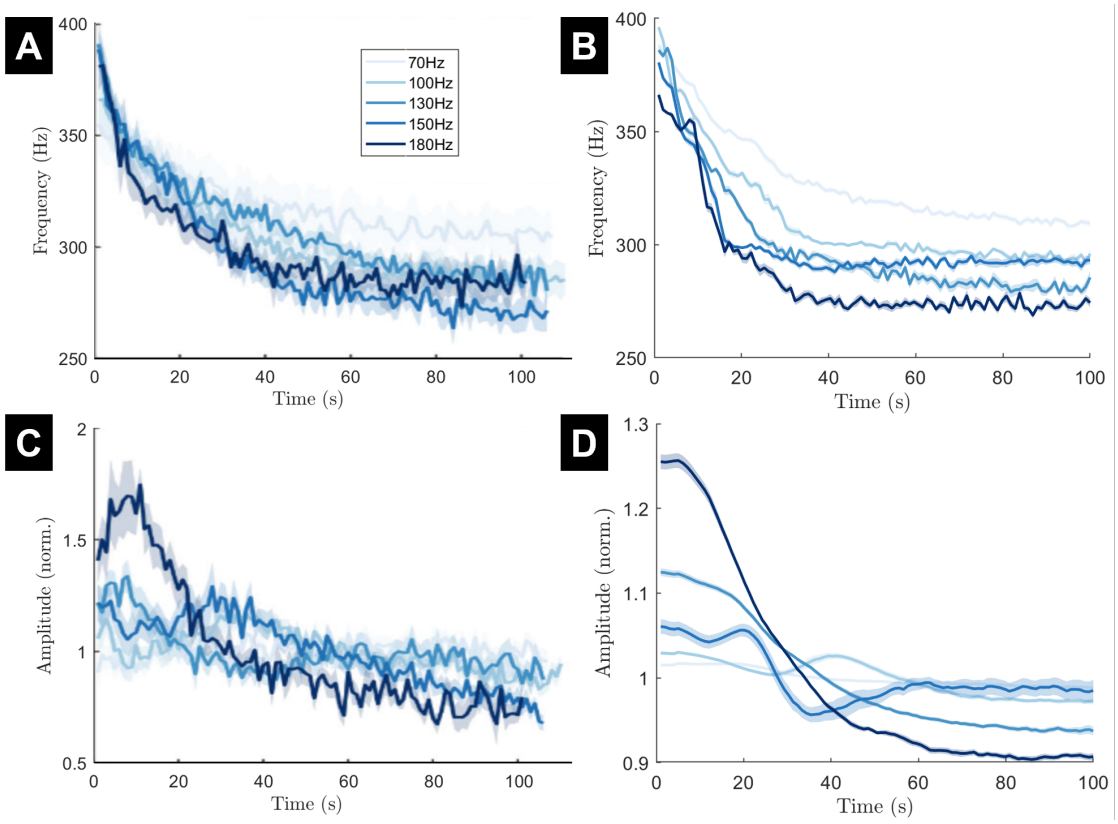


Figure 4.3: The frequency and amplitude of ERNA over time in response to various stimulation frequencies in both data and the fitted model. (A and C) The data ERNA frequency decay and amplitude variation, respectively. Stimulation amplitude was maintained at the patient's therapeutic intensity. (B and D) The ERNA frequency decay and amplitude variation, respectively, from model simulations. The 130Hz line of the model simulation has the same parameters as the simulation from Fig 4.2. Mean (solid line) and standard error of the mean (faded region around solid mean) calculated over 15 trials with different realisations of noise. The colour for each stimulation frequency is the same in data and model panels. Panels A and C are adapted from (Wiest et al. 2023).

in the model initiates and remains around an amplitude of one, similarly to the 1mA stimulation amplitude line in the data.

4.3.5 Variable Medication State

We simulate the fitted model in the on- and off- medication states as was performed in (Wiest et al. 2023). We make a biophysically-motivated model parameter change to reflect medication-dependent vesicle pool changes (see Section 4.4.3.2-*Variable Medication State*). This change provides enough flexibility to the model dynamics to effectively capture the ERNA characteristics with variable medication state (Fig 4.5).

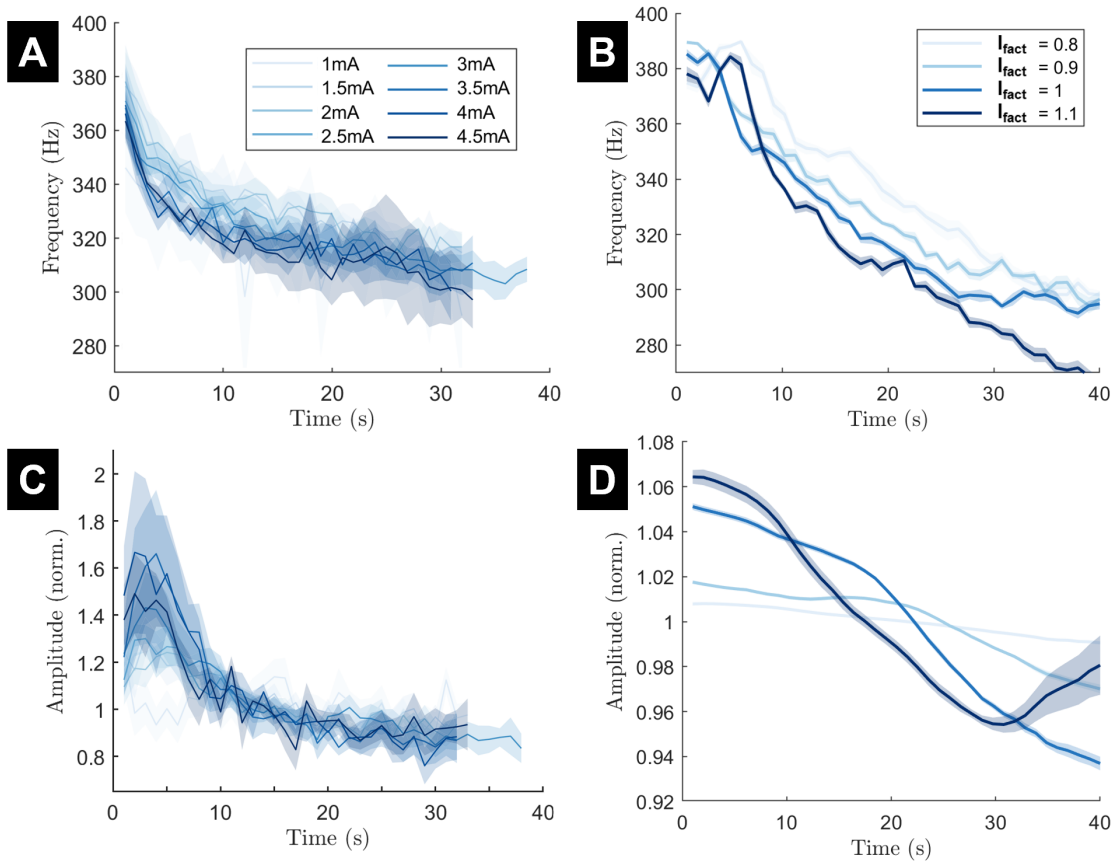


Figure 4.4: The frequency and amplitude of ERNA over time in response to various stimulation amplitudes in both data and the fitted model. (A and C) The data ERNA frequency decay and amplitude variation, respectively. Stimulation frequency is set at 130Hz. (B and D) The ERNA frequency decay and amplitude variation, respectively, from model simulations. The $I_{fact} = 1$ line of the model simulation has the same parameters as the simulation from Fig 4.2 and approximately corresponds to 3mA. Mean (solid line) and standard error of the mean (faded region around solid mean) calculated over 15 trials with different realisations of noise. The colour for each stimulation frequency is the same in data and model panels. Panels A and C have been adapted from (Wiest et al. 2023).

The frequency decays of on-medication and off-medication states initiate at the same frequency of around 380Hz in both the model and the data (Fig 4.5A and B). The model and data frequency responses remain at similar levels and the frequency decays follow similar time constants. This is consistent up to before 60 seconds following stimulation onset, where the lines were seen to significantly separate in the data. The statistical analysis of the model demonstrates that the medication states separate by a significant amount (for $p<0.05$) at similar stages of both the model and the data (see Section 4.4.5 for further details on the statistical analysis). From

this point the on-medication remains higher, finishing the 120 second stimulation window at around 280Hz in both model and data. The off-medication state drops to a lower frequency, stabilising around 260Hz. The amplitude lines also demonstrate similarities, with the off-medication line remaining higher than the on-medication line early in the stimulation window. Towards the end of the stimulation period both amplitude lines drop to lower values than at the start of the stimulation window in both the model and the data (Fig 4.5C and D).

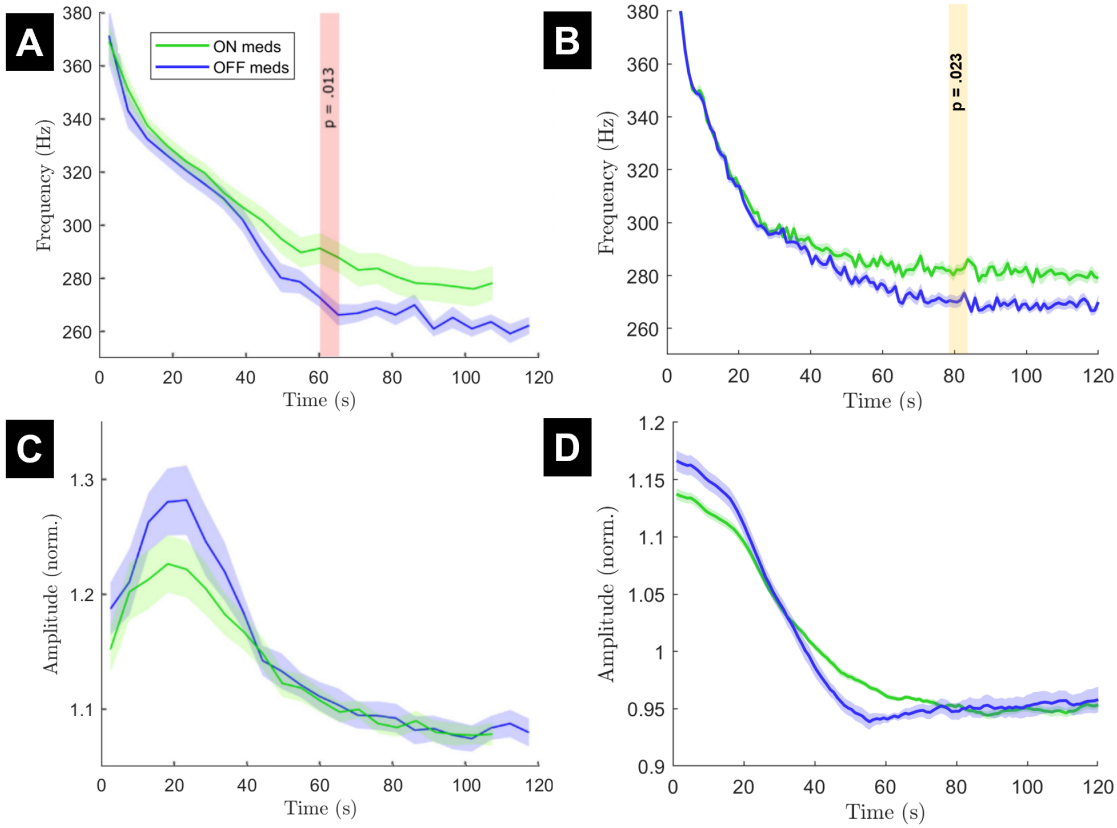


Figure 4.5: The frequency and amplitude of ERNA in response to medication state in both data and the fitted model. (A and C) The data frequency decay and amplitude variation, respectively. The red bar in panel A indicates the time after which the frequency decays of each state are determined to have significantly separated. (B and D) The frequency decay and amplitude variation, respectively, from model simulations. The on-medication line of the model simulation has the same parameters as the simulation from Fig 4.2. Mean (solid line) and standard error of the mean (faded region around solid mean) calculated over 15 trials with different realisations of noise. For panel B, statistical tests in line with the data were performed. We identified the point where significance was achieved at the same level as the data (the yellow bar, $p<0.05$). The colour for each medication state is the same in the data and the model panels. Panels A and C are adapted from (Wiest et al. 2023).

4.3.6 Post Stimulation Bursting

The responses to post stimulation bursting (10 pulses of stimulation at 130Hz every second following termination of a long period of stimulation) also appears to show similarities between the model and the data (Fig 4.6). This condition captures the cumulative effect of successive, brief periods of vesicle depletion and replenishment (different time scale than in Fig 4.2).Vesicle depletion and replenishment over the bursting periods is described in the model by Eqs (4.3) and (4.4) as before, and can be visualised in Fig 4.6E. There was no fitting performed to features specific post stimulation bursting. In the data, the frequency response increases back up towards the early continuous stimulation state within the 20 seconds of bursting stimulation (Fig 4.6A). A similar increase is seen in the model, reaching approximately the same frequency at similar rates of recovery (Fig 4.6B). Amplitude response of ERNA also appears to increase and reach a similar level at the end of the 20 second bursting stimulation window in both the model and the data (Fig 4.6C-D). The dynamics of these evoked responses change at a rate determined by the vesicle replenishment and coupling strength recovery (Fig 4.6E). Coupling strength drops to RtP dominance during each series of stimulation bursts and recovers to RRP dominance between pulse bursts.

4.3.7 Individual Oscillator Perturbation

While the coupling strength between STN neurons and how it varies over stimulation is crucial in our model's ability to reproduce ERNA dynamics, results presented in (Steiner et al. 2019) portray the STN as a mostly disconnected network of neurons. Steiner et al. showed that stimulating individual STN neurons to the point of firing does not cause neighbouring STN neurons to fire. We therefore simulate perturbations to single oscillators in the network in order to determine whether these results can be replicated in the model while still having connectivity between STN neurons. We individually perturb seven of the oscillators from our network (all-to-all connected) with four pulses of 130Hz at the same stimulation amplitude as the model was fitted to (3mA). In (Steiner et al. 2019), four pulses of 20Hz stimulation

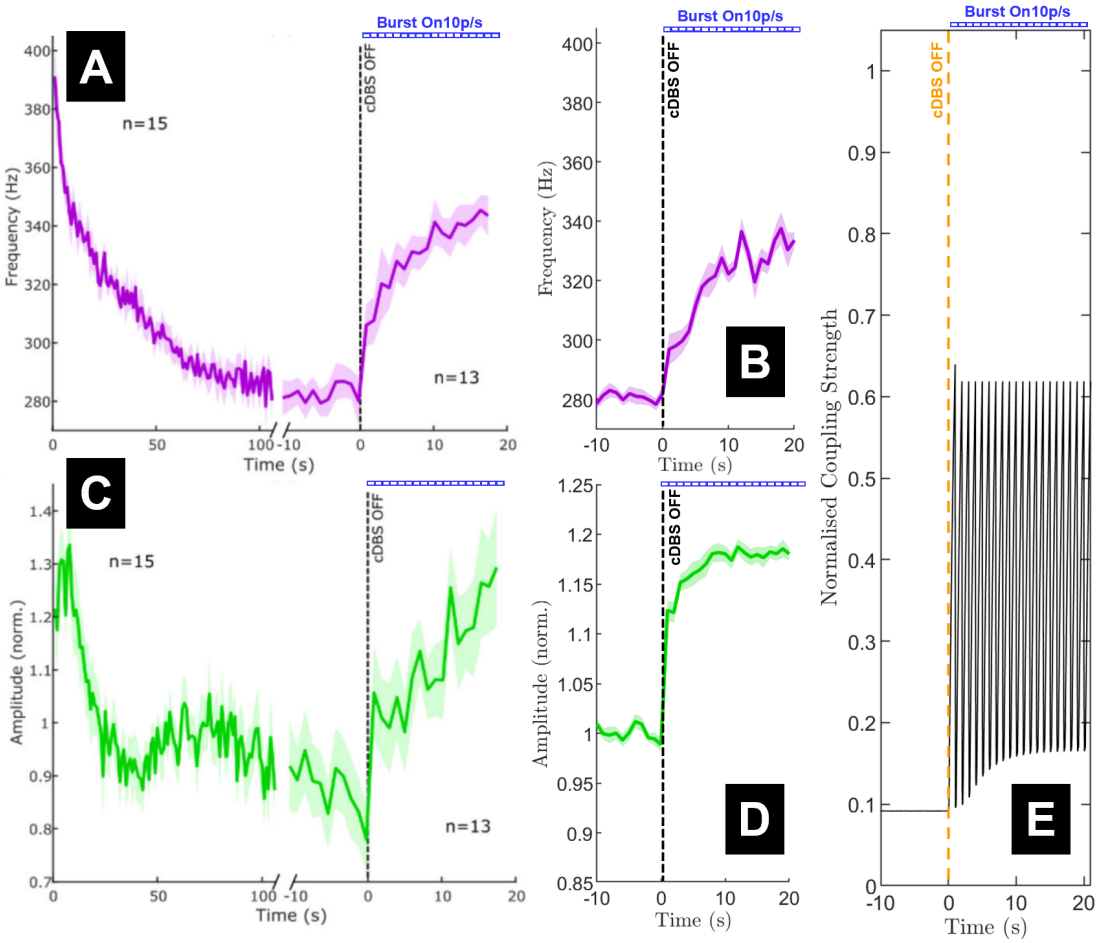


Figure 4.6: The frequency and amplitude of ERNA in response to bursting stimulation post continuous deep brain stimulation (cDBS) termination in both data and the fitted model. (A and C) The data frequency decay and amplitude variation, respectively. (B and D) The frequency decay and amplitude variation, respectively, from model simulations. Mean (solid lines) and standard error of the mean (faded region around solid mean) calculated over 15 trials with different realisations of noise. (E) Coupling strength normalised by k_{mu} through continuous stimulation to termination at time 0 (orange dashed line) with 10 pulse bursts at 130Hz every second for the next 20 seconds. The blue dashed line in every panel (Burst On 10p/s) indicates the presence of bursting stimulation of 10 pulses at 130Hz every second following the termination of cDBS. Panels A and C are adapted from (Wiest et al. 2023).

were used, in this chapter we proceed with 130Hz as the model did not capture the long term 20Hz response. Additionally, 130Hz stimulation would have the effect of faster vesicle depletion which elicits faster phase progression of the oscillators. In the absence of vesicle depletion, a lower rate of phase progression was observed than in Fig 4.7. We record the rate of phase progression in all seven oscillators with each perturbation and compare this against the phase progression of the oscillators

in the absence of stimulation to any part of the network. There appears to be no marked change in phase progression rate of the oscillators across the network in response to a single oscillator being perturbed (Fig 4.7). All of the oscillators not being directly stimulated respond similarly showing a small increase in phase progression, but not enough to experience any additional firing ($< 2\pi$). This is seen across the network regardless of the oscillator being perturbed or observed.

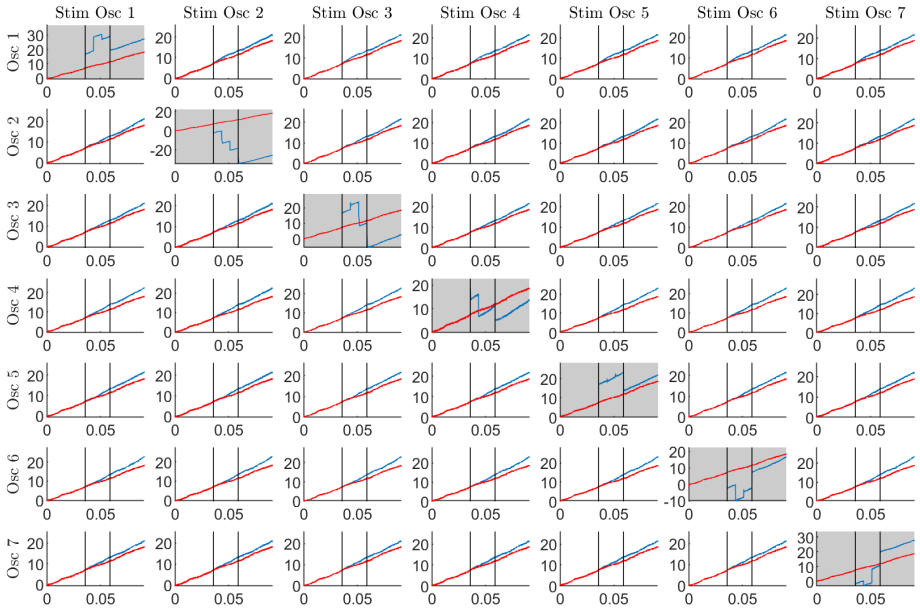


Figure 4.7: The phase progression of individual oscillators in response to the perturbation of a single oscillator in the network for comparison against data (Steiner et al. 2019). Observing phase progression of oscillator indicated by row title during stimulation of oscillator indicated by column title. The grey panels represent a case where we are recording the phase progression from the same oscillator as is being stimulated. White panels indicate a recording from an oscillator not receiving micro-electrode equivalent stimulation. The red lines on each plot represent the phase progression of each oscillator (number indicated by row heading) in the absence of stimulation to any oscillator in the network. The blue lines represent the phase progression of the oscillator in response to stimulation of a single oscillator. Stimulation is applied at 130Hz for four pulses at the fitted stimulation amplitude between the two vertical black lines as was done in the data (Steiner et al. 2019).

4.3.8 Replication of In Vitro Slice Experiments

The behaviour of individual oscillators in a mostly disconnected network interpretation of the modified Kuramoto model matches data from in vitro slice recordings

of the rat STN (Fig 4.8). Observations from the rat STN show the off-stimulation neuronal firing rate is around 20Hz (Hallworth et al. 2003; Wilson et al. 2004). In the presence of constant current electrical stimulation, firing rate increases rapidly to over 200Hz at low stimulation amplitude (<0.5nA) (Hallworth et al. 2003; Wilson et al. 2004) up to over 500Hz in some cases (Kitai and Kita 1987). This was consistent with high-frequency pulsatile stimulation (>120Hz, 200μA) where firing rate of individual neurons was seen to increase over 200Hz (Schor et al. 2022). Using two oscillators to capture the mostly disconnected network, we incorporate the absence of GABAergic input from the GPe in slices by increasing the shift of the coupling function (the noughth order term, f_0, of the Fourier series presented in Eq (4.5)). This is increased until the two oscillators progress at around 20Hz off-stimulation (Fig 4.8B). In the presence of constant current stimulation, the oscillators of the coupling function-shifted network will progress at a frequency greater than 500Hz immediately following stimulation onset (Fig 4.8B). This is observed with stimulation amplitude scaled to match the energy of pulsatile stimulation from the parameter fitting (see Section 4.4.3.3-*Replication of In Vitro Slice Experiments* for details). This was likely a higher stimulation amplitude than these slice experiments used, as the model was fitted to pulsatile stimulation data of around 3mA. Despite the likely disparity in the amplitude of stimulation, the firing rate on-stimulation matches the observations of neuronal firing rate increasing to over 500Hz with stimulation (Kitai and Kita 1987). Furthermore, it is possible that firing rate would reach >500Hz by extrapolating firing rate to higher stimulation amplitudes from other results stimulating STN slices (Hallworth et al. 2003; Wilson et al. 2004). When vesicle depletion is included in this network, the approximate frequency of the oscillator firing rate stabilises around 300Hz.

4.4 Methods

In this section, we first provide an overview of the computational model, starting with an introduction to the Kuramoto model as well as the details of the modifications to the model, in particular the effect of vesicle depletion and replenishment on

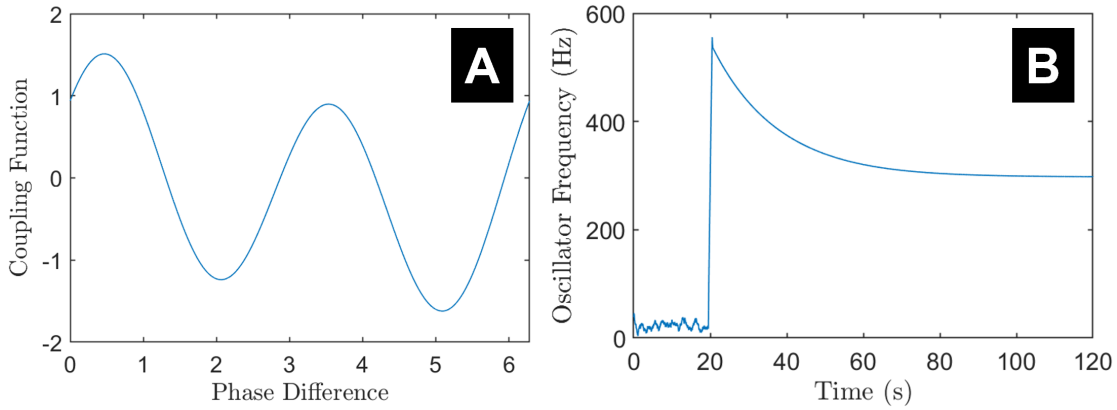


Figure 4.8: The approximate frequency of individual oscillators in a two-oscillator network with the adjusted coupling function and constant current stimulation for comparison of mostly disconnected in vitro slice experiments. (A) Adjusted coupling function after changing noughth order coefficient. (B) Individual oscillator frequency in the two-oscillator network over constant stimulation current injection window of 100 seconds following onset after 20 seconds off-stimulation.

coupling strength. We then present the fitting process used to find model parameter sets that reproduce key characteristics of the slow dynamics of ERNA. Lastly, we describe methodological details for all simulations performed in this chapter based on different experimental paradigms.

4.4.1 The Kuramoto Model

Our approach is to attempt to model the ERNA using as simple a model as possible. This requires a model that can adequately capture responses to stimulation without requiring a large number of complex neurons to be modelled leading to a large number of parameters. Given these characteristics as well as previous ERNA modelling efforts that used phase oscillators (Realmuto et al. 2023), the Kuramoto model (as introduced in Section 1.2.6.3) presents a suitable choice for simulating ERNA. The basic Kuramoto model describes a series of interconnected phase oscillators (Kuramoto 1983), in our case representing neurons (Brown et al. 2004; Weerasinghe et al. 2019).

The evolution of the i^{th} oscillator's phase θ_i (adapted from Eq (1.4) introduced

in Section 1.2.6.3) is given by the stochastic differential equation

$$d\theta_i = (\omega_i + k_t \sum_{j=1}^{N} f(\theta_j - \theta_i) + I_t g(\theta_i))dt + \zeta dW_i \quad \text{for } i = 1, ..., N, \tag{4.1}$$

where ω_i represents the natural frequency of the i^{th} oscillator. The (homogeneous) coupling strength between oscillators at time t is k_t, and f represents the coupling function, which is a 2π-periodic function of phase differences. The phase response of individual oscillators is described by the 2π-periodic PRC which is denoted g, and I_t is the intensity of stimulation at time t modelled as

$$I_t = I \cdot I_{\text{fact}} \cdot u(t), \tag{4.2}$$

where I is the fitted stimulation amplitude and I_{fact} is a factor included to vary stimulation amplitude. $u(t)$ is the stimulation pulse train which takes a value of 1 with the stimulation pulse and 0 otherwise (we are assuming that all oscillators perceive the same level of stimulation). Intrinsic noise is added to each oscillator through independent Wiener processes W_i. The noise standard deviation is set by ζ. The number of Kuramoto oscillators in the model is given by N, which is chosen to be 50 for this chapter unless stated otherwise. We measure synchrony in the network using the order parameter as given by Eq (1.5).

It is necessary to introduce a series of modifications to the Kuramoto model in order to incorporate dynamics that can adequately capture the ERNA response. While we do not include delays or heterogeneous coupling in this chapter, the modifications described below provide enough versatility in the model dynamics to capture the nonlinear behaviour of ERNA.

4.4.1.1 Modelling the Effect of Vesicle Depletion and Replenishment on Coupling Strength

Vesicle depletion and progression towards synaptic failure has been suggested as an underlying mechanism of the ERNA frequency decay (Wiest et al. 2023). However, no clear mechanism describing how vesicle depletion may influence the dynamics

of ERNA has been proposed. We develop the vesicle depletion hypothesis in this chapter and sketch how it could explain the underlying dynamics of ERNA.

Rizzoli and colleagues proposed the three-vesicle pool model of synaptic transmission (see insert in Fig 4.9A) from the observation of three stages of fluorescence in goldfish bipolar cells (Rizzoli and Betz 2005). Firstly, the readily-releasable pool (RRP) is a small but easily-mobilised group of vesicles. Due to their proximity to the synaptic terminal and small number, RRP vesicles are often depleted within a second of stimulation onset and recycle within seconds. Secondly, the recycling pool (RP) is a slightly larger pool of vesicles which are less easily mobilised, but still deplete and recycle within seconds. Finally, the reserve or resting pool (RtP) represents the majority of vesicles at the synaptic terminal. The RtP is the least easily mobilised vesicle pool and its vesicles are depleted over minutes (depletion only occurs under strong stimulation) and recycle over a similarly long time period. The vesicle pools are recruited in this sequential order. The RRP is primarily responsible for synaptic transmission under physiological firing conditions. It is able to recycle vesicles between action potentials under physiological conditions, and was first observed as quanta docked to the synaptic terminal (Rosenmund and Stevens 1996).

In the context of ERNA, however, the STN is experiencing unphysiological stimulation above the threshold required to observe vesicle depletion (Fernández-Alfonso and Ryan 2004). Under these conditions, simulations show the RRP depleted within approximately 10 pulses of stimulation at 100Hz (Kaeser and Regehr 2017). Hence, after prolonged exposure to unphysiological stimulation the majority of the vesicles responsible for synaptic transmission will belong to the RtP (Denker and Rizzoli 2010; Alabi and Tsien 2012). During the early stages of stimulation and vesicle depletion, the number of vesicles remaining at the terminal appears to follow an exponential decay (Alabi and Tsien 2012). Vesicle depletion of STN axonal efferents has been observed in response to STN-DBS in both in vivo and in vitro recordings (Rosenbaum et al. 2014).

Computational models characterising the effect of vesicle depletion on synaptic connectivity and the response of a vesicle pool to stimulation have previously been

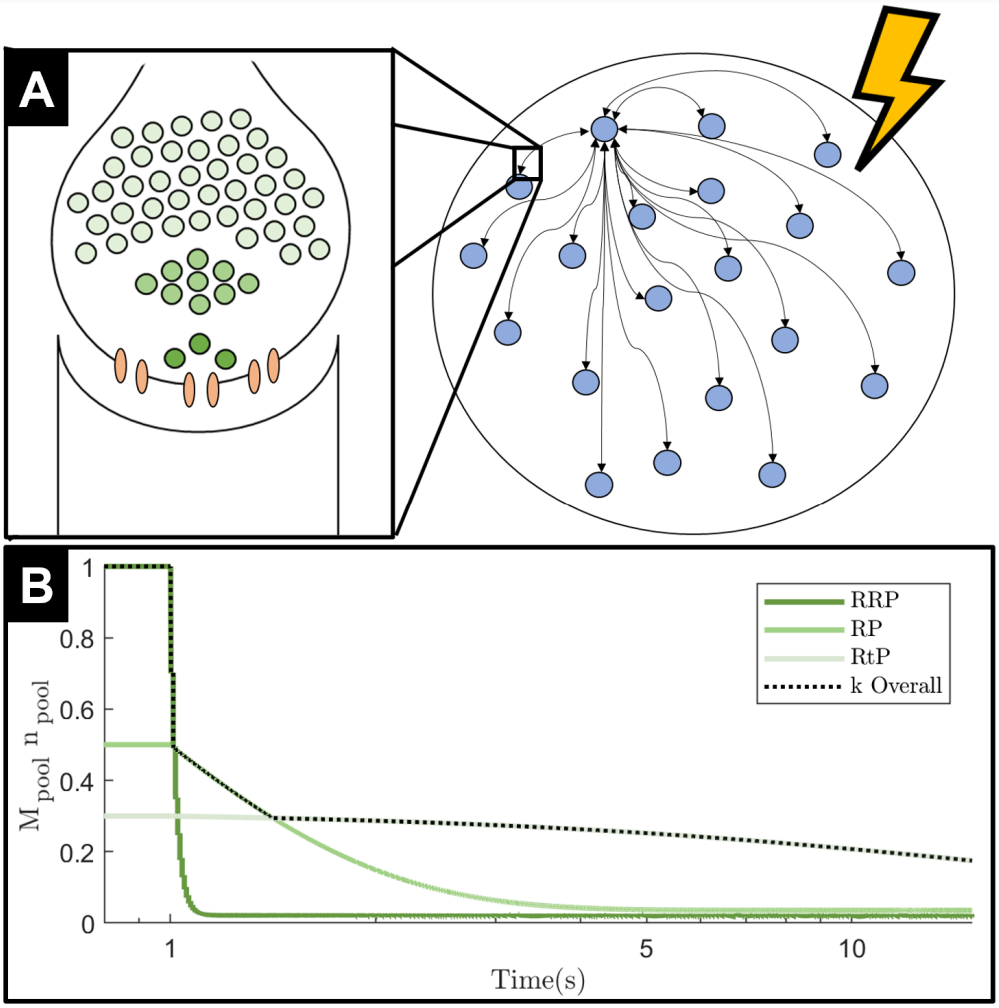


Figure 4.9: Modified Kuramoto model. (A) Right: One population of all-to-all connected Kuramoto oscillators (blue circles), which all receive stimulation of the same magnitude. Only showing bi-directional connections to one example oscillator. Left insert: We zoom in on the synaptic connections between each oscillator which are affected by vesicle depletion. The closest vesicle pool to the synaptic terminal is the RRP (darkest green), followed by the RP (lighter green). The pool furthest away from the synaptic terminal is the RtP (lightest green). Vesicle pool colours are consistent with colours used in panel B. (B) Coupling strength decay curve, with stimulation starting at 1s. The three green colours represent the contribution of each of the three vesicle pools. The black dotted line is the output of the maximum function in Eq (4.4), which dictates the overall coupling strength.

developed (Hennig 2013; Peterson et al. 2014). In the context of the three-vesicle pool model, the interaction of multiple vesicle pools has also been investigated across a range of pool occupancies (Neher 2015; Guo et al. 2015). We employ the first order kinetic model used in (Hennig 2013) to track vesicle pool occupancy. Given the time scale differences over which each pool depletes and replenishes, we model

the dynamics of each pool independently. This simplified approach is sufficient to capture the three different time constants of each vesicle pool (see Fig 4.9B) as seen in data (Rizzoli and Betz 2005). Following (Hennig 2013), we model the occupancy of each vesicle pool $n_{\text{pool}} \in [0, 1]$ (with pool $\in \{\text{RRP}, \text{RP}, \text{RtP}\}$) as

$$\frac{d\text{n}_{\text{pool}}}{dt} = \frac{1 - \text{n}_{\text{pool}}(t)}{\tau_{\text{pool}}} - \sum_j \delta(t - t_j) \cdot p_{\text{pool}} \cdot n_{\text{pool}}(t), \tag{4.3}$$

where τ_{pool} is the time constant of replenishment and p_{pool} is the probability of vesicle release in response to a stimulation pulse for the fitted stimulation amplitude for each vesicle pool. The values used for these parameters are estimated from the time taken to deplete and replenish each of the vesicle pools, respectively, according to data (Rizzoli and Betz 2005; Kaeser and Regehr 2017) – see Appendix B.1. In modelling the evolution of pool occupancy, we focus on the effect of stimulation and ignore spikes not triggered by stimulation. Thus, $\delta(t - t_j)$ is a Dirac function where the t_j's correspond to the time of stimulation.

We model the effect of depletion and replenishment of the three vesicle pools (given by Eq (4.3)) on coupling strength based on three assumptions. First, activity at a synaptic terminal directly corresponds to the number of vesicles released (Chamberland and Tóth 2016), and if fewer vesicles are released into the synapse, the effect of pre-synaptic activity on downstream neurons will be weaker. Thus, we model the effect of vesicle dynamics on coupling strength as proportional to the number of vesicles available.

Second, we translate the occupancy of each vesicle pool into its effect on coupling strength using a factor M_{pool}, which we estimate for each vesicle pool using data as the product of both the pool's relative size (Rizzoli and Betz 2005) and the inverse of its approximate distance from the synaptic terminal (Rizzoli and Betz 2005; Lou et al. 2012; Branco and Staras 2009; Qu et al. 2009; Staras et al. 2010; Südhof 2012; Dittman and Ryan 2019) (less readily-releasable vesicles further from the synaptic terminal have a lower release probability for a given stimulation (Lou et al. 2012)). The values used for the pool-coupling factors, M_{pool}'s, are given and justified in Appendix B.1.

Third, at any point in time, we only consider the effect on coupling strength of the dominant pool (largest $M_{\text{pool}} \cdot n_{\text{pool}}(t)$ at time t). This reflects the sequential nature of vesicle pool depletion and how one pool tends to dominate synaptic transmission at any point in time depending on depletion levels. This allows the vesicle depletion curve to take the form of an exponential decay with three time constants (Fig 4.9B) as seen in (Rizzoli and Betz 2005). Moreover, while on-stimulation coupling strength is impacted (in succession) by the depletion of each vesicle pool, the recovery of coupling strength following stimulation termination is chiefly determined by the replenishment of the RRP. Other vesicle pools do not appear to play a significant role as synaptic activity recovers at a similar rate regardless of the stimulation parameters used during the stimulation window (Fernández-Alfonso and Ryan 2004), i.e. regardless of how depleted the other pools are, which is consistent with this third assumption. Since the RRP is replenished much faster than other pools (within seconds following stimulation termination (Rizzoli and Betz 2005)), the RRP quickly resumes being the primary vesicle pool for synaptic transmission.

Based on these three assumptions, the coupling strength at time t is obtained as

$$k_t = k_\mu \cdot \max(M_{\text{RRP}} \cdot n_{\text{RRP}}(t), M_{\text{RP}} \cdot n_{\text{RP}}(t), M_{\text{RtP}} \cdot n_{\text{RtP}}(t)), \tag{4.4}$$

where k_μ is the steady state coupling strength of the network off stimulation.

4.4.1.2 Coupling Function and PRC

In addition to the modulation of coupling strength over time when the network is exposed to stimulation, we incorporate a second-order Fourier series coupling function f into the model and fit its coefficients (f_i), $i \in \{0, .., 4\}$ to data. The coupling function is thus given by

$$f(x) = f_0 + f_1 \cos(x) + f_2 \sin(x) + f_3 \cos(2x) + f_4 \sin(2x). \tag{4.5}$$

Compared to a sinusoidal or Hodgkin-Huxley-derived coupling function (explored in Appendix B.4.1), this more general coupling function allows the model to capture more complex interactions between neurons.

For the majority of this work, we consider a sinusoidal PRC, i.e. $g(x) = \sin(x)$. The inclusion of a second-order PRC was also considered, as well as sinusoidal and a Hodgkin-Huxley PRC (see Appendix B.4.2). The form of the PRC was not crucial to the intricate dynamics of ERNA as the coupling function was observed to be.

4.4.1.3 Distributions of Oscillators' Natural Frequency

Since the STN is a nonuniform neuronal structure, oscillator's natural frequencies are sampled from a normal distribution, $\omega_i \sim \mathcal{N}(\Omega, \sigma^2)$. We do not constrain the mean Ω and standard deviation σ to a pre-determined narrow frequency band in the fitting process to provide added versatility to the model dynamics. Some in vivo and in vitro recordings of STN neurons showed firing rates of around 20Hz off stimulation (Hallworth et al. 2003; Wilson et al. 2004). However, these recordings are from networks of neurons and may not represent isolated neurons' intrinsic firing rates. This may be supported by the observation of some high-frequency activity off stimulation in the STN (see 4 in Fig 4.2A). We present simulations with natural frequencies constrained to 20Hz in Appendix B.5.

4.4.2 Fitting Process

In order to find a set of parameters for the modified Kuramoto model that yield dynamics similar to ERNA, we fit the model to features of the slow dynamics of ERNA. The fitting methodology used in this chapter is similar to other computational studies (Duchet et al. 2020; Duchet et al. 2021 and Chapter 3) and uses the patternsearch MATLAB function to minimise a cost function representing the distance between the data features and the same features calculated in the model. The Kuramoto model was simulated using a Euler-Maruyama scheme with a timestep $\Delta t = 10^{-4}$s.

The cost function used in the optimisation process is calculated from the on-stimulation ERNA frequency decay (slow dynamics, Fig 4.1B). An approximation of the peak frequency of the ERNA decay in the STN for a trial of 130Hz and 3mA STN

DBS (patient on medication) was obtained using Fig 4.1B from (Wiest et al. 2020) as

$$f_{\mathrm{ERNA}}^{\mathrm{dat}}(t) = 260 + 80e^{-0.07t} \text{ Hz}, \tag{4.6}$$

where t is the time elapsed since DBS was turned on. The estimate $f_{\mathrm{ERNA}}^{\mathrm{dat}}$ is represented by the black line in Fig 4.1C. The Kuramoto model was then simulated for a period of 100 seconds on-stimulation following a 20 second settling period off-stimulation. The model's frequency decay $f_{\mathrm{ERNA}}^{\mathrm{mod}}$ was calculated as the maximum PSD frequency between 240-400Hz for a series of 100ms windows within the 100 second stimulation period. The cost of this feature was obtained as

$$\mathrm{Cost}_{\mathrm{On}} = \sum_{i=1}^{n_t} \left| f_{\mathrm{ERNA}}^{\mathrm{mod}}(t_i) - f_{\mathrm{ERNA}}^{\mathrm{dat}}(t_i) \right|, \tag{4.7}$$

where the t_i's correspond to sampling every 100 ms and n_t is the number of time samples.

Another spectrogram feature was used to limit high frequency activity before stimulation. This was done by calculating the maximum of the complex modulus of the order parameter, $|Z|_{max}$, a metric for the synchronisation of the oscillators in the network. The off-stimulation cost was defined as

$$\mathrm{Cost}_{\mathrm{Off}} = \begin{cases} 0 & \text{if } |Z|_{max} < 0.2, \\ (|Z|_{max}/0.2) - 1 & \text{otherwise}, \end{cases} \tag{4.8}$$

where the value 0.2 acts as a threshold under which the off-stimulation cost is zero, and above which the off-stimulation cost grows linearly with $|Z|_{max}$. The threshold of 0.2 provided enough of a contrast compared to on-stimulation activity, which tended to be much closer to 1.

The on-stimulation feature was chosen as the most important to replicate, and considering the scale of both features, the total cost corresponding to the slow dynamics of ERNA was evaluated as

$$\mathrm{Cost} = 0.9\mathrm{Cost}_{\mathrm{On}} + 0.1\mathrm{Cost}_{\mathrm{Off}}. \tag{4.9}$$

4.4.3 Simulation of Various Stimulation Paradigms

To ascertain the computational model's suitability for investigating ERNA, we validate its performance by subjecting it to various stimulation paradigms that replicate conditions explored across a range of clinical studies.

4.4.3.1 Long-Term Spectrogram

We replicated the long-term spectrogram reported in (Wiest et al. 2020), where DBS is turned on and off in a series of periods of varying lengths for a total of 1200 seconds of continuous observations (Fig 4.2A). In our simulations, stimulation is initially turned on for three 200 second periods separated by 40 second off-stimulation intervals. This is followed by an 80 second off-stimulation period and five 15 second on-stimulation periods with 55 second off-stimulation intervals in between. The on- and off-stimulation period durations were chosen to align most closely with the data (Fig 4.2A). All stimulation periods are at 130Hz and at the same stimulation amplitude as the model was fitted to (3mA). The simulation is initialised with all vesicle pools operating at 100% occupancy. White noise is added to the order parameter (extrinsic noise) using the 'awgn' function of MATLAB with a signal-to-noise ratio of 20. The signal-to-noise ratio and colourbar limits were chosen by visual inspection to resemble the background activity of the data.

4.4.3.2 Simulations for Validation with Variable Neuromodulation

In order to replicate ERNA dynamics in the model under variable stimulation amplitude, as well as in the absence of medication, adjustments to the model have to be made. We provide simple, biophysically-motivated changes to the model and fit the changes by manual parameter tuning to the ERNA frequency in the data (Wiest et al. 2023) at the end of the stimulation window. To validate these changes, we then compare the amplitude of ERNA in the model to that of the data.

Variable Stimulation Amplitude Unlike stimulation frequency, the scale of stimulation amplitude in the model cannot be directly compared to the stimulation amplitude used in the data. This makes interpretation of the stimulation amplitude (I) range more difficult. We assume that increasing stimulation amplitude will increase the rate of vesicle depletion by depleting more vesicles in response to each stimulation pulse, which corresponds to an increase in p_{pool}. Increasing stimulation amplitude should therefore result in similar effects to increasing stimulation frequency in data (Schor and Nelson 2019). We model the effect of changing stimulation amplitude by replacing p_{pool} in Eq (4.3) by

$$p_{\text{pool},I_{\text{fact}}} = p_{\text{pool}} \frac{1}{5} \left(4 + \frac{1}{I_{\text{fact}}}\right), \tag{4.10}$$

where I_{fact} is the stimulation amplitude modulation factor (see Eq (4.2)). These modulations are only appropriate for stimulation amplitudes close to one. Fig 4.4 shows results for stimulation amplitude factors, I_{fact}, between 0.8 and 1.1 (with I_{t} given by Eq (4.2)).

Variable Medication State Medication state is not a direct input to the model, however, like stimulation amplitude the influence of medication state can be included in the model. Before STN-DBS was employed for the treatment of PD, Levodopa was already an established pharmacological option. As such, research is available on Levodopa's effect. Levodopa has been reported to increase long-term potentiation and depression (Calabresi et al. 2015), corresponding to a general increase in longer term spike-timing-dependent plasticity (STDP) dynamics when on Levodopa. In order to maintain long-term STDP dynamics, synaptic terminals are required to maintain higher vesicle pool occupancy to be able to fire when required and modulate synaptic activity accordingly. This may reflect an increased rate of long-term vesicle recycling on-medication. Hence, we adjust the time constant of vesicle recycling for the RtP. We increase the off-medication state ($\tau_{\text{OffMeds,RtP}} = 60$, from $\tau_{\text{OnMeds,RtP}} = 50$) by manual fitting to the final ERNA frequency after 120 seconds of stimulation.

4.4.3.3 Simulation for Validation with Biophysical Evidence

Studies that focus on properties of the STN provide additional information to constrain and assess the computational model.

Replication of In Vitro Slice Experiments Lastly, we aim to reproduce firing rates of STN neurons explanted from rats exceeding 250Hz under in vitro conditions with constant current stimulation (Kitai and Kita 1987; Hallworth et al. 2003; Wilson et al. 2004). These in vitro slices represent neurons mostly disconnected from the rest of the STN. To replicate this condition in the model we reduce the network down to the fewest number of oscillators for which coupling can exist, two oscillators. In order to capture the absence of GABAergic input to the in vitro slice after removal from the brain, we increase the shift of the coupling function between the two oscillators. We adjust the shift of the coupling function so that both oscillators progress with a frequency of approximately 20Hz (f_0 from -0.780 to -0.110 in Eq (4.5)) as seen in the off-stimulation data (Kitai and Kita 1987; Hallworth et al. 2003; Johnson et al. 2023). Constant direct current stimulation is then applied. The stimulation amplitude is adjusted from the value the full model was fitted to by a factor $130 \times \Delta t = 0.013$ to deliver the same stimulation intensity per oscillator in this simulation as in the 130Hz pulsatile stimulation case in the full model. We approximate the instantaneous frequency of the i^{th} oscillator at time t as

$$\nu_{i,t} = \frac{\theta_{i,t+1} - \theta_{i,t}}{2\pi\Delta t}, \tag{4.11}$$

which is then smoothed (moving average, 100ms window) to reduce the effect of noise.

4.4.4 Evaluation of ERNA Frequency and Amplitude Over Time

We visualise the computational output in a manner consistent with the approaches used in the corresponding experimental paradigms (Wiest et al. 2023). We consider the real part of the order parameter Z to approximate the neuronal signals from data, in line with (Weerasinghe et al. 2019). Spectrograms are calculated both

on and off stimulation using the 'pwelch' MATLAB function applied to the real part of Z over 100ms windows. There are no notch filters in place at stimulation frequency or the harmonics as the artefacts of stimulation in the real part of Z of our model are relatively small or nonexistent. The ERNA frequency evolution over time is calculated by finding the frequency of maximum PSD on-stimulation for each of the 100ms windows. ERNA amplitude is calculated by taking the complex modulus of Z. In the data, each second a pulse is skipped to allow for the frequency and amplitude of the evoked response to be recorded. We do not suffer from the same obstacles of stimulation artefact in the model, but we take a similar approach. Both ERNA frequency and amplitude are averaged over moving windows of one second to match the windowing from the data.

4.4.5 Statistics for ERNA Amplitude On and Off Medication

We performed a statistical analysis to determine whether the frequency response differed significantly between medication states, taking the same approach as in the experimental study (Wiest et al. 2023). We used a non-parametric permutation test with 1,000 permutations at each time point across the 15 different simulations for each medication state. This allows us to identify where the different medication states form significantly different clusters. We identify the stage of the simulation where p-value did not extend higher than 0.05 (after this point it did not exceed 0.023, slightly higher than the data (Wiest et al. 2023), 0.013) for the remainder of the simulation window.

4.5 Discussion

In this chapter, we investigated the ability of a single-population phase oscillator model with no network delays to reproduce the key characteristics of ERNA slow dynamics. We showed that when fitted to an approximation of the ERNA frequency decay obtained from patient data, the model is able to reproduce the main characteristics of ERNA slow dynamics. One of the key model additions to replicate

these characteristics is the inclusion of synaptic vesicle depletion as a result of high-frequency stimulation. The model represents a simplification compared to models previously used to study ERNA, while also being able to reproduce characteristics over longer time periods and in response to a wide range of neuromodulatory perturbations. Importantly, the model demonstrates that ERNA slow dynamics can be reproduced with a single neuronal population without dynamic inputs from other structures. This work highlights the fundamental properties required of a phase-oscillator network to reproduce the slow dynamics of ERNA. This information may prove useful in the development of the clinical understanding of ERNA.

4.5.1 Hypothesised Mechanisms and Models of ERNA

Several mechanisms have been hypothesised to explain ERNA in STN-DBS (see Wiest et al. 2023 for a summary). These hypothesise are commonly aligned with the inhibition, excitation and antidromic activation as covered in Section 1.2.3.4. One hypothesis that has gained support is the network between the STN and GPe recurrently modulating activity in both structures. This recurrent network adds delays which through an excitatory-inhibitory loop would explain the promotion of oscillatory activity seen in ERNA (Steiner and Milosevic 2023). This theory is supported by the observations that STN-DBS tends to increase firing rate in the GPe with a pattern resembling ERNA (Hashimoto et al. 2003; Reese et al. 2011), as well as pallidal-DBS producing ERNA in the pallidum of patients with PD (Johnson et al. 2023). It was also demonstrated that a computational model assembled in line with this theory was able to produce ERNA-type responses over an approximately 20ms time period following a stimulation pulse (Schmidt et al. 2020). However, (as discussed in Wiest et al. 2023) extended high-frequency stimulation to the STN would likely lead to depletion of the synapses connecting the STN and GPe preventing the oscillations from continuing over an extended period of time (functional disconnection) (Bergman 2021). This would not allow for the persistent high frequency and high amplitude ERNA remaining after multiple minutes of

stimulation observed in data. To address this shortcoming of the patterned STN-GPe network firing hypothesis it was proposed that DBS may initiate orthodromic activation of terminals to the stimulated structure (Steiner and Milosevic 2023). This activation could also lead to delayed excitation and inhibition, therefore promoting the oscillatory behaviour of ERNA over a longer period of time.

A recent modelling study was able to replicate some of the key ERNA characteristics over a time period of approximately 200ms using a phase oscillator network (Realmuto et al. 2023). The Kuramoto network included delays between distinct sub-populations of oscillators, which would likely be a fundamental reason as to why the network was able to reproduce these evoked oscillatory responses. However, each of these sub-populations were chosen to represent separate basal ganglia structures (globus pallidus internus (GPi), ventral intermediate and the STN). Hence, this model encounters the same functional disconnection contention as proposed by Bergman et al. (Bergman 2021). The network could instead be chosen to represent multiple sub-populations of neurons within a single basal ganglia structure (e.g. the STN for STN-DBS), however, this would likely affect the time constants of inter-sub-population delays due to proximity and connectivity. Additionally, it has been demonstrated that there exists a diverse range of responses to stimulation within neural structures as DBS leads pass through both the STN (Wiest et al. 2022) and pallidum (Cleary et al. 2013). Hence, it is important to explore how closely a single population can reproduce characteristics of ERNA to avoid these contentions and as we investigated in this chapter. However, when considering STN-DBS, the existence of functional connectivity in the STN has been disputed (Steiner et al. 2019). We explored the necessity of intrinsic connectivity of the single population model in this chapter (see Section 4.3.7).

Other computational models have looked at responses evoked by DBS (Basu et al. 2018; Detorakis et al. 2015). These studies closely reproduce characteristics of ERNA fast dynamics for approximately 0.5 to 2 seconds following the immediate initialisation of stimulation. They achieve this through including multiple structures with delays. We instead focus on reproducing long-term ERNA dynamics over

multiple minutes, which has yet to be explored. Additionally, we further expand on the work of previous models by focusing on a model of a single structure, the STN. This avoids the reliance on delays from the network to produce the resonant activity, which would likely experience synaptic failure over this longer time scale (Bergman 2021). This has not been previously considered in models due to many focusing on the short-term responses. In fact, we build synaptic vesicle depletion into the model, which is a fundamental reason the model is capable of reproducing the long-term ERNA dynamics. Additionally, by focusing on a single structure we reduce the number of model parameters which will help to prevent the likelihood of overfitting the model to data. We go beyond these previous studies by modelling ERNA over longer periods of stimulation, and in response to a wider variety of stimulation paradigms to validate our approach.

4.5.2 Proposed Computational Model

Across the many ERNA characteristics discussed in this chapter, we provide a preliminary validation for the modified Kuramoto model across multiple states and inputs. The model demonstrates that it has the required versatility to replicate the frequency shift between off and on-stimulation states as well as the slow dynamics of the spectrogram. The model provides a close reproduction of the frequency decay, despite being a simplification of the system that it is representing. Furthermore, we attempt to biophysically ground and validate the model.

Validation with Variable Neuromodulation The model is able to replicate the frequency and amplitude behaviours for variable inputs and states. In some cases, biophysically-motivated parameter changes are made by manual parameter tuning to match the initial and final frequency values in each of these conditions. However, these parameter changes also provide amplitude responses similar to the data without using these responses as features for fitting. The parameter tuning is only on one parameter and only by a small factor, which does not change the fundamental model dynamics. No tuning was required for the variable stimulation

frequency example which provided the closest replication of the data for both the frequency and amplitude responses.

All variable neuromodulation approaches provided comparable approximations to ERNA dynamics when comparing the mean of the model simulations (Figs 4.3, 4.4 and 4.5). However, the standard error of the mean is much smaller in the model than the data. Each model simulation corresponds to different realisations of natural frequencies, initial conditions and noise, with the ω_i's and white noise drawn from their respective distributions. In the data the different recordings are from different subjects. Hence, to provide more accurate approximations to different subjects we would likely be required to change the parameter set.

Importance of Multiple Vesicle Pools The key modification of the computational model that enables the replication of long-term ERNA characteristics is the multiple vesicle pools. The results (Figs 4.1, 4.3, 4.4 and 4.5) appear to demonstrate frequency decays with at least two rates, in addition to the very fast RRP dynamics. We interpret these different rates of frequency decay as the initial depletion of the RP within the first 5 seconds, followed by depletion of the RtP in the remainder of the stimulation window (see Fig 4.9B). The RRP plays a crucial role in determining the frequency of the network immediately before and after stimulation onset as well as in the post stimulation recovery.

Underlying Oscillator Dynamics We investigate the underlying oscillator behaviour in order to understand how the model is capable of replicating both the frequency and amplitude responses (see Appendix B.2).

Considerations for Other Neural Structures and Across Patients Recent publications have shown that ERNA is not solely a property of the STN (Johnson et al. 2023), however the frequency response can be quite different between structures in particular. While maintaining a similar coupling function, the interaction between individual oscillator natural frequencies as well as coupling strength in the network can be modified to accommodate these changes. In the off-stimulation state, only

natural frequency and coupling, k_μ, affect the phase progression of each oscillator. These parameters and how the coupling strength evolves with time on stimulation (through parameters τ_{pool} and p_{pool}) can be changed to control the frequency that ERNA appears at and decays to. In structures for which ERNA is not observed (for instance in the cortex which is also a common site of neurostimulation) vesicle depletion will still be present. Instead, the other key properties of the model, not having the high natural frequency of the neurons and the coupling function (Fig 4.1E) are the likely factors that prevent other structures producing ERNA. Other responses to DBS that have dynamic frequency profiles, but at much lower frequencies have been observed (Tiruvadi et al. 2022). We investigate the effect of decreasing the natural frequencies of the oscillators in these results (Appendix B.6).

4.5.3 Model Predictions for Further Validation

This chapter has compared model predictions to previously published ERNA data, and in this section we highlight predictions corresponding to conditions for which experimental ERNA data is not available at the time of writing.

Only One Neuronal Population's Dynamics are Required to Produce ERNA The model used in this chapter only requires one neuronal structure with no loops of reciprocal feedback between different structures. Long-term recordings from the STN disconnected from the pallidum in either human or rodent models would clearly demonstrate the role of these inter-structure connections and their necessity to ERNA. Furthermore, recordings of synaptic activity between the STN and GPe after persistent STN-DBS would indicate whether functional disconnection or vesicle depletion is present.

Vesicle Depletion may be Necessary for ERNA Vesicle depletion was one of the fundamental additions to the model. Tracking vesicle depletion could be done through observing the number of vesicles at synaptic terminals during cDBS as vesicle pool sizes have been observed previously (Rizzoli and Betz 2005). This could be challenging to do continuously, however, and instead a micro electrode

study of multiple STN neurons in the presence of DBS could be used to track firing times over the stimulation window. In particular, tracking clustered firing times (following clusters as discussed in Appendix B.2.1) which are expected to evolve with vesicle depletion may be a more realistic validation. Specifically, we would expect firing clusters to be somewhat equally split between at least two clusters before stimulation. Following stimulation onset, firing times will be dominated by one cluster, but this will reduce in dominance over the stimulation period as vesicle depletion occurs. Additionally, using a pharmacological option that modulates vesicle re-uptake will modify the time constants of vesicle depletion. This in turn should modulate the time constants of ERNA frequency decay, which would provide evidence of the necessity of vesicle depletion.

Key Features Required for Coupling Function Coupling functions between neurons are difficult to measure. However, methods to calculate PRCs are well established (Nabi and Moehlis 2011) and coupling functions are an area of active investigation (Gardella et al. 2016). In the absence of methods to measure coupling functions, tracking firing clusters we would be able to evaluate the model's multiple zero-crossing point prediction. Off-stimulation recordings would likely show neuron firing times grouped into as many clusters as there are zero-crossing points.

High Natural Frequency of Neurons is Necessary for the Frequency Decay It is a fundamental property of the model that the oscillators have an intrinsic ability to fire at much higher rates than the off-stimulation network firing rate. We therefore predict that neurons that produce ERNA can fire at much higher frequencies in a fully disconnected state, in addition to having the capacity to fire at much higher rates (Kitai and Kita 1987; Hallworth et al. 2003; Wilson et al. 2004; Schor et al. 2022).

4.5.4 Limitations

ERNA Fast Dynamics The model in its current form is unable to replicate the characteristics of ERNA that are associated with the fast dynamics of vesicle

depletion (see Appendices B.3.1 and B.3.2). The model parameters were fitted to the characteristics of ERNA slow dynamics, which had previously eluded all modelling attempts. It is therefore not surprising that the model's fast dynamics response does not line up as closely with the data as the long-term characteristics. In the data, we see growing inter-pulse evoked potential amplitude over the first 10 pulses before the amplitude steadies. Following termination of stimulation, the high amplitude evoked potentials behave similar to a damped oscillation returning to its pre-stimulation levels over around 20ms (Sinclair et al. 2018). We are able to capture some, but not all of the characteristics of the fast dynamics with our model. In particular, the inter-pulse evoked potentials do not decay between pulses and appear far more sinusoidal and noise-free than the data. Furthermore, oscillations following stimulation offset are not damped (see Appendix B.3.1 for more details).

The model produces higher frequency evoked potentials with low-frequency stimulation. However, unlike the data (Ozturk et al. 2021; Zapata Amaya et al. 2023), the model still produces high frequency activity. We demonstrate that if vesicle depletion did not occur at all with low-frequency stimulation, we would observe results similar to the data (see Appendix B.3.2). If the absence of vesicle depletion is the mechanism that maintains low frequency activity in response to low frequency stimulation, then it is likely a deficiency in the model's ability to replenish fast enough between pulses that prevents us from capturing this response here. Hence, both the shortcomings of inter-pulse activity and response to low-frequency stimulation in the model likely stem from the same cause. We do not model the biophysical details in the dynamics of the RRP in the model and this may prevent us from capturing the short-term dynamics. Further investigation into the recycling of other vesicle pools into the RRP may provide valuable versatility to the dynamics of the model.

Blind Validation of the Model This chapter provides no fully blind validation of the modified Kuramoto model to the ERNA data. Despite reproducing a wide breadth of ERNA characteristics, the authors were not blinded to any of the data

(even the characteristics used for validation, such as amplitude response in the variable neuromodulation sections). This is why this chapter is presented as a theoretical neuroscience investigation with predictions noted for future validation in other studies. However, we still manage to replicate a wide range of previously observed ERNA characteristics, a number of which could not be replicated by more complex previously published models.

Glutamergic/GABAergic Properties of the Coupling Function The fitted second-order coupling function is strongly negatively skewed. For a single, isolated population describing the STN, this makes the biophysical interpretation of the coupling function difficult given that the STN is glutamergic (Bolam et al. 2009; Worbe et al. 2010). However, even in the off-stimulation state the Kuramoto oscillators synchronise into clusters that provide phase advancing effects on the clustered oscillators, as the coupling function is slightly positive at a phase difference of zero (Fig 4.1E). This would indicate a glutamergic tendency of the network. We interpret the negative shift of the coupling function as a phase indiscriminate GABAergic input from the GPe to the STN. This manifests itself in the model as providing a phase advancing and glutamergic (STN dominated) effect when oscillators are synchronised, but phase delaying and GABAergic (GPe dominated) effect when the oscillators are not.

Other Biophysical Simplifications We only simulate 50 coupled phase oscillators representing a larger neuronal network responsible for ERNA. While the number of phase oscillators is lowered for computational efficiency, the network's behaviour approximates that of a larger neuronal population. Additionally, we do not consider the effect of different types of neurotransmitters. Instead, we only model the impact of total vesicle availability to coupling strength. The interplay of multiple types of neurotransmitters and their dynamics between stimulation pulses may have to be considered to provide a more accurate representation of the oscillatory behaviour. Furthermore, the STN receives dynamic inputs from the GPe, cortex and other areas of the brain. Although we demonstrate here that only modelling one population's

dynamics is sufficient to replicate the slow dynamics of ERNA, including inputs from other neuronal structures may be key to reproducing the fast dynamics of ERNA.

4.6 Conclusion

This chapter demonstrates that it is possible to replicate the long-term characteristics of ERNA by only considering the dynamics of a single neuronal structure. While the proposed computational model remains to be validated using follow-up data, this work has the potential to provide insights into the underlying mechanisms of ERNA. Biophysiological properties of the model key to reproduce ERNA activity are revealed to be vesicle depletion, key properties of the coupling function, and high natural frequency of individual oscillators. These properties may inform future investigations into the underlying mechanisms of ERNA.

5
General discussion

Contents

5.1 Contributions 124
5.2 Implications 126
5.3 Common Threads 128
5.4 Limitations 129
5.5 Future Work 130
5.6 Concluding Remarks 133

In this thesis, we characterised a diverse range of responses to DBS from both physiological and artefactual origins. We have captured the stationary response of entrainment and the dynamic response of ERNA using computational models. These models shed further light on the mechanisms of DBS, as well as direct research for novel stimulation approaches through modulating neural activity at specific frequencies with DBS. As the understanding of correlation between the modulation of neural activity at specific frequencies and clinical effect develops, the results presented in this thesis have the potential to inform optimal stimulation parameters to achieve a desired clinical outcome. This impact may be realised through understanding how to avoid negative effects as well driving beneficial rhythms (as has been preliminarily explored in Section 1.2.4.3). Overall, this thesis may provide new insights into how neuromodulation parameters may be used to

achieve tailored stimulation approaches, optimised for patient outcomes.

5.1 Contributions

Neurotechnology

Contributions pertaining to Chapter 2

- We provide a detailed review of the most commonly hypothesised sources of half harmonic artefacts in the sense-stimulation signal pathway and an accompanying checklist for brain computer interface engineers to test their devices against.
- We identify how stimulation artefacts can arise within the signal chain pathway and provide tools or indicate options that can be taken to avoid these artefacts.

Contributions pertaining to Chapter 3

- For sense-stimulation devices used for the purpose of exploiting half harmonic entrainment, we show that a larger area of entrainment likely exists and that stimulation frequency can be chosen accordingly in line with the observations from Chapter 2 to limit aliasing artefact. This therefore limits the necessity of designing specialised artefact removal algorithms.

Neuroscience and Neurology

Contributions pertaining to Chapter 2

- We show that 1:2 entrainment of motocortical FTG in PD patients is unlikely to be of artefactual origin.
- We provide a framework to assess whether a signal at a sub-harmonic of the stimulation frequency is likely to be of physiological or artefactual origin. This is especially important when it is not possible to guarantee that all sources of artefacts have been completely eliminated.
- For 1:2 entrainment of motocortical FTG in PD patients undergoing DBS:

  - We show that neural structures can respond nonlinearly to stimulation. Importantly, demonstrating that entrainment can be lost by increasing stimulation amplitude.
  - We demonstrate that there are predictable (and in some cases unexpected) features of the Arnold tongue, such as the left lean.
  - We document that the entrained rhythm's spectral power increases with decreasing stimulation frequency and amplitude in patient data. This will be important if the amplitude of entrained activity is related to clinical outcomes.
  - We demonstrate that there commonly exists a large region of stimulation parameters that can result in 1:2 entrainment. This may be important when considering impacts of entrainment at different frequencies as well as the interplay of multiple neural rhythms with stimulation.

Contributions pertaining to Chapter 4

- We show that a single population of oscillators is sufficient to capture the long-term ERNA characteristics.
- We observe that vesicle depletion in response to high-frequency stimulation is potentially a fundamental mechanism in the ERNA frequency and amplitude dynamics with time on stimulation.
- We predict the key biophysical properties of a neural structure capable of producing the slow dynamics of ERNA and make predictions that can be tested by clinical researchers to validate or invalidate our model.

Computational Neuroscience

Contributions pertaining to Chapter 3

- We show that a Wilson-Cowan model fitted to off-stimulation patient data can reproduce some of the properties of Arnold tongues measured in PD patients in response to DBS.

- We provide synthetic models of ECoG FTG data off-stimulation that could be used as a tool to further refine stimulation protocols or even to investigate novel stimulation paradigms.

Contributions pertaining to Chapter 4

- We introduce a model that can reproduce the long-term characteristics of ERNA, where models had only previously been used to reproduce ERNA over hundreds of milliseconds.
- We demonstrate that a phase oscillator network of a single population is sufficient to capture ERNA slow dynamics.
- We provide a model that offers a simplification in terms of number of parameters, number of oscillator populations and without including delays, when compared to previously published models that focus on ERNA.
- By analysing the behaviour of individual oscillators in our model, we are able to predict the mechanisms by which ERNA frequency and amplitude are able to change over long-term stimulation periods.

5.2 Implications

In this section we summarise the key implications of this thesis.

Provided sufficient checks are performed as described in Chapter 2, researchers may therefore study sub-harmonic entrainment with confidence. Additionally, given that we have now demonstrated that artefacts can be avoided and recent work has shown that sub-harmonic entrainment can be used as a biomarker to provide clinical benefit, there may be additional interest to clinically exploit this phenomenon. Future device design and clinical approaches that use sub-harmonic entrainment should also be aware that sub-harmonic artefacts can arise and they should take steps to mitigate against this. Chapter 2 aims to outline the key considerations to achieve this and therefore should make it easier to prevent sub-harmonic artefact contamination in future clinical studies.

Chapter 3 contributed to demonstrating the nonlinear responses of neural structures to DBS. In Chapter 3, we demonstrated the loss of entrainment with increasing stimulation amplitude as well as the increase of entrained rhythm amplitude with decreasing stimulation frequency. Both of these points represented fundamental revaluations of the clinical understanding to therapeutic brain stimulation protocols based on entrainment. These findings bring new awareness to the consideration of entraining beneficial rhythms and avoiding pathological rhythms at harmonics of stimulation frequency to therapy development. It is hoped that these findings can provide new insights to into how neuromodulatory parameters can be optimised to patients and pathologies. While we focused on 1:2 entrainment in Chapter 3, the potential to entrain at a range of different sub-harmonic (and supra-harmonic) ratios exists. Furthermore, without understanding how entraining specific rhythms to a certain frequency affects clinical outcomes, it is necessary to be aware of how stimulation may affect neural activity around all harmonics.

In Chapter 4 we provide the first model of ERNA slow dynamics. In addition, we demonstrate that a network of multiple neural structures with feedback and delays is not required to reproduce these ERNA characteristics. The understanding of the underlying mechanisms of ERNA is still at a very early stage and there have been multiple hypotheses proposed. However, only the hypothesis of a STN-pallidal feedback circuit has been explored through computational modelling so far. It is important to explore all plausible hypotheses, especially considering the points of contention around synaptic failure of the STN-GPe circuit in response to high-frequency stimulation. As part of Chapter 4, we propose potential key mechanisms to eliciting ERNA in a single population through vesicle depletion. This work can refine future investigations into the underlying mechanisms of ERNA and potentially improve our understanding of the target structures and mechanisms of both contact selection and aDBS.

5.3 Common Threads

Detailed discussions of the relevant content are provided in the associated chapters. Here, we discuss the common threads that connect the individual chapters together into a single thesis of wider implications.

Chapter 2 is a necessary clarification in order to proceed with confidence to Chapter 3. Unlike Chapter 4, where the physiological origin of ERNA has been confirmed (Sinclair et al. 2019), half harmonic entrainment still provided a point of contention when work commenced on this thesis. Hence, in order to ensure maximum impact of the findings of the modelling work on 1:2 entrainment as well as its feasibility, it was first necessary to demonstrate that this phenomenon was not an artefact. While we focus primarily on 1:2 entrainment in both Chapter 2 and 3, it would be straightforward to adapt the artefact checking and modelling methods to explore other sub-harmonics as well.

Across sub-harmonic entrainment (Chapter 3) and ERNA (Chapter 4) we have been able to produce models that capture both neural phenomena that have raised some of the most perplexing questions from this generation of sense-stimulation devices. Within these two models, we may also have generalisable themes across stationary frequency responses to stimulation in Chapter 3 and dynamic frequency responses to stimulation in Chapter 4. These models predict independent mechanisms to each phenomenon and while some supra-harmonic entrainment can be seen in the results from Chapter 4, it does not play a fundamental role in the resulting dynamics. Hence, the proposed mechanisms could be seen to work together to reproduce the diverse range of responses to DBS.

Through Chapters 3 and 4, we develop models that are as simple as possible while being able to capture the phenomena of interest. In Chapter 3, the sine circle map does not have an amplitude which prevented us from fitting it to data, hence, we used the Wilson-Cowan model. In Chapter 4, the standard Kuramoto model was not able to reproduce the ERNA decay, so we added a custom coupling function and vesicle depletion. In both cases the models have predictive power, being capable of predicting the response of each phenomenon to variable stimulation.

5.4 Limitations

In this thesis, both models presented would benefit from further validation against more datasets. Chapter 3 presents new data and through a novel method of analysis. However, this chapter would benefit from running the same protocol in a larger group of patients to further identify generalisable features of 1:2 FTG entrainment. Additionally, it would be of interest to identify generalisable features of entrainment across a wider range of patients to observe pathology dependence as well as over different times of day to observe circadian dependence. In Chapter 4, we compare the responses of the model across a wide range of neuromodulation paradigms. However, we were aware of all of these findings before the final results of the model were achieved. Hence, there is no fully blind validation of the model at this stage. The model presented in Chapter 4 would benefit from additional data collection to verify some of the predictions made from the model.

The models presented in Chapters 3 and 4 represent biophysical simplifications of the systems that they represent. For both of these chapters we consciously chose models that limited the number of parameters required for fitting the model to the data. This decision was taken in order to improve computational efficiency of the simulations and also in order to avoid overfitting to the data. In both cases these choices are justified as the models are capable of reproducing the features that they were designed to. However, we must be cautious about extrapolating the findings of the model beyond this.

When implementing the findings of the models discussed in Chapters 3 and 4, we must also be cautious to consider their long-term application. Early clinical reports indicate the adjustment of the network to persistent modulation can be observed from long-term stimulation (over the course of months). In these cases, the frequency of the network remains modulated closer to the half harmonic of stimulation when stimulation is turned off than the natural frequency of the network was prior to stimulation. Therefore, there likely exists plasticity dynamics of the network that take effect over longer time frames than considered in this thesis. Additional parameters could be added to these models in order to introduce these

dynamics, for example through STDP (Tass and Majtanik 2006) in phase oscillator models or population activity-dependent plasticity (Abeysuriya et al. 2018) in mean field models. However, at this stage there is not enough data to confidently hypothesise the mechanism or its associated time constants.

There is no consideration of the effects of circadian perturbation in these models. In both Chapters 3 and 4, the data that the model was fitted to was consistently taken within the awake states of patients around the middle of the day. This may have had the effect of improving the consistency of the results, therefore making the data easier to fit to. However, as demonstrated in (Smyth et al. 2023) sub-harmonic entrainment has been observed to be modulated by sleep-wake state. Hence, it may be possible that there exists neural circuit dynamics that are modulated by time of day, which we do not currently consider. Like with the long-term effects of stimulation, there does not exist enough data on the effects of circadian rhythms on either entrainment or ERNA at this stage. Considerations of this important feature would be necessary to include in any chronic adaptive algorithm, in order to provide maximum clinical benefit.

There is an absence of direct links to the clinical relevance or potential outcomes in both of the models presented in this thesis. The clinical relevance of 1:2 FTG entrainment has only recently been established (Oehrn et al. 2023). However, there are still many remaining questions regarding the relationship between entrainment and clinical outcomes. Similarly, while ERNA was shown to be the strongest predictor for contact selection (Xu et al. 2022), it is unclear whether it is correlated with symptoms. A common contribution to this limitation across both Chapters 3 and 4 is the lack of understanding regarding desired neural activity for improved clinical outcomes. If this was to be identified, both of these models might present useful tools in order to aid these clinical investigations.

5.5 Future Work

Future work building on our artefact investigation. As mentioned in Section 2.6.1, it is difficult to completely rule out the potential for artefacts con-

tributing to a recorded signal. This represents an important next step in the artefact investigation regarding entrainment as there will always remain doubt (no matter how small) that some aspect of the signal chain has remained unchecked. Setting up cortical MERs during STN-DBS implantation in a PD patient following Levodopa administration would be able to confirm physiological origin beyond any doubt.

Chapter 2 represents a comprehensive overview of potential causes of artefacts in current systems across currently identified potential sources. However, the framework presented in this will continually require reviews and updates as the technology advances. As mentioned in Chapter 2, nonlinearities in the electrical signal chain are required to observe sub-harmonic artefacts. As technology advances and we will be able to stimulate with a wider variety of pulse shapes or multiple active electrodes simultaneously and a wider variety of more complex ADCs or signal filtering methods will become available. Each of these represent potential artefact sources and will have to be investigated and mitigation methods resolved to avoid the appearance of sub-harmonic artefacts.

While we are able to characterise certain sense-stimulation devices to show that they do not provide sub-harmonic artefacts, it would be beneficial to the field to identify what components of these devices can induce these artefacts. As with our characterisation of the ADCs where we demonstrated that it was possible to avoid sub-harmonic artefacts, we also identified conditions where ADCs would produce sub-harmonic artefacts. The PINS device has shown it is possible to produce sub-harmonic artefacts with the stimulators. Hence, to provide the most value in this section of our analysis and inform future device designers, it would be necessary to identify the components and conditions that can produce sub-harmonic artefacts in this system.

Future work building on our entrainment study. For clinical use, it is important to understand whether sub-harmonic entrainment is possible for all neural rhythms and understand how these rhythms should be modulated for the best clinical outcomes. As stated in Section 1.2.4.2, there exist examples of entrainment

(primarily 1:1) of multiple different neural structures and rhythms. The work presented in this thesis contributes to the question of how DBS affects neural structures, but to have the optimal clinical approach we need to understand what the target state of this modulation is. A key additional rhythm to investigate with entrainment would be beta. Beta has already been investigated with early aDBS algorithms in PD and has demonstrated the ability to affect clinical outcomes (Little et al. 2013; Little et al. 2016). Hence, this may offer a complementary rhythm to FTG in PD for aDBS to target. However, beta has not been studied with entrainment in mind, only attempting to suppress it with stimulation frequency much higher than the beta frequency. Therefore, it could be of clinical relevance to investigate if modulating beta activity (either in frequency or amplitude of the beta signal) would be able to provide additional benefit.

In line with improving clinical outcomes, a benefit of the computational approach is that we can simulate the models to devise the optimal stimulation parameters or even waveform. Investigations into this have already started into devising methods to optimise the stimulation therapy in a way that could not be approached experimentally using trial and error (Duchet et al. 2023). In this thesis, we have already explored different recharge lengths and waveforms (Appendices A.5.2 and A.5.3). Combining these methods with patient specific models could provide an adequate prediction of the neural response to stimulation and could provide a valuable tool in delivering optimal clinical outcomes. However, this work depends on the understanding of clinically beneficial neural states.

Furthermore, it is important to find optimal methods of charting Arnold tongues of interest. There are currently limitations in estimating an accurate representation of the stimulation amplitude axis. Additionally, from the analysis presented in Chapter 3, it is unclear how generalisable the properties of the Arnold tongues are between patients. A robust method to corroborating the models would benefit the clinical approach. An initial attempt at this has been made (which currently the subject of a patent application).

Future work building on our model of ERNA. In Chapter 4, we lay out clear hypotheses that look to validate our model as well as providing further understanding to this phenomenon. These include investigations into vesicle depletion, single population dynamics, coupling and the underlying natural frequency of neurons in regions that produce ERNA. For each prediction provided in Section 4.5.3, we also describe experiments that could be used to validate it.

While the model in Chapter 4 provides a close approximation of the long-term dynamics, work is required to provide a model that simultaneously predicts the short-term dynamics accurately. Models already exist with results that align closely to short-term dynamics data and all rely on reciprocal connections between neural structures to produce ERNA. It may be possible to combine these approaches with the reciprocal connections failing after a short time on stimulation that would produce a model that approximates dynamics on all time scales accurately and agrees with our current physiological understanding of the STN and pallidum.

5.6 Concluding Remarks

In this thesis, we have provided a computational framework that explores non physiological, as well as stationary and dynamic physiological responses to DBS. Collectively, this represents an in-depth analysis into several of the potential observations from sense-stimulation BCIs and has direct implications to neuromodulation therapies for PD. As neither sub-harmonic entrainment nor ERNA is limited to PD, this thesis may present wider implications to other neuropathologies. Furthermore, the computational models proposed in this thesis predict the underlying dynamics responsible for the observed DBS-induced phenomena. To advance current neuromodulatory therapy approaches, a key barrier is understanding how DBS modulates neural activity. It is the hope of this thesis that the results presented here may advance the research of how DBS affects neural circuits. While this research question represents a considerable challenge, DBS has consistently demonstrated the ability to modulate neural activity and clinical investigations continue to indicate the growing potential to provide further clinical benefit.

Appendices

A

Appendix to Entrainment Modelling Chapter

Contents

A.1 Optimisation Details 136
A.1.1 Correlation and Redundancy Between Features 136
A.1.2 Evaluation of Cost 137
A.1.3 Robustness to Noise 137
A.1.4 Top-Ranked Wilson-Cowan Model Parameter Set 138
A.2 Clinical Symptoms of all Patients 138
A.3 Off-Stimulation Data and Model Features in RCS18 and RCS02 138
A.4 Sine Circle Map 141
A.5 Fitting Robustness 142
A.5.1 Consistency Across Best Parameter Fits 142
A.5.2 Alternate Stimulation Pulse Shapes with Recharge All Predict Left Leaning 1:2 Tongues 142
A.5.3 Alternate Stimulation Waveforms Predict Different 1:2 Tongues 143
A.5.4 Tongue Lean and the Wilson-Cowan Vector Field 144
A.5.5 Stimulating the Excitatory Population Instead of the Inhibitory Population 148
A.6 Entrained Signals Exhibit Phase-Locking 148

A.1 Optimisation Details

A.1.1 Correlation and Redundancy Between Features

To see consistent population dynamics and entrainment predictions it is required to fit the Wilson-Cowan model parameters to all three features mentioned in Section 3.3.3.

We demonstrated this by also fitting to each of the three features individually (approximately 1000 local optimisations per feature). The costs of these optimisations, along with the costs from the optimisation of all three features, are plotted in Fig A.1. In each panel, the trade-off between pairs of features is represented by the Pareto front. As expected, optimising only one feature results in low costs for this feature and significant variability for the other two costs. The results of the optimisation to all three features may not have costs as low as the fits to an individual feature, but they are consistently in the bottom most left corner of the plot and the best trade-off between optimising each feature. Moreover, the results of the fits to individual features had greater variability in the entrainment field predictions than the fit to all three features.

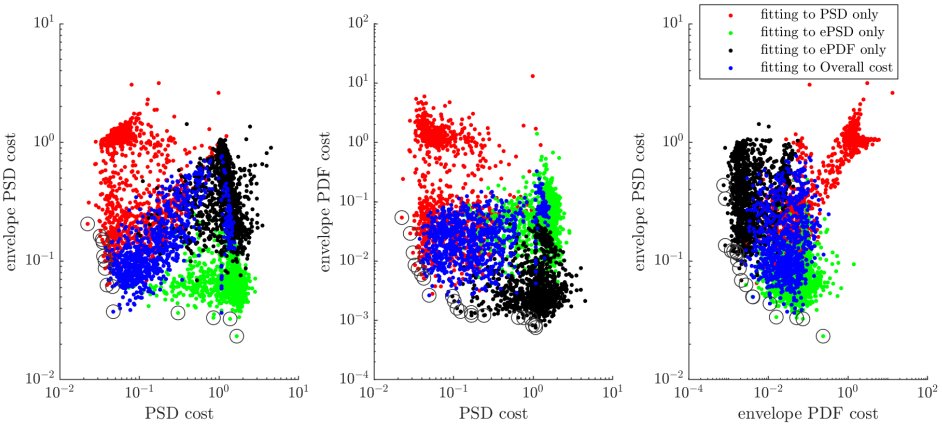


Figure A.1: Feature costs when fitting to a single feature only, compared to fitting to all features. Results of fitting to just the PSD (red), envelope PSD (green), envelope PDF (black), and all three features (blue). Panel A shows the comparison of the PSD cost to envelope PSD cost, panel B PSD to envelope PDF cost, and panel C envelope PDF to envelope PSD cost. In all panels, the Pareto front is highlighted by grey rings.

It does not appear that any of these features are redundant to model off-stimulation local field potentials as shown by the low correlation (there is little overlap of costs for the four optimisations in Fig A.1) and the Pareto front in the three panels of Fig A.1. Hence, to capture the full time-domain-based dynamics it is necessary to fit to all three features.

A.1.2 Evaluation of Cost

For each parameter set, the model is forward simulated using the Euler-Maruyama scheme for a four second time period, with an additional 0.1 second settling period, and a time step of 10^{-4} seconds. Following the model simulation, the transient of the settling period is removed and the population activity is z-scored. The three features are then computed in the exact same manner as the data features. The overall cost against the data is calculated by

$$\text{cost} = \frac{1}{3}\sum_{n=1}^{3}\left(\frac{\sum_{i=1}^{L_n}(X_{n,i}^{\text{data}} - X_{n,i}^{\text{model}})^2}{\sum_{i=1}^{L_n}(X_{n,i}^{\text{data}} - \overline{X_n^{\text{data}}})^2}\right), \tag{A.1}$$

where $n = [1, 2, 3]$ for the three features and L_n is the length of each feature, X_n, as in (Duchet et al. 2020). The optimiser then looks to minimise the cost, which maximises the coefficient of determination, $R^2 = 1 - \text{cost}$.

A.1.3 Robustness to Noise

Stochasticity introduces the possibility during optimisation that for a given simulation, the randomly generated noise vector may be particularly favourable to minimise the feature costs. However, this parameter set would not represent a local minimum on average. The four second time period of model forward simulation is chosen as a trade-off between minimal run time and sufficient individual simulations to minimise the effect of variability due to stochasticity on the parameter set R^2. Following the evaluation of the best model parameter fits, each of the top 20 model parameter sets are simulated three additional times and the features calculated with a different random noise vector. This ensures that the optimal fit was not the result of a single, favourable noise vector. In RCS10 for example, the six

top parameter sets featured in S1 A.5.1 all maintained an R^2 value above 0.92 across the three additional simulations.

A.1.4 Top-Ranked Wilson-Cowan Model Parameter Set

Parameters of the top-ranked Wilson-Cowan model fit are given in Table A.1. The top-ranked parameter set from RCS18 had a smaller, but wider off-stimulation gamma peak making the final parameter ranking more prone to variation from noise (see Fig A.2B1). This introduce more variability in the entrainment predictions, but the 1:2 tongue was still consistently predicted to be left leaning in the top 20 parameter sets.

Table A.1: Parameter set from the best ranked fits. The given parameter sets had an average R^2 value of 0.961, PSD cost of 0.038, envelope PSD cost of 0.072 and PDF cost of 0.008 for RCS02, R^2 value of 0.944, PSD cost of 0.052, envelope PSD cost of 0.070 and PDF cost of 0.046 for RCS10, R^2 value of 0.868, PSD cost of 0.156, envelope PSD cost of 0.221 and PDF cost of 0.019 for RCS18, across the 50 simulations lasting 100 seconds each.

Parameter	ω_{EE}	ω_{EI}	ω_{IE}	$\tau_E(s)$	$\tau_I(s)$	η_E	η_I	b	ζ
RCS02	4.795	7.224	4.913	$6.424 \cdot 10^{-3}$	$4.853 \cdot 10^{-3}$	1.977	-1.020	2.216	0.087
RCS10	1.130	1.722	3.311	$9.322 \cdot 10^{-3}$	$7.329 \cdot 10^{-3}$	3.065	0.709	9.273	0.048
RCS18	2.590	7.679	7.140	$8.595 \cdot 10^{-3}$	$1.131 \cdot 10^{-2}$	4.007	-0.436	3.329	0.038

A.2 Clinical Symptoms of all Patients

The clinical UPDRS scores for each patient are given in Table A.2. The clinical effects of FTG entrainment were not explored here.

A.3 Off-Stimulation Data and Model Features in RCS18 and RCS02

Off-stimulation data features (PSD, envelope PSD and envelope PDF) are shown for RCS02 and RCS18 in Fig A.2. The features of the top ranked models' fits are compared to data features for RCS02 and RCS18 in Fig A.3.

Table A.2: Patient clinical symptom summary. All assessments were done 90 days pre-operation. A few supplemental sub-scores are included (*MDS-UPDRS Part IV,** sum of all MDS-UPDRS-III tremor scores for each side, off medication).

Patient	UPDRS III OFF-med	UPDRS III ON-med	% change UPDRS when ON	time with dyskinesia* (years)	Functional impact of dyskinesia*	OFF-med tremor score**
RCS02	49	5	90%	4	0	L: 2; R: 0
RCS10	89	42	53%	0	0	L: 9; R: 11
RCS18	30	7	76%	2	1	L: 1; R: 1

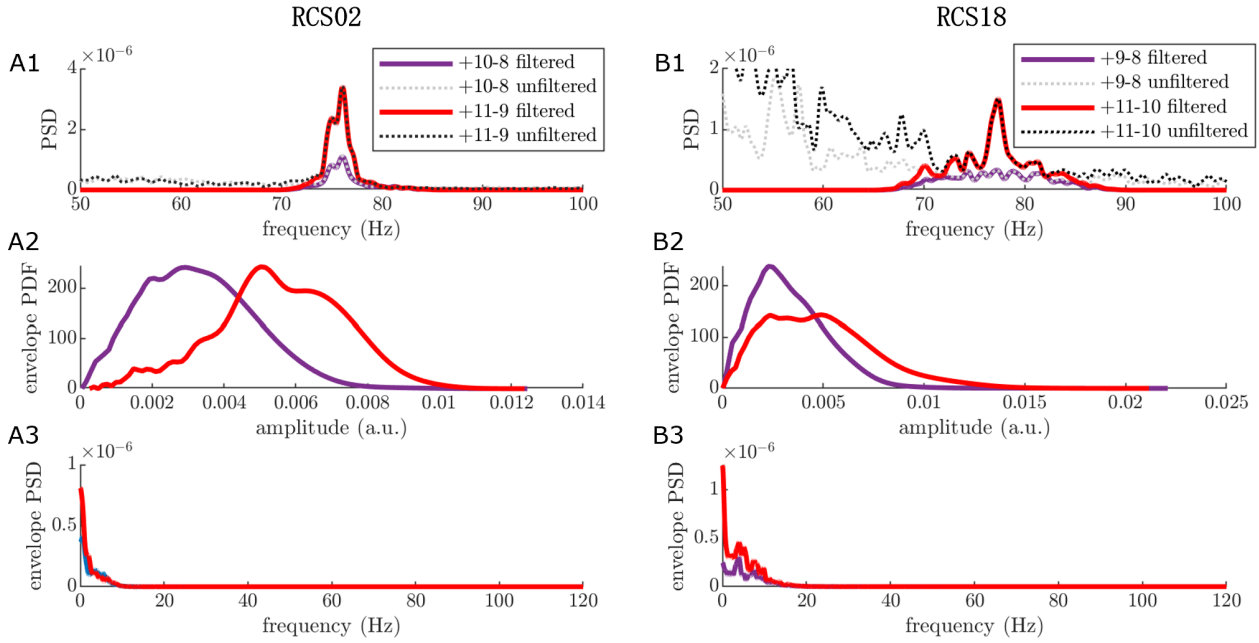


Figure A.2: Features of prestimulation human cortical recordings to fit Wilson-Cowan model parameters in RCS02 and RCS18. Off-stimulation features are obtained as described in the main text. The three data features are PSD (1), envelope PDF (2) and envelope PSD (3), for the selected epoch. Panels A1-3 are calculated from RCS02 cortical data filtered between 72 and 78Hz, as the gamma peak occurred at 75Hz. The fitting process for RCS02 was performed with the features from the 11-9 contact pair as the objective. Panels B1-3 are calculated from RCS18 cortical data filtered between 75 and 81Hz, as the gamma peak occurred at 78Hz. The fitting process for RCS18 was performed with the features from the 11-10 contact pair as the objective. The solid red and purple lines display the band-pass filtered cortical signals. The black and grey dotted line in the PSD plot.

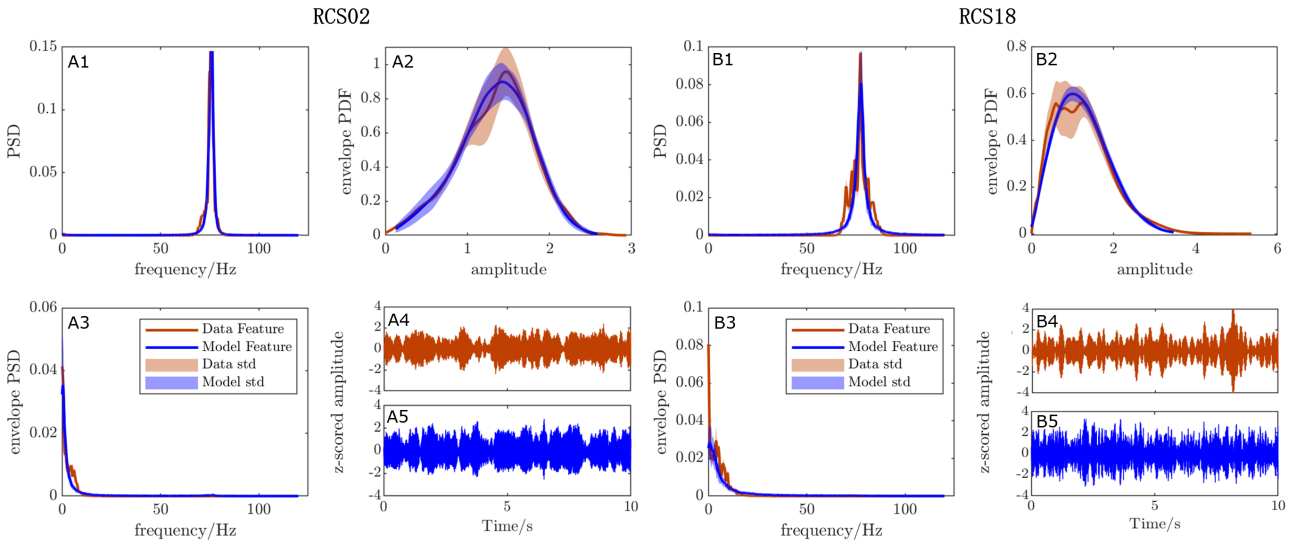


Figure A.3: Comparison of the cortical FTG features for z-scored data and the features from the z-scored model output of the best ranked model parameter set for RCS02 and RCS18. Panels A1-5 are the features for RCS02 and Panels B1-5 are the features for RCS18. $R^2 = 0.961$ for RCS02 and $R^2 = 0.868$ for RCS18 on average across 50 simulations lasting 100 seconds each. The features are PSD (1), envelope PDF (2), and envelope PSD (3). (4 and 5) Comparison of the band-passed, z-scored, off-stimulation time series from patient data (4) and model output (5) show that the model is capable of replicating similar time-domain dynamics. In all panels, the data is in red, and the model in blue.

A.4 Sine Circle Map

The sine circle map is the simplest model that describes the influence of periodic stimulation on an oscillator and can provide a first level description of gamma entrainment during 130Hz stimulation. It is described in detail in Section 1.2.6.1 and Eq (1.2).

By simulating the sine circle map, we are able to observe a 1:2 Arnold tongue (Fig 2.2A), which predicts 1:2 entrainment for a 75Hz oscillator at 130Hz stimulation. There exists a specific range of stimulation amplitudes for which we would expect to see 1:2 entrainment of the oscillator at a resultant frequency of 65Hz. This is in agreement with the observations by Swann et al. (Swann et al. 2016; Swann et al. 2018a) and provides theoretical grounds for expecting 1:2 entrainment during high-frequency stimulation.

While the sine circle map can provide a first level description of gamma entrainment, its simplicity results in significant limitations. Firstly, as the oscillator stays on the unit circle, there is no variable amplitude of oscillations. This makes anything more than analysis of a single neuronal unit unreliable. Secondly, the sine circle map only represents a single oscillator. Therefore, it is difficult to draw comparisons to ECoG signals that arise from interacting populations of neurons. Thirdly, it is known that pulse shape impacts entrainment behaviour; however, as the sine circle map is stroboscopic, realistic pulses cannot be used. Hence, a model which captures the interaction of neurons, is representative of larger neuronal populations and for which realistic pulse shapes can be used would be more suitable. We therefore consider an interacting neural populations model that is fitted to patient data to predict stimulation parameters that lead to 1:2 entrainment (see Sections 1.2.6.2 and 3.3.1).

A.5 Fitting Robustness

A.5.1 Consistency Across Best Parameter Fits

The left lean of the tongue over the normalised stimulation amplitude axis is a consistent feature across the top model parameter fits, example for RCS10 is shown in Fig A.4.

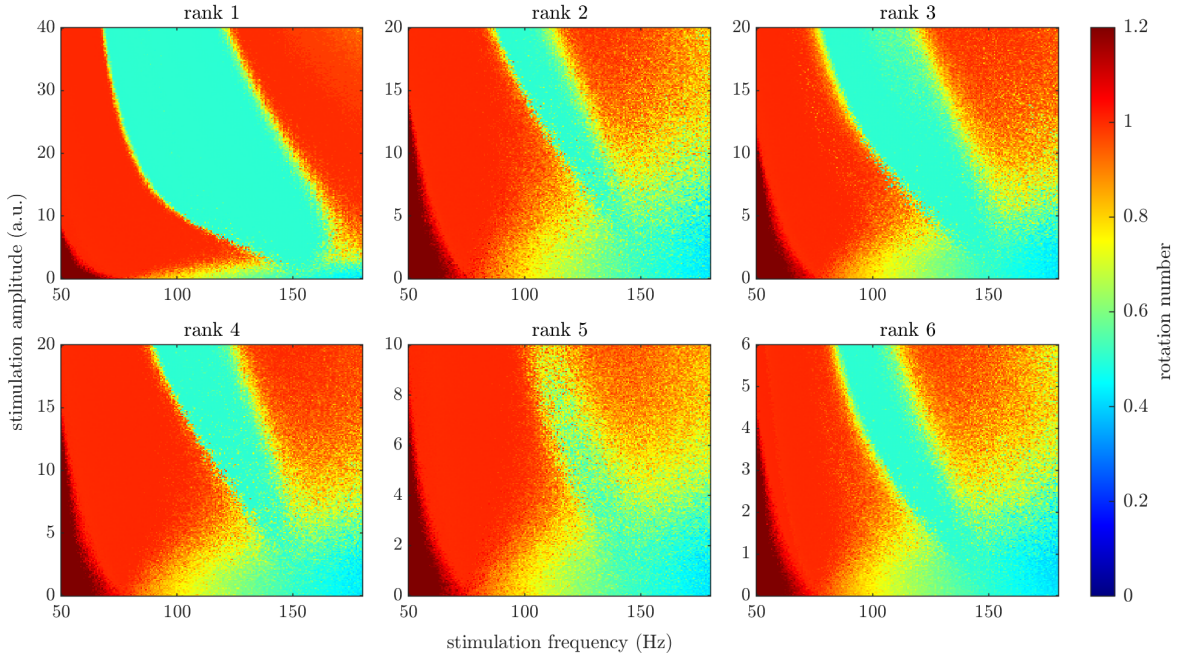


Figure A.4: The entrainment fields for the top six ranked parameter fits of the Wilson-Cowan model to RCS10. All model parameter fits presented here had an R^2 value greater than 0.92. Rank five's entrainment field is observed over a smaller range of stimulation parameters due to the smaller and noisy 1:2 tongue.

A.5.2 Alternate Stimulation Pulse Shapes with Recharge All Predict Left Leaning 1:2 Tongues

Throughout this study, we have used the simplest pulse shape with no recharge. However, to achieve charge balancing at the site of stimulation, DBS requires a recharge component following the initial pulse. This component can be active when recharge is a set proportion of the stimulation period, or passive when charge is allowed to flow from the stimulation site via the electrode. The amplitude of the charge balancing component is calculated depending on the frequency of the

stimulation and the amplitude of the positive pulse, so that the positive pulse and the negative charge balance have equal areas.

Across pulses with various recharge duration, the 1:2 tongue is present and exhibits a left lean as shown in Fig A.5 (example for RCS10). Despite these similarities, the tongues are present across different amplitude ranges. When recharge is present, the shortest recharge lengths require the greatest amplitude to observe the same extent of the 1:2 tongue. This is attributed to the immediate recharge cancelling the effect of the preceding pulse in the model.

Neurons are likely to respond to hyperpolarising and depolarising stimulation in different capacities. Immediately after a depolarising stimulation pulse, it is likely that a high proportion of the effected neurons will fire. The following hyperpolarising recharge will simply reduce membrane potential during the refractory period. Because of this asymmetrical effect and for simplicity, we chose to use a stimulation pulse with no recharge in this study. However, the prediction of a left leaning 1:2 tongue holds for pulses with recharge of various durations as shown in Fig A.5.

If the model does approximately capture the response of neurons to stimulation pulses with recharge, we would expect that passive recharge or recharge over a longer window would achieve entrainment at lower stimulation amplitudes. Entrainment at lower stimulation amplitudes would potentially increase the efficiency of stimulation protocols that are designed to entrain brain oscillations and minimise the side effects experienced from high stimulation amplitudes.

A.5.3 Alternate Stimulation Waveforms Predict Different 1:2 Tongues

As the model is fitted to off-stimulation data, it is possible to apply a variety of stimulation waveforms to either population to predict entrainment responses. Fig A.6 shows the entrainment behaviour for RCS10 at high stimulation frequency for four waveforms: a single time step pulse with no recharge (the same as for Fig 3.5B), a sine wave, a sawtooth wave, and a square wave. The amplitude scale for each waveform is normalised by the integral of the square of the waveform. This

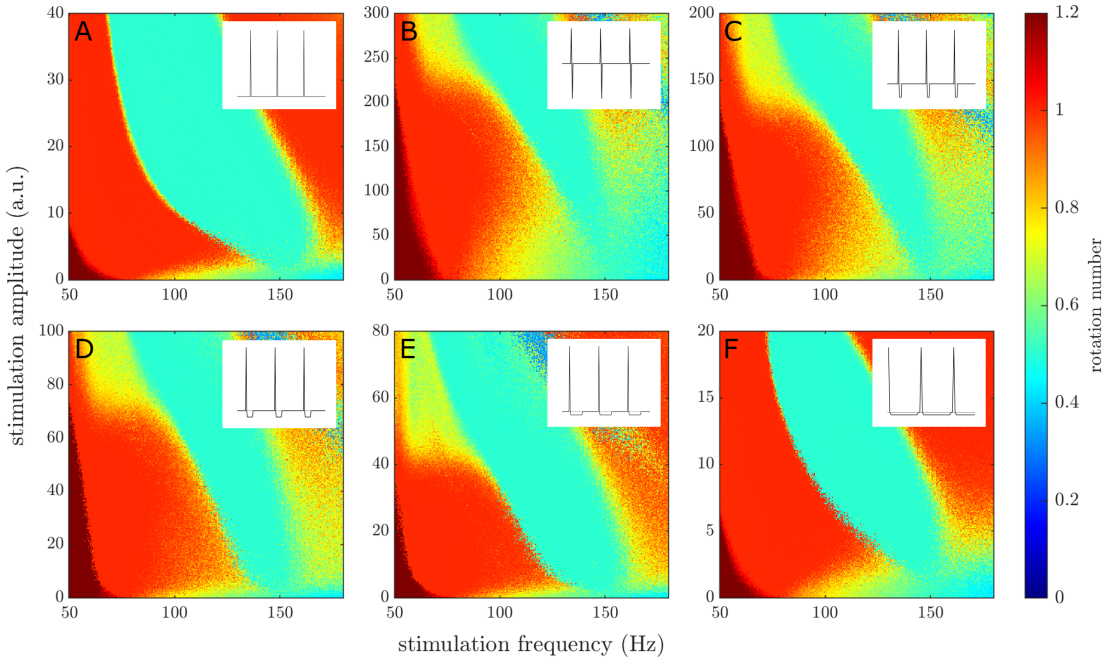


Figure A.5: A comparison of six different stimulation pulse recharges applied to the inhibitory population of the top ranked Wilson-Cowan model fitted to RCS10. The panels are categorised as a pulse with no recharge (A), which is the pulse used throughout the majority of the study, $100\mu s$ recharge (B), $400\mu s$ recharge (C), $1ms$ recharge (D), $2ms$ recharge (E), and whole period recharge (F), which can be used to approximate passive recharge. The inserts represent a couple of the periods of the corresponding stimulation pulse and the grey line indicates an amplitude of zero.

ensures that amplitude levels correspond to the same energy across the waveforms in Fig A.6. The sine wave and the single time step pulse have similar 1:2 tongues at frequencies greater than 150Hz, while the square and sawtooth waves are able to maintain 1:2 entrainment at higher stimulation amplitudes. Additionally, the three non-pulsatile waveforms are able to maintain 1:2 entrainment at lower stimulation frequencies and amplitudes than the pulsatile waveform. This is important to note as a patient may not be able to withstand the higher amplitudes on this scale without experiencing side effects.

A.5.4 Tongue Lean and the Wilson-Cowan Vector Field

The left lean of the 1:2 tongue can be explained by analysing deterministic trajectories of the population activities in the E-I activity phase space. Fig A.7 shows that in the 1:2 entrainment region for RCS10, two positive pulses of stimulation occur

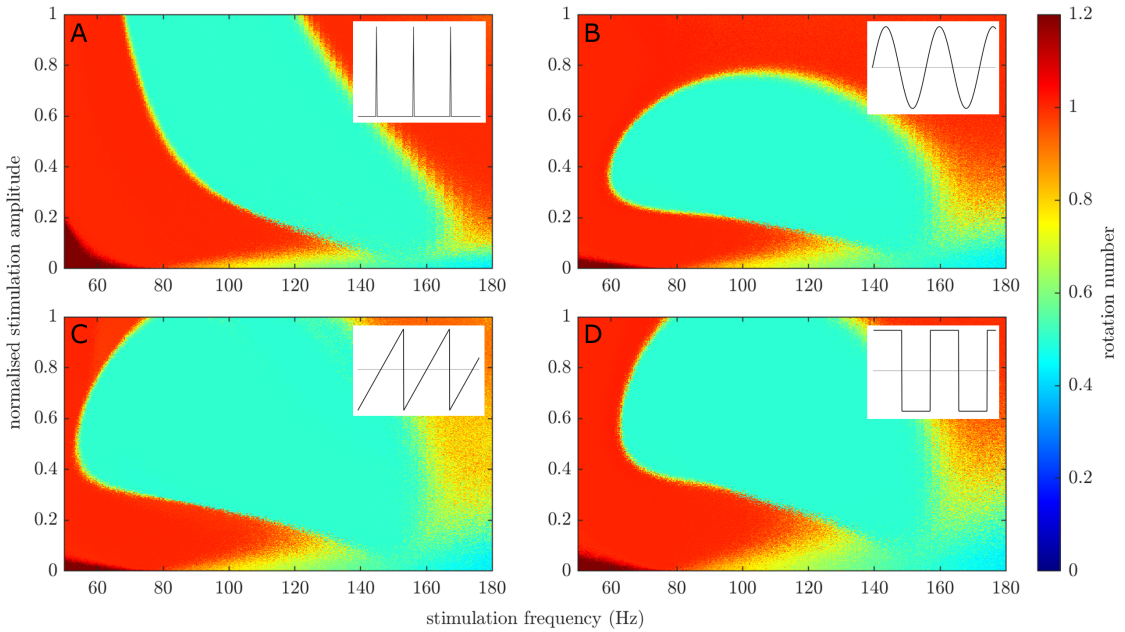


Figure A.6: A comparison of four different waveforms of stimulation applied to the top-ranked Wilson-Cowan model fitted to RCS10. In each panel, stimulation takes the form of a single time step pulse with no recharge (A), a sine wave (B), a sawtooth wave (C), and a square wave (D). Stimulation amplitude is normalised against the integral of the square of the waveform. The inserts represent a couple of periods/cycles of the corresponding stimulation waveform and the grey line indicates an amplitude of zero.

for each circuit completion of the periodic trajectory (Fig A.7C). As stimulation amplitude and/or frequency are increased, the pulse that occurs at larger values of excitatory activity drops to lower values. Increased frequency (Fig A.7D) means less time for population dynamics to reach more extreme activities. Increased amplitude (Fig A.7A) pushes the activity further away from the fixed point and, hence, requires more time to reach the same value of excitatory population activity.

By considering stimulation parameters along the top right boundary of the 1:2 tongue, these effects can account for the left lean of the tongue. On the boundary, the pulse at higher excitatory population activity of the 1:2 entrained trajectory exactly crosses the fixed point in the absence of noise. In a noisy system it would cross either side of the fixed point, with these cycles corresponding to either 1:2 or 1:1 entrainment. From stimulation parameters on the boundary, changing one stimulation parameter requires mutually changing the other in the opposite direction to maintain this relationship of the higher excitatory activity pulse to the fixed point.

For instance, if we increase stimulation frequency and there is less time between the successive positive pulses, we must decrease stimulation amplitude to maintain this relationship. This can be seen in the transition from trajectory A to D in Fig A.7. Hence, this gives us a relationship for the upper bound of the 1:2 tongue where the system transitions to 1:1 entrainment for increasing frequency or amplitude. As this is the upper bound of the tongue, this means that it must be left leaning.

The direction of the 1:2 tongue lean depends on the vector field. The entrained trajectory requires more time between pulses to reach the same location within the vector field as stimulation amplitude is increased. The rate of change of population activity is slowed down each period as it consistently reaches darker and slower regions of the colour-scaled angular phase velocity, as shown in the inserts of Fig A.7. If, however, the higher excitatory activity pulse reached a lighter coloured region of increased angular phase velocity, it would require less time between successive pulses to reach the same location within the vector field, i.e. increased stimulation frequency. Therefore, through differences in the vector field, for this hypothetical example, we would predict that increased amplitude would require an increase in frequency to maintain 1:2 entrainment. Unlike the results of our fitting process, this hypothetical example would produce a right leaning 1:2 tongue with a preference for speeding up the natural frequency.

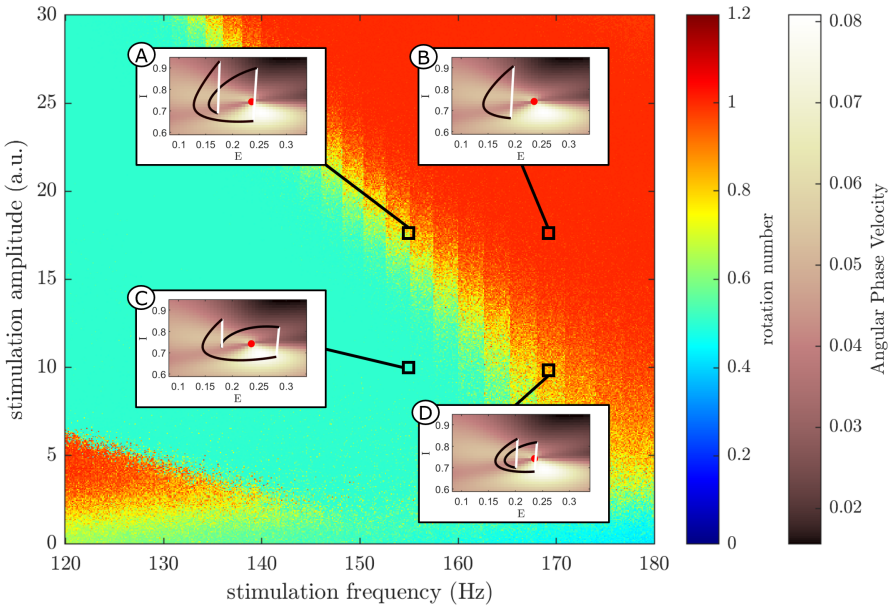


Figure A.7: Deterministic trajectories in phase space and the left lean of the 1:2 tongue (example for RCS10). On each of the four trajectory panels, the red dot represents the fixed point for the parameter set. The colourscale of the trajectory is chosen so that white represents a larger jump over an individual time step (following a stimulation pulse) and black is a smaller jump. The angular phase velocity colourbar indicates the magnitude of the vector field, with the colourscale of the entrainment field being identical to Fig 3.5B. Trajectory A (Amplitude = 18, Frequency = 155Hz) and D (Amplitude = 10, Frequency = 170Hz) show phase space trajectories of stimulation parameters on the 1:2 tongue boundary. Trajectory B (Amplitude = 18, Frequency = 170Hz) lies within the 1:1 tongue and trajectory C (Amplitude = 10, Frequency = 155Hz) is in the 1:2 tongue. The stimulation provided is a single time step pulse with no recharge over the rest of the period.

A.5.5 Stimulating the Excitatory Population Instead of the Inhibitory Population

Throughout this paper, we stimulate the models consistently through the inhibitory population as described in the main text. However, the 1:2 tongue is still present when stimulating the excitatory population and while observing the inhibitory population activity (to avoid the population dynamics being dominated by stimulation artefact). Moreover, the key features of the 1:2 tongue are maintained regardless of the population being stimulated. As seen for RCS10 in Fig A.8 and Fig 3.5D, both 1:2 tongues originate at low amplitude from 150Hz stimulation and have a clear left lean towards lower frequencies. Conversely, stimulation of the excitatory population does not produce 1:2 entrainment at frequencies greater than 150Hz for a single time step pulse with no recharge. 1:2 entrainment above 150Hz was observed in both the model for stimulation of the inhibitory population, in Fig 3.5D, as well as in the data presented in Fig 3.5F. Furthermore, the 1:2 tongue resulting from stimulation of the excitatory population transitions to 1:1 entrainment at approximately one quarter the height of the 1:2 tongue of inhibitory stimulation. In the model, 1:2 tongues of similar characteristics originating from both the excitatory and inhibitory population is not a surprise. The network dynamics are responsible for the features of the 1:2 tongue. Therefore, a strong periodic stimulus to either population will likely result in the network behaving with a similar response.

A.6 Entrained Signals Exhibit Phase-Locking

By the definition of entrainment, if oscillators are entrained to a signal then they must exhibit some level of phase-locking. This is observed differently for 1:1 and 1:2 entrainment. For pulsatile stimulation and a 1:1 entrained oscillator, every pulse will occur around the same phase as every cycle of stimulation is matched by a cycle of oscillations. For a 1:2 entrained oscillator, every oscillation cycle experiences two pulses of stimulation. This signal is still phase-locked, but every other pulse occurs around the same phase.

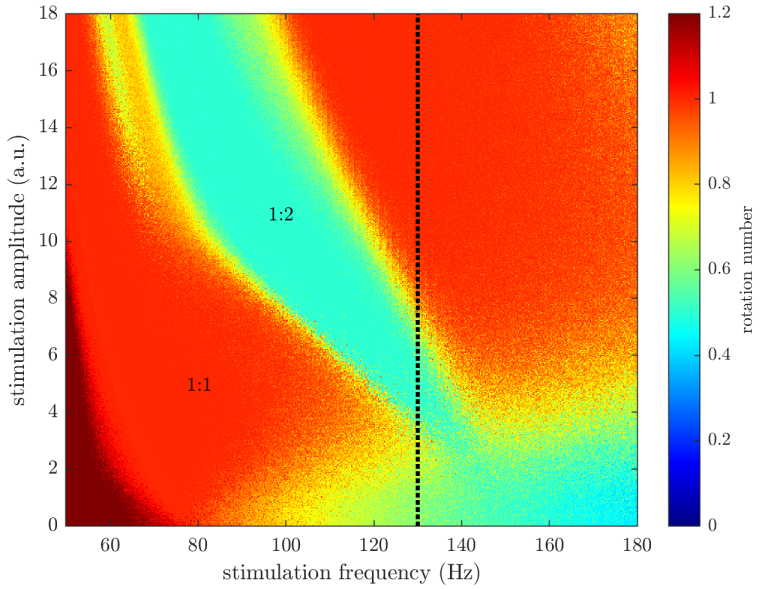


Figure A.8: Entrainment field resulting from excitatory stimulation in the Wilson-Cowan model (top-rank fitted to RCS10). Stimulation is for a single time step pulse with no recharge, but applied to the excitatory population and rotation number measured from the inhibitory population. The black dotted line is used to highlight the case of 130Hz stimulation frequency.

As different modes of entrainment are reflected in the phases at time of stimulation pulses, it is possible to categorise different entrainment regions by plotting these phases. While it is not possible to record from the same contact that is stimulating, it is possible to observe the stimulation artefact from the neighbouring subcortical contacts. By tracking these artefacts and verifying that they align with the stimulating frequency, it is possible to find approximate time stamps of the stimulating pulse train. We record the corresponding phases by taking the Hilbert transform of the cortical signal at these time stamps. Prior to passing the signal through the Hilbert transform, the signals are band-passed between 70Hz and 80Hz for this 149.3Hz stimulation case. This isolates the potentially 1:2 entrained signal, the main observation of interest for this study. These results are plotted in Fig A.9.

For Fig A.9A, off stimulation, the recording of phases was triggered by sham stimulation at 149.3Hz. As there is no stimulation, there is no entrainment in panelA.9 A as shown by the absence of preferred phases. Panels A.9B and D did not display 1:2 entrainment in their respective PSDs and do not display preferred

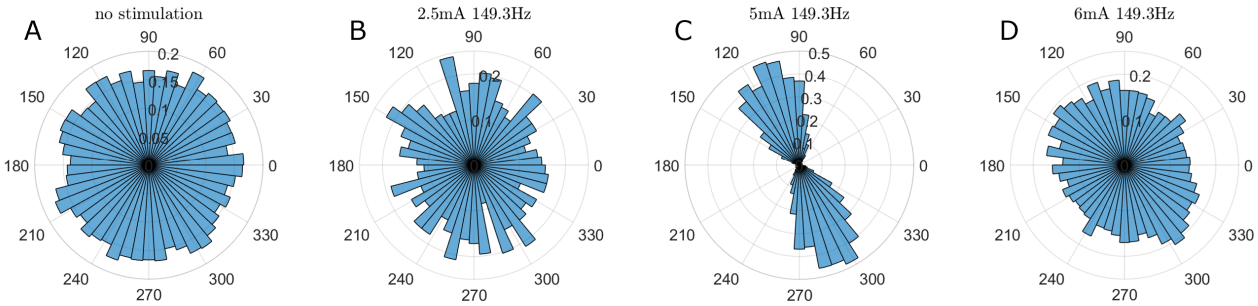


Figure A.9: Cortical gamma phases at the time of stimulation for four different stimulation settings in RCS10. Each panel is plotted as a polar histogram and normalised as a probability density function estimate where the sum of the area of the bars equals one. The signals were band-passed between 70 and 80Hz prior to identifying the phases. (A) No stimulation with sham stimulation triggers to record cortical gamma phase at 149.3Hz, (B) 2.5mA for the recording that did not show 1:2 entrainment, (C) 5mA where 1:2 entrainment was observed and (D) 6mA where 1:2 entrainment was not observed.

phases. In contrast, panel A.9C had a half harmonic peak above the predicted baseline in its PSD and was recorded as seeing 1:2 entrainment. Its corresponding polar histogram displays phases grouped around two, approximately polar opposite, phases. This is in agreement with the spectral evaluation and what we would expect to see from a 1:2 entrained signal.

B

Appendix to ERNA Modelling Chapter

Contents

B.1 Fitted Model Parameter Set 151
B.2 Explaining Model Dynamics 154
B.2.1 Amplitude Response 154
B.2.2 Frequency Response 154
B.3 Current Model Shortcomings 156
B.3.1 Fast Dynamics 156
B.3.2 Subtherapeutic Stimulation 156
B.4 Fitting Robustness 158
B.4.1 Sensitivity of Coupling Function 158
B.4.2 Sensitivity of Phase Response Curve 160
B.5 Alternative Parameter Set with Lower Natural Frequency 162
B.6 Dynamic Oscillations 164

B.1 Fitted Model Parameter Set

The results of the fitting process (outlined in Section 4.4.2) are presented in Table B.1. All model parameters presented in the top row of Table B.1 were optimisable parameters for the fitting procedure. Some of the parameters were additionally subject to manual parameter tuning in order to provide model dynamics that resembled the data more closely. However, this represented only small adjustments by comparison to their fitted value. The bottom row of parameters in Table B.1

are parameters of the three-vesicle pool model and were largely determined from data as detailed below, with a small amount of manual parameter tuning within the bounds set by the data.

Parameter	$k_\mu(rad/s)$	$I(rad/s)$	$\zeta(rad)$	$\Omega(Hz)$	$\sigma(Hz)$
Value	11976	72053	5.920	249	26.317
Parameter	f_0	f_1	f_2	f_3	f_4
Value	-0.780	0.198	0.302	0.851	0.998
Parameter	M_{RRP}	M_{RP}	M_{RtP}	$\tau_{\mathrm{RRP}}(s)$	$\tau_{\mathrm{RP}}(s)$
Value	1	0.5	0.3	1	10
Parameter	$\tau_{\mathrm{RtP}}(s)$	$p_{\mathrm{RRP}}(s^{-1})$	$p_{\mathrm{RP}}(s^{-1})$	$p_{\mathrm{RtP}}(s^{-1})$	
Value	50	0.3	0.02	0.00035	

Table B.1: Fitted model parameter set. The base model parameter set for all simulations. The bottom two rows are parameters of the three-vesicle pool model.

The time constant of each pool τ_{pool} is estimated using the approximate time required to replenish the vesicle pool through recycling in the absence of unphysiological stimulation. The RRP recycles quickly, on the order of seconds (Rizzoli and Betz 2005), we therefore chose τ_{RRP} to be 1 second. The RP also recycles quickly on the order of seconds (Rizzoli and Betz 2005), and given the size difference between the RRP and the RP, τ_{RRP} is taken to be 10 seconds. The RtP takes longer to replenish recycling on the order of minutes (Rizzoli and Betz 2005), τ_{RRP} is therefore chosen to be 50 seconds.

The probability of vesicle release by a stimulation pulse p_{pool} is estimated from the time taken to deplete each vesicle. The RRP is expected to deplete within 10 pulses of unphysiological stimulation (Kaeser and Regehr 2017), the RP over seconds and the RtP over minutes (Rizzoli and Betz 2005). The value of p_{pool} is taken to be inversely proportional to the number of pulses required to deplete each pool. The proportionality constant is set in combination with τ_{pool} according to the stable occupancy of each pool on 130Hz stimulation. Therefore, p_{RRP} is given a value of 0.3 (corresponding to 9 pulses on 130Hz stimulation), p_{RP} a value of 0.02 (corresponding to one second on 130Hz stimulation or 130 pulses) and p_{RtP} a value of 0.0035 (one minute or 7800 pulses) to align with these observations.

The estimated contribution of each vesicle pool on coupling strength, M_{pool}, is modelled as proportional to the product of the relative size of each vesicle pool (N_{pool}) and the inverse of the vesicle pools distance from the synaptic terminal (d_{pool}),

$$M_{\text{pool}} = \eta \frac{N_{\text{pool}}}{d_{\text{pool}}}, \tag{B.1}$$

where η is a normalising factor, the same across vesicle pools.

The RRP is the smallest vesicle pool, usually approximated to be between $1-2\%$ of the overall number of vesicles (Rizzoli and Betz 2005). Additionally, RRP vesicles are usually considered to be either docked or very close to the synaptic terminal. Given the approximate size of vesicle pool around 20nm (Südhof 2012; Dittman and Ryan 2019) in diameter, we estimate the average distance of RRP vesicles to the synaptic terminal to be on the scale of 10nm. The important consideration for N_{pool} is the relative size between pools. We therefore take the total number of vesicles as 100, and taking the percentage of vesicles in the RRP as 1%, we obtain $N_{\text{RRP}}/d_{\text{RRP}} = 0.1\text{nm}^{-1}$. We choose the normalising factor $v = 10\text{nm}$ (across all pools), which gives $M_{\text{RRP}} = 1$. The RP contains slightly more vesicles at around $10-20\%$ (Rizzoli and Betz 2005), but is located further from the synaptic terminal. Furthermore, the RP must release fewer vesicles to the synapse when full compared to the RRP. Electron microscopy and neurotransmitter release simulations suggests that the majority of vesicles located proximal to the synapse are located within 500nm of the terminal (Rizzoli and Betz 2005; Branco and Staras 2009; Qu et al. 2009; Dittman and Ryan 2019), therefore we estimate the average distance of the RP vesicles to the synaptic terminal as 200nm. Taking the percentage of vesicles in the RP as 10%, we obtain $N_{\text{RP}}/d_{\text{RP}} = 0.05\text{nm}^{-1}$ and $M_{\text{RP}} = 0.5$. Lastly, the RtP represents the majority of vesicles, $80-90\%$ (Rizzoli and Betz 2005), and given the percentages taken for the other vesicle pools we will assume the RtP represents 89%. Estimates for the furthest distance vesicle pools take from the synaptic terminal are between 1µm (Dittman and Ryan 2019) and 5µm (Rizzoli and Betz 2005; Staras et al. 2010), we therefore take an approximate distance of 3µm. We obtain $M_{\text{RtP}} = 0.3$.

B.2 Explaining Model Dynamics

B.2.1 Amplitude Response

One of the benefits of using computational models is that we have the ability to investigate the dynamics that may be responsible for the ERNA characteristics in the simulations. Here we investigate what causes the amplitude variation seen over the longer time period. By recording the phase difference between one random oscillator against all the others, we are able to observe clustering behaviour over both the off- and on-stimulation periods (Fig B.1). Fig B.1Bi shows that in the steady off-stimulation state we see two clusters approximately anti-phase (due to the coupling function, see Fig 4.1E), which result in low amplitude activity. In on-stimulation histograms of Figs B.1Bii, iii and iv, it can be seen that there is a shift away from an even distribution between each cluster, with a preference to synchronise to one cluster. The development of this distribution of phases between clusters over the stimulation window accounts for the amplitude variation. Firstly, the histograms of Figs B.1Biii and iv do not differ greatly as can be seen from the amplitude dynamics with little variation after approximately 50 seconds of stimulation. In the early part of the stimulation window there is greater coupling around a single cluster at an approximate ratio of 25:1 oscillators in each group compared to the smaller cluster. In the later part of the stimulation window, this ratio shrinks to around 10:1 as coupling strength drops further and there is less attraction to stay coupled to the dominant cluster.

B.2.2 Frequency Response

The on-stimulation frequency response can be explained by investigating the dynamics of individual oscillators as well. After each stimulation pulse, the oscillators are pushed towards synchronisation around a single phase due to the sinusoidal PRC. This would occur for any PRC with a stable zero-crossing point. Furthermore, this occurs regardless of the length of time following stimulation onset as this is a property that is independent of vesicle depletion's effect on coupling strength.

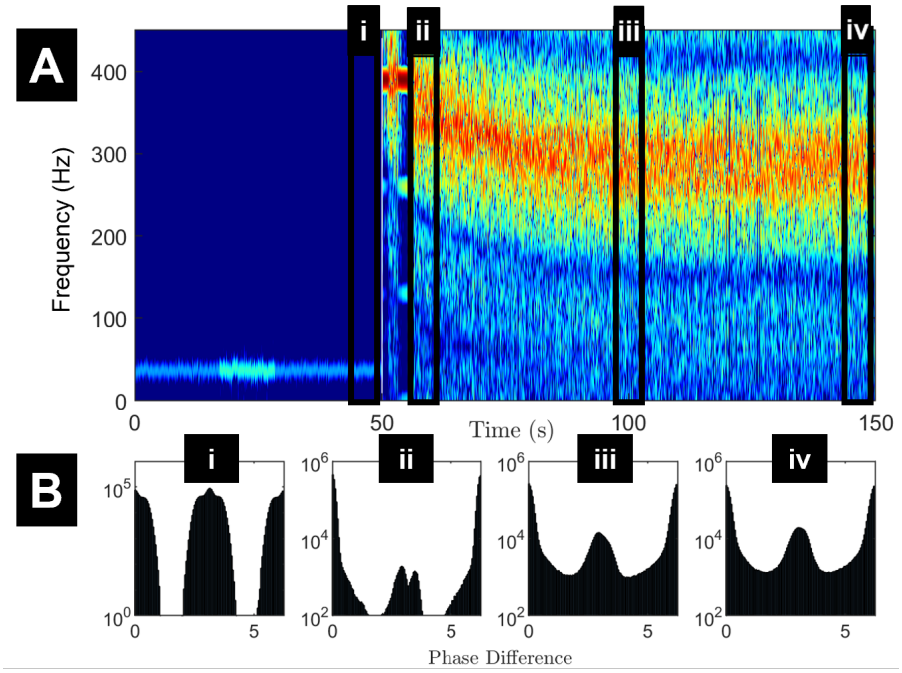


Figure B.1: Clustering of oscillators explains the amplitude dynamics over continuous stimulation. (A) Spectrogram of network activity (Same as in Fig 4.1A) over 50 seconds off stimulation before turning on stimulation for 100 seconds. The black boxes labelled i, ii, iii and iv refer to the periods clustering was observed over for the histograms in panel B. (B) Histograms of phase difference for four five second periods. (i) 44 to 49 seconds, (ii) 55 to 60 seconds (to avoid brief period of entrainment), (iii) 97.5 to 102.5 seconds, and (iv) 144 to 149 seconds. (i) Plotted with a y axis limit of 10^0 to 10^6, whereas the other a plotted with a limit of 10^2 to 10^6, to demonstrate the lack of activity observed outside the clusters.

Early in the stimulation window, before vesicle depletion has reduced coupling strength too greatly, the oscillators remain mostly synchronised around a single phase for the majority of the remaining inter-pulse interval (see Fig B.1Bii). Given that coupling strength is still high and that the coupling function is positive for zero phase difference, this increases the frequency of the network at this early stage. Later in the stimulation window, as coupling strength reduces, fewer oscillators remain synchronised and for a shorter period of time (see Fig B.1Biii and iv). As coupling strength is much weaker, there is less of a contribution to oscillator phase advancement from the interaction with other oscillators. As the stimulation PRC integrates to zero and noise is drawn from a random distribution with a mean of zero, both of these potential phase effecting mechanisms trend to having zero net effect with enough time. Hence, with a much lower coupling strength, the primary effect

on oscillator phase progression comes from the natural frequency of the individual oscillators (Eq (4.1)). Therefore, the network trends to a frequency close to the fitted mean of the natural frequencies of all the oscillators in the network after a long period of high frequency stimulation (see $\Omega = 249$ in Table B.1).

B.3 Current Model Shortcomings

B.3.1 Fast Dynamics

For comparison to the fast ERNA dynamics reported in (Sinclair et al. 2018), DBS is turned on at 130Hz for a period of 100ms with 50ms of observations off-stimulation either side of the DBS window. This follows an initial 10 seconds of the model settling. Initially coupling strength decayed with time on-stimulation following our three-vesicle pool model with the parameters obtained from the fitting process (Table B.1). Coupling strength begins to recover with a one second time constant as dictated by RRP recovery. However, high frequency and high amplitude dynamics are maintained during the 100ms following stimulation termination due to coupling strength remaining low at this time scale (Fig B.2). Model dynamics return to low frequency conditions within around one second following stimulation termination (see for example Fig 4.2B). We also note that inter-pulse dynamics are very regular and do not resemble typical ERNA signals. Hence, our fitted model reproduces the slow dynamics of ERNA, but is unable to capture its fast dynamics. This may be due to the slow replenishment of vesicles in our simplified model on this time scale, and introducing more complex dynamics such as vesicle mixing between pools or STN-GPe excitatory/inhibitory connections may be necessary to reproduce fast ERNA dynamics.

B.3.2 Subtherapeutic Stimulation

Subtherapeutic stimulation at 20Hz is capable of eliciting evoked potentials (Ozturk et al. 2021). Similar responses were also seen at lower stimulation frequencies of 3Hz (Zapata Amaya et al. 2023). These evoked potentials had increased amplitude compared to baseline, but no high frequency content. 20Hz stimulation may be

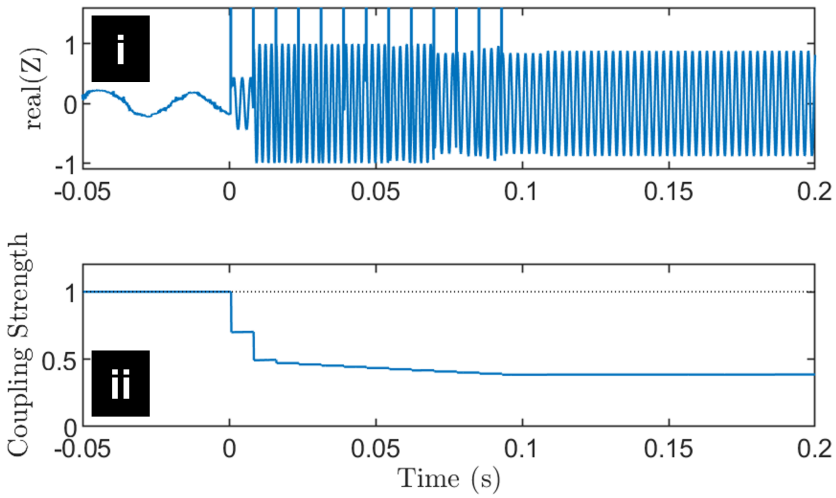


Figure B.2: Fast dynamics of ERNA for 100ms of 130Hz stimulation pulses. (i) The approximate amplitude response with stimulation artefact artificially superimposed on the signal following the simulation for demonstration purposes. (ii) The corresponding coupling strength of the network.

considered on the borderline of physiological-unphysiological stimulation (Denker and Rizzoli 2010), while 3Hz stimulation is certainly within the physiological limits. However, this is dependent on the neural structure being stimulated and 20Hz may even be considered within physiological frequencies in some structures, especially if this stimulation frequency is close to the natural frequency of the neuronal ensemble.

The application of low frequency stimulation to our model does not align with these results, however. For both 3Hz and 20Hz we still see the promotion of high frequency activity (Figs B.3A and E). Stimulation at 3Hz produces evoked responses at lower frequencies compared to higher stimulation frequencies tried. Hints from literature can help us investigate this shortcoming further. Stimulation at 10Hz has been shown to not cause vesicle depletion in some cases (Fernández-Alfonso and Ryan 2004). Hence, it is likely that little vesicle depletion will be observed in response to 20Hz stimulation. Furthermore, as 20Hz stimulation elicits very similar responses to 3Hz stimulation (Zapata Amaya et al. 2023), it could be expected that these two stimulation paradigms elicit similar neural responses. Hence, we investigate the evoked response in the absence of vesicle depletion for 20Hz stimulation (Fig B.3I), otherwise the model and parameters remain unchanged.

Without vesicle depletion in the model, we do not see the evolution of high frequency activity (see Figs B.3I and L). However, we still see the promotion of high amplitude activity, which is in line with (Ozturk et al. 2021; Zapata Amaya et al. 2023) (see Fig B.3K). This is primarily due to the maintenance of a higher coupling strength from the lack of vesicle depletion. Therefore, it is likely that improving the fast dynamics of the model as suggested in the previous section (especially with regards to the dynamics of the RRP) would make the model behave more similarly to data in response to subtherapeutic stimulation.

B.4 Fitting Robustness

Here we explore how changing the coupling function and the PRC in the fitted model affects the ERNA response to stimulation.

B.4.1 Sensitivity of Coupling Function

A second-order Fourier series coupling function was able to capture more complex neuronal interactions than the sine function commonly used in the Kuramoto model. As shown in the main text, fitting the Fourier series coefficients provided slow dynamics closely approximating the ERNA spectrogram. For comparison we also simulate the model with a sinusoidal coupling function and a coupling function derived from the Hodgkin-Huxley neuron model (Nabi and Moehlis 2011), while all other parameters remain constant (see Fig B.4). These coupling functions do not lead to ERNA dynamics (Figs B.4B and C). Additionally, the dynamics of the sine coupling function result in activity at a much higher frequency off-stimulation (around 200-250Hz), and at a much higher amplitude (Fig B.4B). This is due to simpler clustering behaviour compared to the fitted coupling function, which favours two clusters in the absence of stimulation. The sine coupling function does not give rise to changes in oscillation frequency with stimulation despite vesicle depletion remaining present (Figs B.4B). The Hodgkin-Huxley derived coupling function shows a response where frequency increases with time on stimulation and vesicle depletion (Figs B.4C). While these results are based on model parameters

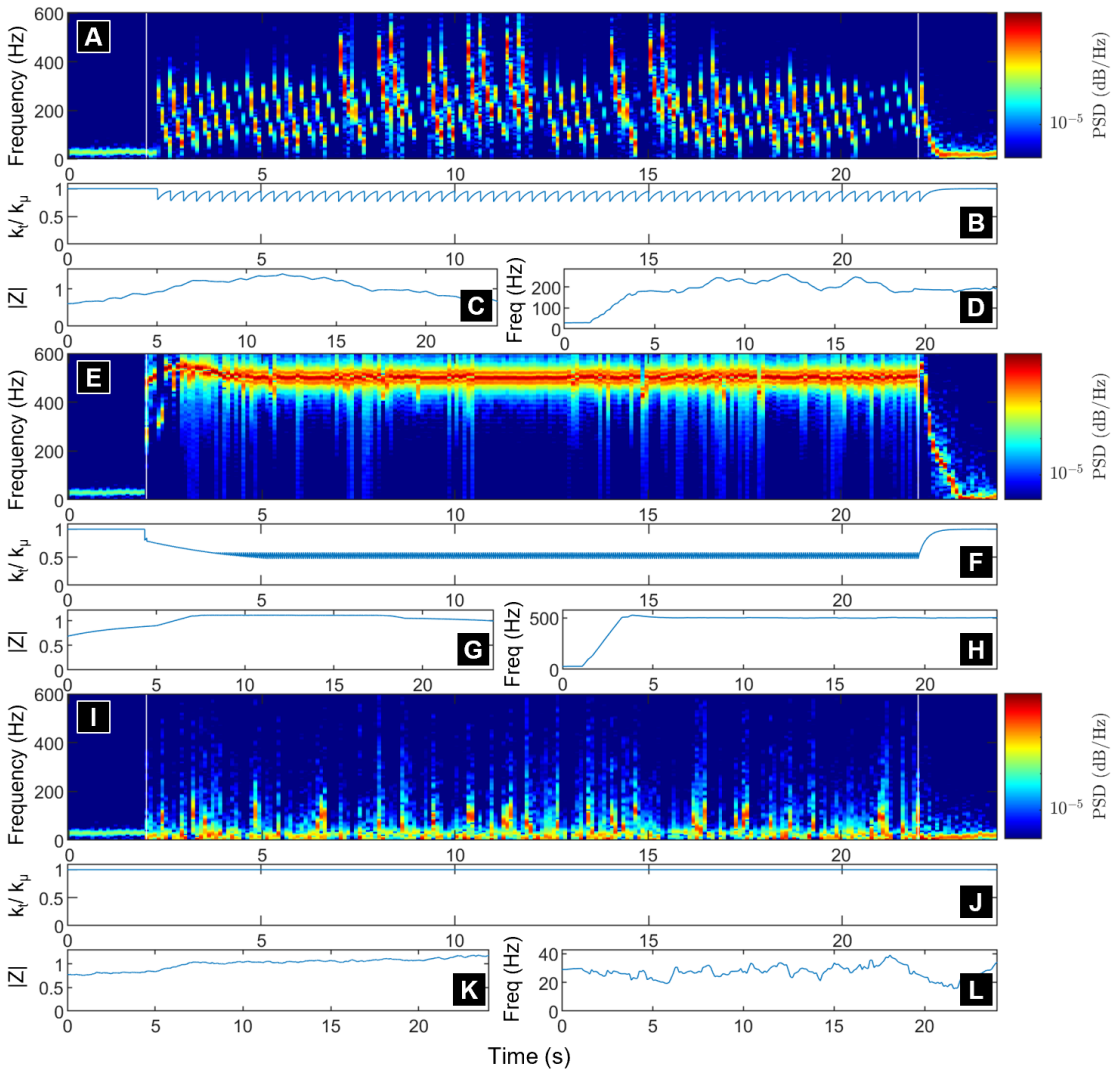


Figure B.3: Response of the model to low frequency stimulation with and without vesicle depletion as a theoretical mechanism of subtherapeutic stimulation. (A, E and I) Spectrogram with stimulation frequency at 3Hz (A) and 20Hz (E and I). Stimulation onset at two seconds into simulation indicated by white line. (B, F and J) The evolution of coupling strength for each simulation. (C, G and K) Amplitude of oscillations over whole simulation. (D, H and L) Peak frequency response for each of the 100ms windows over the whole simulation. (A-H) Vesicle depletion consistent with Eqs (4.3) and (4.4). (I-L) No vesicle depletion.

obtained for the second-order Fourier coupling function, attempts to fit to the slow dynamics of the ERNA frequency decay using each of these coupling functions were made, but no promising results were obtained.

The Fourier series fitted coupling function is a key element of the model to reproduce the ERNA frequency decay, therefore we also investigate the sensitivity

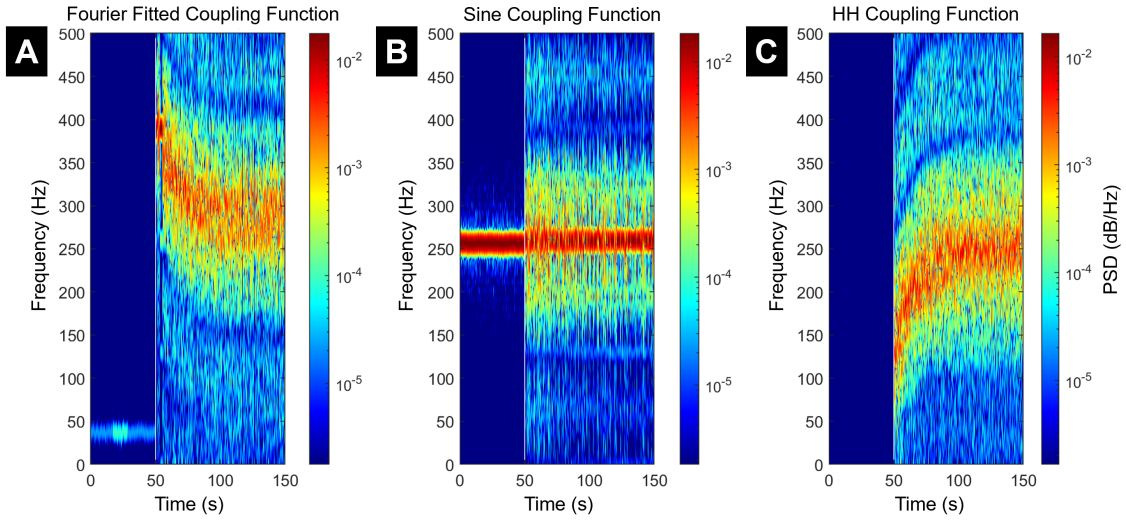


Figure B.4: Effect of the coupling function on ERNA slow dynamics. 50 seconds off-stimulation followed by 200 seconds on-stimulation. (A) The fitted second-order Fourier series coupling function used in the rest of the study, similar figure to Fig 4.1A. (B) Sinusoidal coupling function. (C) Hodgkin-Huxley (HH) derived coupling function. Other than coupling function changes, all other model parameters remain the same.

of the five fitted coefficient values. For each of the Fourier series coefficients we re-simulate the computational model after modulating the coefficients by the factors 0, 0.25, 0.5, 1, 2 and 4 (Fig B.5). The columns corresponding to the first-order coefficients (f_1 and f_2) show little variability for all factors (including 0) both on- and off-stimulation. Hence, the first order coefficients are not only not very sensitive, but may not be necessary for the model. The other three coefficients all seem to produce more notable changes to the spectrograms when modulated. The changes result in either failing to reproduce off-stimulation dynamics, on-stimulation dynamics, or both such that the resulting spectrogram no longer matches all characteristics of the slow ERNA dynamics.

B.4.2 Sensitivity of Phase Response Curve

We also compare different types of PRCs (Fig B.6). We scale the Hodgkin-Huxley PRC to a maximum amplitude of one to provide a comparable scale to the sinusoidal PRC. We consider a constant PRC of magnitude $1/\sqrt{2}$. These PRCs are chosen so that we can identify the role of the PRC in the computational model. As the constant PRC does not replicate the on-stimulation dynamics, it is likely that

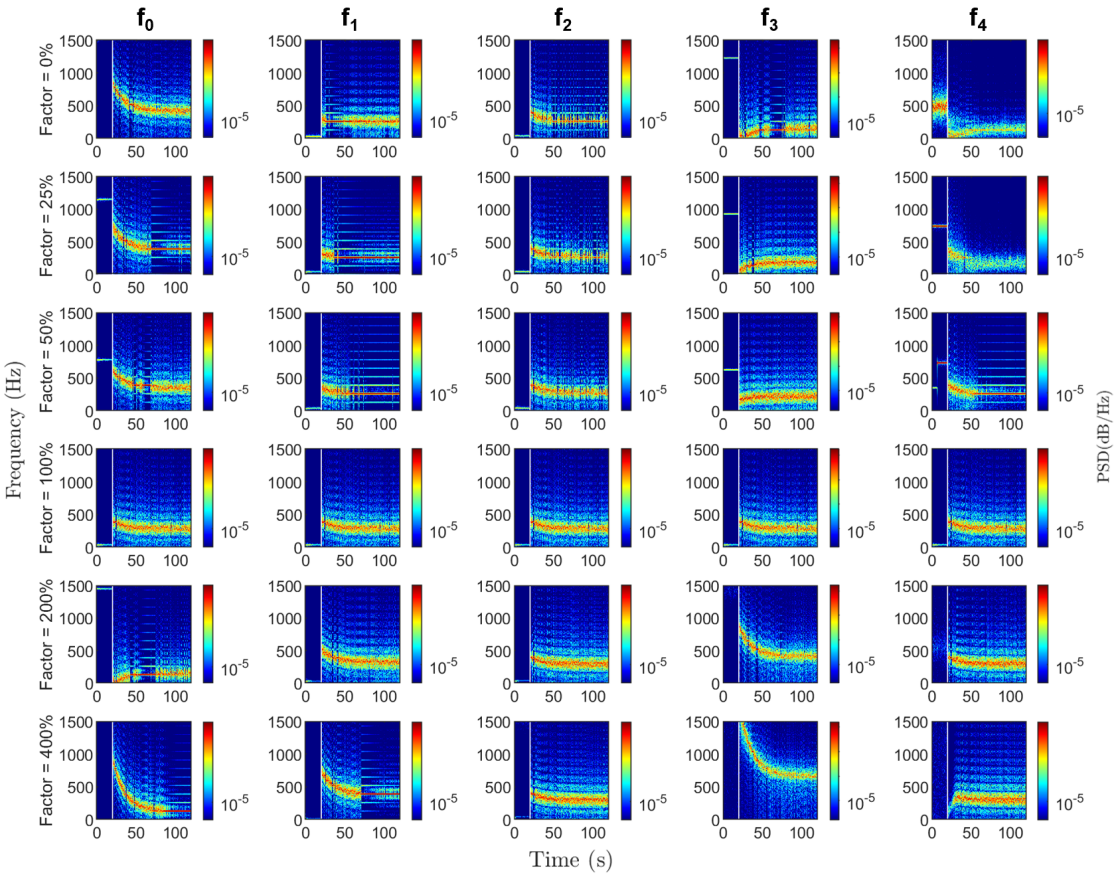


Figure B.5: Effect of modulating each Fourier coefficient of the coupling function on ERNA slow dynamics. Spectrograms showing 20 seconds off-stimulation followed by 100 seconds on-stimulation, observed over the large frequency range of [0Hz,1500Hz] due to high frequency activity in some of the simulations. Columns ordered by Fourier coefficients: f_0 correspond to the vertical shift, f_1 and f_2 are coefficients corresponding to the first harmonic components (cosine and sine, respectively), and f_3 and f_4 are coefficients corresponding to the second harmonic components (cosine and sine, respectively). Rows ordered by the factor multiplying the coefficients. Factor of 100% represents no change to the coefficient with respect to the fitted results, so this row has the same parameters for each of the coefficient simulations.

a synchronising effect from the PRC is required to reproduce ERNA. This is in agreement with the results from Appendix Section B.2. The Hodgkin-Huxley PRC (Fig B.6B) is chosen as a more biophysical representation, and we do see the peak of the frequency decay start at 390Hz (the third harmonic of stimulation frequency) before dropping down. There is intermittent locking at the 5:2 harmonic (325Hz for 130Hz stimulation frequency) before dropping further and locking to the second harmonic of stimulation (at 260Hz). However, unlike the sine PRC and the data,

the locking to components of stimulation frequency is much stronger to the point where activity only seems to appear at these components. This could be due to the sharper gradient of the Hodgkin-Huxley PRC at the zero-crossing point having a stronger synchronising effect on the oscillators than the sinusoidal PRC. As the fitting was performed using the sinusoidal PRC, it is certainly possible that by fitting with the Hodgkin-Huxley PRC instead we could observe a response that more closely resembles the data.

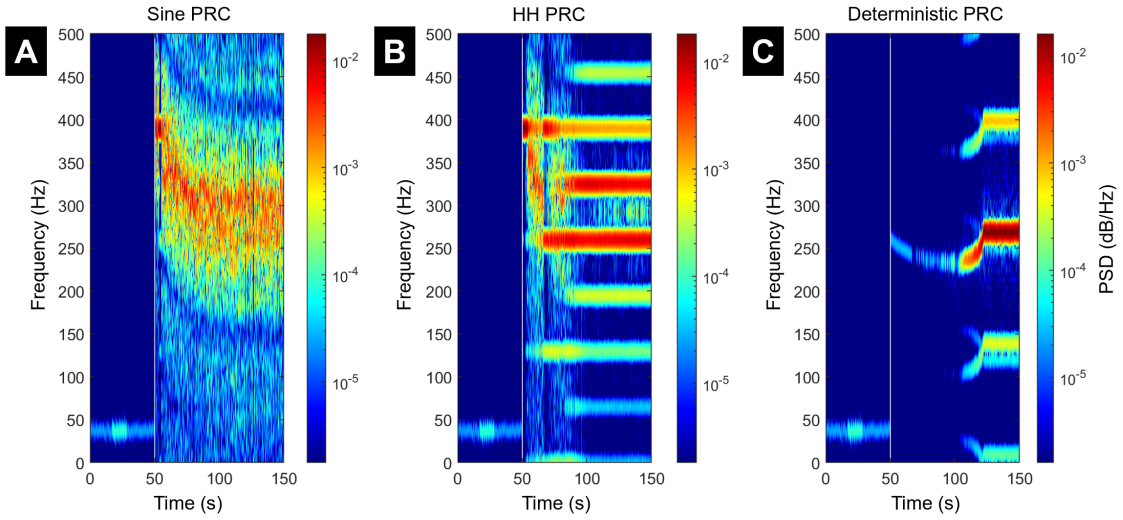


Figure B.6: Effect of the PRC on ERNA slow dynamics. 50 seconds off-stimulation followed by 200 seconds on-stimulation. (A) sinusoidal PRC, similar simulation to Fig 4.1A. (B) Hodgkin-Huxley (HH) PRC. (C) Constant PRC. Other than PRC changes all parameters remain the same as the main body of this study.

B.5 Alternative Parameter Set with Lower Natural Frequency

We explore the modified Kuramoto model further by constraining the natural frequencies of individual oscillators to lower frequencies. Results from STN slice experiments could indicate that individual STN oscillators have natural frequencies around 20Hz. Previously, we assumed that 20Hz was the frequency of the overall neural ensemble and did not reflect individual neuron properties, therefore not constraining the ω_i's in the model. Here, we constrain the mean natural frequency of oscillators (Ω) to 20Hz. Given the model set up, it is possible to maintain

similar off-stimulation dynamics by countering the decrease in natural frequency by a corresponding increase in the noughth order shift of the coupling function f_0 (see values in Table B.2).

Parameter	$\Omega(Hz)$	$\sigma(Hz)$	f_0	p_{RtP}	$\tau_{\mathrm{RtP}}(s)$
Values for Fig B.7	20	2.11	-0.68	0.00035	50
Values for Fig B.8	20	2.11	-0.68	0.00007	10

Table B.2: Alternative parameter sets for low natural frequency simulations. All other parameters remain unchanged from Table B.1.

Following the adjustments to natural frequency and f_0, we simulate the model while keeping all other parameters the same as the fitted model (Fig B.7). We see similar amplitude dynamics decreasing over the stimulation window (Fig B.7C) as with the fitted model. However, as coupling strength continues to decrease over the stimulation window, we see the frequency decay reach much lower values towards the end of the stimulation window (Fig B.7B). It continues to decrease to a value lower than that seen from the ERNA data (<100Hz).

Given how vesicle depletion changes the coupling strength during stimulation, it is not possible to maintain the same dynamics on-stimulation with this same method. Hence, in order to maintain a similar frequency decay, the long term dynamics of the RtP (as dictated by τ_{RtP} and p_{RtP}) are modulated (see second row of Table B.2) such that the frequency at the end of the 100-second stimulation window approximately matches that of the fitted modified Kuramoto model from the main part of this study (Fig 4.1)A. While it is possible to maintain higher frequency dynamics (Fig B.8B), the amplitude decay does not demonstrate any substantial variation, remaining somewhat constant (Fig B.8C). Hence, in order to see amplitude variation it may be required that RtP occupancy and therefore coupling strength decreases low enough such that oscillators can move between clusters. By reducing coupling strength closer to zero we allow the network to oscillate at a similar frequency to the natural frequency of the individual oscillators. While it stands to reason that this could be achieved with an alternative resolution of the coupling function, we have explored

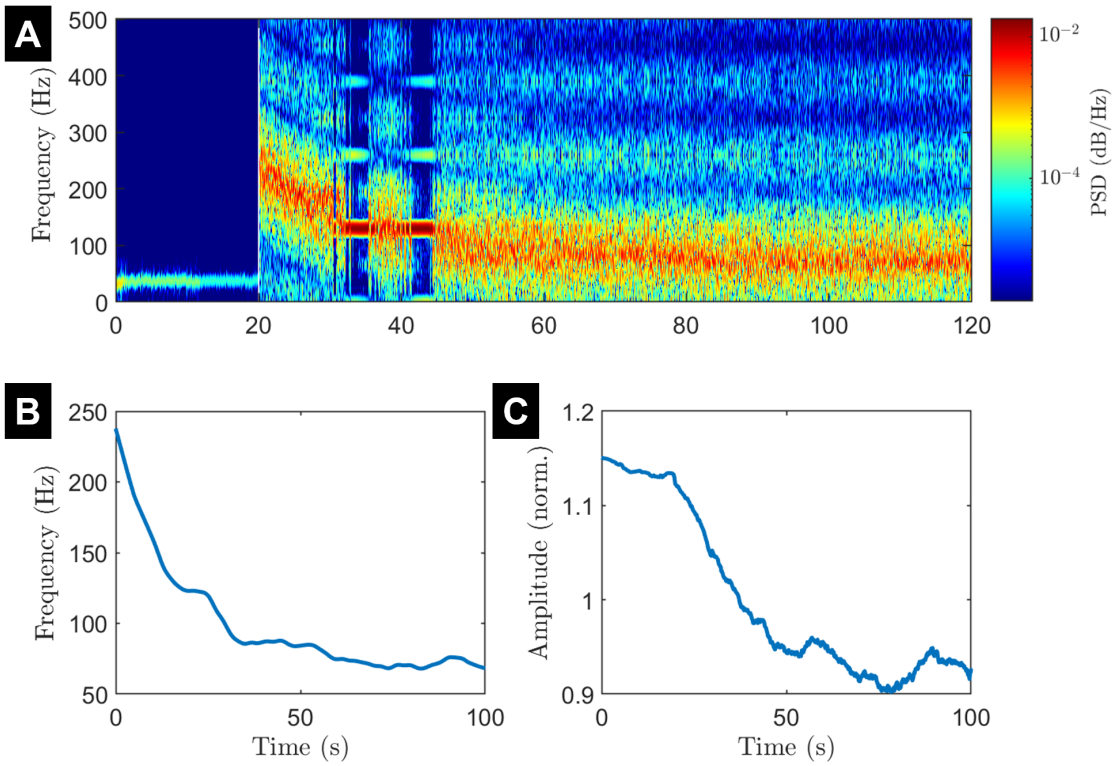


Figure B.7: Slow dynamics for lowered natural frequency model with all other parameters remaining the same. (A) The spectrogram of 20 seconds off-stimulation followed by 100 seconds on-stimulation. (B) The on-stimulation frequency decay. (C) the on-stimulation amplitude response.

this hypothesis in detail. We have repeated the fitting process with constrained natural frequencies to 20Hz and have not observed encouraging results.

B.6 Dynamic Oscillations

In addition to the high frequency responses of ERNA, other dynamics frequency responses have been observed at lower frequencies (Tiruvadi et al. 2022). In response to 130Hz stimulation of the subcallosal cingulate, dynamic oscillations in the 10-50Hz band were elicited (Fig B.9A, the PSD spectrogram is low-pass filtered at 25Hz to remove stimulation artefacts) (Tiruvadi et al. 2022). Over the course of roughly 200 seconds of stimulation, multiple individual frequency decays are observed starting from between 10-50Hz before dropping in frequency and amplitude.

It is possible to simulate the fitted Kuramoto model with small parameter adjustments to elicit a similar response to the dynamic oscillations. We decrease the

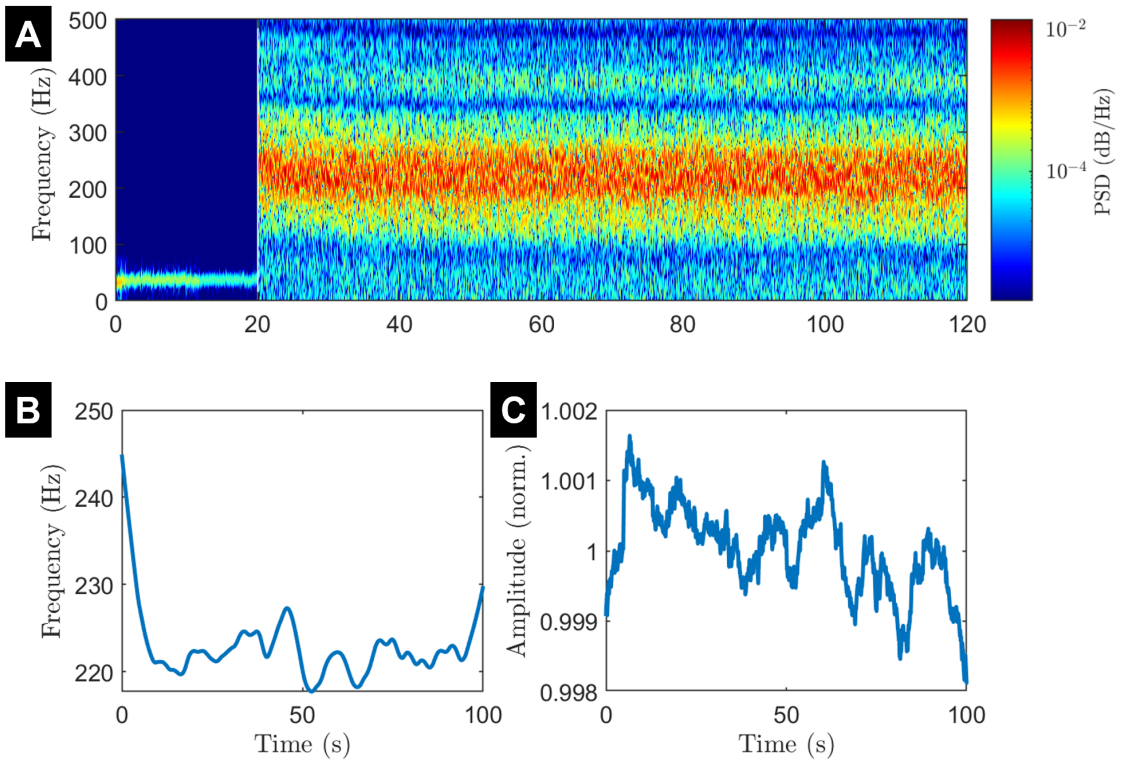


Figure B.8: Slow dynamics for lowered natural frequency model with coupling strength changed to approximately fit to frequency decay. (A) The spectrogram of 20 seconds off-stimulation followed by 100 seconds on-stimulation. (B) The on-stimulation frequency decay. (C) the on-stimulation amplitude response.

mean and standard deviation of the natural frequency distribution by a factor of 10 ($\Omega = 24.9Hz$ and $\sigma = 2.632$) and decrease the off-stimulation coupling strength by a factor of 20 ($k_\mu = 599$). This reduces the frequency of our ERNA response to something similar to the dynamic oscillations (Fig B.9B). All other parameters remain unchanged from Table B.1. In the model, we can see two initial frequency responses between 20 and 50Hz that decrease in frequency. Amplitude decreases as well with the higher frequency response having a lower amplitude and disappearing first. The model also shows highly coupled off-stimulation activity at 50Hz, which was not seen in the data. This could be addressed through increased noise and multiple model units to provide a more distributed off-stimulation response. An alternative would be to refit the model with adjusted cost features to provide a better fit to the dynamic oscillation data. These results indicate that the same mechanisms that we postulate may be responsible for ERNA, such as vesicle depletion, may

also be responsible for the appearance of dynamic oscillations.

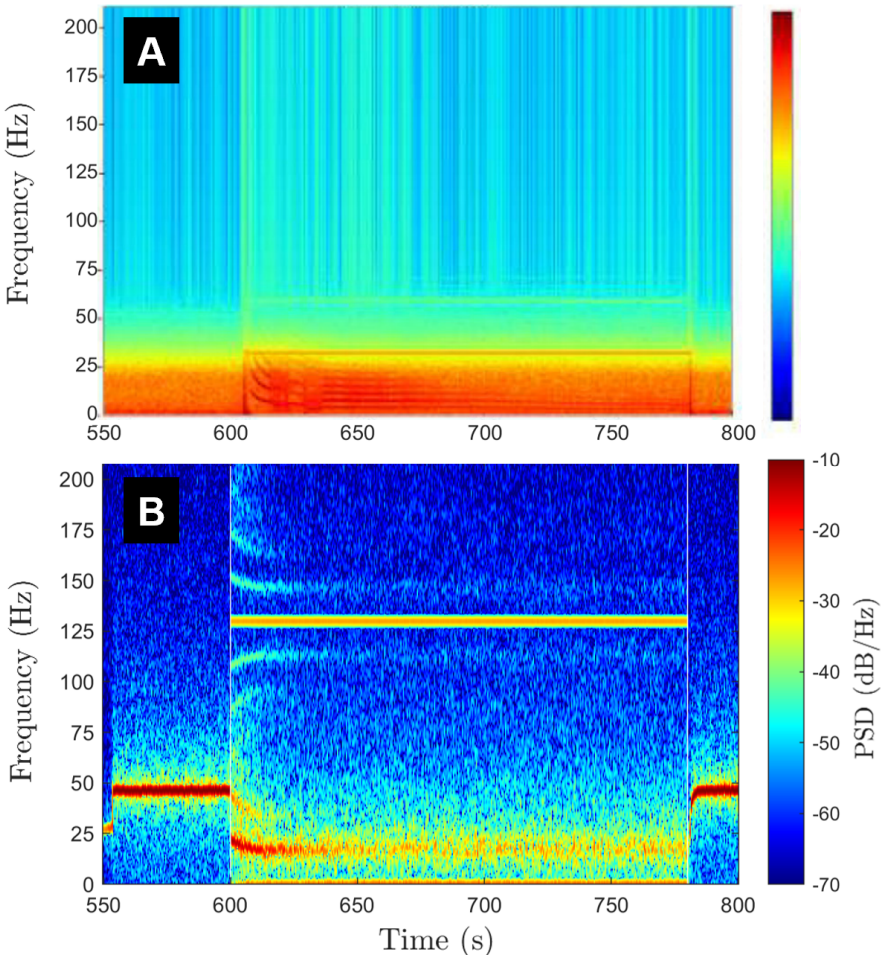


Figure B.9: Comparison of model dynamics with small parameter adjustments to dynamic oscillations example from data. (A) Dynamic oscillations from data of 130Hz stimulation of the subcallosal cingulate, adapted from (Tiruvadi et al. 2022) (no colourscale axis provided in the data). Data are low-pass filtered at 25Hz to remove stimulation artefacts. (B) Example of dynamic oscillation-type behaviour from 130Hz stimulation of the adjusted ERNA Kuramoto model.

References

Abbasi, Omid, Jan Hirschmann, Georg Schmitz, Alfons Schnitzler, and Markus Butz (2016). "Rejecting deep brain stimulation artefacts from MEG data using ICA and mutual information". In: *Journal of Neuroscience Methods* 268. DOI: 10.1016/j.jneumeth.2016.04.010.

Abeysuriya, Romesh G., Jonathan Hadida, Stamatios N. Sotiropoulos, Saad Jbabdi, Robert Becker, Benjamin A.E. Hunt, Matthew J. Brookes, and Mark W. Woolrich (2018). "A biophysical model of dynamic balancing of excitation and inhibition in fast oscillatory large-scale networks". In: *PLoS Computational Biology* 14 (2). DOI: 10.1371/journal.pcbi.1006007.

Alabi, Abdul Rasheed A. and Richard W. Tsien (2012). "Synaptic vesicle pools and dynamics". In: *Cold Spring Harbor Perspectives in Biology* 4 (8). DOI: 10.1101/cshperspect.a013680.

Alarie, Michaela E., Nicole R. Provenza, Michelle Avendano-Ortega, Sarah A. McKay, Ayan S. Waite, Raissa K. Mathura, Jeffrey A. Herron, Sameer A. Sheth, David A. Borton, and Wayne K. Goodman (2022). "Artifact characterization and mitigation techniques during concurrent sensing and stimulation using bidirectional deep brain stimulation platforms". In: *Frontiers in Human Neuroscience* 16. DOI: 10.3389/fnhum.2022.1016379.

Alavi, Seyed Mojtaba, Amin Mirzaei, Alireza Valizadeh, and Reza Ebrahimpour (2022). "Excitatory deep brain stimulation quenches beta oscillations arising in a computational model of the subthalamo-pallidal loop". In: *Scientific Reports* 12 (1). DOI: 10.1038/s41598-022-10084-4.

Ali, Mohsin M., Kristin K. Sellers, and Flavio Fröhlich (July 2013). "Transcranial alternating current stimulation modulates large-scale cortical network activity by network resonance". In: *Journal of Neuroscience* 33.27, pp. 11262–11275. DOI: 10.1523/JNEUROSCI.5867-12.2013.

Arnol'd, V I (Aug. 1983). "Remarks on the perturbation theory for problems of Mathieu type". In: *Russian Mathematical Surveys* 38.4, pp. 215–233. DOI: 10.1070/rm1983v038n04abeh004210.

Arruda, Beatriz S., Carolina Reis, James J. Sermon, Alek Pogosyan, Peter Brown, and Hayriye Cagnan (2021). "Identifying and modulating distinct tremor states through peripheral nerve stimulation in Parkinsonian rest tremor". In: *Journal of NeuroEngineering and Rehabilitation* 18 (1). DOI: 10.1186/s12984-021-00973-6.

Ashwin, Peter, Stephen Coombes, and Rachel Nicks (2016). "Mathematical Frameworks for Oscillatory Network Dynamics in Neuroscience". In: *Journal of Mathematical Neuroscience* 6 (1). DOI: 10.1186/s13408-015-0033-6.

Asllani, Malbor, Paul Expert, and Timoteo Carletti (July 2018). "A minimally invasive neurostimulation method for controlling abnormal synchronisation in the neuronal activity". In: *PLoS Computational Biology* 14.7, e1006296. DOI: 10.1371/journal.pcbi.1006296.

Basu, Ishita, Britni Crocker, Kara Farnes, Madeline M. Robertson, Angelique C. Paulk, Deborah I. Vallejo, Darin D. Dougherty, Sydney S. Cash, Emad N. Eskandar, Mark A. Kramer, and Alik S. Widge (2018). "A neural mass model to predict electrical stimulation evoked responses in human and non-human primate brain". In: *Journal of Neural Engineering* 15 (6). DOI: 10.1088/1741-2552/aae136.

Benabid, A. L., P. Pollak, A. Louveau, S. Henry, and J. De Rougemont (1987). "Combined (thalamotomy and stimulation) stereotactic surgery of the vim thalamic nucleus for bilateral parkinson disease". In: *Stereotactic and Functional Neurosurgery* 50 (1-6). DOI: 10.1159/000100803.

Benabid, Alim Louis, Stephan Chabardes, John Mitrofanis, and Pierre Pollak (2009). *Deep brain stimulation of the subthalamic nucleus for the treatment of Parkinson's disease*. DOI: 10.1016/S1474-4422(08)70291-6.

Bergman, Hagai (2021). *The Hidden Life of the Basal Ganglia*. MIT Press. DOI: 10.7551/mitpress/14075.001.0001.

Bick, Christian, Marc Goodfellow, Carlo R Laing, and Erik A Martens (2020). "Understanding the dynamics of biological and neural oscillator networks through exact mean-field reductions: a review". In: *The Journal of Mathematical Neuroscience* 10.1, p. 9. DOI: 10.1186/s13408-020-00086-9.

Bolam, J. P., M. T.C. Brown, J. Moss, and P. J. Magill (2009). "Basal Ganglia: Internal Organization". In: *Encyclopedia of Neuroscience*. DOI: 10.1016/B978-008045046-9.01294-8.

Bolam, J. P., J. J. Hanley, P. A.C. Booth, and M. D. Bevan (2000). "Synaptic organisation of the basal ganglia". In: *Journal of Anatomy* 196 (4). DOI: 10.1017/S0021878299005944.

Borisyuk, Roman M. and Alexandr B. Kirillov (Feb. 1992). "Bifurcation analysis of a neural network model". In: *Biological Cybernetics* 66.4, pp. 319–325. DOI: 10.1007/BF00203668.

Bosman, Conrado A., Carien S. Lansink, and Cyriel M.A. Pennartz (June 2014). "Functions of gamma-band synchronization in cognition: From single circuits to functional diversity across cortical and subcortical systems". In: *European Journal of Neuroscience* 39.11, pp. 1982–1999. DOI: 10.1111/ejn.12606.

Branco, Tiago and Kevin Staras (2009). "The probability of neurotransmitter release: Variability and feedback control at single synapses". In: *Nature Reviews Neuroscience* 10 (5). DOI: 10.1038/nrn2634.

Brandão, Pedro Renato P., Renato Puppi Munhoz, Talyta Cortez Grippe, Francisco Eduardo Costa Cardoso, Brenda Macedo de Almeida e Castro, Ricardo Titze-de-Almeida, Carlos Tomaz, and Maria Clotilde Henriques Tavares (2020). "Cognitive impairment in Parkinson's disease: A clinical and pathophysiological overview". In: *Journal of the Neurological Sciences* 419. DOI: 10.1016/j.jns.2020.117177.

Brown, Eric, Jeff Moehlis, and Philip Holmes (Apr. 2004). "On the phase reduction and response dynamics of neural oscillator populations". In: *Neural Computation* 16.4, pp. 673–715. DOI: 10.1162/089976604322860668.

Burton, Emma J., Ian G. McKeith, David J. Burn, E. David Williams, and John T. O'Brien (2004). "Cerebral atrophy in Parkinson's disease with and without dementia: A comparison with Alzheimer's disease, dementia with Lewy bodies and controls". In: *Brain* 127 (4). DOI: 10.1093/brain/awh088.

Byrne, Áine, Reuben D. O'Dea, Michael Forrester, James Ross, and Stephen Coombes (2020). *Next-generation neural mass and field modeling*. DOI: 10.1152/JN.00406.2019.

Cagnan, Hayriye, David Pedrosa, Simon Little, Alek Pogosyan, Binith Cheeran, Tipu Aziz, Alexander Green, James Fitzgerald, Thomas Foltynie, Patricia Limousin, Ludvic Zrinzo, Marwan Hariz, Karl J. Friston, Timothy Denison, and Peter Brown (2017). "Stimulating at the right time: Phase-specific deep brain stimulation". In: *Brain* 140 (1). DOI: 10.1093/brain/aww286.

Calabresi, Paolo, Veronica Ghiglieri, Petra Mazzocchetti, Ilenia Corbelli, and Barbara Picconi (2015). "Levodopa-induced plasticity: A doubleedged sword in parkinson's disease?" In: *Philosophical Transactions of the Royal Society B: Biological Sciences* 370 (1672). DOI: 10.1098/rstb.2014.0184.

Calabresi, Paolo, Barbara Picconi, Alessandro Tozzi, Veronica Ghiglieri, and Massimiliano Di Filippo (2014). *Direct and indirect pathways of basal ganglia: A critical reappraisal*. DOI: 10.1038/nn.3743.

Caldwell, D. J., J. A. Cronin, R. P.N. Rao, K. L. Collins, K. E. Weaver, A. L. Ko, J. G. Ojemann, J. N. Kutz, and B. W. Brunton (2020). "Signal recovery from stimulation artifacts in intracranial recordings with dictionary learning". In: *Journal of Neural Engineering* 17 (2). DOI: 10.1088/1741-2552/ab7a4f.

Cassidy, Michael, Paolo Mazzone, Antonio Oliviero, Angelo Insola, Pietro Tonali, Vincenzo Di Lazzaro, and Peter Brown (June 2002). "Movement-related changes in synchronization in the human basal ganglia". In: *Brain* 125.6, pp. 1235–1246. DOI: 10.1093/brain/awf135.

Castilla-Cortázar, Inma, Gabriel A. Aguirre, Giovana Femat-Roldán, Irene Martín-Estal, and Luis Espinosa (2020). "Is insulin-like growth factor-1 involved in Parkinson's disease development?" In: *Journal of Translational Medicine* 18 (1). DOI: 10.1186/s12967-020-02223-0.

Chamberland, Simon and Katalin Tóth (2016). "Functionally heterogeneous synaptic vesicle pools support diverse synaptic signalling". In: *Journal of Physiology* 594 (4). DOI: 10.1113/JP270194.

Chan, Diane, Ho-Jun Suk, Brennan L. Jackson, Noah Pollak Milman, Danielle Stark, Elizabeth B. Klerman, Erin Kitchener, Vanesa S. Fernandez Avalos, Arit Banerjee, Sara D. Beach, Joel Blanchard, Colton Stearns, Aaron Boes, Brandt Uitermarkt, Phillip Gander, Matthew Howard III, Eliezer J. Sternberg, Alfonso Nieto-Castanon, Sheeba Anteraper, Susan Whitfield-Gabrieli, Emery Brown, Edward S. Boyden, Bradford Dickerson, and Li-Huei Tsai (2021). "Gamma Frequency Sensory Stimulation in Probable Mild Alzheimer's Dementia Patients: Results of a Preliminary Clinical Trial". In: *SSRN Electronic Journal*. DOI: 10.2139/ssrn.3846540.

Chen, Paula, Taewoo Kim, Evan Dastin-Van Rijn, Nicole R. Provenza, Sameer A. Sheth, Wayne K. Goodman, David A. Borton, Matthew T. Harrison, and Jerome Darbon (2022). "Periodic Artifact Removal With Applications to Deep Brain Stimulation". In: *IEEE Transactions on Neural Systems and Rehabilitation Engineering* 30. DOI: 10.1109/TNSRE.2022.3205453.

Chen, Yue, Bozhi Ma, Hongwei Hao, and Luming Li (2021). "Cause of Subharmonics in Local Field Potentials Recorded by Sensing-Enabled Neurostimulator". In: *Proceedings of the Annual International Conference of the IEEE Engineering in Medicine and Biology Society, EMBS*. DOI: 10.1109/EMBC46164.2021.9630422.

Chiken, Satomi and Atsushi Nambu (2016). "Mechanism of Deep Brain Stimulation: Inhibition, Excitation, or Disruption?" In: *Neuroscientist* 22 (3). DOI: 10.1177/1073858415581986.

Church, Frank C. (2021). "Review treatment options for motor and non-motor symptoms of parkinson's disease". In: *Biomolecules* 11 (4). DOI: 10.3390/biom11040612.

Cleary, Daniel R., Ahmed M. Raslan, Jonathan E. Rubin, Diaa Bahgat, Ashwin Viswanathan, Mary M. Heinricher, and Kim J. Burchiel (2013). "Deep brain stimulation entrains local neuronal firing in human globus pallidus internus". In: *Journal of Neurophysiology* 109 (4). DOI: 10.1152/jn.00420.2012.

Coombes, Stephen and Áine Byrne (2019). "Next Generation Neural Mass Models". In: DOI: 10.1007/978-3-319-71048-8_1.

Cowan, Jack D., Jeremy Neuman, and Wim van Drongelen (Jan. 2016). "Wilson–Cowan Equations for Neocortical Dynamics". In: *Journal of Mathematical Neuroscience* 6.1, pp. 1–24. DOI: 10.1186/s13408-015-0034-5.

Cutsuridis, Vassilis (2019). *Multiscale Models of Brain Disorders*. Springer, pp. 167–184.

Das, Rupam, Farshad Moradi, and Hadi Heidari (2020). *Biointegrated and Wirelessly Powered Implantable Brain Devices: A Review*. DOI: 10.1109/TBCAS.2020.2966920.

Debarros, Jean, Lea Gaignon, Shenghong He, Alek Pogosyan, Moaad Benjaber, Timothy Denison, Peter Brown, and Huiling Tan (2020). "Artefact-free recording of local field potentials with simultaneous stimulation for closed-loop Deep-Brain Stimulation". In: vol. 2020-July. DOI: 10.1109/EMBC44109.2020.9176665.

Degos, Bertrand, Jean Michel Deniau, Anne Marie Thierry, Jacques Glowinski, Laurent Pezard, and Nicolas Maurice (2005). "Neuroleptic-induced catalepsy: Electrophysiological mechanisms of functional recovery induced by high-frequency stimulation of the subthalamic nucleus". In: *Journal of Neuroscience* 25 (33). DOI: 10.1523/JNEUROSCI.1056-05.2005.

Deng, Jiahui and Guoming Luan (2017). "Mechanisms of Deep Brain Stimulation for Epilepsy and Associated Comorbidities". In: *Neuropsychiatry* s1. DOI: 10.4172/neuropsychiatry.1000s1005.

Denker, Annette and Silvio O. Rizzoli (2010). "Synaptic vesicle pools: An update". In: *Frontiers in Synaptic Neuroscience* (OCT). DOI: 10.3389/fnsyn.2010.00135.

Detorakis, Georgios, Antoine Chaillet, Stéphane Palfi, and Suhan Senova (2015). "Closed-loop stimulation of a delayed neural fields model of parkinsonian STN-GPe network: a theoretical and computational study". In: *Frontiers in Neuroscience* 9. DOI: 10.3389/fnins.2015.00237.

Dittman, Jeremy S. and Timothy A. Ryan (2019). "The control of release probability at nerve terminals". In: *Nature Reviews Neuroscience* 20 (3). DOI: 10.1038/s41583-018-0111-3.

Dong, Jie, Sarah Hawes, Junbing Wu, Weidong Le, and Huaibin Cai (Mar. 2021). "Connectivity and Functionality of the Globus Pallidus Externa Under Normal Conditions and Parkinson's Disease". In: *Frontiers in Neural Circuits* 15, p. 8. DOI: 10.3389/FNCIR.2021.645287/BIBTEX.

Duchet, Benoit, Filippo Ghezzi, Gihan Weerasinghe, Gerd Tinkhauser, A. A. Kühn, Peter Brown, Christian Bick, and Rafal Bogacz (July 2021). "Average beta burst duration profiles provide a signature of dynamical changes between the on and off medication states in Parkinson's disease". In: *PLoS Computational Biology* 17 (7), e1009116. DOI: 10.1371/journal.pcbi.1009116.

Duchet, Benoit, James J Sermon, Gihan Weerasinghe, Timothy Denison, and Rafal Bogacz (Apr. 2023). "How to entrain a selected neuronal rhythm but not others: open-loop dithered brain stimulation for selective entrainment". In: *Journal of Neural Engineering* 20.2, p. 026003. DOI: 10.1088/1741-2552/acbc4a.

Duchet, Benoit, Gihan Weerasinghe, Hayriye Cagnan, Peter Brown, Christian Bick, and Rafal Bogacz (Dec. 2020). "Phase-dependence of response curves to deep brain stimulation and their relationship: from essential tremor patient data to a Wilson–Cowan model". In: *Journal of Mathematical Neuroscience* 10 (1). DOI: 10.1186/s13408-020-00081-0.

Fernández-Alfonso, Tomás and Timothy A. Ryan (2004). "The kinetics of synaptic vesicle pool depletion at CNS synaptic terminals". In: *Neuron* 41 (6). DOI: 10.1016/S0896-6273(04)00113-8.

Fleming, J. E., M. Benjaber, R. Toth, M. Zamora, K. Landin, A. Kavoosi, J. Ottoway, T. Gillbe, R. J. Piper, T. Noone, H. Campbell, I. Gillbe, M. Kaliakatsos, M. Tisdall, A. Valentin, and T. Denison (2023). "An embedded intracranial seizure monitor for objective outcome measurements and rhythm identification". In: vol. 2023 - July. DOI: 10.1109/EMBC40787.2023.10340850.

Follett, Kenneth A., Frances M. Weaver, Matthew Stern, Kwan Hur, Crystal L. Harris, Ping Luo, William J. Marks, Johannes Rothlind, Oren Sagher, Claudia Moy, Rajesh Pahwa, Kim Burchiel, Penelope Hogarth, Eugene C. Lai, John E. Duda, Kathryn Holloway, Ali Samii, Stacy Horn, Jeff M. Bronstein, Gatana Stoner, Philip A. Starr, Richard Simpson, Gordon Baltuch, Antonio De Salles, Grant D. Huang, and Domenic J. Reda (2010). "Pallidal versus Subthalamic Deep-Brain Stimulation for Parkinson's Disease". In: *New England Journal of Medicine* 362 (22). DOI: 10.1056/nejmoa0907083.

Frey, Jessica, Jackson Cagle, Kara A. Johnson, Joshua K. Wong, Justin D. Hilliard, Christopher R. Butson, Michael S. Okun, and Coralie de Hemptinne (2022). "Past, Present, and Future of Deep Brain Stimulation: Hardware, Software, Imaging, Physiology and Novel Approaches". In: *Frontiers in Neurology* 13. DOI: 10.3389/fneur.2022.825178.

Fröhlich, Flavio (Nov. 2015). *Tuning out the blues - Thalamo-cortical rhythms as a successful target for treating depression*. DOI: 10.1016/j.brs.2015.07.040.

Gardella, Christophe, Olivier Marre, and Thierry Mora (2016). "A tractable method for describing complex couplings between neurons and population rate". In: *eNeuro* 3 (4). DOI: 10.1523/ENEURO.0160-15.2016.

Gardner, John (Oct. 2013). "A history of deep brain stimulation: Technological innovation and the role of clinical assessment tools". In: *Social Studies of Science* 43 (5), pp. 707–728. DOI: 10.1177/0306312713483678.

Gilron, Ro'ee, Simon Little, Randy Perrone, Robert Wilt, Coralie de Hemptinne, Maria S. Yaroshinsky, Caroline A. Racine, Sarah S. Wang, Jill L. Ostrem, Paul S. Larson, Doris D. Wang, Nick B. Galifianakis, Ian O. Bledsoe, Marta San Luciano, Heather E. Dawes, Gregory A. Worrell, Vaclav Kremen, David A. Borton, Timothy Denison, and Philip A. Starr (May 2021). "Long-term wireless streaming of neural recordings for circuit discovery and adaptive stimulation in individuals with Parkinson's disease". In: *Nature Biotechnology* 39.9, pp. 1078–1085. DOI: 10.1038/s41587-021-00897-5.

Guerra, Andrea, Donato Colella, Margherita Giangrosso, Antonio Cannavacciuolo, Giulia Paparella, Giovanni Fabbrini, Antonio Suppa, Alfredo Berardelli, and

Matteo Bologna (July 2021). "Driving motor cortex oscillations modulates bradykinesia in Parkinson's disease". In: *Brain*. DOI: 10.1093/brain/awab257.

Guo, Jun, Jian Long Ge, Mei Hao, Zhi Cheng Sun, Xin Sheng Wu, Jian Bing Zhu, Wei Wang, Pan Tong Yao, Wei Lin, and Lei Xue (2015). "A Three-Pool Model Dissecting Readily Releasable Pool Replenishment at the Calyx of Held". In: *Scientific Reports* 5. DOI: 10.1038/srep09517.

Güttler, Christopher, Jennifer Altschüler, Kaloyan Tanev, Saskia Böckmann, Jens Kersten Haumesser, Vadim V. Nikulin, Andrea A. Kühn, and Christoph van Riesen (Apr. 2021). "Levodopa-Induced Dyskinesia Are Mediated by Cortical Gamma Oscillations in Experimental Parkinsonism". In: *Movement Disorders* 36.4, pp. 927–937. DOI: 10.1002/mds.28403.

Halje, Pär, Martin Tamtè, Ulrike Richter, Mohsin Mohammed, M. Angela Cenci, and Per Petersson (2012). "Levodopa-Induced Dyskinesia Is Strongly Associated with Resonant Cortical Oscillations". In: *Journal of Neuroscience* 32.47, pp. 16541–16551. DOI: 10.1523/JNEUROSCI.3047-12.2012.

Hallworth, Nicholas E., Charles J. Wilson, and Mark D. Bevan (2003). "Apamin-sensitive small conductance calcium-activated potassium channels, through their selective coupling to voltage-gated calcium channels, are critical determinants of the precision, pace, and pattern of action potential generation in rat subthalamic nucleus neurons in vitro". In: *Journal of Neuroscience* 23 (20). DOI: 10.1523/jneurosci.23-20-07525.2003.

Hammer, Lauren H., Ryan B. Kochanski, Philip A. Starr, and Simon Little (2022). "Artifact Characterization and a Multipurpose Template-Based Offline Removal Solution for a Sensing-Enabled Deep Brain Stimulation Device". In: *Stereotactic and Functional Neurosurgery* 100 (3). DOI: 10.1159/000521431.

Hanslmayr, Simon, Nikolai Axmacher, and Cory S. Inman (July 2019). *Modulating Human Memory via Entrainment of Brain Oscillations*. DOI: 10.1016/j.tins.2019.04.004.

Hashimoto, Takao, Christopher M. Elder, Michael S. Okun, Susan K. Patrick, and Jerrold L. Vitek (2003). "Stimulation of the subthalamic nucleus changes the firing pattern of pallidal neurons". In: *Journal of Neuroscience* 23 (5). DOI: 10.1523/jneurosci.23-05-01916.2003.

Hegeman, Daniel J., Ellie S. Hong, Vivian M. Hernández, and C. Savio Chan (2016). *The external globus pallidus: Progress and perspectives*. DOI: 10.1111/ejn.13196.

Hennig, Matthias H. (2013). "Theoretical models of synaptic short term plasticity". In: *Frontiers in Computational Neuroscience* (APR 2013). DOI: 10.3389/fncom.2013.00045.

Herrington, Todd M., Jennifer J. Cheng, and Emad N. Eskandar (Jan. 2016). "Mechanisms of deep brain stimulation". In: *Journal of Neurophysiology* 115 (1), pp. 19–38. DOI: 10.1152/jn.00281.2015.

Herron, Jeffrey, Scott Stanslaski, Tom Chouinard, Rob Corey, Timothy Denison, and Heather Orser (2018). "Bi-directional brain interfacing instrumentation". In: DOI: 10.1109/I2MTC.2018.8409795.

Holt, Abbey B. and Theoden I. Netoff (2013). "Computational modeling of epilepsy for an experimental neurologist". In: *Experimental Neurology* 244. DOI: 10.1016/j.expneurol.2012.05.003.

Hoppensteadt, Frank C. and Eugene M. Izhikevich (Nov. 1998). "Thalamo-cortical interactions modeled by weakly connected oscillators: Could the brain use FM radio

principles?" In: *BioSystems*. Vol. 48. Biosystems, pp. 85–94. DOI: 10.1016/S0303-2647(98)00053-7.

Huang, Wei A., Iain M. Stitt, Ehsan Negahbani, D. J. Passey, Sangtae Ahn, Marshall Davey, Moritz Dannhauer, Thien T. Doan, Anna C. Hoover, Angel V. Peterchev, Susanne Radtke-Schuller, and Flavio Fröhlich (May 2021). "Transcranial alternating current stimulation entrains alpha oscillations by preferential phase synchronization of fast-spiking cortical neurons to stimulation waveform". In: *Nature Communications* 12.1, pp. 1–20. DOI: 10.1038/s41467-021-23021-2.

Jaeger, D. and H. Kita (2011). *Functional connectivity and integrative properties of globus pallidus neurons*. DOI: 10.1016/j.neuroscience.2011.07.050.

Jakobs, Martin, Anton Fomenko, Andres M Lozano, and Karl L Kiening (2019). "Cellular, molecular, and clinical mechanisms of action of deep brain stimulation—a systematic review on established indications and outlook on future developments". In: *EMBO Molecular Medicine* 11 (4). DOI: 10.15252/emmm.201809575.

Javed, Nismat and Marco Cascella (2020). *Neuroanatomy, Globus Pallidus*.

Johnson, Kara A., Jackson N. Cagle, Janine Lobo Lopes, Joshua K. Wong, Michael S. Okun, Aysegul Gunduz, Aparna Wagle Shukla, Justin D. Hilliard, Kelly D. Foote, and Coralie De Hemptinne (2023). "Globus pallidus internus deep brain stimulation evokes resonant neural activity in Parkinson's disease". In: *Brain Communications* 5 (2). DOI: 10.1093/braincomms/fcad025.

Johnson, Luke, Ivan Alekseichuk, Jordan Krieg, Alex Doyle, Ying Yu, Jerrold Vitek, Matthew Johnson, and Alexander Opitz (2020). "Dose-dependent effects of transcranial alternating current stimulation on spike timing in awake nonhuman primates". In: *Science Advances* 6 (36). DOI: 10.1126/sciadv.aaz2747.

Johnson, Matthew D., Svjetlana Miocinovic, Cameron C. McIntyre, and Jerrold L. Vitek (2008). "Mechanisms and Targets of Deep Brain Stimulation in Movement Disorders". In: *Neurotherapeutics* 5 (2). DOI: 10.1016/j.nurt.2008.01.010.

Kaeser, Pascal S. and Wade G. Regehr (2017). "The readily releasable pool of synaptic vesicles". In: *Current Opinion in Neurobiology* 43. DOI: 10.1016/j.conb.2016.12.012.

Kalia, Lorraine V. and Anthony E. Lang (2015). "Parkinson's disease". In: *The Lancet* 386 (9996). DOI: 10.1016/S0140-6736(14)61393-3.

Kitai, S. T. and H. Kita (1987). "Anatomy and Physiology of the Subthalamic Nucleus: A Driving Force of the Basal Ganglia". In: *The Basal Ganglia II*. Ed. by Malcolm B. Carpenter and A. Jayaraman. Boston, MA: Springer US, pp. 357–373.

Koeglsperger, Thomas, Carla Palleis, Franz Hell, Jan H. Mehrkens, and Kai Bötzel (2019). "Deep brain stimulation programming for movement disorders: Current concepts and evidence-based strategies". In: *Frontiers in Neurology* 10 (MAY). DOI: 10.3389/fneur.2019.00410.

Koller, William, Rajesh Pahwa, Karen Busenbark, Jean Hubble, Steve Wilkinson, Anthony Lang, Paul Tuite, Elspeth Sime, Andres Lazano, Robert Hauser, Teresita Malapira, Donald Smith, Daniel Tarsy, Edison Miyawaki, Thorkild Norregaard, Theresa Kormos, and C. Warren Olanow (1997). "High-frequency unilateral thalamic stimulation in the treatment of essential and Parkinsonian tremor". In: *Annals of Neurology* 42 (3). DOI: 10.1002/ana.410420304.

Komarov, M. and A. Pikovsky (2014). "The Kuramoto model of coupled oscillators with a bi-harmonic coupling function". In: *Physica D: Nonlinear Phenomena* 289. DOI: 10.1016/j.physd.2014.09.002.

Koronowski, Kevin B. and Paolo Sassone-Corsi (2021). "Communicating clocks shape circadian homeostasis". In: *Science* 371 (6530). DOI: 10.1126/science.abd0951.

Krause, Matthew R., Pedro G. Vieira, Bennett A. Csorba, Praveen K. Pilly, and Christopher C. Pack (2019). "Transcranial alternating current stimulation entrains single-neuron activity in the primate brain". In: *Proceedings of the National Academy of Sciences of the United States of America* 116 (12). DOI: 10.1073/pnas.1815958116.

Kuramoto, Y (1983). *Chemical Oscillations, Waves and Turbulence*. Springer.

Lea-Carnall, Caroline A., Marcelo A. Montemurro, Nelson J. Trujillo-Barreto, Laura M. Parkes, and Wael El-Deredy (Feb. 2016). "Cortical Resonance Frequencies Emerge from Network Size and Connectivity". In: *PLoS Computational Biology* 12.2, e1004740. DOI: 10.1371/journal.pcbi.1004740.

Lim, Jeffrey, Po T. Wang, Alireza K. Bidhendi, Omid M. Arasteh, Susan J. Shaw, Michelle Armacost, Hui Gong, Charles Y. Liu, Payam Heydari, An H. Do, and Zoran Nenadic (2018). "Characterization of Stimulation Artifact Behavior in Simultaneous Electrocorticography Grid Stimulation and Recording". In: vol. 2018-July. DOI: 10.1109/EMBC.2018.8513216.

Lim, Jeffrey, Po T. Wang, Haoran Pu, Charles Y. Liu, Spencer Kellis, Richard A. Andersen, Payam Heydari, An H. Do, and Zoran Nenadic (2019). "Dipole Cancellation as an Artifact Suppression Technique in Simultaneous Electrocorticography Stimulation and Recording". In: vol. 2019-March. DOI: 10.1109/NER.2019.8716961.

Lio, Guillaume, Stéphane Thobois, Bénédicte Ballanger, Brian Lau, and Philippe Boulinguez (2018). *Removing deep brain stimulation artifacts from the electroencephalogram: Issues, recommendations and an open-source toolbox*. DOI: 10.1016/j.clinph.2018.07.023.

Little, Simon, Alex Pogosyan, Spencer Neal, Baltazar Zavala, Ludvic Zrinzo, Marwan Hariz, Thomas Foltynie, Patricia Limousin, Keyoumars Ashkan, James FitzGerald, Alexander L. Green, Tipu Z. Aziz, and Peter Brown (2013). "Adaptive deep brain stimulation in advanced Parkinson disease." In: *Annals of neurology* 74 (3). DOI: 10.1002/ana.23951.

Little, Simon, Elina Tripoliti, Martijn Beudel, Alek Pogosyan, Hayriye Cagnan, Damian Herz, Sven Bestmann, Tipu Aziz, Binith Cheeran, Ludvic Zrinzo, Marwan Hariz, Jonathan Hyam, Patricia Limousin, Tom Foltynie, and Peter Brown (2016). *Adaptive deep brain stimulation for Parkinson's disease demonstrates reduced speech side effects compared to conventional stimulation in the acute setting*. DOI: 10.1136/jnnp-2016-313518.

Lou, Xuelin, Fan Fan, Mirko Messa, Andrea Raimondi, Yumei Wu, Loren L. Looger, Shawn M. Ferguson, and Pietro De Camilli (2012). "Reduced release probability prevents vesicle depletion and transmission failure at dynamin mutant synapses". In: *Proceedings of the National Academy of Sciences of the United States of America* 109 (8). DOI: 10.1073/pnas.1121626109.

Lowet, Eric, Mark J. Roberts, Alina Peter, Bart Gips, and Peter De Weerd (Aug. 2017). "A quantitative theory of gamma synchronization in macaque V1". In: *eLife* 6. DOI: 10.7554/eLife.26642.

Marras, Connie, K. Ray Chaudhuri, Nataliya Titova, and Tiago A. Mestre (2020). "Therapy of Parkinson's Disease Subtypes". In: *Neurotherapeutics* 17 (4). DOI: 10.1007/s13311-020-00894-7.

McIntyre, Cameron C. and Ross W. Anderson (2016). "Deep brain stimulation mechanisms: the control of network activity via neurochemistry modulation". In: *Journal of Neurochemistry*. DOI: 10.1111/jnc.13649.

Meissner, Wassilios, Arthur Leblois, David Hansel, Bernard Bioulac, Christian E. Gross, Abdelhamid Benazzouz, and Thomas Boraud (2005). "Subthalamic high frequency stimulation resets subthalamic firing and reduces abnormal oscillations". In: *Brain* 128 (10). DOI: 10.1093/brain/awh616.

Milosevic, Luka, Suneil K. Kalia, Mojgan Hodaie, Andres M. Lozano, Alfonso Fasano, Milos R. Popovic, and William D. Hutchison (2018). "Neuronal inhibition and synaptic plasticity of basal ganglia neurons in Parkinson's disease". In: *Brain* 141 (1). DOI: 10.1093/brain/awx296.

Mitarai, Namiko, Uri Alon, and Mogens H. Jensen (June 2013). "Entrainment of noise-induced and limit cycle oscillators under weak noise". In: *Chaos* 23.2, p. 023125. DOI: 10.1063/1.4808253.

Muthuraman, Muthuraman, Manuel Bange, Nabin Koirala, Dumitru Ciolac, Bogdan Pintea, Martin Glaser, Gerd Tinkhauser, Peter Brown, Gunther Deuschl, and Sergiu Groppa (Dec. 2020). "Cross-frequency coupling between gamma oscillations and deep brain stimulation frequency in Parkinson's disease". In: *Brain* 143.11, pp. 3393–3407. DOI: 10.1093/BRAIN/AWAA297.

Nabi, Ali and Jeff Moehlis (2011). "Single input optimal control for globally coupled neuron networks". In: *Journal of Neural Engineering* 8 (6). DOI: 10.1088/1741-2560/8/6/065008.

Neher, Erwin (2015). "Merits and Limitations of Vesicle Pool Models in View of Heterogeneous Populations of Synaptic Vesicles". In: *Neuron* 87 (6). DOI: 10.1016/j.neuron.2015.08.038.

Netoff, Theoden, Michael A. Schwemmer, and Timothy J. Lewis (2012). "Experimentally estimating phase response curves of neurons: Theoretical and practical issues". In: DOI: 10.1007/978-1-4614-0739-3_5.

Neumann, Wolf-Julian, Leon A Steiner, and Luka Milosevic (2023). "Neurophysiological mechanisms of deep brain stimulation across spatiotemporal resolutions". In: *Brain*. DOI: 10.1093/brain/awad239.

Nie, Yingnan, Xuanjun Guo, Xiao Li, Xinyi Geng, Yan Li, Zhaoyu Quan, Guanyu Zhu, Zixiao Yin, Jianguo Zhang, and Shouyan Wang (2021). "Real-time removal of stimulation artifacts in closed-loop deep brain stimulation". In: *Journal of Neural Engineering* 18 (6). DOI: 10.1088/1741-2552/ac3cc5.

Notbohm, Annika, Jürgen Kurths, and Christoph S. Herrmann (Feb. 2016). "Modification of brain oscillations via rhythmic light stimulation provides evidence for entrainment but not for superposition of event-related responses". In: *Frontiers in Human Neuroscience* 10.FEB2016. DOI: 10.3389/fnhum.2016.00010.

Noury, Nima, Joerg F. Hipp, and Markus Siegel (2016). "Physiological processes non-linearly affect electrophysiological recordings during transcranial electric stimulation". In: *NeuroImage* 140. DOI: 10.1016/j.neuroimage.2016.03.065.

Nowak, Magdalena, Catharina Zich, and Charlotte J. Stagg (Apr. 2018). "Motor Cortical Gamma Oscillations: What Have We Learnt and Where Are We Headed?" In:

Current Behavioral Neuroscience Reports 5.2, pp. 136–142. DOI: 10.1007/s40473-018-0151-z.

Oehrn, Carina R, Stephanie Cernera, Lauren H Hammer, Maria Shcherbakova, Jiaang Yao, Amelia Hahn, Sarah Wang, Jill L Ostrem, Simon Little, and Philip A Starr (2023). "Personalized chronic adaptive deep brain stimulation outperforms conventional stimulation in Parkinson's disease". In: *medRxiv*. DOI: 10.1101/2023.08.03.23293450.

Okun, Michael S., Hubert H. Fernandez, Samuel S. Wu, Lindsey Kirsch-Darrow, Dawn Bowers, Frank Bova, Michele Suelter, Charles E. Jacobson IV, Xinping Wang, Clifford W. Gordon, Pam Zeilman, Janet Romrell, Pam Martin, Herbert Ward, Ramon L. Rodriguez, and Kelly D. Foote (2009). "Cognition and mood in Parkinson's disease in subthalamic nucleus versus globus pallidus interna deep brain stimulation: The COMPARE trial". In: *Annals of Neurology* 65 (5). DOI: 10.1002/ana.21596.

Oliveria, Seth F (2018). "The dark history of early deep brain stimulation". In: *The Lancet Neurology* 17 (9). DOI: 10.1016/s1474-4422(18)30237-0.

Onslow, Angela C.E., Matthew W. Jones, and Rafal Bogacz (Aug. 2014). "A canonical circuit for generating phase-amplitude coupling". In: *PLoS ONE* 9.8, e102591. DOI: 10.1371/journal.pone.0102591.

Oswal, Ashwini, Martijn Beudel, Ludvic Zrinzo, Patricia Limousin, Marwan Hariz, Tom Foltynie, Vladimir Litvak, and Peter Brown (2016). "Deep brain stimulation modulates synchrony within spatially and spectrally distinct resting state networks in Parkinson's disease". In: *Brain* 139 (5). DOI: 10.1093/brain/aww048.

Oswal, Ashwini, Peter Brown, and Vladimir Litvak (2013). *Synchronized neural oscillations and the pathophysiology of Parkinson's disease*. DOI: 10.1097/WCO.0000000000000034.

Ou, Zejin, Jing Pan, Shihao Tang, Danping Duan, Danfeng Yu, Huiqi Nong, and Zhi Wang (2021). "Global Trends in the Incidence, Prevalence, and Years Lived With Disability of Parkinson's Disease in 204 Countries/Territories From 1990 to 2019". In: *Frontiers in Public Health* 9. DOI: 10.3389/fpubh.2021.776847.

Ozen, Simal, Anton Sirota, Mariano A. Belluscio, Costas A. Anastassiou, Eran Stark, Christof Koch, and György Buzsáki (2010). "Transcranial electric stimulation entrains cortical neuronal populations in rats". In: *Journal of Neuroscience* 30 (34). DOI: 10.1523/JNEUROSCI.5252-09.2010.

Ozturk, Musa, Ashwin Viswanathan, Sameer A. Sheth, and Nuri F. Ince (2021). "Electroceutically induced subthalamic high-frequency oscillations and evoked compound activity may explain the mechanism of therapeutic stimulation in Parkinson's disease". In: *Communications Biology* 4 (1). DOI: 10.1038/s42003-021-01915-7.

Papasavvas, Christoforos A., Andrew J. Trevelyan, Marcus Kaiser, and Yujiang Wang (Mar. 2020). "Divisive gain modulation enables flexible and rapid entrainment in a neocortical microcircuit model". In: *Journal of Neurophysiology* 123.3, pp. 1133–1143. DOI: 10.1152/JN.00401.2019.

Pérez-Cervera, Alberto, Tere M-Seara, and Gemma Huguet (Sept. 2019). "A Geometric Approach to Phase Response Curves and Its Numerical Computation Through the Parameterization Method". In: *Journal of Nonlinear Science* 29.6, pp. 2877–2910. DOI: 10.1007/s00332-019-09561-4.

Peterson, Adam J., Dexter R.F. Irvine, and Peter Heil (2014). "A model of synaptic vesicle-pool depletion and replenishment can account for the interspike interval

distributions and nonrenewal properties of spontaneous spike trains of auditory-nerve fibers". In: *Journal of Neuroscience* 34 (45). DOI: 10.1523/JNEUROSCI.0903-14.2014.

Pietras, Bastian, Federico Devalle, Alex Roxin, Andreas Daffertshofer, and Ernest Montbrió (2019). "Exact firing rate model reveals the differential effects of chemical versus electrical synapses in spiking networks". In: *Physical Review E* 100 (4). DOI: 10.1103/PhysRevE.100.042412.

Pikovsky, Arkady, Michael Rosenblum, Jürgen Kurths, and Robert C. Hilborn (2002). "Synchronization: A Universal Concept in Nonlinear Science". In: *American Journal of Physics* 70 (6). DOI: 10.1119/1.1475332.

Pycroft, Laurie, John Stein, and Tipu Aziz (Jan. 2018). "Deep brain stimulation: An overview of history, methods, and future developments". In: *Brain and Neuroscience Advances* 2, p. 239821281881601. DOI: 10.1177/2398212818816017.

Qian, Xing, Yue Chen, Yuan Feng, Bozhi Ma, Hongwei Hao, and Luming Li (2017). "A method for removal of deep brain stimulation artifact from local field potentials". In: *IEEE Transactions on Neural Systems and Rehabilitation Engineering* 25 (12). DOI: 10.1109/TNSRE.2016.2613412.

Qu, Lei, Yulia Akbergenova, Yunming Hu, and Thomas Schikorski (2009). "Synapse-to-synapse variation in mean synaptic vesicle size and its relationship with synaptic morphology and function". In: *Journal of Comparative Neurology* 514 (4). DOI: 10.1002/cne.22007.

Ramírez, Rey R., Brian H. Kopell, Christopher R. Butson, Bradley C. Hiner, and Sylvain Baillet (2011). "Spectral signal space projection algorithm for frequency domain MEG and EEG denoising, whitening, and source imaging". In: *NeuroImage* 56 (1). DOI: 10.1016/j.neuroimage.2011.02.002.

Realmuto, Jonathan, Jessica Vidmark, and Terence Sanger (2023). "Modeling deep brain stimulation evoked responses with phase oscillator networks". In: *2023 11th International IEEE/EMBS Conference on Neural Engineering (NER)*, pp. 1–4. DOI: 10.1109/NER52421.2023.10123849.

Reese, René, Arthur Leblois, Frank Steigerwald, Monika Pötter-Nerger, Jan Herzog, H. Maximilian Mehdorn, Günther Deuschl, Wassilios G. Meissner, and Jens Volkmann (2011). "Subthalamic deep brain stimulation increases pallidal firing rate and regularity". In: *Experimental Neurology* 229 (2). DOI: 10.1016/j.expneurol.2011.01.020.

Rizzoli, Silvio O. and William J. Betz (2005). "Synaptic vesicle pools". In: *Nature Reviews Neuroscience* 6 (1). DOI: 10.1038/nrn1583.

Rodriguez-Oroz, M. C., J. A. Obeso, A. E. Lang, J. L. Houeto, P. Pollak, S. Rehncrona, J. Kulisevsky, A. Albanese, J. Volkmann, M. I. Hariz, N. P. Quinn, J. D. Speelman, J. Guridi, I. Zamarbide, A. Gironell, J. Molet, B. Pascual-Sedano, B. Pidoux, A. M. Bonnet, Y. Agid, J. Xie, A. L. Benabid, A. M. Lozano, J. Saint-Cyr, L. Romito, M. F. Contarino, M. Scerrati, V. Fraix, and N. Van Blercom (2005). "Bilateral deep brain stimulation in Parkinson's disease: A multicentre study with 4 years follow-up". In: *Brain* 128 (10). DOI: 10.1093/brain/awh571.

Rosenbaum, Robert, Andrew Zimnik, Fang Zheng, Robert S. Turner, Christian Alzheimer, Brent Doiron, and Jonathan E. Rubin (2014). "Axonal and synaptic failure suppress the transfer of firing rate oscillations, synchrony and information during high frequency deep brain stimulation". In: *Neurobiology of Disease* 62. DOI: 10.1016/j.nbd.2013.09.006.

Rosenmund, Christian and Charles F. Stevens (1996). "Definition of the readily releasable pool of vesicles at hippocampal synapses". In: *Neuron* 16 (6). DOI: 10.1016/S0896-6273(00)80146-4.

Schäfer, Garsten, Michael G. Rosenblum, Jürgen Kurths, and Hans Henning Abel (1998). "Heartbeat synchronized with ventilation". In: *Nature* 392 (6673). DOI: 10.1038/32567.

Scheller, Ute, Roxanne Lofredi, Bernadette C.M. van Wijk, Assel Saryyeva, Joachim K. Krauss, Gerd Helge Schneider, Daniel Kroneberg, Patricia Krause, Wolf Julian Neumann, and Andrea A. Kühn (2019). "Pallidal low-frequency activity in dystonia after cessation of long-term deep brain stimulation". In: *Movement Disorders* 34 (11). DOI: 10.1002/mds.27838.

Schmidt, Stephen L., David T. Brocker, Brandon D. Swan, Dennis A. Turner, and Warren M. Grill (2020). "Evoked potentials reveal neural circuits engaged by human deep brain stimulation". In: *Brain Stimulation* 13 (6). DOI: 10.1016/j.brs.2020.09.028.

Schor, Jonathan S., Isabelle Gonzalez Montalvo, Perry W.E. Spratt, Rea J. Brakaj, Jasmine A. Stansil, Emily L. Twedell, Kevin J. Bender, and Alexandra B. Nelson (2022). "Therapeutic Deep Brain Stimulation Disrupts Movement-Related Subthalamic Nucleus Activity in Parkinsonian Mice". In: *eLife* 11. DOI: 10.7554/elife.75253.

Schor, Jonathan S. and Alexandra B. Nelson (2019). "Multiple stimulation parameters influence efficacy of deep brain stimulation in parkinsonian mice". In: *Journal of Clinical Investigation* 129 (9). DOI: 10.1172/JCI122390.

Schulder, Michael, Akash Mishra, Antonios Mammis, Andres Horn, Alexandre Boutet, Patric Blomstedt, Stephan Chabardes, Oliver Flouty, Andres M. Lozano, Joseph S. Neimat, Francisco Ponce, Philip A. Starr, Joachim K. Krauss, Marwan Hariz, and Jin Woo Chang (2023). "Advances in Technical Aspects of Deep Brain Stimulation Surgery". In: *Stereotactic and Functional Neurosurgery* 101 (2). DOI: 10.1159/000529040.

Sermon, James J., Moaad Benjaber, Benoit Duchet, Juan Anso, Maria Olaru, Philip A. Starr, and Timothy Denison (2024a). "1:2 entrainment is not a device-induced artefact, except when it is". In: *Brain Stimulation* 17.2, pp. 149–151. DOI: 10.1016/j.brs.2024.01.010.

Sermon, James J., Maria Olaru, Juan Anso, Stephanie Cernera, Simon Little, Maria Shcherbakova, Rafal Bogacz, Philip A. Starr, Timothy Denison, and Benoit Duchet (2023). "Sub-harmonic entrainment of cortical gamma oscillations to deep brain stimulation in Parkinson's disease: Model based predictions and validation in three human subjects". In: *Brain Stimulation*. DOI: 10.1016/j.brs.2023.08.026.

Sermon, James J., Christoph Wiest, Huiling Tan, Timothy Denison, and Benoit Duchet (2024b). "Evoked Resonant Neural Activity Long-Term Dynamics can be Reproduced by a Computational Model with Vesicle Depletion". In: *bioRxiv*. DOI: 10.1101/2024.02.25.582012.

Shahlaie, Kiarash, Paul S. Larson, and Philip A. Starr (2011). "Intraoperative computed tomography for deep brain stimulation surgery: Technique and accuracy assessment". In: *Neurosurgery* 68 (SUPPL. 1). DOI: 10.1227/NEU.0b013e31820781bc.

Sinclair, Nicholas C., James B. Fallon, Kristian J. Bulluss, Wesley Thevathasan, and Hugh J. McDermott (2019). "On the neural basis of deep brain stimulation evoked

resonant activity". In: *Biomedical Physics and Engineering Express* 5 (5). DOI: 10.1088/2057-1976/ab366e.

Sinclair, Nicholas C., Hugh J. McDermott, Kristian J. Bulluss, James B. Fallon, Thushara Perera, San San Xu, Peter Brown, and Wesley Thevathasan (May 2018). "Subthalamic nucleus deep brain stimulation evokes resonant neural activity". In: *Annals of Neurology* 83 (5), pp. 1027–1031. DOI: 10.1002/ana.25234.

Sinclair, Nicholas C., Hugh J. McDermott, Wee Lih Lee, San San Xu, Nicola Acevedo, Angus Begg, Thushara Perera, Wesley Thevathasan, and Kristian J. Bulluss (2022). "Electrically evoked and spontaneous neural activity in the subthalamic nucleus under general anesthesia". In: *Journal of Neurosurgery* 137 (2). DOI: 10.3171/2021.8.JNS204225.

Sironi, Vittorio A. (2011). "Origin and evolution of deep brain stimulation". In: *Frontiers in Integrative Neuroscience* 5. DOI: 10.3389/fnint.2011.00042.

Smyth, Clay, Md Fahim Anjum, Shravanan Ravi, Timothy Denison, Philip Starr, and Simon Little (2023). "Adaptive Deep Brain Stimulation for sleep stage targeting in Parkinson's disease". In: *Brain Stimulation* 16.5, pp. 1292–1296. DOI: https://doi.org/10.1016/j.brs.2023.08.006.

Sorkhabi, Majid Memarian, Moaad Benjaber, Peter Brown, and Timothy Denison (2020). "Physiological Artifacts and the Implications for Brain-Machine-Interface Design". In: vol. 2020-October. DOI: 10.1109/SMC42975.2020.9283328.

Stanslaski, Scott, Jeffrey Herron, Tom Chouinard, Duane Bourget, Ben Isaacson, Vaclav Kremen, Enrico Opri, William Drew, Benjamin H. Brinkmann, Aysegul Gunduz, Tom Adamski, Gregory A. Worrell, and Timothy Denison (2018). "A Chronically Implantable Neural Coprocessor for Investigating the Treatment of Neurological Disorders". In: *IEEE Transactions on Biomedical Circuits and Systems* 12 (6). DOI: 10.1109/TBCAS.2018.2880148.

Staras, Kevin, Tiago Branco, Jemima J. Burden, Karine Pozo, Kevin Darcy, Vincenzo Marra, Arjuna Ratnayaka, and Yukiko Goda (2010). "A Vesicle Superpool Spans Multiple Presynaptic Terminals in Hippocampal Neurons". In: *Neuron* 66 (1). DOI: 10.1016/j.neuron.2010.03.020.

Starr, Philip A. (2002). "Placement of deep brain stimulators into the subthalamic nucleus or globus pallidus internus: Technical approach". In: *Stereotactic and Functional Neurosurgery* 79 (3-4). DOI: 10.1159/000070828.

Steiner, Leon A. and Luka Milosevic (2023). "A convergent subcortical signature to explain the common efficacy of subthalamic and pallidal deep brain stimulation". In: *Brain Communications* 5 (2). DOI: 10.1093/braincomms/fcad033.

Steiner, Leon Amadeus, Federico J. Barreda Tomás, Henrike Planert, Henrik Alle, Imre Vida, and Jörg R.P. Geiger (2019). "Connectivity and dynamics underlying synaptic control of the subthalamic nucleus". In: *Journal of Neuroscience* 39 (13). DOI: 10.1523/JNEUROSCI.1642-18.2019.

Stiefel, Klaus M., Boris S. Gutkin, and Terrence J. Sejnowski (2008). "Cholinergic neuromodulation changes phase response curve shape and type in cortical pyramidal neurons". In: *PLoS ONE* 3 (12). DOI: 10.1371/journal.pone.0003947.

Südhof, Thomas C. (2012). "The presynaptic active zone". In: *Neuron* 75 (1). DOI: 10.1016/j.neuron.2012.06.012.

Swann, Nicole C., Coralie De Hemptinne, Svjetlana Miocinovic, Salman Qasim, Sarah S. Wang, Nathan Ziman, Jill L. Ostrem, Marta San Luciano, Nicholas B. Galifianakis, and Philip A. Starr (June 2016). "Gamma oscillations in the

hyperkinetic state detected with chronic human brain recordings in parkinson's disease". In: *Journal of Neuroscience* 36.24, pp. 6445–6458. DOI: 10.1523/JNEUROSCI.1128-16.2016.

Swann, Nicole C., Coralie De Hemptinne, Margaret C. Thompson, Svjetlana Miocinovic, Andrew M. Miller, Ro'Ee Gilron, Jill L. Ostrem, Howard J. Chizeck, and Philip A. Starr (May 2018a). "Adaptive deep brain stimulation for Parkinson's disease using motor cortex sensing". In: *Journal of Neural Engineering* 15.4. DOI: 10.1088/1741-2552/aabc9b.

Swann, Nicole C., Coralie De Hemptinne, Svjetlana Miocinovic, Salman Qasim, Jill L. Ostrem, Nicholas B. Galifianakis, Marta San Luciano, Sarah S. Wang, Nathan Ziman, Robin Taylor, and Philip A. Starr (2018b). "Chronic multisite brain recordings from a totally implantable bidirectional neural interface: Experience in 5 patients with Parkinson's disease". In: *Journal of Neurosurgery* 128 (2). DOI: 10.3171/2016.11.JNS161162.

Tass, Peter A and Milan Majtanik (2006). "Long-term anti-kindling effects of desynchronizing brain stimulation: A theoretical study". In: *Biological Cybernetics* 94.1, pp. 58–66. DOI: 10.1007/s00422-005-0028-6.

Thenaisie, Yohann, Chiara Palmisano, Andrea Canessa, Bart J. Keulen, Philipp Capetian, Mayte Castro Jiménez, Julien F. Bally, Elena Manferlotti, Laura Beccaria, Rodi Zutt, Grégoire Courtine, Jocelyne Bloch, Niels A. Van Der Gaag, Carel F. Hoffmann, Eduardo Martin Moraud, Ioannis U. Isaias, and M. Fiorella Contarino (2021). *Towards adaptive deep brain stimulation: Clinical and technical notes on a novel commercial device for chronic brain sensing*. DOI: 10.1088/1741-2552/ac1d5b.

Thevathasan, Wesley, Nicholas C. Sinclair, Kristian J. Bulluss, and Hugh J. McDermott (2020). "Tailoring Subthalamic Nucleus Deep Brain Stimulation for Parkinson's Disease Using Evoked Resonant Neural Activity". In: *Frontiers in Human Neuroscience* 14. DOI: 10.3389/fnhum.2020.00071.

Tiruvadi, Vineet, Ki Sueng Choi, Robert E. Gross, Robert Butera, Viktor Jirsa, and Helen Mayberg (2022). "Dynamic Oscillations Evoked by Subcallosal Cingulate Deep Brain Stimulation". In: *Frontiers in Neuroscience* 16. DOI: 10.3389/fnins.2022.768355.

Tiruvadi, Vineet, Samuel James, Bryan Howell, Mosadoluwa Obatusin, Andrea Crowell, Patricio Riva-Posse, Robert E. Gross, Cameron C. McIntyre, Helen S. Mayberg, and Robert Butera (2023). "Mitigating Mismatch Compression in Differential Local Field Potentials". In: *IEEE Transactions on Neural Systems and Rehabilitation Engineering* 31. DOI: 10.1109/TNSRE.2022.3217469.

Tsang, E. W., C. Hamani, E. Moro, F. Mazzella, U. Saha, A. M. Lozano, M. Hodaie, R. Chuang, T. Steeves, S. Y. Lim, B. Neagu, and R. Chen (June 2012). "Subthalamic deep brain stimulation at individualized frequencies for Parkinson disease". In: *Neurology* 78.24, pp. 1930–1938. DOI: 10.1212/WNL.0b013e318259e183.

Udupa, Kaviraja and Robert Chen (2015). "The mechanisms of action of deep brain stimulation and ideas for the future development". In: *Progress in Neurobiology* 133. DOI: 10.1016/j.pneurobio.2015.08.001.

Velarde, Osvaldo Matías, Germán Mato, and Damián Dellavale (Aug. 2017). "Mechanisms for pattern specificity of deep-brain stimulation in Parkinson's disease". In: *PLoS ONE* 12.8, e0182884. DOI: 10.1371/journal.pone.0182884.

Veltz, Romain and Terrence J. Sejnowski (Dec. 2015). "Periodic forcing of inhibition-stabilized networks: Nonlinear resonances and phase-amplitude coupling". In: *Neural Computation* 27.12, pp. 2477–2509. DOI: 10.1162/NECO_a_00786.

Weerasinghe, Gihan, Benoit Duchet, Christian Bick, and Rafal Bogacz (Aug. 2021). "Optimal closed-loop deep brain stimulation using multiple independently controlled contacts". In: *PLOS Computational Biology* 17.8. Ed. by Lyle J. Graham, e1009281. DOI: 10.1371/journal.pcbi.1009281.

Weerasinghe, Gihan, Benoit Duchet, Hayriye Cagnan, Peter Brown, Christian Bick, and Rafal Bogacz (2019). "Predicting the effects of deep brain stimulation using a reduced coupled oscillator model". In: *PLoS Computational Biology* 15 (8). DOI: 10.1371/journal.pcbi.1006575.

Welter, Marie Laure, Jean Luc Houeto, Anne Marie Bonnet, Paul Boulos Bejjani, Valérie Mesnage, Didier Dormont, Soledad Navarro, Philippe Cornu, Yves Agid, and Bernard Pidoux (2004). "Effects of High-Frequency Stimulation on Subthalamic Neuronal Activity in Parkinsonian Patients". In: *Archives of Neurology* 61 (1). DOI: 10.1001/archneur.61.1.89.

Wiest, C., G. Tinkhauser, A. Pogosyan, M. Bange, M. Muthuraman, S. Groppa, F. Baig, A. Mostofi, E. A. Pereira, H. Tan, P. Brown, and F. Torrecillos (Sept. 2020). "Local field potential activity dynamics in response to deep brain stimulation of the subthalamic nucleus in Parkinson's disease". In: *Neurobiology of Disease* 143. DOI: 10.1016/j.nbd.2020.105019.

Wiest, C., G. Tinkhauser, A. Pogosyan, S. He, F. Baig, F. Morgante, A. Mostofi, E. A. Pereira, H. Tan, P. Brown, and F. Torrecillos (May 2021). "Subthalamic deep brain stimulation induces finely-tuned gamma oscillations in the absence of levodopa". In: *Neurobiology of Disease* 152. DOI: 10.1016/j.nbd.2021.105287.

Wiest, C., F. Torrecillos, G. Tinkhauser, A. Pogosyan, F. Morgante, E.A. Pereira, and H. Tan (May 2022). "Finely-tuned gamma oscillations: Spectral characteristics and links to dyskinesia". In: *Experimental Neurology* 351, p. 113999. DOI: 10.1016/J.EXPNEUROL.2022.113999.

Wiest, Christoph, Shenghong He, Benoit Duchet, Alek Pogosyan, Moaad Benjaber, Timothy Denison, Harutomo Hasegawa, Keyoumars Ashkan, Fahd Baig, Ilaria Bertaina, Francesca Morgante, Erlick A. Pereira, Flavie Torrecillos, and Huiling Tan (2023). "Evoked resonant neural activity in subthalamic local field potentials reflects basal ganglia network dynamics". In: *Neurobiology of Disease* 178. DOI: 10.1016/j.nbd.2023.106019.

Williams, David, Marina Tijssen, Gerard Van Bruggen, Andries Bosch, Angelo Insola, Vincenzo Di Lazzaro, Paolo Mazzone, Antonio Oliviero, Angelo Quartarone, Hans Speelman, and Peter Brown (July 2002). "Dopamine-dependent changes in the functional connectivity between basal ganglia and cerebral cortex in humans". In: *Brain* 125.7, pp. 1558–1569. DOI: 10.1093/brain/awf156.

Wilson, Charles J., Angela Weyrick, David Terman, Nicholas E. Hallworth, and Mark D. Bevan (2004). "A Model of Reverse Spike Frequency Adaptation and Repetitive Firing of Subthalamic Nucleus Neurons". In: *Journal of Neurophysiology* 91 (5). DOI: 10.1152/jn.00924.2003.

Wilson, Hugh R. and Jack D. Cowan (1972). "Excitatory and Inhibitory Interactions in Localized Populations of Model Neurons". In: *Biophysical Journal* 12.1, pp. 1–24. DOI: 10.1016/S0006-3495(72)86068-5.

Worbe, Y., J. Yelnik, and S. Lehéricy (2010). "Basal Ganglia". In: *Encyclopedia of Behavioral Neuroscience*. Ed. by George F. Koob, Michel Le Moal, and Richard F. Thompson. Oxford: Academic Press, pp. 118–126. DOI: https://doi.org/10.1016/B978-0-08-045396-5.00170-6.

Xu, San San, Wee Lih Lee, Thushara Perera, Nicholas C. Sinclair, Kristian J. Bulluss, Hugh J. McDermott, and Wesley Thevathasan (2022). "Can brain signals and anatomy refine contact choice for deep brain stimulation in Parkinson's disease?" In: *Journal of Neurology, Neurosurgery and Psychiatry* 93 (12). DOI: 10.1136/jnnp-2021-327708.

Yousif, Nada, Michael Mace, Nicola Pavese, Roman Borisyuk, Dipankar Nandi, and Peter Bain (Jan. 2017). "A Network Model of Local Field Potential Activity in Essential Tremor and the Impact of Deep Brain Stimulation". In: *PLoS Computational Biology* 13.1, e1005326. DOI: 10.1371/journal.pcbi.1005326.

Zamora, Mayela, Sebastian Meller, Filip Kajin, James J. Sermon, Robert Toth, Moaad Benjaber, Derk-Jan Dijk, Rafal Bogacz, Gregory A. Worrell, Antonio Valentin, Benoit Duchet, Holger A. Volk, and Timothy Denison (Sept. 2021). "Case Report: Embedding "Digital Chronotherapy" Into Medical Devices—A Canine Validation for Controlling Status Epilepticus Through Multi-Scale Rhythmic Brain Stimulation". In: *Frontiers in Neuroscience* 15, p. 1196. DOI: 10.3389/fnins.2021.734265.

Zapata Amaya, Valentina, Joshua E. Aman, Luke A. Johnson, Jing Wang, Remi Patriat, Meghan E. Hill, Colum D. MacKinnon, Scott E. Cooper, David Darrow, Robert McGovern, Noam Harel, Gregory F. Molnar, Michael C. Park, Jerrold L. Vitek, and David Escobar Sanabria (2023). "Low-frequency deep brain stimulation reveals resonant beta-band evoked oscillations in the pallidum of Parkinson's Disease patient". In: *Frontiers in Human Neuroscience* 17. DOI: 10.3389/fnhum.2023.1178527.

Zhang, Milin, Zijian Tang, Xilin Liu, and Jan Van der Spiegel (2020). *Electronic neural interfaces*. DOI: 10.1038/s41928-020-0390-3.